Stationaire, isotoop-tijdafhankelijke kinetische analyse en multischaalmodellering van de kobalt-gekatalyseerde Fischer-Tropsch-Synthese

Cobalt Catalyzed Fischer-Tropsch Synthesis Kinetics via Steady State Isotopic Transient Kinetic Analysis and Multi-Scale Modeling

Jonas Van Belleghem

Promotoren: prof. dr. ir. J. W. Thybaut, prof. dr. ir. G. B. Marin
Proefschrift ingediend tot het behalen van de graad van
Doctor in de ingenieurswetenschappen: chemische technologie

Vakgroep Chemische Proceskunde en Technische Chemie
Voorzitter: prof. dr. ir. G. B. Marin
Faculteit Ingenieurswetenschappen en Architectuur
Academiejaar 2016 - 2017

UNIVERSITEIT
GENT

ISBN 978-90-8578-971-0
NUR 952, 913
Wettelijk depot: D/2017/10.500/6

Examination board:

Prof. Dr. Ir. Gert De Cooman, voorzitter	Universiteit Gent
Prof. Dr. Ir. Mark Saeys*, secretaris	Universiteit Gent
Prof. Dr. Denis Constales*	Universiteit, Gent
Prof. Dr. Ir. De Chen*	NTNU
Dr. Sander van Bavel	Shell Global Solutions
Dr. Vitaly Ordomsky*	CNRS - Université Lille
Prof. Dr. Ir. Joris W. Thybaut, promotor	Universiteit Gent
Prof. Dr. Ir. Guy B. Marin, promotor	Universiteit Gent

*member of the faculty reading committee

Universiteit Gent
Faculteit Ingenieurswetenschappen en Architectuur
Vakgroep Chemische Proceskunde en Technische Chemie
Laboratorium voor Chemische Techniek
Technologiepark 914
B-9052 Gent
België
Tel.: ++32 (0)9 331 17 57
Fax: ++32 (0)9 331 17 59
http://www.lct.ugent.be

This work was supported by a doctoral fellowship from the Fund for Scientific Research Flanders (FWO), the 'Long Term Structural Methusalem Funding by the Flemish Government’, BRISK – Biofuels Research Infrastructure for Sharing Knowledge – for a transnational access grant and the STEVIN Supercomputer Infrastructure at Ghent University, funded by Ghent University, the Flemish Supercomputer Center (VSC), the Hercules Foundation and the Flemish Government – department EWI.

Acknowledgements

Dankwoord

Vier jaar, zo veel tijd is erover gegaan om het onderhavige werk neer te schrijven. Deze periode heeft mij zowel op persoonlijk als op wetenschappelijk vlak veel bijgebracht en ik ben ervan overtuigd dat ik de komende jaren nog vaak aan mijn doctoraatsperiode zal terugdenken. Verschillende mensen verdienen het om hier vermeld te worden en hebben elk op hun manier bijgedragen tot het tot stand komen van dit werk.

Vooreerst wil ik Prof. Guy B. Marin bedanken om mij toe te laten om aan het Labo voor Chemische Technologie (LCT) een doctoraat aan te vangen. Prof. Joris W. Thybaut ben ik dankbaar om in mij te geloven dat ik een doctoraat tot een goed einde zou brengen. Daarnaast wil ik jullie beide, als promotoren van mijn doctoraat, bedanken voor het nodige geduld aan de dag te leggen bij het nalezen van mijn manuscripten en thesis. De commentaren en discussies waren voor mij zeer leerrijk en hebben zeker bijgedragen tot zowel de vorm, structuur als de wetenschappelijk inhoud van de teksten.

A special thanks also to Prof. De Chen for offering me the unique opportunity to spend the fall of 2014 at the Chemical Engineering Department of the Norwegian University of Science and Technology. The chance of performing experiments with the SSITKA set-up was certainly an added value for my development as a chemical engineer and the acquired experimental data were crucial for the progression of my PhD. Next to this, I also want to thank Cristian for helping me with the experiments. Furthermore, I also want to express my gratitude to Jia, Yanying, Andreas and other people from NTNU for their kindness during my stay.

Prof. Denis Constales wil ik ook graag bedanken voor de vele vruchtvolle discussies omtrent numerieke methodes voor het oplossen van partiële en gewone differentiaal vergelijkingen. Uw geduld, oprechte interesse en uitgebreide kennis zijn zeer waardevol geweest voor mij.

Ook een woordje van dank aan het administratief personeel en technisch personeel, meer in het bijzonder Georges, van het LCT en de mensen van de technische ondersteuning van de HPC-infrastructuur voor het meehelpen oplossen van problemen.

Daarnaast heb ik ook veel te danken aan de thesisstudenten die de thesisonderwerpen omtrent Fischer-Tropsch kozen. Ismaël, Jenoff en Arne bedankt voor alles. Ik vond de samenwerkingen steeds prettig en wens jullie het allerbeste toe.

Verder wil ik ook de mededoctoraatstudenten van het LCT bedanken voor zowel de vele wetenschappelijke discussies als de vele leuke activiteiten. In het bijzonder wil ik Bart, die ondertussen het labo heeft verlaten, Kenneth en Jeroen bedanken voor hun steun, vele discussies en leuke middagpauzes.

Bedankt ook aan de vrienden van de scouts. Samen leiding geven op Zaterdagmiddag, de vele kampen, de vele vergaderingen, … waren zeer aangenaam en de ideale manier om mij van het doctoraatswerk af te leiden en eens praktisch bezig te zijn. Ook de vrienden waarmee ik samen in het middelbaar of aan de universiteit heb gestudeerd wil ik via deze weg bedanken om van tijd tot tijd voor de nodige afleiding te zorgen. Zeker ook Tobias, bedankt om tijdens mijn verblijf aan NTNU tot in Trondheim af te komen.

Daarnaast wil ik zeker mijn familie en, in het bijzonder mijn ouders, de ouders van mijn liefste schat en broer bedanken voor de onvoorwaardelijke steun tijdens de voorbije vier jaar. We, Jolien en ik, kunnen altijd bij jullie terecht.

En dat brengt mij bij de laatste persoon die ik wil bedanken; mijn allerliefste schat, Jolien. De voorbije jaren zijn voor mij niet altijd even gemakkelijk geweest. Toch, ondanks alles, stond jij altijd met open armen voor mij klaar. Dit doctoraat had er zonder jou niet geweest.

Jonas

Herfst 2016

Table of Contents

Acknowledgements .... **i**

Table of Contents .... **iii**

List of Figures .... **ix**

List of Tables .... **xxiii**

List of Symbols .... **xxvii**

Glossary .... **xli**

Summary .... **xlvii**

Samenvatting .... **lxi**

Chapter 1 Introduction **1**

1.1 Feedstocks – Gas to Liquids, Coal to Liquids and Biomass to Liquids (GtL, CtL and BtL) 2

  1.1.1 Gas-to-Liquids (GtL) FTS 2

  1.1.2 Coal to Liquids (CtL) FTS 5

  1.1.3 Biomass to Liquids (BtL) FTS 5

1.2 Process overview 6

  1.2.1 Syngas production 6

1.2.2 The FTS step 7
1.3 FTS chemistry 12
1.3.1 Product distribution 12
1.3.2 Catalysts 14
1.3.3 Reaction mechanism 15
1.3.4 Metal particle size effects 19
1.4 Multi-scale modelling 21
1.4.1 Microkinetic modeling 21
1.4.2 Steady State Isotopic Transient Kinetic Analysis (SSITKA) 22
1.4.3 Industrial reactor modeling 24
1.5 Scope and outline of the thesis 24
1.6 References 26
Chapter 2 Methodology 33
2.1 Experimental procedures 34
2.1.1 Steady State Isotopic Transient Kinetic Analysis set-up 34
2.1.2 Experimental data treatment 37
2.1.3 Catalyst preparation, characterization, activation and testing 39
2.2 Modeling procedures 40
2.2.1 Mircokinetic modeling of metal catalysis 40
2.2.2 Vienna Ab Initio Simulation Package (VASP) 48
2.2.3 Reaction network generation 49
2.2.4 Reactor equations 51
2.2.5 Numerical routines 54
2.2.6 Regression 57
2.2.7 Reaction path analysis 60

2.3 References 62

Chapter 3 A Single-Event MicroKinetic Model for the Cobalt Catalyzed Fischer-Tropsch Synthesis* 67

3.1 Introduction 68
3.2 Procedures 69
  3.2.1 Experimental data 69
  3.2.2 Modeling procedures 70
3.3 Results and discussion 78
  3.3.1 Experimental data 78
  3.3.2 Regression results 81
  3.3.3 Assessment of the model parameters 87
  3.3.4 Surface coverages 92
3.4 Deviations from the ASF distribution: methane and ethene selectivity 95
3.5 Degree of rate control analysis 99
3.6 Impact of atomic chemisorption enthalpies on catalyst performance 101
3.7 Comparison between Fe and Co catalysts. 103
3.8 Conclusions 107
3.9 References 108

Chapter 4 Numerical Methods and Complex Reaction Network Generation for Steady State Isotopic Transient Kinetic Analysis* 115

4.1 Introduction 116
4.2 Modeling procedures 118
  4.2.1 Numerical integration 118
  4.2.2 Moving grid 124
  4.2.3 Error analysis 124

4.2.4 The Jacobian Matrix 125
4.2.5 Microkinetic model 127
4.3 Reaction network generation accounting for isotopes 128
4.3.1 Impact on reaction network generation 128
4.3.2 Reducing the number of species and elementary steps 129
4.3.3 Expression for the net production rates 132
4.4 Effect of numerical methods on the required CPU time 138
4.4.1 Selection of a numerical discretization scheme 138
4.4.2 CPU time reduction by semi-analytical treatment of the Jacobian matrix 141
4.4.3 Selection of a backward differentiation solver 142
4.5 Effect of the level of detail accounted for in the reaction network 144
4.6 Kinetic simulations 147
4.7 Conclusions 150
4.8 References 151

Chapter 5 Microkinetic Model Validation Based on Steady State Isotopic Transient Kinetic Analysis 155

5.1 Introduction 156
5.2 Procedures 157
5.2.1 Experimental data 157
5.2.2 Modeling procedures 157
5.3 The Single-Event MicroKinetic model 159
5.3.1 Rate coefficients and reaction rate expressions 162
5.4 Results 167
5.4.1 Experimental Results 167
5.4.2 Chemisorption energies 170

- 5.4.3 Regression results 172
- 5.4.4 Assessment of the model parameters 177
- 5.4.5 Surface coverages 182
- 5.4.6 Reaction path analysis 184
- 5.5 Conclusions 187
- 5.6 References 189

Chapter 6 Simulation of an Industrial Trickle Bed Reactor 193

- 6.1 Introduction 194
- 6.2 Multi-scale reactor model 197
  - 6.2.1 Models for the different scales 197
  - 6.2.2 Correlations and thermodynamic models 205
- 6.3 Numerical solution strategy 216
  - 6.3.1 Pellet scale 216
  - 6.3.2 Reactor scale 217
- 6.4 Simulation results 220
  - 6.4.1 Pellet scale 220
  - 6.4.2 Reactor scale 226
- 6.5 Conclusions 237
- 6.6 References 238

Chapter 7 Conclusions and Future Work 243

Appendix A: Gas and liquid properties 249

- A.1 Gas phase properties 249
- A.2 Liquid phase properties 257
- A.3 References 264

List of Figures

Figure 1-1: West Texas Intermediate crude oil price in US $ per barrel (red) [1] and the annual number of research papers published on the topic ‘Fischer-Tropsch Synthesis’ (green) [2]. The crude oil price is adjusted for inflation by means of the Consumer Price Index. 2

Figure 1-2: Generalized overview of a Fischer-Tropsch Synthesis production facility [8]. 6

Figure 1-3: A typical obtained product distribution in commercial operation at High Temperature Fischer-Tropsch (green) and Low Temperature Fischer-Tropsch (red) conditions [8]. 8

Figure 1-4: High Temperature Fischer-Tropsch (HTFT) reactor technologies. (a): Circulating Fluidized Bed Reactor (CFBR). (b): Fixed Fluidized Bed Reactor (FFBR). Adopted from [5]......9

Figure 1-5: Low Temperature Fischer-Tropsch (LTFT) reactor technologies. (a): Slurry Bubble Column Reactor (SBCR). (B): Multi-Tubular Trickle Bed Reactor (MTTBR). Adopted from [9]. 11

Figure 1-6: Typical product spectrum of the Co catalysed Fischer-Tropsch Synthesis. Adopted from [28]. (a): Molar fraction as function of the carbon number. (b): Alkene to alkane ratio as function of the carbon number. 13

Figure 1-7: The carbene mechanism as proposed by Brady and Pettit [68, 69]............................16

Figure 1-8: The CO insertion mechanism as proposed by Pichler and Schulz [88]. 18

Figure 1-9: The hydroxycarbene mechanism [89]. 19

Figure 1-10: Structure sensitivity relationships. Adopted from [90]. 20

Figure 1-11: The Co particle size effect on the Turnover Frequency. Adopted from [92]. 21

Figure 2-1: Schematic representation of the Steady State Isotopic Transient Kinetic Analysis set-up at NTNU. The blue lines enclose the feed section. The red rectangle encompasses the reactor section. The analysis section is indicated by the yellow rectangle [1]. 35

Figure 2-2: Automated reaction network generation. (a) and (d) Standardized label representation of metal ethyl and metal propyl respectively. (b) and (c) Boolean matrix representation of metal ethyl and metal propyl respectively. Adapted from Lozano-Blanco et al. [18]. 50

Figure 3-1: CO conversion, X_{CO}, as a function of space time, $W/F_{CO,0}$, at a H_2/CO molar inlet ratio of 10, a CO inlet partial pressure of 5.5 kPa, a total pressure of 185 kPa and different temperatures: ■, full line: 483K; ●, dashed line: 493 K; ▲, dotted line: 503K. The symbols correspond to the experimental observations, the lines correspond to the model simulations obtained by integrating eq. [2–27] and eq. [2–28] in which the net production rates are calculated as explained by eq. [2–15] and using the set of parameters of Table 3-4. 79

Figure 3-2: Selectivity, S_i, toward the different observed *n*-alkanes (a) and 1-alkenes (b) as a function of the temperature at H_2/CO molar inlet ratio of 10, a CO inlet partial pressure of 5.5 kPa and a total pressure of 185 kPa at 6 % CO conversion. The symbols correspond to the experimental observations, the lines to the model simulations obtained by integrating eq. [2-27] and eq. [2–28] in which the net production rates are calculated as explained by eq. [2–15] and using the set of parameters of Table 3-4. ■, full line: C_1; ●, dashed line: C_2; ▲, dotted line: C_3; ▼, dash dotted line: C_4; ♦ , dash dot dotted line: C_5. 79

Figure 3-3: CO conversion, X_{CO}, as function of space time, $W/F_{CO,0}$, at a temperature of 493 K, a CO inlet partial pressure of 5.5 kPa, a total pressure of 185 kPa and different H_2/CO molar inlet ratios: ■, full line: 5 ●, dashed line: 7; ▲ and dotted line: 10. The symbols correspond to the experimental observations, the lines correspond to the model simulations obtained by integrating eq. [2–27] and eq. [2–28] in which the net production rates are calculated as explained by eq. [2–15] and using the set of parameters of Table 3-4. 81

Figure 3-4: Experimental and model calculated outlet molar flow rates, F_i, at 3 - 10 H_2/CO molar inlet ratios, 483 K-503 K temperature range, 3.7 kPa-16.7 kPa CO inlet partial pressure, 7.2 - 36.3 $(kg_{cat}s)mol_{CO}^{-1}$ space time, $W/F_{CO,0}$, and 185 kPa total pressure. The calculated outlet molar flow rates are obtained by integrating eq. [2–27] and eq. [2–28] in which the net production rates are calculated as explained by eq. [2–15] and using the set of parameters given in Table 3-4. (a): methane; (b): ethane (○) and propane (△); (c): *n*-butane (▽) and *n*-pentane (◇); (d): *n*-hexane (+); (e): ethene (○) and propene (△) and (f): 1-butene (▽) and 1-pentene (◇). 86

Figure 3-5: Residual diagrams for the CO conversion, X_{CO}, and outlet molar flow rates, F_i, of *n*-alkanes and 1-alkenes as a function of CO inlet partial pressure (a, d and g respectively), H_2/CO molar inlet ratio (b, e and h respectively) and temperature (c, f and i respectively) at 3 – 10 H_2/CO molar inlet ratio, 483 K – 503 K temperature range, 3.7 kPa – 16.7 kPa CO inlet partial pressure, 7.2 – 36.3 $(kg_{cat}s)mol_{CO}^{-1}$ space time, $W/F_{CO,0}$, and 185 kPa total pressure. Residuals are determined by the difference between the calculated value obtained by integrating eq. [2–27] and eq. [2–28] in which the net production rates are calculated as explained by eq. [2–15] and using the set of parameters given in Table 3-4 and the experimentally observed value. For d – i: □: C_1; ○: C_2, △: C_3, ▽: C_4, ◇:C_5 , +:C_6......87

Figure 3-6: The reaction energy diagram for methane and water formation starting from CO and 3 H_2......91

Figure 3-7: The surface coverage as function of space time, $W/F_{CO,0}$. The simulation results are obtained by integrating eq. [2–27] and eq. [2–28] in which the net production rates are calculated as explained by eq. [2–15] using the set of parameters of Table 3-4. The inlet conditions for the simulations are a CO inlet partial pressure of 5.5 kPa, a H_2/CO molar inlet ratio of 10, a temperature of 483 K and a total pressure of 185 kPa. Full line – black: H^*, dashed line – black: CO^{**}, dotted line – black: O^{**}, dash dotted line – black: *, dash dot dotted line – black: OH^*, full line – grey: $C_nH_{2n+1}^*$, dashed line – grey: C^{***}, dotted line – grey: CH_2^{**}, dash dotted line – grey: $C_nH_{2n}^*$, dash dot dotted line – grey: CH^{***}. 94

Figure 3-8: Reaction path analysis at a H_2/CO molar inlet ratio of 10, a temperature of 483 K, a CO inlet partial pressure of 5.5 kPa, a total pressure of 185 kPa and space time, $W/F_{CO,0}$, 20

$(kg_{cat}s)mol_{CO}^{-1}$. The simulation is performed by integrating eq. [2–27] and eq. [2–28] in which the net production rates are calculated as explained by eq. [2–15] and using the parameters of Table 3-4. The elementary reactions indicated by black arrows are at quasi-equilibrium as confirmed by affinity calculations, see Table 3-8. The reactions which are not at quasi-equilibrium are presented by the colored arrows. The thickness of these arrows are scaled to the reaction rate. The reaction families considered in the SEMK model are assigned a separate color, i.e., CH_2^{**} insertion/deinsertion (yellow – purple), $C_nH_{2n+1}^{*}$ hydrogenation (red), beta hydride elimination/ addition (green/cyan). The other elementary steps are indicated in blue. The number indicated at the tail of an arrow is the differential disappearance factor, eq. [2–50]. The number indicated at the tip of an arrow is the differential formation factors, eq.[2–51]. H_2 has not been included not to overload the figure. 97

Figure 3-9: The degree of rate control, eq. [2–53], at (a) different temperatures (black: 483K; dark grey: 493 K; light grey: 503 K) and a H_2/CO molar inlet ratio of 10 and (b) different H_2/CO molar inlet ratios (black: 5; dark grey: 7; light grey 10) and a temperature of 483 K. The other conditions for the simulations were a CO inlet partial pressure of 5.5 kPa a total pressure of 185 kPa and a space time, $W/F_{CO,0}$, of 20 $(kg_{cat}\ s)\ mol_{CO}^{-1}$. The simulations are performed by integrating eq. [2–27] and eq. [2–28] in which the net production rates are calculated as explained by eq [2–15] and using the set of parameters given in Table 3-4. 1: H_2 chemisorption, 2: CO chemisorption, 3: CO^{**} dissociation, 4: C^{***} hydrogenation, 5: CH^{***} hydrogenation, 6: CH_2^{**} hydrogenation, 7: CH_2^{**} insertion, 8: $C_nH_{2n+1}^{*}$ hydrogenation, 9: beta hydride elimination, 10: C_nH_{2n} chemisorption, 11: O^{**} hydrogenation and 12: OH^{*} hydrogenation.................................101

Figure 3-10: The CO conversion, X_{CO}, (dotted line) and C_{5+} selectivity, S_{C5+}, (full line) as a function of the hydrogen atomic chemisorption enthalpy, Q_H, (a), the carbon atomic chemisorption enthalpy, Q_C, (b) and oxygen atomic chemisorption enthalpy, Q_O, (c) at a temperature of 493 K, a H_2/CO molar inlet ratio of 2, a total pressure of 2.0 MPa and a space time, $W/F_{CO,0}$, of 50 $(kg_{cat}s)mol_{CO}^{-1}$. The results are obtained by integrating eq. [2–27] and eq. [2–28] in which the net production rates are calculated as explained by eq [2–15] and using the set of parameters given in Table 3-4. 102

Figure 3-11: Comparison of Co to Fe catalysts. a: CO conversion, X_{CO}, as function of space time, $W/F_{CO,0}$, for Co (black) and Fe (grey) catalysts. b: surface coverage of H^{*} (full line), CO^{**}

(dashed line) and OH^{*}+O^{**} (dash dotted line) for Co (black) and Fe (grey) catalysts as function of space time. The results are obtained by integrating eq. [2–27] and eq. [2–28] in which the net production rates are calculated as explained by eq. [2–15]. For the simulations for the Co catalyst, the parameters of Table 3-4 are used. For the simulations of the Fe catalyst, the parameters reported by Lozano et al. [30] are employed. The reaction conditions were a temperature of 493 K, a H_2/CO molar inlet ratio of 2 and a total pressure of 2.0 MPa. 106

Figure 4-1: Discretization of the spatial domain. A control volume is centered around grid point x_j ranging from x_w to x_e which are points located halfway the discretization points..................118

Figure 4-2: The Total Variation Diminishing area in the flux limiter diagram [42]...................121

Figure 4-3: Graphical representation of the Jacobian matrix. Full line: Main diagonal. Squares: derivatives of the net production rate terms, i.e., the first terms of the right hand side of eq. [4-1]. Dashed lines: derivatives of the discretized convective terms of the right hand side of eq. [4-1] when using flux limiter functions, eq. [4-4] to eq. [4-6]...126

Figure 4-4: Global symmetry numbers of unlabeled and labeled propane. 129

Figure 4-5: Graphical representation of the different type of subsets introduced in the reaction network. 1: group comprising those species with a maximum carbon number, CN_{det} for which all possible isotopologues and isotopomers are followed. 2: complement of group 1 for which subsets are introduced. These subsets are illustrated for the isotopic labeled metal propyl species and is done on the basis of the labeling of the carbon atom on a position *i* in the chain with $1 \leq i \leq CN_{max} - CN_{det}$ (a and b) or the isotopic labeling of the penultimate and ultimate carbon atom (c – f). 131

Figure 4-6: Illustration of the methylene insertion and methylene deinsertion step between the two types of subsets introduced in the metal alkyl species...133

Figure 4-7: Deviation, eq. [4-9], of the simulation results obtained with the various Flux Limiter (FL) functions from the benchmark solution as function of the number of grid points. a_2= 0.1 s. $W/F_{CO,0}$ = 40 (kg_{cat} s) mol_{CO}^{-1}. Dotted line: GPR-1/2, dashed line: Superbee, full line: MUSCL, grey band: other FL functions. The simulations were performed for the methanation reaction. The results were obtained by integrating eq. [4-1] with the DASPK solver. 139

Figure 4-8: CPU time as function of the number of grid points. a_2 = 0.01 s. a: $W/F_{CO,0}$ = 4 $(kg_{cat}\ s)mol_{CO}^{-1}$. b: $W/F_{CO,0}$ = 40 $(kg_{cat}\ s)mol_{CO}^{-1}$. c: $W/F_{CO,0}$ = 400 $(kg_{cat}\ s)mol_{CO}^{-1}$. 1: Full line: Superbee, dashed line: SMART, dotted line: SPL-1/3, dash dotted line: GVA-1/2, dash dot dotted line: van Albada, grey band: MUSCL, Koren, Minmod, H-CUI, H-QUICK, SMARTER and GPR-1/2, dark grey band OSPRE and van Leer. 2: Full line: van Albada, dashed line: van Leer, dotted line: OSPRE and dash dotted line: GVA-1/2. The simulations were performed for the methanation reaction. The results were obtained by integrating eq. [4-1] with the DASPK solver. 141

Figure 4-9: Transient responses of isotopically labeled alkanes obtained with reaction networks with 3 different levels of detail (I, II and III) as function of time. I: CN_{max} = CN_{det} = 5. II: CN_{max} = 5 and CN_{det} = 2. III: CN_{max} = 5 and CN_{det} = 1 with (a) methane, (b) ethane and (c) propane. Black lines: normalized concentrations (full line: alkane with only ^{12}C, dotted line: alkane with only one ^{12}C and dash-dotted line: alkane with two ^{12}C atoms). Grey line: the total fraction of ^{12}C. $W/F_{CO,0}$ = 4 $(kg_{cat}s)mol_{CO}^{-1}$. a_2 = 0.01 s. n_{gp} = 100. The results were obtained by integrating eq. [4-1] with DASPK. 145

Figure 4-10: Normalized transient responses of propane (I) and metal propyl (II). I: Full black line: $^{12}CH_3{}^{12}CH_2{}^{13}CH_3$, dashed black line: $^{12}CH_3{}^{13}CH_2{}^{12}CH_3$, full grey line: $^{12}CH_3{}^{13}CH_2{}^{13}CH_3$, dashed grey line: $^{13}CH_3{}^{12}CH_2{}^{13}CH_3$. II: Full black line: $M^{12}CH_2{}^{12}CH_2{}^{13}CH_3$, dashed black line: $M^{12}CH_2{}^{13}CH_2{}^{12}CH_3$, dotted black line: $M^{13}CH_2{}^{12}CH_2{}^{12}CH_3$, full grey line: $M^{12}CH_2{}^{13}CH_2{}^{13}CH_3$, dashed grey line: $M^{13}CH_2{}^{12}CH_2{}^{13}CH_3$, dotted grey line: $M^{13}CH_2{}^{13}CH_2{}^{12}CH_3$. $W/F_{CO,0}$ = 4 $(kg_{cat}s)mol_{CO}^{-1}$. a_2 = 0.01 s. n_{gp} = 100. The results were obtained by integrating eq. [4-1] with DASPK. 146

Figure 5-1: Schematic representation of the application of the Message Passing Interface (MPI) to the regression software. 159

Figure 5-2: Transient responses of Ar (●), ^{12}CO (▲) and $^{12}CH_4$ (◆, — •) after a switch from $Ar/^{12}CO/H_2$ to $Kr/^{13}CO/H_2$ at a H_2/CO molar inlet ratio of 5, a CO inlet partial pressure of 5.5

kPa, a total pressure of 185 kPa, a temperature of 493 K and a space time, $W/F_{CO,0}$, of 23 $(kg_{cat}\ s)\ mol_{CO}^{-1}$. The symbols correspond to the experimental observations, the line to the model simulations obtained by integrating eqs. [2–30] – [2–35] in which the net formation rates are calculated as explained by eq [2–15] and using the reaction mechanism and set of parameters of the originally developed Single-Event MicroKinetic model, see Table 3–1 and Table 3–4. The simulated responses of Ar and ^{12}CO are not shown as these responses visually coincide with the response of $^{12}CH_4$. 160

Figure 5-3: The considered Fischer-Tropsch Synthesis reaction mechanism. 162

Figure 5-4: CO conversion, X_{CO}, as function of space time, $W/F_{CO,0}$. a: H_2/CO molar inlet ratio of 10, a CO inlet partial pressure of 5.5 kPa, a total pressure of 185 kPa and different temperature: ■, full line: 483 K; ●, dashed line: 493 K; ▲, dotted line: 503 K. b: temperature of 483 K, a CO inlet partial pressure of 5.5 kPa, a total pressure of 185 kPa and different H_2/CO molar inlet ratios: ■, full line: 5; ●, ▲, dashed line: 10. The symbols correspond to the experimental observations, the lines are obtained by integrating eq. [2–35] in which the net formation rates are calculated as explained by eq. [2–15] and using the set of parameters of Table 5-3. 167

Figure 5-5: Anderson-Schulz-Flory distribution of total concentration of alkanes and alkenes (a), alkanes (b) and alkenes (c) at a H_2/CO molar inlet ratio of 10, a CO inlet partial pressure of 5.5 kPa, a total pressure of 185 kPa, CO conversion of 7% and different temperature: □, full line: 483 K; ○, dashed line: 493 K; △, dotted line: 503 K. The symbols correspond to the experimental observations, the lines are obtained by integrating eq. [2–35] in which the net formation rates are calculated as explained by eq. [2–15] and using the set of parameters of Table 5-3. 168

Figure 5-6: CO surface residence time, τ_{CO}, (a and c) and CH_4 surface residence time, τ_{CH4}, (b and d), see eq. [2–7], as function of space time, $W/F_{CO,0}$. a and b: H_2/CO molar inlet ratio of 10, a CO inlet partial pressure of 5.5 kPa, a total pressure of 185 kPa and different temperature: ■, full line: 483 K; ●, dashed line: 493 K; ▲, dotted line: 503 K. c and d: temperature of 493 K, a CO inlet partial pressure of 5.5 kPa, a total pressure of 185 kPa and different H_2/CO molar inlet ratios: ■, full line: 5; ▲, dashed line: 10. The symbols correspond to the experimental observations, the lines are obtained by integrating eqs. [2–30] – [2–35] in which the net formation rates are calculated as explained by eq. [2-15] and using the set of parameters of Table 5-3. 170

Figure 5-7: Experimental and model calculated outlet concentrations, C_i, at 5 – 10 H_2/CO molar inlet ratio, 483 K – 503 K, a CO inlet partial pressure of 5.5 kPa, a total pressure of 185 kPa and space time, $W/F_{CO,0}$, varying between 7 and 29 $(kg_{cat}\ s)mol^{-1}$. The calculated outlet concentrations are obtained by integrating eq. [2-30] to [2–35] in which the net production rates are calculated as explained by eq. [2–15] and using the set of parameters given in Table 5-3. (a): methane (☐), ethane (○), propane (△), *n*-butane (▽), *n*-pentane (◇) and *n*-hexane (✚). (b): ethene (○), propene (△), 1-butene (▽) and 1-pentene (◇). 176

Figure 5-8: Experimental (symbols) and model calculated (lines) normalized outlet concentrations of Ar (●,—), CO(▲, – –) and CH_4 (◆, – •), at a CO inlet partial pressure of 5.5 kPa, total pressure of 185 kPa, a H_2/CO molar inlet ratio of 5 (a and b) or 10 (c), a temperature of 483 K (a and c) or 503 K (b) and a space time, $W/_{FCO,0}$, of 23 (a), 20 (b) and 29 (c) $(kg_{cat}s)mol_{CO}^{-1}$ The calculated normalized outlet concentrations are obtained by integrating eq. [2–30] to [2–35] in which the net production rates are calculated as explained by eq. [2–15] and using the set of parameters given in Table 5-3. These responses were part of the experimental data used in the regression. 176

Figure 5-9: Experimental (symbols) and model calculated (lines) normalized outlet concentrations of Ar (●,—), CO(▲, – –) and CH_4 (◆, – •), at a CO inlet partial pressure of 5.5 kPa, total pressure of 185 kPa, a H_2/CO molar inlet ratio of 5 (b) or 10 (a and c), a temperature of 493 K (a and c) or 503 K (b) and a space time, $W/_{FCO,0}$, of 17 (a), 11 (b) and 23 (c) $(kg_{cat}s)mol_{CO}^{-1}$ The calculated normalized outlet concentrations are obtained by integrating eq. [2–30] to [2–35] in which the net production rates are calculated as explained by eq. [2–15] and using the set of parameters given in Table 5-3. These responses were not part of the experimental data used in the regression and, hence, are used for model validation purposes. 177

Figure 5-10: The surface coverage as a function of space time, $W/F_{CO,0}$. a-c: the surface coverage on both site types scaled with their relative abundance, indicated by "×". d-f: The surface coverage on the "*" sites. g-h: The surface coverage on the "#" sites. The simulation results are obtained by integrating eq. [2–35] in which the net formation rates are calculated as explained by eq. [2–15] and using the set of parameters of Table 5-3. The inlet conditions for the simulation are a CO inlet partial pressure of 5.5 kPa, a H_2/CO molar inlet ratio of 10, a temperature of 483 K and a total pressure of 185kPa. Full line – black:$H^{\$}$; dashed line – black: $CO^{\$\$}$; dotted line – black: $O^{\$\$}$; dash dotted line – black: \$; dash dot dotted line – black: $OH^{\$}$; open dotted line-black: $HCO^{\$}$; full line – grey: $C_nH_{2n+1}{}^{\$}$; dashed line-grey: $C^{\$\$\$}$; dotted line – grey: $CH_2{}^{\$\$}$; dash dotted line-grey: $C_nH_{2n}{}^{\$}$; dash dot dotted line – grey: $CH^{\$\$\$}$; open dotted line – grey: $HCOH^{\$\$}$. (\$ = ×, * or #). 184

Figure 5-11: Reaction path analysis at a H_2/CO molar inlet ratio of 10, a temperature of 483 K, a CO inlet partial pressure of 5.5 kPa and space time, $W/F_{CO,0}$, of 23 $(kg_{cat}s)mol_{CO}{}^{-1}$. The simulation is performed by integrating eq. [2–35] in which the net formation rates are calculated as explained by eq. [2–15] and using the set of parameters of Table 5-3. The elementary reaction indicated by black arrows are at quasi-equilibrium as confirmed by affinity calculations, see eq. [2–52]. The reactions which are not at quasi-equilibrium are indicated by the colored arrows. The color of the arrow is related to the reaction rate of the elementary step as indicated. The numbers at the tail of an arrow are the differential disappearance factor, eq. [2–50]. The numbers at the tip are the differential formation factor, eq. [2–51]. The triangles indicate the direction of the net elementary reaction rate and the value in the triangle is the rate of the elementary reaction divided by the net CO consumption rate. 186

Figure 6-1: The Multi-Tubular Trickle Bed Reactor and the three scales which are accounted for by the multi-scale model. 197

Figure 6-2: The different resistances to mass transfer considered in the single gas phase reactor (a) and the gas liquid reactor (b). 201

Figure 6-3: Discretization of the pellet. Dashed lines: spheres through which diffusive flux occurs. Area between the dashed lines: the spherical shell in which the reactions take place..... 216

Figure 6-4: Solution strategy for the reactor model equations. C_i^{step1} the concentration of species *i* after the first step of the integration procedure [mol m_f^{-3}], N_i the flux of species *i* at the catalyst pellet surface [mol $(m_p^2s)^{-1}$] and C_i^l the concentration of species *i* at iteration l [mol m_f^{-3}] in the second step of the integration procedure. 218

Figure 6-5: Typical profiles in a catalyst pellet with a 4 mm diameter at 495 K, a total pressure of 2.0 MPa and a bulk H_2 to CO molar ratio of 2. The simulation results are obtained by integrating eqs. [6-1] - [6-2] with eqs. [6-4] - [6-6] as boundary conditions. The integration is performed with the DASPK solver after applying the numerical methods outlined in section 6.3. Other specifications of the catalyst pellet are provided in Table 6-1. Diffusion coefficients, liquid properties, … are calculated as explained in section 6.2.2. a: concentration of CO (—), H_2 (– –), methane (–·) and the H_2/CO molar ratio (–··). b: R_{CO} (—) and S_{C5+} (– –). c: concentration of C_2H_6 (—), C_3H_8 (– –), $_n$-C_4H_{10} (···) and C_{5+} (–·). d: concentration of C_2H_4 (—), C_3H_6 (– –), 1-C_4H_8 (···). 221

Figure 6-6: Contour plot of (a): CO consumption rate [10^{-3}mol$_{CO}$ (kg$_{cat}$ s)$^{-1}$], (b): selectivity to C_{5+} [mol mol^{-1}] and (c): C_{5+} productivity [10^{-3} mol (kg$_{cat}$s)$^{-1}$]. The total pressure was set at 2 MPa and the catalyst pellet diameter at 4 mm. The simulation results are obtained by integrating eqs. [6-1] and [6-2] with eqs. [6-4] and [6-6] as boundary conditions by applying the numerical methods outlined in section 6.3. Other specification of the catalyst pellet are provided in Table 6-1. Diffusion coefficients, liquid properties, … are calculated as explained in section 6.2.2. 223

Figure 6-7: Contour plot of (a): CO consumption rate [10^{-3}mol$_{CO}$ (kg$_{cat}$ s)$^{-1}$], (b): selectivity to C5+ [mol mol^{-1}] and (c): C_{5+} productivity [10^{-3} mol (kg$_{cat}$s)$^{-1}$]. The bulk syngas ratio was set at 2 and the catalyst pellet diameter at 4 mm. The simulation results are obtained by integrating eqs. [6-1] and [6-2] with eqs. [6-4] and [6-6] as boundary conditions by applying the numerical methods outlined in section 6.3. Other specification of the catalyst pellet are provided in Table 6-1. Diffusion coefficients, liquid properties, … are calculated as explained in section 6.2.2. ...224

Figure 6-8: Contour plot of (a): CO consumption rate [10^{-3}mol$_{CO}$ (kg$_{cat}$ s)$^{-1}$], (b): selectivity to C_{5+} [mol mol^{-1}] and (c): C_{5+} productivity [10^{-3} mol (kg$_{cat}$s)$^{-1}$]. The temperature was set at 495 K and the catalyst pellet diameter at 4 mm. The simulation results are obtained by integrating eqs. [6-1] and [6-2] with eqs. [6-4] and [6-6] as boundary conditions by applying the numerical methods outlined in section 6.3. Other specification of the catalyst pellet are provided in Table 6-1. Diffusion coefficients, liquid properties, … are calculated as explained in section 6.2.2. 224

Figure 6-9: Contour plot of (a): CO consumption rate [10^{-3}mol$_{CO}$ (kg$_{cat}$ s)$^{-1}$], (b): selectivity to C_{5+} [mol mol^{-1}] and (c): C_{5+} productivity [10^{-3} mol (kg$_{cat}$s)$^{-1}$] at (I): 2 Mpa and 495 K, (II): syngas bulk ratio of 2 and 495 K and (III): 2 Mpa and syngas bulk ratio of 2. The simulation results are obtained by integrating eqs. [6-1] and [6-2] with eqs. [6-4] and [6-6] as boundary conditions by applying the numerical methods outlined in section 6.3. Other specification of the catalyst pellet are provided in Table 6-1. Diffusion coefficients, liquid properties, … are calculated as explained in section 6.2.2. 226

Figure 6-10: Typical profiles in a FTS reactor with reactor dimensions, operating conditions and inlet compositions as in Table 6-2. The simulation results are obtained by integrating eqs. [6-1], [6-2], [6-7], [6-8], [6-13] and [6-17] with eqs. [6-4], [6-5], [6-9] and [6-19] as boundary conditions. The integration is performed with the DASPK solver after applying the numerical methods outlined in section 6.3. Diffusion coefficients, liquid properties, … are calculated as explained in section 6.2.2 . a: concentration of H_2 (—), CO (– –), and the H_2/CO molar ratio (···). b: CO conversion (– –) and temperature (—). c: concentration of CH_4 (—), C_2H_6 (– –), C_3H_8 (···), *n*-C_4H_{10} (–·) and C_{5+} (–··). d: concentration of C_2H_4 (—), C_3H_6 (– –), 1-C_4H_8 (···)....................229

Figure 6-11: Contour plot of (a): CO conversion [mol mol^{-1}], (b): C_{5+} selectivity [mol mol^{-1}] and (c): C_{5+} molar yield [mol mol^{-1}] as function of inlet bulk syngas ratio [mol mol^{-1}] and inlet temperature [K]. Other inlet conditions, reactor dimension, … are taken from Table 6-2. The simulation results are obtained by integrating eqs. [6-1], [6-2], [6-7], [6-8], [6-13] and [6-17] with eqs. [6-4], [6-5], [6-9] and [6-19] as boundary conditions. The integration is performed with the DASPK solver after applying the numerical methods outlined in section 6.3. The transfer parameters and gas and liquid properties are calculated as explained in section 6.2.2................230

Figure 6-12: Contour plot of (a): CO conversion [mol mol^{-1}], (b): C_{5+} selectivity [mol mol^{-1}] and (c): C_{5+} molar yield [mol mol^{-1}] as function of inlet pressure [MPa] and inlet temperature [K]. Other inlet conditions, reactor dimension, … are taken from Table 6-2. The simulation results are obtained by integrating eqs. [6-1], [6-2], [6-7], [6-8], [6-13] and [6-17] with eqs. [6-4], [6-5], [6-9] and [6-19] as boundary conditions. The integration is performed with the DASPK solver after applying the numerical methods outlined in section 6.3. The transfer parameters and gas and liquid properties are calculated as explained in section 6.2.2. 231

Figure 6-13: Contour plot of (a): CO conversion [mol mol^{-1}], (b): C_{5+} selectivity [mol mol^{-1}] and (c): C_{5+} molar yield [mol mol^{-1}] as function of the inlet bulk syngas ratio [mol mol^{-1}] and inlet pressure [MPa]. Other inlet conditions, reactor dimension, … are taken from Table 6-2. The simulation results are obtained by integrating eqs. [6-1], [6-2], [6-7], [6-8], [6-13] and [6-17] with eqs. [6-4], [6-5], [6-9] and [6-19] as boundary conditions. The integration is performed with the DASPK solver after applying the numerical methods outlined in section 6.3. The transfer parameters and gas and liquid properties are calculated as explained in section 6.2.2...............232

Figure 6-14: Contour plot of (a): CO conversion [mol mol^{-1}], (b): C_{5+} selectivity [mol mol^{-1}] and (c): C_{5+} molar yield [mol mol^{-1}] at (I): 3MPa and inlet temperature of 495 K, (II): inlet bulk syngas ratio of 2 and 495K and (III): 3MPa and bulk syngas ratio of 2. Other inlet conditions, reactor dimension, … are taken from Table 6-2. The simulation results are obtained by integrating eqs. [6-1], [6-2], [6-7], [6-8], [6-13] and [6-19] with eqs. [6-4], [6-5], [6-9] and [6-19] as boundary conditions. The integration is performed with the DASPK solver after applying the numerical methods outlined in section 6.3. The transfer parameters and gas and liquid properties are calculated as explained in section 6.2.2...233

Figure 6-15: Contour plot of the (a) maximum temperature [K] in the reactor and pressure drop [Pa] (b) as function of the inlet temperature and catalyst pellet diameter. Other inlet conditions, reactor dimension, … are taken from Table 6-2. The simulation results are obtained by integrating eqs. [6-1], [6-2], [6-7], [6-8], [6-13] and [6-17] with eqs. [6-4], [6-5], [6-9] and [6-19] as boundary conditions. The integration is performed with the DASPK solver after applying the numerical methods outlined in section 6.3. The transfer parameters and gas and liquid properties are calculated as explained in section 6.2.2...234

Figure 6-16: Temperature profile in the reactor in a gas (—) or a gas-liquid reactor (– –). Inlet conditions, reactor dimension, … are taken from Table 6-2. The simulation results are obtained by integrating eqs. [6-1], [6-2], [6-10], [6-11], [6-14] and [6-18] with eqs. [6-4], [6-5], [6-9] and [6-19] as boundary conditions. The integration is performed with the DASPK solver after applying the numerical methods outlined in section 6.3. The transfer parameters and gas and liquid properties are calculated as explained in section 6.2.2. 235

Figure 6-17: Temperature field in the catalyst bed of a gas-solid reactor. Inlet conditions, reactor dimension, … are taken from Table 6-2. The simulation results are obtained by integrating eqs. [6-1], [6-2], [6-7],[6-8],[6-13], [6-15], [6-16] and [6-17] with eqs. [6-4], [6-5], [6-9], [6-19] and

[6-20] as boundary conditions. The integration is performed with the DASPK solver after applying the numerical methods outlined in section 6.3. The transfer parameters and gas and liquid properties are calculated as explained in section 6.2.2 236

List of Tables

Table 1-1: Fischer-Tropsch Synthesis (FTS) production facilities [3-5, 7-9]. 3

Table 2-1: The switch time constant of various SSITKA/Step-response set-ups. 36

Table 2-2: Summary of criteria to assess the presence of intrinsic kinetic conditions. 51

Table 3-1: Elementary reactions and reaction families considered in the reaction network [35]. .73

Table 3-2: Rate expression for the elementary steps considered in the reaction network. 75

Table 3-3: The net rate of formation of the various gas phase components and surface species...77

Table 3-4: Forward single-event pre-exponential factors, $\tilde{A}^f$, activation energies, E_a^f, atomic chemisorption enthalpies of hydrogen, Q_H, carbon, Q_C, and oxygen, Q_O, surface reaction enthalpies, ΔH_r^0, and single-event surface reaction entropies, $\Delta\tilde{S}_r^0$ at 493 K. The values in plain font are determined a priori from open source data bases and statistical thermodynamic considerations, see section 2.2.1.3. The values indicated in bold font are estimated by non-linear regression of the model to the experimental data in which the responses are simulated by integrating eq. [2–27] and eq. [2–28] in which the net production rates are calculated as explained by eq. [2-15]. The values in italic font are derived from the ones obtained from the non-linear regression, see section 2.2.1.4. 83

Table 3-5: Binary correlation coefficients, eq. [2–49], between the parameter estimates reported in Table 3-4 as determined by non-linear regression of the model to the experimental data. The model responses are obtained by integrating eq. [2–27] and eq. [2–28] in which the net production rates are calculated as explained by eq. [2–15]. 1, 2 and 3: the atomic chemisorption enthalpies of hydrogen, carbon and oxygen respectively; 4, 5, 6, 7, 8, 9, 10, 11 and 12: activation energy of CO^{**} dissociation, C^{***} hydrogenation, CH^{***} hydrogenation, CH_2^{**} hydrogenation, CH_2^{**} insertion, $C_nH_{2n+1}^{*}$ hydrogenation, $C_nH_{2n+1}^{*}$ beta hydride elimination, O^{**} hydrogenation and OH^{*} hydrogenation respectively..85

Table 3-6: The surface coverages of the various surface species at a CO inlet partial pressure of 5.5 kPa, a H_2/CO molar inlet ratio of 10, temperature of 483 K, a total pressure of 185 kPa and 5 % CO conversion. The surface coverages are obtained by integrating eq. [2–27] and eq. [2–28] in which the net production rates are calculated as explained by eq [2–15] using the set of parameters of Table 3-4..93

Table 3-7: The effect of the H_2/CO molar inlet ratio, $F_{H2,0}/F_{CO,0}$, on the relative surface coverages of H^*, CH_2^{**} and CH_3^* at a CO inlet partial pressure of 5.5 kPa, a total pressure of 185 kPa, a temperature of 493 K and 5% CO conversion. The simulation results are obtained by integrating eq. [2–27] and eq. [2–28] in which the net production rates are calculated as explained by eq. [2–15] and using the set of parameters given in Table 3-4. The relative surface coverages are obtained by dividing the surface coverage of surface species *i* at a $F_{H2,0}/F_{CO,0}$ by the maximum surface coverage of surface species *i* found at the different $F_{H2,0}/F_{CO,0}$. 95

Table 3-8: The affinity [kJ mol^{-1}] of the various elementary surface reactions considered in the reaction network calculated as explained by eq. [2–52] at a CO inlet partial pressure of 5.5 kPa, a H_2/CO molar inlet ratio of 10, a total pressure of 185 kPa, a temperature of 483 K and 2 values for the space time, $W/F_{CO,0}$. The required surface coverages are obtained by integrating eq. [2–27] and eq. [2–28] in which the net production rates are calculated as explained by eq. [2–15] and using the set of parameters given in Table 3-4..98

Table 3-9: Comparison between the activation energies, E_a, and atomic chemisorption enthalpy, Q_i, for Co and Fe catalyzed FTS. The values for Co are taken from Table 3-4. The values for Fe are adopted from Lozano et al [30]. 104

Table 4-1: Reaction conditions and properties of the catalyst pellets, dilution material and reactor characteristics. 119

Table 4-2: The flux limiter functions considered in the case study. κ indicates the behavior of the FL function around r_j=1. Two values means that 2 linear schemes are mixed around r_j=1, one value indicates which linear κ scheme is followed around r_j=1. M indicates the maximum bound. [26, 28, 30, 44-50] 122

Table 4-3: Number of species in the reaction network as a function of the carbon number of the longest hydrocarbon considered in the reaction network (CN_{max}). CN_{det}: the maximum chain length of hydrocarbons for which all isotopologues and for each isotopologue all isotopomers are accounted for in a reaction network. 129

Table 4-4: The CPU time in minutes for different space times ($W/F_{CO,0}$) and different switch time constants (a_2). The Jacobian matrix was calculated by finite differences (FD) or semi-analytically (SA). The simulation results were obtained by integrating eq. [4-1] with the DASPK solver. For the reaction network CN_{max} = CN_{det} =5........ 142

Table 4-5: CPU time in minutes required by the different solvers for different space times ($W/F_{CO,0}$) and different switch time constants (a_2). The simulation results were obtained by integrating eq. [4-1]. For the reaction network CN_{max} = CN_{det} =5. (*) exceeds the wall time limit of 4320 minutes. 143

Table 4-6: The required CPU time in minutes for different space times ($W/F_{CO,0}$) and different switch time constants (a_2) obtained with reaction networks with 3 different levels of detail (I, II and III). I: CN_{max} = CN_{det} = 5. II: CN_{max} = 5, CN_{det} = 2. III: CN_{max} = 5 and CN_{det} = 1. The results were obtained by integrating eq. [4-1] with DASPK. 147

Table 4-7: Effect of operating conditions on the surface residence time, eq. [2–7], of the different alkanes and alkenes. The CO conversion amounts to 0.11 for all the simulations. The simulation results are obtained by integrating eq. [4-1] with the DASPK solver. 148

Table 5-1: The net formation rate of the various gas phase components and surface species. 165

Table 5-2: Ab initio determined chemisorption energies (kJ mol^{-1}) of metal alkyl species with 1 to 3 carbon atoms on a terrace site and a step site. 171

Table 5-3: Forward single-event pre-exponential factors, $\tilde{A}^f$, activation energies, E_a^f, atomic chemisorption enthalpies of hydrogen, Q_H, carbon, Q_C, and oxygen, Q_O, on both type of surface sites, surface reaction enthalpies, ΔH_r^0, and single-event surface reaction entropies, $\Delta\tilde{S}_r^0$ at 493 K. The values in plain font are determined a priori from open source data banks and statistical thermodynamics calculations, see section 2.2.1.3. The values indicated in bold font are determined by non-linear regression of the model to the experimental data in which the model responses are obtained by integrating eqs. [2–30] to [2-35] in which the net production rates are calculated as explained by eq [2-15]. The values in italic font are derived values from the values obtained from the non-linear regression. The values in parenthesis next to the values in bold font are the t values, eq. [2–48], multiplied with 10^{-5}....173

Table 6-1: Properties of the catalyst pellet....207

Table 6-2: Reactor and catalyst pellet dimensions, operating conditions and inlet stream specifications....227

Table A-1: Atomic diffusion volumes [1]....250

Table A-2: Coefficients for estimating the gas mixture viscosity based on the method of Chung et al. [1]....255

Table A-3: Coefficients for the calculation of B_i....257

Table A-4: Coefficient to calculate the partial molar volume at infinite dilution [6]....258

Table A-5: Coefficients to calculate the Henry coefficients at infinite dilution [6]....260

Table A-6: The liquid physical properties [7-9]....261

List of Symbols

Roman symbols

$a_{GL,v}$	Total contact area between the gas and liquid phase per reactor volume	$m_{GL}^2\ m_r^{-3}$
$a_{GS,v}$	Total surface area of the catalyst pellet per reactor volume	$m_p^2\ m_r^{-3}$
a_i	Parameter controlling the shape of the input function used in the modeling of Steady State Isotopic Transient Kinetic Analysis experiments ($i = 1,2,3$). a_2 is also referred to as the switch time constant.	$-$ or s
$a_{X,i}$	Number of atoms X in component i	$-$
A	Pre-exponential factor	s^{-1}, $(Pa\ s)^{-1}$ or $(MPa\ s)^{-1}$
A_i	Affinitiy of elementary reaction i	$J\ mol^{-1}$
A_m	Logartithmic average of A_r and A_u	m^2
A_r	Heat exchanging surface area at the bed side	m^2
A_u	Heat exchanging surface area at the heat transfer medium side	m^2
A_k^i	peak area of component k on detector i	$-$
$\underline{b}$	Vector of adjustable model parameters	$-$
C_i	Concentration of component i	$mol\ m^{-3}$
$C_{i,G}$	Gas phase concentration of component i	$mol\ m_G^{-3}$

$C_{i,L}$	Liquid phase concentration of component i	$mol\ m_L^{-3}$
$C_{i,p}$	The concentration of component i in the wax phase inside the catalyst pellet pores	$mol\ m_L^{-3}$
$c_{p,i}$	Isobaric molar heat capacity of component i	$J\ (mol\ K)^{-1}$
$c_{p,G}$	Isobaric specific heat capacity of the gas	$J(kg\ K)^{-1}$
$c_{p,L}$	Isobaric specific heat capacity of the liquid	$J(kg\ K)^{-1}$
$c_{p,p}$	Isobaric specific heat capacity of the catalyst pellet	$J\ (kg\ K)^{-1}$
$C_{tot,G}$	The total gas concentration	$mol\ m_G^{-3}$
$C_{tot,L}$	The total liquid concentration	$mol\ m_L^{-3}$
$c_{v,i}$	Isochoric molar heat capacity of a component i	$J\ (mol\ K)^{-1}$
$C_{C_iH_{2i+2}}^{{}^{12}C}$	The concentration of the alkanes with i carbon atoms and a ^{12}C atoms at a position in the chain	$mol\ m^{-3}$
$C_{C_iH_{2i+2}}^{j,{}^{12}C}$	The concentration of the alkanes with i carbon atoms and a ^{12}C at the jth position in the chain.	$mol\ m^{-3}$
$C_{C_iH_{2i+2}}^{\left\{\ {}^*C_{i-CN_{det}} \cdots\ {}^*C_i\right\}_j}$	The concentration of the alkanes with i carbon atoms of which the last CN_{det} carbon atoms have the isotopic labeling sequence as indicated by $\left\{\ {}^*C_{i-CN_{det}} \ldots\ {}^*C_i\right\}_j$	$mol\ m^{-3}$
CF_i	Calibration factor of component i	$-$
CN	The carbon number of a hydrocarbon	$-$
CN_{det}	The maximum chain length of hydrocarbons for which all the isotopologues and for each isotopologue all isotopomers are accounted for in a reaction network.	$-$
CN_{max}	The carbon number of the longest hydrocarbon considered in a network	$-$
d_h	Hydraulic diameter	m
d_p	Catalyst pellet diameter	m_p
d_r	Reactor diameter	m_r

D_{AB}	Gas phase molecular bond energy of gas phase component AB	$J\ mol^{-1}$
$D_{e,i}$	Effective diffusion coefficient of component i in the wax phase inside the catalyst pellet pores	$m_f^3\left(m_p\ s\right)^{-1}$
$D_{er,i,X}$	Effective radial diffusion coefficient of component i in phase X ($X = L\ or\ G$)	$m_f^3(m_r\ s)^{-1}$
D_i	Diffusion coefficient of component i	$m^2\ s^{-1}$
D_{ij}	Binary diffusion coefficient	$m^2\ s^{-1}$
$D_{i,L}$	Diffusion coefficient of component i in the liquid phase	$m^2\ s^{-1}$
D_{im}	Molecular diffusion coefficient of component i	$m^2\ s^{-1}$
E_a	Activation energy	$J\ mol^{-1}$
$\underline{f}$	Short notation for the right hand side of a set of ordinary differential equations	$-$
f_G	Gas phase friction factor	$-$
$f_{i,G}$	Gas phase fugacity of component i	Pa
$f_{i,L}$	Liquid phase fugacity of component i	Pa
f_{LGG}	Gas-liquid friction factor	$-$
F_c	Calculated F value for the global significance of the model	$-$
F_i	Molar flow rate of component i	$mol\ s^{-1}$
h	Planck constant	$J\ s$
h	Step size	$-$
h_w	Heat transfer coefficient at the wall	$W\ (m^2\ K)^{-1}$
H	Enthalpy	$J\ mol^{-1}$
$\Delta H_{r,i}$	The enthalpy change corresponding to the production of one mole of component i starting from the reactants.	$J\ mol^{-1}$
$\Delta H^{0,\ddagger}$	The standard activation enthalpy	$J\ mol^{-1}$
ΔH_r^0	The standard reaction enthalpy	$J\ mol^{-1}$

He_i	Henry coefficient of component i	Pa
He_i^{∞}	Henry coefficient of component i at infinite dilution	Pa
$I_i(t)$	Normalized transient response of component i	$-$
$\underline{\underline{I}}$	Identity matrix	$-$
$\left(\frac{\partial \underline{f}}{\partial \underline{y}}\right)_{ij}$	Element of the Jacobian matrix on the ith row and j^{th} column	$-$
k	Kinetic coefficient of an elementary step	s^{-1} or $(Pa\ s)^{-1}$
k_b	Boltzmann constant	$J\ K^{-1}$
$K_{i,GL}$	The gas-liquid mass transfer coefficient of component i	$m_f^3(m_{GL}^2\ s)^{-1}$
$k_{i,GS}$	The gas-solid mass transfer coefficient of component i	$m_f^3\left(m_p^2\ s\right)^{-1}$
$k_{i,XI}$	Mass transfer coefficient from the bulk X phase to the gas-liquid interface. (X = liquid or gas).	$m_f^3(m_{GL}^2\ s)^{-1}$
K	Thermodynamic equilibrium coefficient of an elementary step	$-$
L_i	Surface concentration of surface species i	$mol\ kg_{cat}^{-1}$
$L_i^{\ ^{12}C}$	The surface concentration of the surface species i with a ^{12}C atom	$mol\ kg_{cat}^{-1}$
$L_{C_iH_{2i+1}}^{\ ^{12}C}$	The surface concentration of the metal alkyls with i carbon atoms and a ^{12}C atoms at a position in the chain	$mol\ kg_{cat}^{-1}$
$L_{C_iH_{2i+1}}^{j,\ ^{12}C}$	The surface concentration of the metal alkyls with i carbon atoms and a ^{12}C at the jth position in the chain.	$mol\ kg_{cat}^{-1}$
$L_{C_iH_{2i+1}}^{\left\{\ ^{*}C_{i-CN_{det}} \cdots\ ^{*}C_i\right\}_j}$	The concentration of the metal alkyls with i carbon atoms of which the last CN_{det} carbon atoms have the isotopic labeling sequence as indicated by $\left\{\ ^{*}C_{i-CN_{det}} \dots\ ^{*}C_i\right\}_j$	$mol\ kg_{cat}^{-1}$

M_i	Molecular mass of component i	$g\ mol^{-1}$
n	Number	$-$
N_A	Avogadro constant	$-$
$N_{^{12}C}(\cdot)$	Operator determining the number of ^{12}C	$-$
N_i	Molar flux of component i	$mol\ (m^2\ s)^{-1}$
Nu	Nusselt number: ratio of convective to conductive heat transfer	$-$
p	Pressure	Pa or MPa
p_i	Partial pressure of component i	Pa or MPa
$p_{sat,i}$	Saturation pressure of component i	Pa
$P_m(t)$	A polynomial of degree m in t	$-$
Pe	Péclet number: ratio of convective transport to diffusive transport	$-$
$Pe_{r,X}$	Péclet number for radial effective diffusion in phase X ($X =\ G\ or\ L$)	$-$
Pr	Prandtl number: ratio of kinematic viscosity to the thermal diffusivity	$-$
Q_i	Atomic chemisorption enthalpy of atom i	$J\ mol^{-1}$
r	Ratio of the concentration gradient of the upwind control volume boundary to that of the downwind control volume boundary	$-$
r	Radial position coordinate of the catalyst pellet or reactor	m_p or m_r
r_i	Reaction rate of elementary step i	$mol\ (kg_{cat}\ s)^{-1}$
r_p	Catalyst pellet radius	m_p
R	Universal gas constant	$J(mol\ K)^{-1}$
R_i	Net production rate of component i	$mol\ (kg_{cat}\ s)^{-1}$
Re	The Reynolds number: ratio of inertial forces to viscous forces	$-$
S	Entropy	$J(K\ mol)^{-1}$

S_i	Selectivity to component i	$mol\ mol^{-1}$
$\Delta\tilde{S}^{0,\ddagger}$	The single-event standard activation entropy	$J(K\ mol)^{-1}$
$\tilde{S}^{0,\ddagger}$	Transition state single event standard entropy	$J(K\ mol)^{-1}$
$\tilde{S}^{0}_{surf,i}$	The single-event standard entropy of surface species i	$J(K\ mol)^{-1}$
S^{0}_{trans}	The translational entropy	$J(K\ mol)^{-1}$
$\Delta\tilde{S}^{0}_{r}$	The single-event standard reaction entropy	$J(K\ mol)^{-1}$
Sc	Schmidt number: ratio of kinematic viscosity to molecular mass diffusivity	$-$
Sh	Sherwood number: ratio of convective mass transfer to conductive mass transfer	$-$
t	Time	s
t	Independent variable	$-$
t_c	Calculated t value for the individual parameter significance	$-$
T	Temperature	K
T_c	Critical temperature	K
T_{cool}	The temperature of the cooling medium	K
T_r	Reduced temperature	$-$
$u_{s,G}$	Superficial velocity of the gas phase	$m_G^3(m_r^2\ s)^{-1}$
$u_{s,L}$	Superficial velocity of the liquid phase	$m_L^3(m_r^2\ s)^{-1}$
U	Overall heat transfer coefficient	$W(m_r^2\ K)^{-1}$
V_c	Molar critical volume	$m^3\ mol^{-1}$
$\overline{v}_i^{\infty}$	Partial molar volume of component i at infinite dilution	m^3mol^{-1}
$v_{i,L}$	Liquid molar volume of component i	$m^3\ mol^{-1}$
V_{mol}	Molar volume	$m^3\ mol^{-1}$
$\left[V(\underline{b})\right]_{ii}$	i^{th} diagonal element of the variance covariance matrix	
W	Catalyst mass	kg

We	Weber number: ratio of inertial forces to surface tension	$-$
w_i	Weighing factor of response i	$-$
w_n	Mass fraction of hydrocarbons with n carbon atoms in a mixture	$-$
x	Dimensionless reactor coordinate	$-$
x_i	Mole fraction of component i in the liquid phase	$mol\, mol^{-1}$
X_i	Conversion of reactant i	$mol\, mol^{-1}$
X_G	Lockhart-Martinelli parameter	$-$
y_i	Molar fraction of component i in the gas phase	$mol\, mol^{-1}$
y_{ij}	Experimental response i in experiment *j*	$-$
$\hat{y}_{ij}$	Model calculated response i in experiment *j*	$-$
$\underline{y}$	Vector of dependent variables	$-$
z	Number of nearest neighbors	$-$
z	Axial reactor distance	m_r
$\left\{{}^{12}C_1\ {}^{*}C_2 \cdots\ {}^{*}C_i\right\}_j$	j^{th} element of the set of all the possible isotopologues and isotopomers of a metal alkyl chain with i carbon atoms and the carbon atom attached to the metal surface is a ^{12}C. The '*' indicates that the carbon atom has a specific isotopic label, i.e., '12' or '13'.	
$\left\{\ {}^{*}C_{i-NC_{det}} \cdots\ {}^{*}C_i\right\}_j$	j^{th} element of all the possible isotopologues and isotopomers which can be formed with the last CN_{det} carbon atoms of a metal alkyl chain with i carbon atoms. The '*' indicates that the isotopic label, i.e., '12' or '13'is specifically followed for that carbon atom.	$-$

Superscripts

f	forward
$pred$	predictor
r	reduced
r	reverse
ss	Steady state
0	Standard
$\ddagger$	Transition state
$*$	Free site
$\sim$	Single-event
$'$	Isotopically labeled counterpart

Subscripts

ads	Adsorption
ass	Association
ave	Average
ba	Beta hydride addition
be	Beta hydride elimination
c	critical
$chem$	Chemisorption
$comp$	Component
$dehyd$	Dehydrogenation
des	Desorption
det	Detailed
$diss$	Dissociation
e	East
exp	Experiment

ext	External
f	Fluid
G	gas
gl	Global
gp	Gridpoint
hyd	Hydrogenation
i, j, k	Counters
int	internal
L	liquid
m	Mixture
max	Maximum
md	Methylene deinsertion
mi	Methylene insertion
min	Minimum
p	Propagation
p	Pellet
par	Parameter
$prod$	products
r	reactor
$reactant$	reactant
ref	Reference
rep	Replicate
$resp$	Response
rot	Rotational
sat	saturation
$solv$	solvent
$surf$	surface
t	Termination
tot	Total
$trans$	translational

w	West
0	Initial condition
‡	Transition state
—	Vector

Greek symbols

α	Chain growth probability	$-$
α_i	Coefficient of a linear multistep method	$-$
α_r	Heat transfer coefficient at the bed side	$W(m^2\ K)^{-1}$
α_u	Heat transfer coefficient at the heat transfer medium side	$W(m^2\ K)^{-1}$
β_i	Coefficient of a linear multistep method	$-$
β_t	Liquid saturation	$-$
γ_i^∞	Activity coefficient at infinite dilution of component i	$-$
γ_r^∞	Activity coefficient at infinite dilution of a reference solute	$-$
Γ	Ratio of terrace sites to the total site coverage	$-$
δ	Reactor tube thickness	m
Δ	Indicates a difference in a quantity	$-$
ε_b	Bed porosity	$m_f^3\ m_r^{-3}$
ε_G	Fraction of the reactor volume occupied by the gas (gas hold-up)	$m_G^3\ m_r^{-3}$
ε_L	Fraction of the reactor volume occupied by the liquid (liquid hold-up)	$m_L^{-3} m_r^{-3}$
ε_p	Pellet porosity	$m_f^3\ m_p^{-3}$
θ_j	Surface coverage of surface species j	$-$
λ_{er}	Effective radial thermal conductivity	$W(m_r\ K)^{-1}$
λ_{eG}	Contribution of the gas to λ_{er} due to lateral	$W(m_r\ K)^{-1}$

	mixing	
λ_{eL}	Contribution of the liquid to λ_{er} due to lateral mixing	$W(m_r\,K)^{-1}$
λ_G	Gas thermal conductivity	$W\,(m\,K)^{-1}$
λ_L	Liquid thermal conductivity	$W\,(m\,K)^{-1}$
λ_p	Thermal conductivity of the catalyst pellet	$W(m^2\,K)^{-1}$
λ_r	Thermal conductivity of the reactor material	$W(m\,K)^{-1}$
λ_{er}^{b}	Contribution of the bed to λ_{er}	$W(m_r\,K)^{-1}$
λ_{er}^{f0}	Contribution of the stagnant fluid to λ_{er}	$W(m_r\,K)^{-1}$
λ_{er}^{ff}	Contribution of the flowing fluid to λ_{er}	$W(m_r\,K)^{-1}$
μ_G	Gas phase dynamic viscosity	$Pa\,s$
μ_L	Liquid phase dynamic viscosity	$Pa\,s$
$\nu_{i,j}^{f}$	the forward stoichiometric coefficient of the ith elementary step belonging to the jth gas phase component or surface species which is by convention negative	$-$
$\nu_{i,j}^{r}$	the reverse stoichiometric coefficients of the ith elementary reaction belonging to the jth gas phase component or surface species which is by convention positive	$-$
ρ_b	Bulk density of the catalyst bed	$kg_{cat}\,m_r^{-3}$
ρ_G	Mass density of the gas phase	$kg\,m^{-3}$
ρ_{ij}	Binary correlation coefficient	$-$
ρ_L	Mass density of the liquid phase	$kg\,m^{-3}$
ρ_p	Catalyst pellet density	$kg_{cat}\,m_p^{-3}$
σ	Symmetry number	$-$
σ_i	Experimental error on response i	$-$
σ_L	Surface tension	$N\,m^{-1}$
τ	Tortuosity of the catalyst pellet	$m_f^2\,m_p^2$
τ_b	Bed residence time	s

τ_i	Mean surface residence time of surface species leading to component i	s
φ	Flux limiter	$-$
φ	Measured signal on a MS	$-$
$\varphi_{i,j}^{d}$	the differential disappearance rate of gas phase component or surface species i leading to gas phase component or surface species j	$-$
$\varphi_{j,i}^{f}$	the differential formation rate of gas phase component or surface species i from gas phase component or surface species j	$-$
$\chi_{RC,r}$	Degree of rate control by elementary reaction r	$-$
ω_i	Acentric factor of component i	$-$

Abbreviations

AE	Algebraic Equation
ASF	Anderson-Schulz-Flory
BDF	Backward Differentiation Formula
BtL	Biomass to liquids
CFBR	Circulating Fluidized Bed Reactor
CNT	Carbon nanotubes
CPU	Central Processing Unit
CtL	Coal to liquids
DAE	Differential Algebraic Equation
DASPK	Differential Algebraic Equation solver
DFT	Density Functional Theory
DS	Discretization Scheme
FBR	Fixed Bed Reactor
FD	Finite Difference
FFBR	Fixed Fluidized Bed Reactor
FID	Flame Ionization Detector

FL	Flux Limiter
FOU	First Order Upwind
FTS	Fischer-Tropsch Synthesis
GC	Gas Chromatograph
GPL	Generalized Piecewise Linear
GtL	Gas to liquids
H-CUI	Name of a Flux Limiter function
H-QUICK	Name of a Flux Limiter function
HTFT	High Temperature Fischer-Tropsch
IRLS	Iteratively reweighted least squares
Koren	Name of a Flux Limiter function
LMM	Linear Multistep Methods
LSODA	Ordinary Differential Equations solver similar to LSODE
LSODE	Livermore Solver for Ordinary Differential Equations
LTFT	Low Temperature Fischer-Tropsch
Minmod	Name of a Flux Limiter function
MOL	Method of Lines
MPI	Message Passing Interface
MS	Mass Spectrometer
MSD	Mass Selective Detector
MTTBR	Multi-Tubular Trickle Bed Reactor
MUSCLE	Name of a Flux Limiter function
ODE	Ordinary Differential Equation
ODRPACK	Orthogonal Distance Regression Package
OSPRE	Name of Flux Limiter function
PAW	Projector Augmented Wave
PBE	Perdew, Burke and Ernzerhof's 1996 exchange and correlation functional
PDE	Partial Differential Equation

PFR	Plug Flow Reactor
PR	Polynomial Ratio
RHS	Right Hand Side
RMM-DIIS	Residual Minimization Method with Direct Inversion in Iterative Subspace
SA	Semi-analytically
SBCR	Slurry Bubble Column Reactor
SEMK	Single-Event MicroKinetic
SMART	Name of a Flux Limiter function
SMARTER	Name of a Flux Limiter function
SMDS	Shell Middle Distillate Synthesis
SOCD	Second Order Central Differencing
SOU	Second Order Upwinding
SPD	Slurry Phase Distillate
SPL	Symmetric Piecewise Linear
SSITKA	Steady State Isotopic Transient Kinetic Analysis
SSQ	Sum of Squares
Superbee	Name of a Flux Limiter function
TBR	Trickle Bed Reactor
TCD	Thermal Conductivity Detector
TEM	Transmission Electron Microscopy
TOF	Turnover Frequency
TVD	Total Variation Diminishing
UBI-QEP	Unity Bond Index Quadratic Exponential Potential
VASP	Vienna Ab initio Simulation Package
van Albada	Name of a Flux Limiter function
van Leer	Name of a Flux Limiter function
VODE	Ordinary Differential Equations solver similar to LSODE
WGS	Water Gas Shift

Glossary

Activation energy	For an elementary step, the difference in internal energy between transition state and reactants. A measure for the temperature dependence of the rate coefficient.
Active site	Also called active center. Those sites for sorption which are responsible for subsequent reaction.
Adsorption	The preferential concentration of a species at the interface between two phases. Adherence of the atoms, ions or molecules of a gas or liquid to the surface of another substance.
Arrhenius relation	Expresses the dependence of a rate coefficient k corresponding with a chemical reaction on the temperature T and activation energy, Ea: $k=A\ \exp(E_a/RT)$ with R the universal gas constant, T the temperate and A the pre-exponential factor.
Catalyst	A source of active centers regenerated at the end of a closed reaction sequence.
Chemisorption	Also known as chemical adsorption. Adsorption in which the forces involved are valence forces of the same kind as those operating in the formation of chemical compounds. Chemisorption strongly depends on the surface and the adsorbed species, and only one layer of chemisorbed molecules is formed. Its energy of adsorption is the same order of magnitude as in chemical reactions, and the adsorption may be activated.
Conversion	Measure for the amount of a reactant that has been transformed into

	products as a result of a chemical reaction.
Corrector	Implicit discretization scheme used to find the numerical approximation of the dependent variables of a set of ordinary differential equations at the next discretization point of the independent variable, i.e., t_{n+1}, after applying a predictor to predict the values of these dependent variables at t_{n+1}.
Deactivation	The decrease in conversion in a catalytic reaction with time of run under constant reaction conditions.
Differential disappearance factor	The differential disappearance factor, $\varphi_{i,j}^{d}$, of a component i leading to a component j is obtained by dividing the corresponding reaction rate, $r_{i,j}$, by the sum of all the elementary steps in which component i is consumed. ($\varphi_{i,j}^{d} = r_{i,j}/\sum_k r_{i,k}$)
Differential formation factor	The differential formation factor, $\varphi_{j,i}^{f}$, of component i from a component j is obtained by dividing the corresponding reaction rate, $r_{j,i}$, by the sum of all the elementary steps in which component i is formed. ($\varphi_{i,j}^{f} = r_{j,i}/\sum_k r_{k,i}$)
Elementary step	The irreducible act of reaction in which reactants are transformed into products directly, i.e., without passing through an intermediate that is susceptible to isolation.
Effectiveness factor	Ratio of actual reaction rate for a porous catalyst to reaction rate that would be observed if the total surface area throughout the catalyst interior were exposed to a fluid of the same composition and temperature as that found at the outside of the particle.
Gas Chromatography (GC)	The process in which the components of a mixture are separated from one another by injecting the sample into a carrier gas which is passing through a column or over a bed of packing with different affinities for adsorptive of the components to be separated.
Group contribution method	A technique to estimate and predict thermodynamic and other properties from molecular structures, i.e., atoms, atomic groups, bond type etc.

Inhibition	Decrease in rate occasioned by a substance (inhibitor, poison) which may be produced by the reaction itself or may be a foreign substance.
Intermediate	Is formed from a reactant and transforms into a product during a chemical reaction. The intermediate is often a short-lived and unstable species that cannot directly be detected during a reaction.
Internal diffusion	Also called intraparticle diffusion. Motion of molecules within the particles of a solid phase that has a sufficiently large porosity to allow this motion.
Intraparticle diffusion	Motion of molecules within particles of a solid phase. (See also Internal diffusion).
Isotopologue	A molecular entity that differs in isotopic composition, e.g., CH_4 CH_3D
Isotopomer	Isomers having the same number of each isotopic atom but differing in their positions.
Langmuir-Hinshelwood-Hougen-Watson (LHHW) mechanism	It is assumed that both reactants must be adsorbed on the catalyst in order to react. Normally adsorption-desorption steps are essentially at equilibrium and a surface step is rate-determining. Adsorption steps can also be rate-determining.
Mechanism	A sequence of elementary steps in which reactants are converted into products, through the formation of intermediates.
Network	When several single reactions take place in a system, these parallel and consecutive reactions constitute a network.
Objective function	Is a function used during optimization problems which have to be minimized or maximized by choosing the best set of variables which determines the values of this function.
Pseudo-steady state	Its mathematical expression is that the time rate of change of the concentration of all active centres in a reaction sequence is equal to zero
Parameter estimation	Process of estimating the parameters of a relation between independent and dependent variables as to describe a chemical

	reaction as good as possible.
Parity diagram	A 2-dimensional scatter plot in which the model calculated values of the responses are displayed against the experimentally observed values
Performance figure	In a performance figure, the response values, both experimentally observed as well as model calculated ones, are displayed against an independent variables, e.g., conversion as a function of space-time.
Physisorption	Also known as physical adsorption. Adsorption in which the forces involved are intermolecular forces (van der Waals forces) of the same kind as those responsible for deviation from ideal gas behavior or real gases as the condensation of vapors, and which do not involve a significant change in the electronic orbital patterns of the species involved. Physisorption usually occurs at temperatures near the boiling point of adsorbate, and multilayer can occur. The heat of adsorption is usually significantly less than 40 kJ/mol.
Porosity	A measure of the void spaces in a material, expressed as the ratio of the volume of voids to the total volume of the material.
Predictor	Explicit discretization scheme to predict the numerical approximation of the dependent variables of a set of ordinary differential equations at the next discretization point of the independent variable, i.e., t_{n+1}. Terminology used in conjunction with a corrector.
Pre-exponential factor	The temperature-independent factor of a rate coefficient, also called the frequency factor.
Reaction family	Classification of elementary reaction steps on the basis of same features
Reaction rate	The number of moles of a component created by a chemical reaction per unit of time, volume or catalyst weight.
Rate-determining step	If, in a reaction sequence, consisting of *n* steps, *(n-1)* steps are reversible and if the rate of each of these *(n-1)* steps is potentially larger in either direction than the rate of the *n*th step, the latter is said

	to be rate-determining. The rate-determining step need not be reversible.
Rate-limiting step	An elementary reaction of which the rate constant has a strong effect on the overall reaction rate. The rate-limiting steps are identified by means of a degree of rate control analysis, i.e., $\chi = (\partial \ln(R)/\partial \ln(k_i))_{k_{j\neq i,K_i}}$. The steps with the highest degree of rate control have the strongest effect on the overall reaction rate. Rate-controlling step is used as a synonym for rate-limiting step. If in a degree of rate control analysis, the degree of rate control is exactly one for one step, the step is considered to be the rate determining step.
Residual plot	A 2-dimensional scatter plot in which the residuals, i.e., the differences between the model simulated values and the observed values, are put against the independent (or dependent) variable values.
Selectivity	Measure for the amount in which a product is formed from the reactants as a result of a chemical reaction
Single Event MicroKinetics	Single Event MicroKinetics: A kinetic modeling concept in which elementary steps are grouped into reaction families mainly based on enthalpic/energetic considerations. By accounting for the symmetry effects of reactant and transition state a unique, single-event rate coefficient suffices per reaction family. As a result, the number of adjustable parameters is greatly reduced. (abbrev.: SEMK)
Steady state	A system in steady-state has certain properties that are time-independent.
Surface coverage	Ratio of the amount of adsorbed substance to the monolayer capacity (also, sometimes defined for metals as the ratio of the number of adsorbed atoms or groups to the number of metal surface atoms).
Support	Also called carrier. Material, usually of high surface area, on which the active catalytic material, present as the minor component, is

	dispersed. The support may be catalytically inert, but it may contribute to the overall catalytic activity.
Syngas	Mixture of CO and H_2
Transition state	Also called activated complex. The configuration of highest potential energy along the path of lowest energy between reactants and products.
Transition state theory	Theory to calculate the rate of an elementary reaction from a knowledge of the properties of the reacting components and their concentrations. Differs from collision theory in that it takes into account the internal structure of reactant components.
Turnover frequency	The number of molecules reacting per active site per unit time.

Summary

Fischer-Tropsch Synthesis (FTS) catalytically converts syngas, i.e., a mixture of CO and H_2, mainly into linear alkanes and 1-alkenes which can be further processed to liquid transportation fuels with a low sulfur, nitrogen and aromatic content. The product distribution can be fine-tuned to also produce oxygen containing compounds which can be used as base chemicals in the chemical process industry. Syngas can be derived from any carbon containing feedstock, i.e., coal, natural gas or biomass. As such, the FTS process has experienced strong renewed interest since the mid-nineties of the 20th century in academia and industry.

The FTS reaction is catalyzed by transition metals such as Ru, Fe, Co and Ni [1]. Only Co and Fe have, so far, been applied on the industrial scale. The low water-gas shift activity of the Co based catalysts makes them the preferred ones when the primary resource for the synthesis gas is methane. Next to this, Co based catalysts also have a higher activity and better stability than Fe based catalysts [1].

For the construction of a multi-scale model, a microkinetic model that adequately captures the effect of the operating conditions on the reactant conversion and product yields is one of the major prerequisites. Therefore, a Single-Event MicroKinetic (SEMK) model, originally developed for the Fe catalyzed FTS [2], has been validated for the Co catalyzed FTS. The validation was performed based on experimental data acquired in a fixed bed reactor. The experimental data were acquired over a broad range of operating conditions. The SEMK model was regressed to these experimental data points, i.e., the model adjustable parameters were varied until the model could satisfactorily describe the experimental data. The regression resulted in a globally significant model with physicochemically meaningful parameter values, i.e., the final estimates for the adjustable model parameters were in agreement with literature reported

values, the latter being based on regression to experimental data or obtained from ab initio calculations. The regression results are illustrated in Figure 1 as parity diagrams of the product yields.

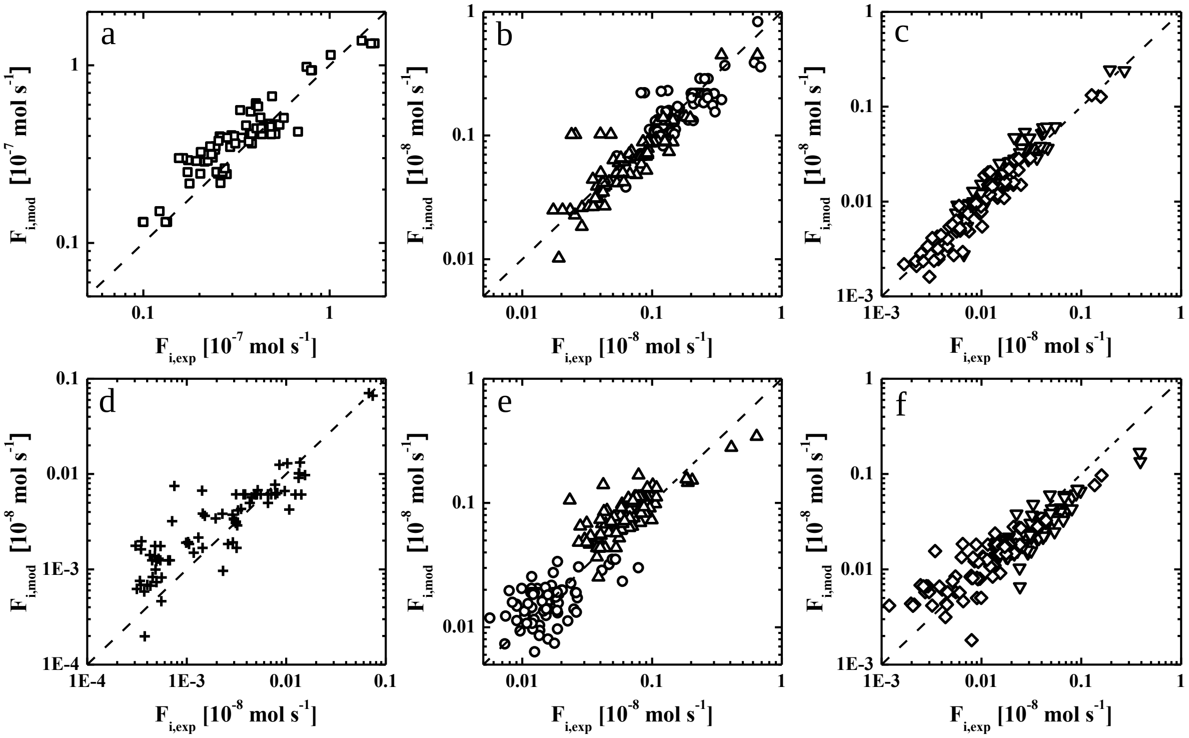

Figure 1: Experimental and model calculated outlet molar flow rates, F_i, at 3 – 10 H_2/CO molar inlet ratios, 483 K – 503 K temperature, 3.7 kPa – 16.7 kPa CO inlet partial pressure, 7.2 – 36.3 $(kg_{cat}s)mol_{CO}^{-1}$ space time, i.e., $W/F_{CO,0}$, and 185 kPa total pressure for a Co/CNT catalyst, see Section 2.1.3. The calculated outlet molar flow rates are obtained by integrating eq. [2–27] and eq. [2–28] in which the net production rates are calculated as explained by eq. [2–15] and using the set of parameters given in Table 3-4. (a): methane; (b): ethane (○) and propane (△); (c):*n*-butane (▽) and *n*-pentane (◇); (d): *n*-hexane (✚); (e): ethene (○) and propene (△) and (f): 1-butene (▽) and 1-pentene (◇).

The unique features of the developed SEMK model compared to other microkinetic models described in literature are that there are no a priori assumptions concerning a rate determining step and that the reversibility of every elementary reaction step has been accounted in the microkinetic model. Furthermore, the activation energies are carbon number independent. This microkinetic model has been exploited in a reaction path analysis and degree of rate control analysis to better understand the underlying chemistry of the FTS and the effect of parameter values on the observed activity and selectivity. The result of the reaction path analysis for typical operating conditions included in the experimental data is illustrated in Figure 2.

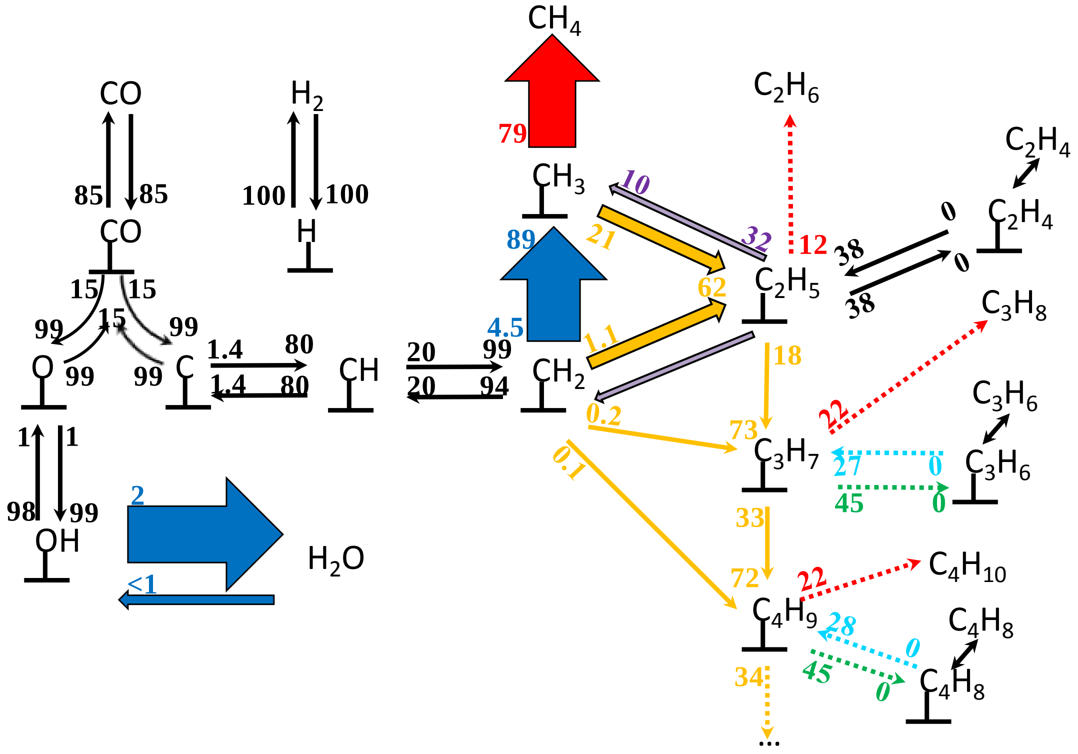
CH_4
79
CO
H_2
85
85
100
100
CO
H
CH_3
10
89
21
32
12
C_2H_6
C_2H_4
C_2H_4
38
0
0
38
C_2H_5
62
15
15
15
99
99
99
99
O
C
1.4
80
1.4
80
CH
20
99
20
94
4.5
CH_2
1.1
0.2
18
C_3H_8
22
C_3H_6
73
C_3H_7
27
0
C_3H_6
45
0
0.1
1
1
98
99
OH
2
<1
H_2O
33
72
22
C_4H_{10}
C_4H_8
C_4H_9
28
0
45
0
34
C_4H_8
...

Figure 2: Reaction path analysis at a H_2/CO molar inlet ratio of 10, a temperature of 483 K, a CO inlet partial pressure of 5.5 kPa, a total pressure of 185 kPa and space time, i.e., $W/F_{CO,0}$, of 20 $(kg_{cat}s)mol_{CO}^{-1}$ for a Co/CNT catalyst, see Section 2.1.3. The simulation is performed by integrating eq. [2–27] and eq. [2–28] in which het net production rates are calculated as explained by eq. [2–15] and using the parameters of Table 3-4. The elementary reactions indicated by the black arrows are at quasi-equilibrium as confirmed by affinity calculations, see Table 3-8. The reactions which are not at quasi-equilibrium are presented by the colored arrows. The thickness of these arrows is scaled to the reaction rate. The reaction families considered in the SEMK model are assigned a separate color, i.e., CH_2^{**} insertion/deinsertion (yellow – purple), $C_nH_{2n+1}^*$ hydrogenation (red), beta hydride elimination/ addition (green – cyan). The other elementary steps are indicated in blue. The number indicated at the tail of an arrow is the differential disappearance factors, eq. [2–50]. The number indicated at the tip of an arrow is the differential formation factors, eq. [2–51]. H_2 has not been included not to overload the figure.

An important finding from the reaction path analysis is the kinetic relevance of the reversibility of the first CH_2^{**} insertion step, see yellow and purple arrows in Figure 2. This originates from the higher chemisorption enthalpy of CH_3^{*} compared to $C_nH_{2n+1}^{*}$ with more than one carbon atom, a feature coinciding with findings from solid state ab initio calculations [3]. This contributes to the typically observed deviations from Anderson-Schulz-Flory distribution, i.e., a higher methane and lower ethene selectivity than would be expected according to a set of entirely carbon number independent parameters within a reaction family. By means of the degree of rate control analysis the OH^{*} hydrogenation, blue in Figure 2, and CH_2^{**} hydrogenation, blue in Figure 2, have been identified as the kinetically most relevant steps. The catalyst activity is, hence, controlled by the OH^{*} and CH_2^{**} hydrogenation while CH_2^{**} hydrogenation also determines the selectivity. It is noted that the removal of water precursors from the Co catalyst surface has also been identified as a rate-determining step in the CO conversion by means of surface science studies [4].

The inclusion of atomic chemisorption enthalpies in the SEMK model allows to address the difference in activity between an Fe and a Co based catalyst based on intrinsic properties of the catalyst material. For the Fe catalyst, the water formation reactions are found to be quasi-equilibrated from the reactor entrance. This is the result of the higher oxygen atomic chemisorption enthalpy on Fe catalysts compared to Co catalysts. This results, for the Fe catalyst, in increasing surface coverages of the oxygen containing species with space time or equivalently with increasing partial pressure of H_2O, as one of the major FTS products. As a consequence, the CO surface coverage and the number of free sites decreases as a function of space time which causes the CO dissociation reaction to become one of the kinetically relevant reaction steps. Hence, water has an inhibiting effect on the activity of an Fe catalyst.

The FTS process is still one of the most challenging processes to investigate [5]. Recent experimental data have demonstrated that the metal particle size of the catalytically active phase affects the CO conversion and selectivities [6]. Smaller particles were found to be less active for FTS and resulted in higher methane yields compared to larger metal particles. An interesting technique which provides key insights in such effects is Steady State Isotopic Transient Kinetic Analysis (SSITKA) [7]. In such an experiment, the reactant feed to the reactor can be switched between different isotopically labeled reactants. If both feed lines are operated under identical conditions, the catalyst is operated at steady state while the exchange of isotopes by the reactions from the reactants to the products can be followed by means of mass spectrometry. As such, more detailed information can be obtained about the catalyst at the investigated operating conditions. SSITKA has also been applied for the elucidation of support effects, promoter effects, … Combining SSITKA with microkinetic modeling will provide more insights on the aforementioned phenomena [8].

Therefore, a modeling strategy for SSITKA data has been devised. The modeling of this type of data involves solving a set of partial differential, ordinary differential and algebraic equations [9]. The numerical solutions of the partial differential equations are, due to the specific nature of these equations, particularly difficult to obtain. Major efforts have been put in the selection of a numerical discretization scheme of the spatial derivative optimizing accuracy and CPU time. For low switch time constants, i.e., a_2 (eq. [2–34]) ≤ 0.1 s, the van Leer and van Albada flux limiter functions yield the lowest CPU time, see Figure 3. For larger switch time constants, i.e. $a_2 \geq 1.0$ s, linear discretization schemes can be applied. The developed modeling strategy also required a dedicated reaction network generation methodology specifically accounting for the isotopic labeling. The devised methodology reduces the exponential dependence of the number of considered species on the carbon number to a quadratic one. A pictorial representation of the reaction network generation methodology is given in Figure 4. This has shown to reduce the required CPU time considerably, i.e., a factor up to 10 can be achieved.

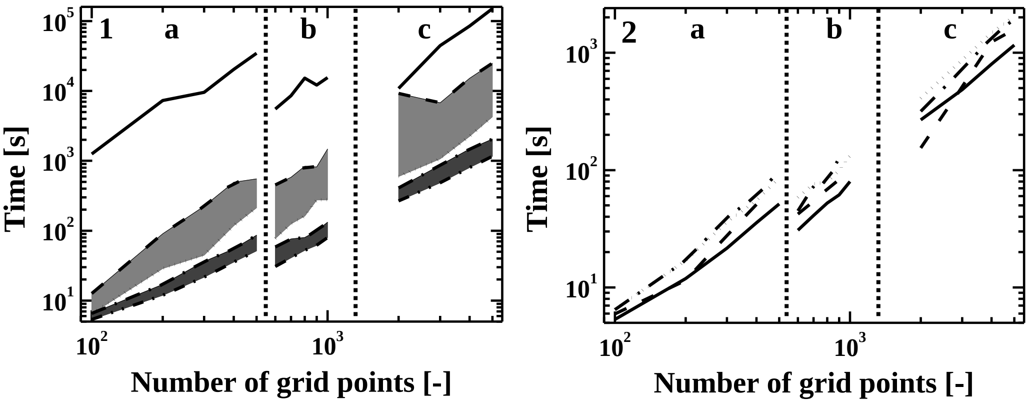

Figure 3: CPU time as function of the number of grid points. a_2 (eq. [2–34]) = 0.01 s. a: $W/F_{CO,0}$ = 4 (kg_{cat} s)mol_{CO}^{-1}. b: $W/F_{CO,0}$ = 40 (kg_{cat} s)mol_{CO}^{-1}. c: $W/F_{CO,0}$ = 400 (kg_{cat} s)mol_{CO}^{-1}. 1: Full line: Superbee, dashed line: SMART, dotted line: SPL-1/3, dash dotted line: GVA-1/2, dash dot dotted line: van Albada, grey band: MUSCL, Koren, Minmod, H-CUI, H-QUICK, SMARTER and GPR-1/2, dark grey band OSPRE and van Leer. 2: Full line: van Albada, dashed line: van Leer, dotted line: OSPRE and dash dotted line: GVA-1/2. The simulations were performed for the methanation reaction. The results were obtained by integrating eq. [4–1] with the DASPK solver in which the net production rates are calculated as explained by eq. [2–15].

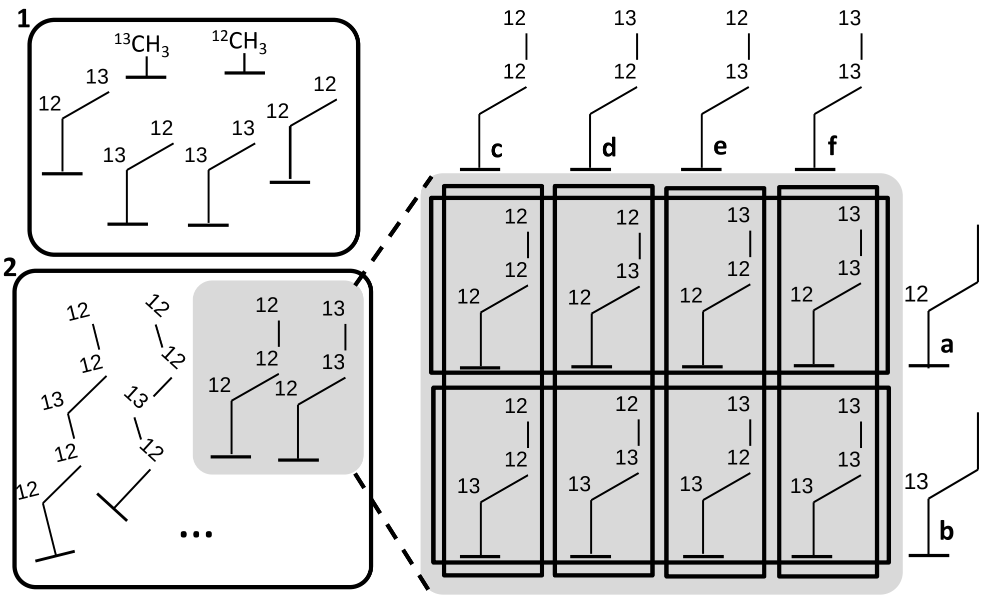

Figure 4: Graphical representation of the reaction network generation. The isotopically labeled metal alkyl species are categorized into subsets. 1: group comprising those species with a maximum carbon number, CN_{det} for which all possible isotopologues and isotopomers are followed. 2: complement of group 1 for which subsets are introduced. These subsets are illustrated for the isotopic labeled metal propyl species and is done on the basis of the labeling of the carbon atom on a position *i* in the chain with $1 \leq i < CN_{max} - CN_{det}$ (a and b) or the isotopic labeling of the last CN_{det} carbon atoms (c –f).

The SEMK model, which was successfully regressed to the steady state data, has been used in the assessment of the transient responses of CO and CH_4 acquired on a Co/CNT catalyst, see section 2.1.3. The first modeling results showed that additional reaction steps were required in the SEMK model. Therefore, also taking inspiration from the literature [10-12], the SEMK model was extended to account for two site types on which both CO dissociation and chain growth steps were considered at different reaction rates. The results of the regression of the extended SEMK model to experimental data is depicted in Figure 5 for the transient responses of CH_4 and CO. It is noted that the SEMK model constructed in this thesis for the modeling of SSITKA data specifically takes into account H_2 adsorption, hydrogenation steps in the hydrocarbon chain growth reactions and water formation reactions. Furthermore, activation energies and atomic chemisorption enthalpies have been considered in the extended SEMK model. As such, this SEMK model can be used for the simulation of more than one SSITKA experiment without the need of re-estimating the kinetic parameters for different reaction conditions.

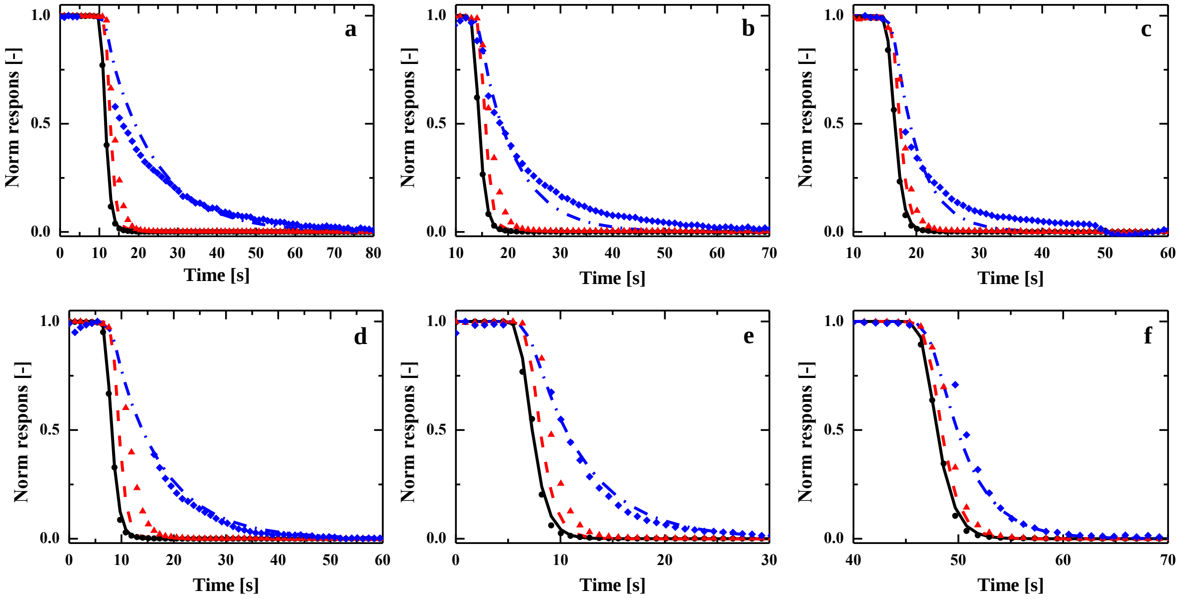

Figure 5: Experimental (symbols) and model calculated (lines) normalized outlet concentrations of Ar (●,—), CO(▲, – –) and CH_4 (◆, – •), at H_2/CO molar ratio of 5 (a-c) and 10 (d-f), a temperature 483 K (a,d), 493 K (b,e) and 503 K (c,f), a CO inlet partial pressure of 5.5 kPa, a total pressure of 1.85 kPa and space time, i.e., $W/F_{CO,0}$, of 23 (a), 23 (b), 20 (c), 29 (d), 17 (e) and 11 (f) $(kg_{cat}s)mol_{CO}^{-1}$ for a Co/CNT catalyst, see Section 2.1.3. The calculated normalized outlet concentrations are obtained by integrating eqs. [2–30] to [2–35] in which the net production rates are calculated as explained by eq. [2–15] and using the set of parameters given in Table 5-3.

As SSITKA data intrinsically contain information on the surface coverage of surface species, the regression of the extended SEMK model resulted in surface coverages which are closer to experimentally obtained values. Furthermore, based on an assessment of the atomic chemisorption enthalpies, the nature of the two site types included in the model could be linked to terrace sites and step sites. The ratio of terrace sites to the total site coverage amounts to 0.72.

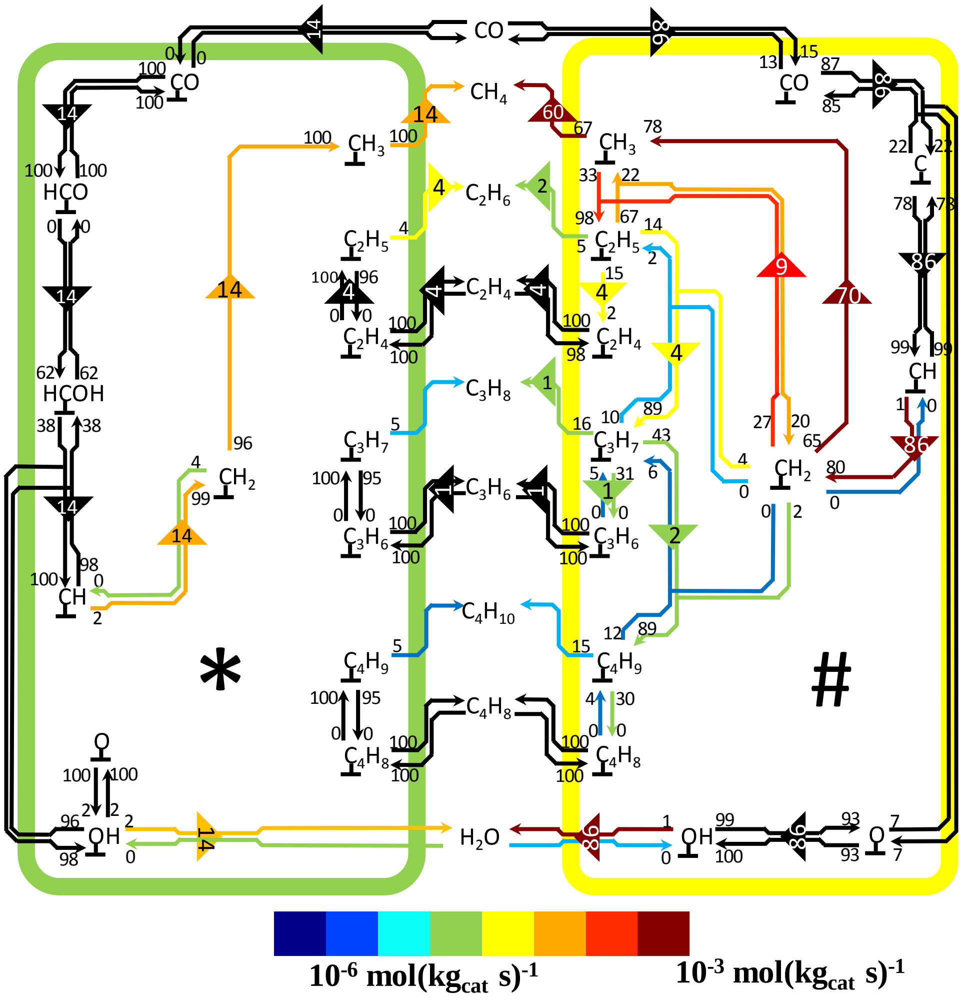
CO
CO
CO
HCO
HCOH
CH
CH4
CH3
CH3
C2H6
C2H5
C2H5
C2H4
C2H4
C2H4
C3H8
C3H7
C3H7
C3H6
C3H6
C3H6
C4H10
C4H9
C4H9
C4H8
C4H8
C4H8
CH2
CH2
C
CH
O
OH
OH
O
H2O
*
#
14
98
60
9
70
86
86
86
14
14
14
14
14
4
2
4
4
1
4
4
2
1
10-6 mol(kgcat s)-1
10-3 mol(kgcat s)-1

Figure 6: Reaction path analysis at a H_2/CO molar inlet ratio of 10, a temperature of 483 K, a CO inlet partial pressure of 5.5 kPa and space time, $W/F_{CO,0}$, of 23 $(kg_{cat}s)mol_{CO}^{-1}$. The simulation is performed by integrating eq. [2–35] in which the net formation rates are calculated as explained by eq. [2–15] and using the set of parameters of Table 5-3. The elementary reaction indicated by black arrows are at quasi-equilibrium as confirmed by affinity calculations, see eq. [2–52]. The reactions which are not at quasi-equilibrium are indicated by the colored arrows. The color of the arrow is related to the reaction rate of the elementary step as indicated. The numbers at the tail of an arrow are the differential disappearance factor, eq. [2–50]. The numbers at the tip are the differential formation factor, eq. [2–51]. The triangles indicate the direction of the net elementary reaction rate and the value in the triangle is the rate of the elementary reaction divided by the net CO consumption rate. The reactions in the green rectangle occur on the terrace sites, the reactions in the yellow rectangle occur on the step sites.

The results of a reaction path analysis are presented in Figure 6. The step sites contribute most significantly to the CO conversion. Furthermore, chain growth only takes place at these sites of the Co catalyst. The terrace sites convert CO to a lesser extent and the converted CO on these terrace sites ends up solely in methane. The alkenes which are produced on the step sites are partially hydrogenated to the corresponding alkanes on the terrace sites.

Apart from fundamental insights in the important reaction pathways and surface coverages, the SEMK model for Co catalyzed FTS can also be applied in a multi-scale model for the simulation and optimization of an industrial reactor unit. The complementary scales which have to be included in such a multi-scale model for a Trickle Bed Reactor are related to the catalyst pellet and the reactor, see Figure 7. For the catalyst pellet, a model has been developed accounting for diffusion in a spherically shaped pellet. At the reactor scale, the model accounts for convective mass transfer by means of a plug flow model. In order to assess the impact of the highly exothermic FTS reaction, radial dispersion effects have also been included at the reactor scale. The combination of a detailed SEMK model with a catalyst pellet scale and reactor scale model allows studying the complex interplay and, hence, obtain qualitative and quantitative insights, between elementary reactions occurring on the Co catalyst surface and heat and mass transfer phenomena occurring on larger scales.

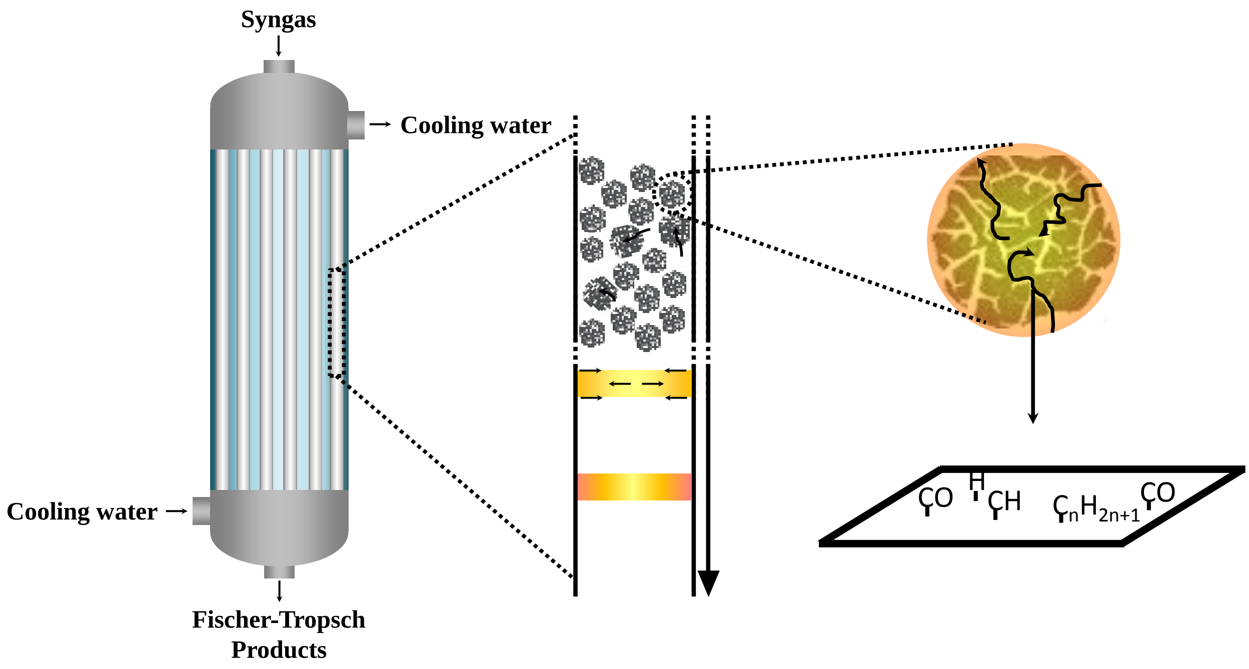

Figure 7: The Multi-Tubular Trickle Bed Reactor and the three scales which are accounted for by the multi-scale model, i.e., the reactor scale, the catalyst pellet scale and the scale of the reactions occurring on the Co metal particles.

Strong diffusional limitations exist in the catalyst pellet pores. The CO concentration changes from the bulk concentration at the catalyst pellet surface to zero in only the outer 10% of the catalyst pellet which is accompanied by a strongly increasing effective H_2/CO molar ratio. The latter occurs due to the higher H_2 diffusion coefficient compared to that of CO. This reduces both the maximum obtainable CO consumption rate in a catalyst pellet and the selectivity to heavier hydrocarbons. An extensive set of simulations at varying reaction conditions indicate that a substoichiometric H_2/CO molar ratio, i.e., a H_2/CO molar ratio < 2, is beneficial for the C_{5+} selectivity. Furthermore, at such low H_2/CO molar ratios, the C_{5+} selectivity is less sensitive to the temperature and, hence, the net CO consumption rate can be increased by increasing the temperature without impacting the C_{5+} selectivity negatively. This is illustrated in Figure 8.

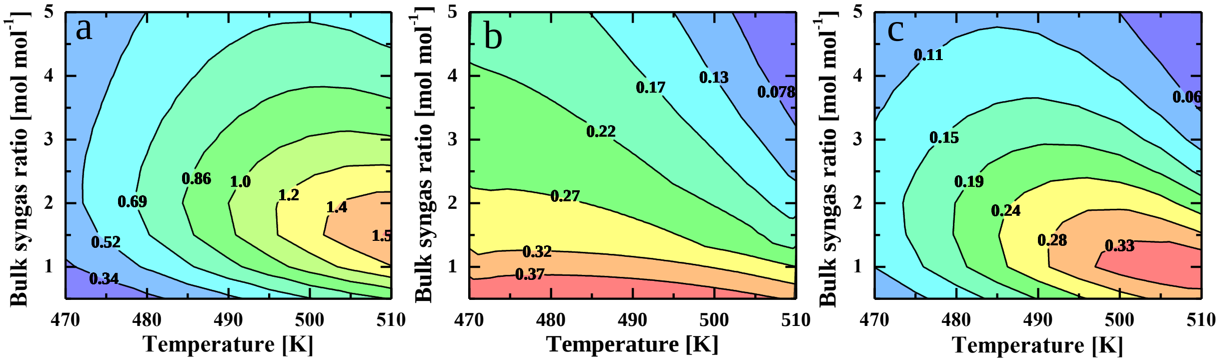

Figure 8: Contour plot of (a): CO consumption rate [10^{-3} mol_{CO} $(kg_{cat}\ s)^{-1}$], (b): selectivity to C_{5+} [mol mol^{-1}] and (c): C_{5+} productivity [10^{-3} mol $(kg_{cat}s)^{-1}$]. The total pressure was set at 2 MPa and the catalyst pellet diameter at 4 mm. The simulation results are obtained by integrating eqs. [6–1] and [6–2] with eqs. [6–4] and [6–6] as boundary conditions by applying the numerical methods outlined in Section 6.3. Other specifications of the catalyst pellet are provided in Table 6-1. Diffusion coefficients, liquid properties, … are calculated as explained in Section 6.2.2.

Simulations with the reactor model show that the phenomena on the catalyst pellet primarily control the behavior of the industrial reactor. A liquid recycle increases the heat transfer coefficient and, hence, reduces the maximum temperature in the reactor. Including radial dispersion effects illustrates that the highly exothermic FTS reaction effectively induces radial temperature profiles in the reactor.

Overall, a fundamental SEMK model for Co catalyzed FTS has been developed. This model has been extended to allow the simulation of SSITKA data requiring a combination of numerical methods, high performance computing and a specifically devised reaction network size reduction technique. The strategic advantage of a multi-scale model in order to obtain insights into the complex interplay of reactions and transfer phenomena and the simultaneous optimization of the catalyst and industrial reactor unit has also been demonstrated.

1. Dry, M.E., *The Fischer-Tropsch process: 1950-2000.* Catalysis Today, 2002. **71**(3-4): p. 227-241.
2. Lozano-Blanco, G., J.W. Thybaut, K. Surla, P. Galtier, and G.B. Marin, *Single-event microkinetic model for Fischer-Tropsch synthesis on iron-based catalysts.* Industrial & Engineering Chemistry Research, 2008. **47**(16): p. 5879-5891.

3. Cheng, J., T. Song, P. Hu, C.M. Lok, P. Ellis, and S. French, *A density functional theory study of the a-olefin selectivity in Fischer-Tropsch synthesis.* Journal of Catalysis, 2008. **255**(1): p. 20-28.
4. Weststrate, C.J., P. van Helden, and J.W. Niemantsverdriet, *Reflections on the Fischer-Tropsch synthesis: Mechanistic issues from a surface science perspective.* Catalysis Today, In Press.
5. van Santen, R.A., A.J. Markvoort, I.A.W. Filot, M.M. Ghouri, and E.J.M. Hensen, *Mechanism and microkinetics of the Fischer-Tropsch reaction.* Physical Chemistry Chemical Physics, 2013. **15**(40): p. 17038-17063.
6. den Breejen, J.P., P.B. Radstake, G.L. Bezemer, J.H. Bitter, V. Froseth, A. Holmen, and K.P. de Jong, *On the Origin of the Cobalt Particle Size Effects in Fischer-Tropsch Catalysis.* Journal of the American Chemical Society, 2009. **131**(20): p. 7197-7203.
7. Shannon, S.L. and J.G. Goodwin, *Characterization of Catalytic Surfaces by Isotopic-Transient Kinetics during Steady-State Reaction.* Chemical Reviews, 1995. **95**(3): p. 677-695.
8. Ledesma, C., J. Yang, D. Chen, and A. Holmen, *Recent Approaches in Mechanistic and Kinetic Studies of Catalytic Reactions Using SSITKA Technique.* Acs Catalysis, 2014. **4**(12): p. 4527-4547.
9. Berger, R.J., F. Kapteijn, J.A. Moulijn, G.B. Marin, J. De Wilde, M. Olea, D. Chen, A. Holmen, L. Lietti, E. Tronconi, and Y. Schuurman, *Dynamic methods for catalytic kinetics.* Applied Catalysis a-General, 2008. **342**(1-2): p. 3-28.
10. van Dijk, H.A.J., J.H.B.J. Hoebink, and J.C. Schouten, *A mechanistic study of the Fischer-Tropsch synthesis using transient isotopic tracing. Part-1: Model identification and discrimination.* Topics in Catalysis, 2003. **26**(1-4): p. 111-119.
11. van Dijk, H.A.J., J.H.B.J. Hoebink, and J.C. Schouten, *A mechanistic study of the Fischer-Tropsch synthesis using transient isotopic tracing. Part 2: Model quantification.* Topics in Catalysis, 2003. **26**(1-4): p. 163-171.
12. Yang, J., Y. Qi, J. Zhu, Y.A. Zhu, D. Chen, and A. Holmen, *Reaction mechanism of CO activation and methane formation on Co Fischer-Tropsch catalyst: A combined DFT, transient, and steady-state kinetic modeling.* Journal of Catalysis, 2013. **308**: p. 37-49.

Samenvatting

Fischer-Tropsch Synthese (FTS) zet syngas, d.i., een mengsel van CO en H_2, katalytisch om naar voornamelijk lineaire alkanen en 1-alkenen die verder verwerkt kunnen worden tot vloeibare brandstoffen met een laag zwavel-, stikstof- en aromatengehalte. De productdistributie kan ook afgesteld worden op de productie van zuurstofhoudende componenten die gebruikt kunnen worden als basischemicaliën in de chemische industrie. Syngas kan gevormd worden uit elke koolstofhoudende bron, d.i., steenkool, aardgas of biomassa. Hierdoor is er een sterke hernieuwde interesse in het FTS-proces in zowel de academische sector als de industrie sinds midden de Jaren 90 van de 20ste eeuw.

De FTS-reactie wordt gekatalyseerd door transitiemetalen zoals Ru, Fe, Co en Ni [1]. Enkel Co en Fe zijn, tot op heden, gebruikt op industriële schaal. Co-gebaseerde katalysatoren hebben een lage water-gas-shift activiteit en worden daardoor verkozen boven Fe-gebaseerde katalysatoren wanneer methaan gebruikt word als primaire bron voor het syngas. Daarenboven hebben Co-gebaseerde katalysatoren een hogere activiteit en een betere stabiliteit dan Fe-gebaseerde katalysatoren [1].

Voor de constructie van een multischaalmodel is een microkinetisch model dat adequaat het effect van reactiecondities op de reactantconversie en productopbrengsten vat, onontbeerlijk. Daarom werd een *Single-Event* MicroKinetisch (SEMK) model, origineel ontwikkeld voor Fe-gekatalyseerde FTS [2], gevalideerd voor Co-gekatalyseerde FTS. De validatie werd doorgevoerd aan de hand van experimentele data opgemeten in een gepaktbedreactor. De experimentele data werden opgemeten over een breed bereik van reactiecondities. Het SEMK-model is geregresseerd geworden naar deze experimentele datapunten, d.i., de te bepalen modelparameters werden gevarieerd totdat het model de experimentele data accuraat beschreef.

De regressie resulteerde in een globaal significant model met fysisch-chemisch betekenisvolle parameterwaarden, d.i., de finale schattingen voor de te bepalen modelparameters kwamen overeen met in de literatuur gerapporteerde waarden. Deze laatste zijn gebaseerd op regressie naar experimentele data of verkregen door *ab initio*-berekeningen. De regressieresultaten zijn voorgesteld in Figuur 1 als pariteitsgrafieken van de productopbrengsten.

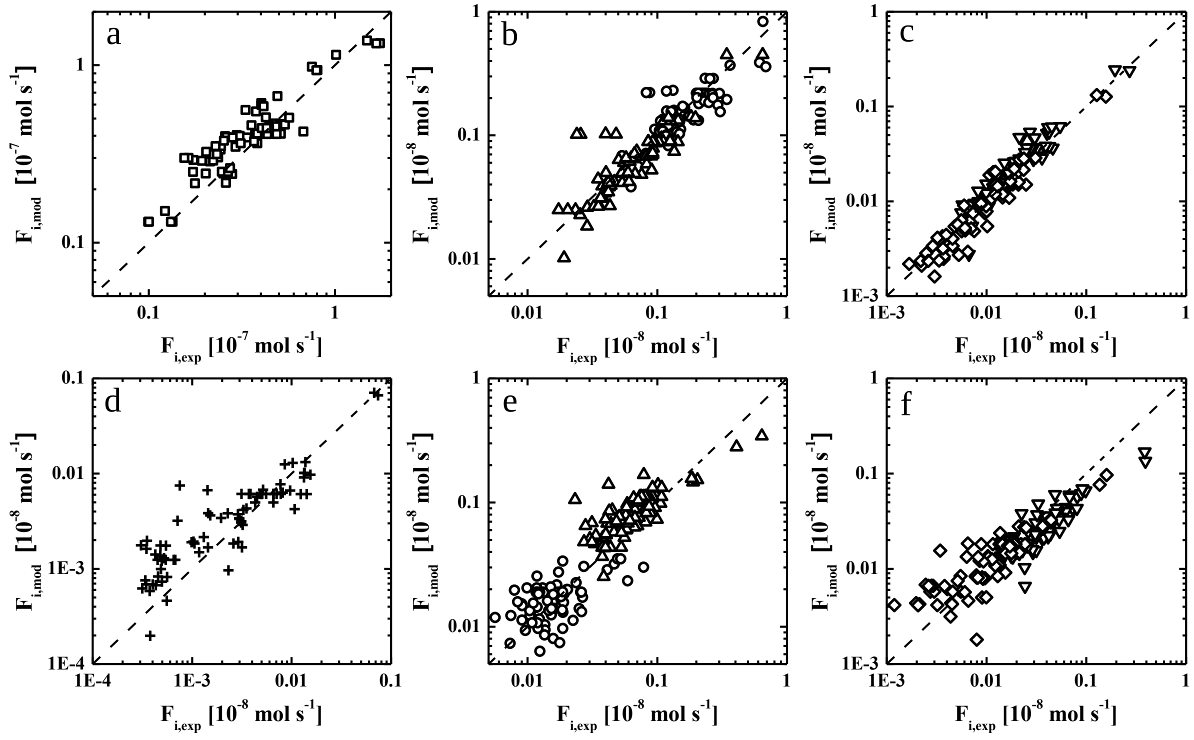

Figuur 1: Experimentele en modelberekende molaire uitlaatdebieten, F_i [mol s^{-1}], bij 3-10 H_2/CO-molaire inlaatverhouding, 483 K-503 K temperatuur, 3.7 kPa-16.7 kPa CO-inlaatpartieeldruk, 7.2-36.3 (kg_{kat} s)mol_{CO}^{-1} ruimtetijd, d.i., $W/F_{CO,0}$ en 185 kPa totaaldruk voor een Co/CNT katalysator, zie Sectie 2.1.3. De berekende molaire uitlaatdebieten zijn verkregen door verg. [2–27] en verg. [2–28] te integreren waarbij de nettoproductiesnelheden zijn berekend geworden als aangegeven door verg. [2–15] en gebruik te maken van de parameters van Tabel 3-4. (a): methaan; (b): ethaan (○) en propaan (△); (c): *n*-butaan (▽) en *n*-pentaan (◇); (d): *n*-hexaan (✚); (e): etheen (○) en propeen (△) en (f): 1-buteen (▽) en 1-penteen (◇).

De unieke eigenschappen van het ontwikkelde SEMK-model in vergelijking met andere microkinetische modellen, beschreven in de literatuur, zijn dat er geen *a priori* aannames gemaakt zijn betreffende een snelheidsbepalende stap en dat de reversibiliteit van elke elementaire reactiestap opgenomen is in het microkinetische model. Voorts zijn de activeringsenergieën koolstofnummeronafhankelijk. Een reactiepadanalyse werd opgesteld voor het gevalideerde microkinetisch model samen met een analyse van de snelheidcontrolerende elementaire stappen om zo de onderliggende chemie van de FTS en het effect van parameterwaarden op de geobserveerde activiteit en selectiviteit beter te begrijpen. Het resultaat van de reactiepadanalyse voor een typische reactieconditie voorkomend in de experimentele data is geïllustreerd in Figuur 2.

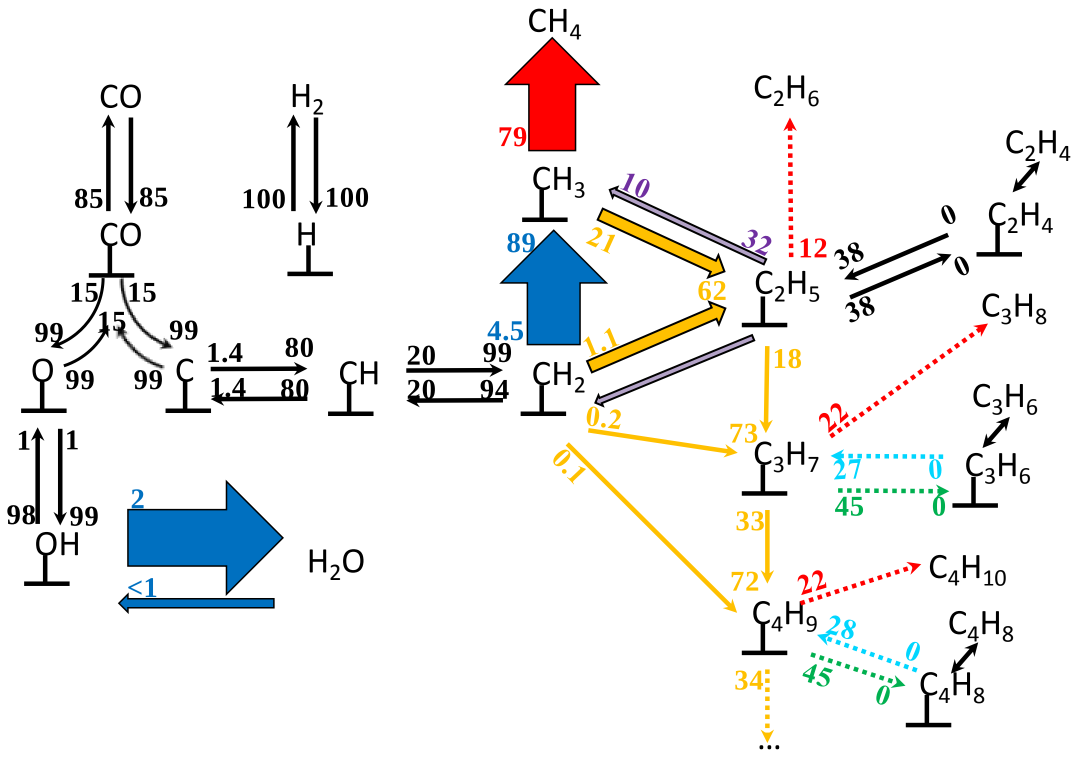
CH4
79
C2H6
C2H4
CO
H2
85
85
100
100
CH3
10
CO
H
89
21
32
12
38
0
C2H4
0
38
15
15
62
C2H5
C3H8
99
15
99
4.5
1.4
80
20
99
1.1
18
O
99
99
C
1.4
80
CH
20
94
CH2
C3H6
0.2
22
1
1
73
C3H7
27
0
C3H6
0.1
45
0
98
99
2
OH
33
H2O
72
22
C4H10
<1
C4H9
28
C4H8
0
45
0
C4H8
34
...

Figuur 2: Reactiepadanalyse bij een H_2/CO-molaire inlaatverhouding van 10, een temperatuur van 483 K, een CO-inlaatpartieeldruk van 5.5 kPa, een totaaldruk van 185 kPa en een ruimtetijd, d.i., $W/F_{CO,0}$, van 20 $(kg_{cat}s)mol_{CO}^{-1}$ voor een Co/CNT katalysator, zie Sectie 2.1.3. De simulatieresultaten zijn verkregen door verg. [2–27] en verg. [2–28] te integreren waarbij de nettoproductiesnelheden zijn berekend geworden als aangegeven door verg. [2–15] en gebruik te maken van de parameters van Tabel 3-4. De elementaire stappen die bij quasi-evenwicht zijn, zijn aangegeven in het zwart. Dit werd bepaald door middel van affiniteitsberekeningen, zie Tabel 3-4. De reacties die niet bij quasi-evenwicht zijn, zijn voorgesteld door de gekleurde pijlen. De dikte van deze pijlen is geschaald met de reactiesnelheid. De reactiefamilies die opgenomen zijn in het SEMK-model hebben een kleur toegewezen gekregen, d.i., CH_2^{**}-insertie/-desertie (geel – paars), $C_nH_{2n+1}^{*}$-hydrogenering (rood), beta-hydride-eliminatie/-additie (groen/cyaan). De andere elementaire stappen zijn voorgesteld in het blauw. Het nummer aan de staart van een pijl is de differentiële verdwijnfactor, zie verg. [2–50]. Het nummer aan het hoofd van een pijl is de differentiële vormingsfactor, zie verg. [2–51]. H_2 is niet opgenomen om de figuur niet te overladen.

Een belangrijke bevinding van de reactiepadanalyse is de kinetische relevantie van de reversibiliteit van de eerste CH_2^{**}-insertiestap. Dit komt door de hogere chemisorptie-enthalpie van het CH_3^{*}species op het metaaloppervlak in vergelijking met de $C_nH_{2n+1}^{*}$species met meer dan één koolstofatoom. Deze eigenschap komt overeen met bevindingen verkregen via 'vaste stof ab initio'-berekeningen [3]. Dit draagt bij aan de typisch geobserveerde afwijkingen van de Anderson-Schulz-Flory-verdeling, d.i., een hogere methaan- en lagere etheenselectiviteit dan verwacht zou worden gebaseerd op een groep van totaal koolstofonafhankelijke parameters binnen een reactiefamilie. De OH^{*}-hydrogenering en de CH_2^{**}-hydrogenering werden geïdentificeerd als de kinetisch meest relevante stappen. De katalysatoractiviteit wordt dus gecontroleerd door OH^{*}- en CH_2^{**}-hydrogenering waarbij CH_2^{**}-hydrogenering ook de selectiviteit bepaald. Het verwijderen van de waterprecursoren van het Co-katalysatoroppervlak zijn ook door oppervlakstudies geïdentificeerd als de snelheidslimiterende stap voor de conversie van CO [4].

Door de introductie van de atomaire chemisorptie-enthalpiën in het SEMK-model kan het verschil in activiteit tussen een Fe- en een Co-gebaseerde katalysator gerelateerd worden aan intrinsieke eigenschappen van deze katalysatormaterialen. De watervormingsstappen zijn op een Fe-gebaseerde katalysator bij quasi-evenwicht van bij het begin van de reactor. Dit is het resultaat van een hogere atomaire chemisorptie-enthalpie van zuurstof op Fe-gebaseerde katalysatoren ten op zicht van Co-gebaseerde katalysatoren. Dit resulteert in een toenemende oppervlakconcentratie van de zuurstofhoudende species als functie van de ruimtetijd of, daarmee equivalent, toenemende partieeldruk van H_2O als een van de belangrijkste FTS-reactieproducten. Water heeft dus een inhibiterend effect op de activiteit van Fe-gebaseerde katalysatoren.

Tot op heden is het FTS-proces één van de meest uitdagende processen om te onderzoeken [5]. Recente experimentele studies hebben uitgewezen dat de grootte van het metaaldeeltje van de katalytisch actieve fase een effect heeft op de conversie van CO en de productselectiviteit [6]. Kleinere metaaldeeltjes zijn minder actief voor de FTS en resulteren in hogere methaanopbrengsten in vergelijking met grotere metaaldeeltjes. Een interessante techniek die kan worden aangewend om extra inzichten te verwerven in zulke fenomenen is de stationaire isotope tijdsafhankelijk kinetische analyse (SSITKA) [7]. In een SSITKA-experiment kan de reactorvoeding worden gewisseld tussen 2 voedingen met verschillende isotopisch gelabelde reactanten. In het geval dat beide voedingslijnen worden geopereerd onder exact dezelfde werkingsvoorwaarden blijft de katalysator stationair bedreven terwijl de uitwisseling van isotopen ten gevolge van reactie van de reactanten naar de producten gevolgd kan worden met behulp van massaspectrometrie (MS). Op deze manier kan er veel meer gedetailleerde informatie verkregen worden over de katalysator bij de bestudeerde werkingsvoorwaarden. SSITKA werd ook toegepast om extra inzichten te verkrijgen over effecten van het dragermateriaal, promotoreffecten, … Een combinatie van SSITKA met microkinetisch modelering laat toe om nog extra inzichten te verwerven in de voorgenoemde fenomenen [8].

Daarom is er een modeleringsstrategie uitgedacht voor het simuleren van SSITKA-data. Bij het modeleren van dit type van data moet er een verzameling van partiële, gewone en algebraïsche vergelijkingen worden opgelost [9]. Het vinden van een numerieke oplossing van deze verzameling van vergelijkingen is door de aard van de partiële differentiaalvergelijkingen bijzonder moeilijk. Er is dan ook een uitgebreide studie doorgevoerd om een discretisatieschema voor de ruimtelijke afgeleide te kunnen selecteren die rekening houdt met zowel de rekentijd als de accuraatheid. Voor lage wisseltijdsconstanten, d.i., a_2 (verg. [2–34]) ≤ 0.1s, resulteerden de van Leer en van Albada flux-limiterende functies in de laagste rekentijden. Bij hogere wisseltijdsconstanten, d.i., $a_2 \geq 1$ s, kunnen lineaire discretisatieschema's worden aangewend. De ontwikkelde modeleringsstrategie moest ook rekening houden met de isotope labels in de reactienetwerkgenerering. De uitgedachte reactienetwerkgenereringsmethodologie reduceert de exponentiële afhankelijkheid van het aantal species met het koolstofgetal tot een kwadratische afhankelijkheid. Een pictografische weergave van de reactienetwerkgenereringsmethodologie is voorgesteld in Figuur 4. Deze reactienetwerkgenereringsmethodologie reduceert de rekentijd met een factor 10.

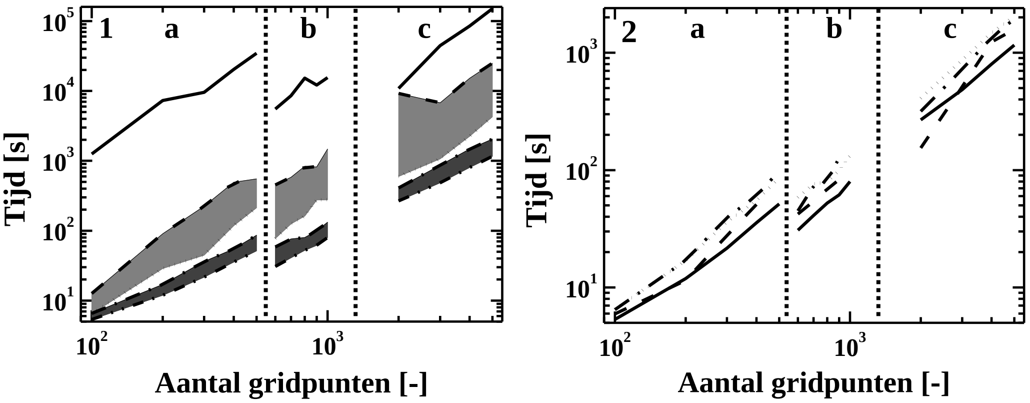

Figuur 3: CPU-tijd als functie van het aantal gridpunten. a_2 (verg. [2–34]) = 0.01 s. a: $W/F_{CO,0}$ = 4 (kg_{cat} s)mol_{CO}^{-1}. b: $W/F_{CO,0}$ = 40 (kg_{cat} s)mol_{CO}^{-1}. c: $W/F_{CO,0}$ = 400 (kg_{cat} s)mol_{CO}^{-1}. 1: Volle lijn: Superbee, gestreepte lijn: SMART, stippellijn: SPL-1/3, streep-stippellijn: GVA-1/2, streep-stip-stippellijn: van Albada, grijze band: MUSCL, Koren, Minmod, H-CUI, H-QUICK, SMARTER and GPR-1/2, donker grijze band: OSPRE en van Leer. 2: Volle lijn: van Albada, gestreepte lijn: van Leer, stippellijn: OSPRE en streep-stippellijn: GVA-1/2. De simulaties werden doorgevoerd voor de methanatiereactie. De resultaten werden verkregen door integreren van verg. [4–1] met de DASPK-oplossingsprocedure waarbij de nettoproductiesnelheden zijn berekend zoals aangeven door verg. [2–15].

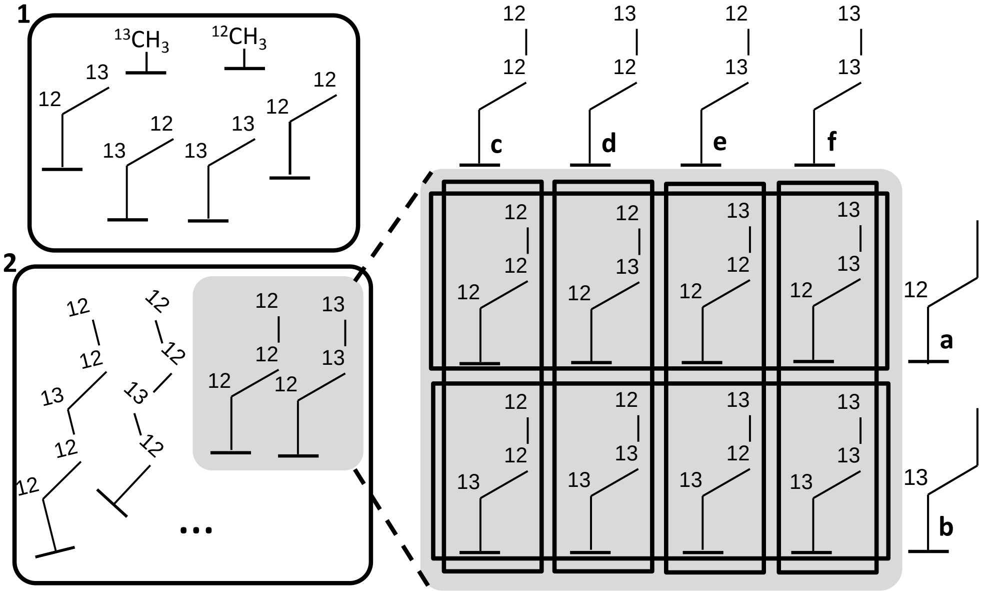

Figuur 4: Grafische voorstelling van de reactienetwerkgenerering. De isotoop gelabelde metaalalkylspecies worden onderverdeeld in deelverzamelingen. 1: groep met een maximum koolstofgetal, CN_{det}, waarvoor alle mogelijke isotopologen en isotopomeren worden gevolgd. 2: complement van groep 1 waarvoor deelverzamelingen worden geïntroduceerd. Deze deelverzamelingen zijn geïllustreerd voor de isotoop gelabelde metaalpropylspecies en wordt gedaan op basis van de koolstofatomen op een positie i in de keten met $1 \leq i < CN_{max} - CN_{det}$ (a en b) of de isotope label van de laatste CN_{det} koolstofatomen (c-f).

Het SEMK-model dat geregresseerd was naar de stationaire experimentele data is gebruikt geweest voor de simulatie van de tijdsafhankelijke responsen van CO en CH_4 opgemeten in SSITKA-experimenten voor een Co/CNT-katalysator, zie Sectie 2.1.3. De eerste modeleringsresultaten toonden aan dat er bijkomende reactiestappen nodig waren in het SEMK-model. Daarom werden er, ook gebaseerd op gerapporteerde resultaten in de literatuur [10-12], 2 types van actieve centra geïntroduceerd in het SEMK-model waarbij op beide centra CO-dissociatie en ketengroei werden beschouwd. De regressieresultaten verkregen met het uitgebreide SEMK-model zijn voorgesteld in Figuur 5 voor de tijdsafhankelijke responsen van CO en CH_4. Het dient opgemerkt te worden dat het SEMK-model dat in dit proefschrift is ontwikkeld voor de modelering van SSITKA-data specifiek rekening houdt met H_2-adsorptie, hydrogeneringsstappen in de ketengroeireacties en watervormingsreacties. Verder werden activeringsenergieën en atomaire chemisorptie-enthalpiën in rekening gebracht in het uitgebreide

SEMK-model. Daardoor kan dit SEMK-model worden gebruikt voor simulatie van meer dan één SSITKA-experiment zonder dat de te bepalen modelparameters moeten herschat worden bij andere werkingsvoorwaarden.

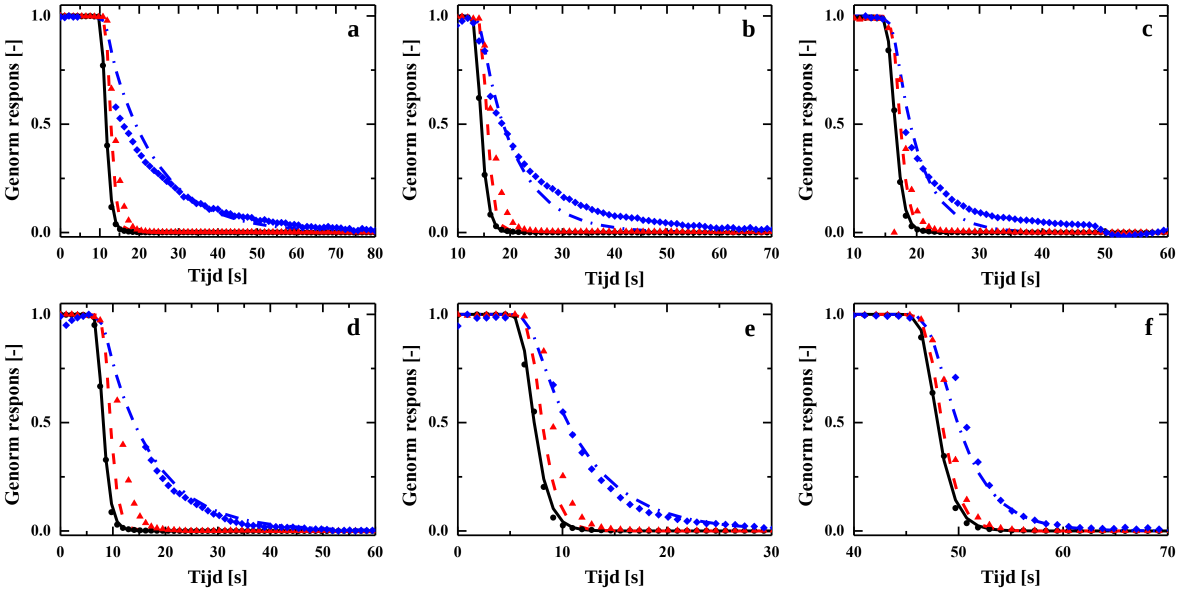

Figuur 5: Experimentele (symbolen) en modelberekende (lijnen) van de genormaliseerde uitlaatconcentraties van Ar (●,—), CO(▲, – –) en CH_4 (◆, – •), bij een molaire H_2/CO-inlaatverhouding van 5 (a-c) en 10 (d-f), een temperatuur van 483 K (a,d), 493 K (b,e) en 503 K (c,f), een CO-inlaatpartieeldruk van 5.5 kPa, een totaaldruk van 1.85 kPa en ruimtetijd, d.i., $W/F_{CO,0}$, van 23 (a), 23 (b), 20 (c), 29 (d), 17 (e) and 11 (f) $(kg_{cat}s)mol_{CO}^{-1}$ voor een Co/CNT-katalysator, zie Sectie 2.1.3. De berekende genormaliseerde uitlaatconcentraties zijn verkregen door integreren van verg. [2–30] – [2–35] waarbij de nettoproductiesnelheden zijn berekend zoals aangeven door verg. [2–15] en gebruik te maken van de parameters van Tabel 5-3.

Aangezien SSITKA-data intrinsiek informatie bevat over de bedekkingsgraden van sommige, kinetisch relevante oppervlakspecies, resulteerde de regressie van het uitgebreide SEMK-model in bedekkingsgraden die beter corresponderen met experimenteel vastgestelde bedekkingsgraden. Een diepgaandere analyse van het SEMK-model liet toe om de aard van de twee verschillende centra te koppelen aan terrascentra enerzijds en stapcentra anderzijds. De verhouding van terrascentra t.o.v. de totale hoeveelheid centra op het Co-katalysatoroppervlak bedraagt 0.72.

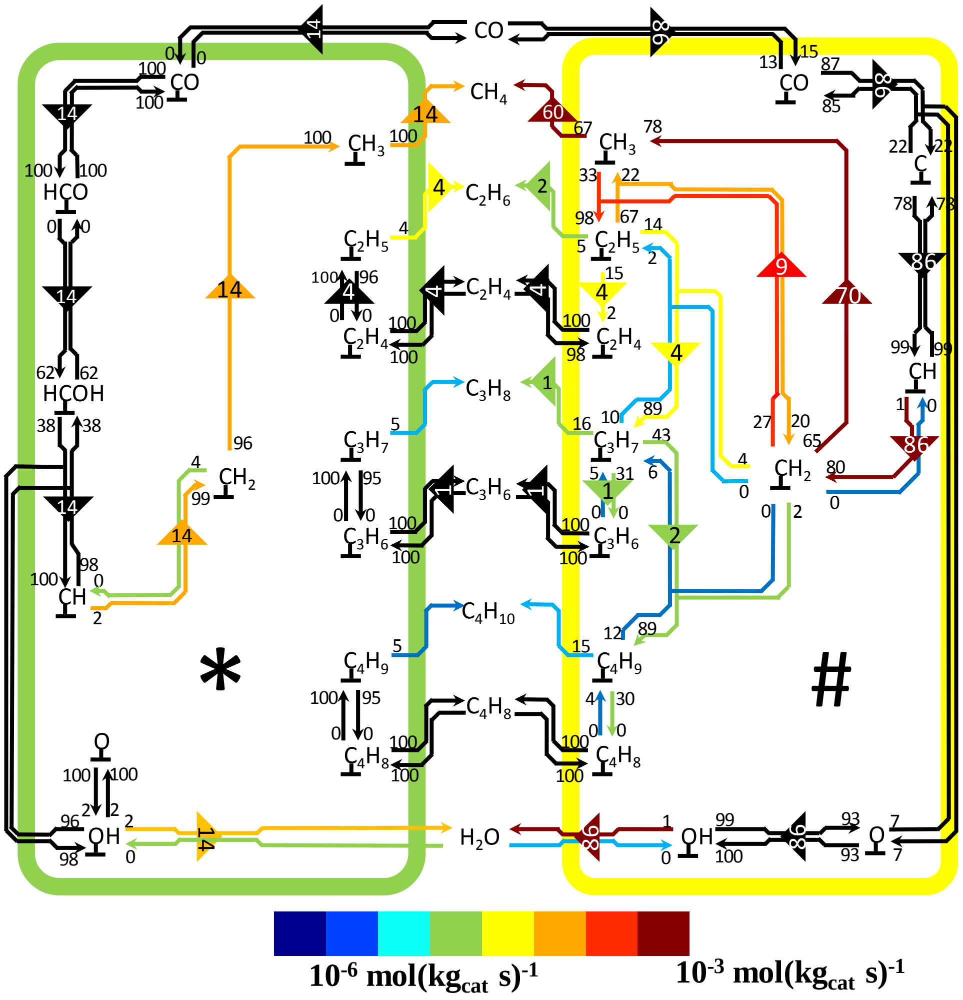

Figuur 6: Reactiepadanalyse bij een H_2/CO-molaire inlaatverhouding van 10, een temperatuur van 483 K, a CO-inlaatpartieeldruk van 5.5 kPa en een ruimtetijd, W/$F_{CO,0}$, van 23 (kg_{cat}s)mol_{CO}^{-1}. De simulatieresultaten zijn verkregen door integreren van verg. [2–35] waarbij de nettoproductiesnelheden zijn berekend zoals aangegeven door verg. [2–15] en gebruik te maken van de parameters van Tabel 5-3. De elementaire reacties weergegeven in het zwart zijn bij quasi-evenwicht, verg. [2–52]. De reacties die niet bij quasi-evenwicht zijn, zijn weergeven door middel van de gekleurde pijlen. De kleur van de pijlen is gerelateerd van de reactiesnelheid zoals aangegeven. Het getal bij de staart van de pijl is de differentiële verdwijnfactor, verg. [2–50]. Het getal bij het hoofd van de pijl is de differentiële vormingsfactor, verg. [2–51]. De driehoeken geven de richting van de nettoreactiesnelheid van de elementaire reactie aan en het getal in de driehoek is de snelheid van de elementaire stap relatief t.o.v. de nettoverdwijnsnelheid van CO. De reacties in de groene rechthoek gaan door op de terrascentra, de reacties in de gele rechthoek op de stepcentra.

De resultaten van een reactiepadanalyse zijn voorgesteld in Figuur 6. De stapcentra dragen het meest bij tot de CO conversie en enkel op deze centra is er ketengroei. De terrascentra dragen veel minder bij tot de CO conversie. Daarnaast verdwijnt de CO die wordt omgezet op deze centra enkel in methaan. De alkenen die worden geproduceerd op stapcentra worden gedeeltelijk gehydrogeneerd tot de overeenkomstige alkanen op de terrascentra.

Naast fundamentele inzichten in de belangrijke reactiepaden en oppervlakspecies, kan het SEMK-model voor de Co-gebaseerde FTS ook worden toegepast in een multischaalmodel voor de simulatie en optimalisatie van een industriële eenheid. De bijkomende schalen die in rekeningen moeten worden gebracht voor een multischaalmodel van een sijpelkolomreactor zijn de schaal van de katalysatorkorrel en de schaal van de reactor zelf, zie Figuur 7. Voor de katalysatorkorrelschaal is er een model ontworpen dat rekening houdt met diffusie in een sferische korrel. Op de reactorschaal houdt het model hoofdzakelijk rekening met convectief transport. Om de impact na te kunnen gaan van de zeer exotherme FTS-reactie, werden radiale dispersie-effecten ook in rekening gebracht. De combinatie van een gedetailleerd SEMK-model met een model voor de katalysatorkorrel en de reactor laat toe om het complexe samenspel tussen elementaire reacties die doorgaan op het Co-katalysatoroppervlak en warmte- en massatransportfenomenen die plaatsvinden op grotere schalen te bestuderen en dus meer kwalitatieve en kwantitatieve inzichten te verwerven.

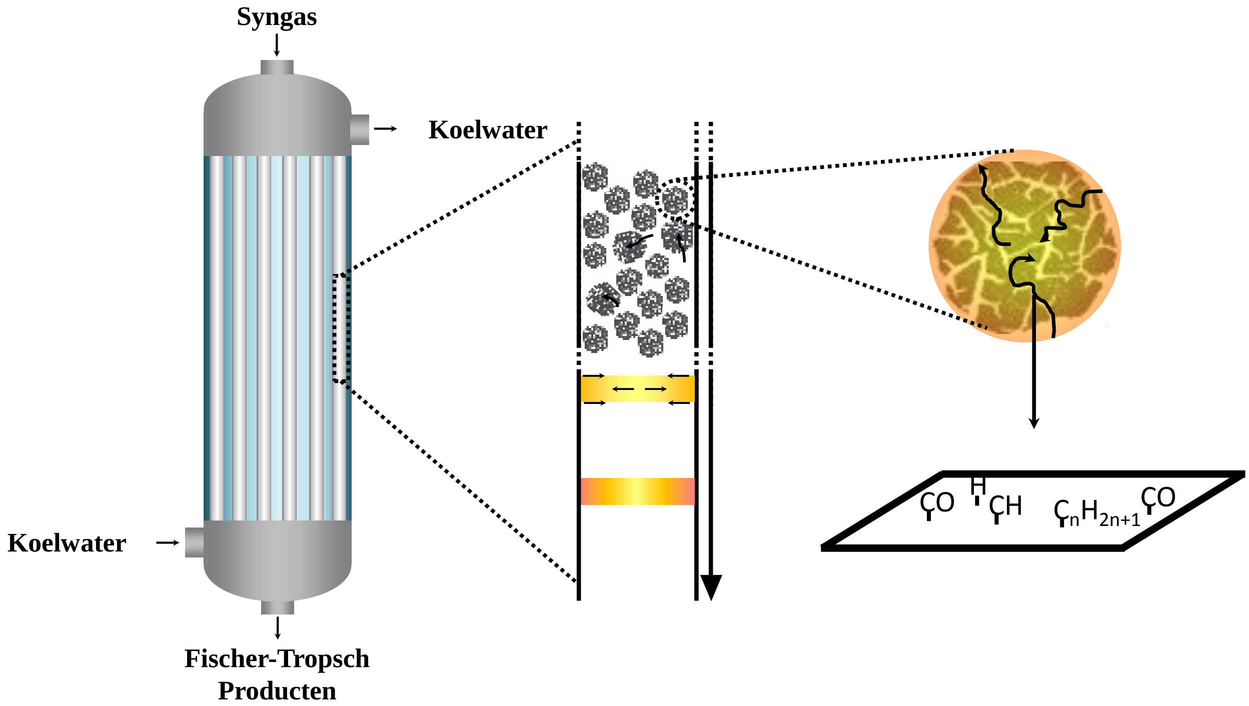

Figuur 7: De multi-tubulaire sijpelkolomreactor en de drie schalen die in rekening worden gebracht voor het multischaalmodel, d.i., de reactorschaal, de katalysatorkorrelschaal en de schaal van de reacties die doorgaan op het Co-metaaldeeltje.

In de poriën van de katalysator werden sterke concentratiegradiënten waargenomen. De CO-concentratie is enkel verschillende van nul in de buitenste 10% van de katalysatorkorrel. Dit gaat gepaard met een sterke toename in de molaire H_2/CO-verhouding. Dit treedt op doordat de H_2-diffusiecoëfficiënt groter is dan de CO-diffusiecoëfficiënt. Dit reduceert zowel de maximum verkrijgbare CO-verdwijnsnelheid in de katalysatorkorrel als de selectiviteit naar langere koolwaterstoffen. Een uitgebreide studie bij variërende werkvoorwaarden toont aan dat een substoichiometrische, molaire H_2/CO-verhouding, d.i., een H_2/CO-verhouding < 2, gunstig is voor de C_{5+} selectiviteit. Daarnaast is de C_{5+} selectiviteit minder gevoelig voor de temperatuur bij deze lagere molaire H_2/CO-verhoudingen. Zo kan de CO-consumptiesnelheid verhoogd worden door de temperatuur te laten toenemen zonder dat de C_{5+} selectiviteit nadelig wordt beïnvloed. Dit is geïllustreerd in Figuur 8.

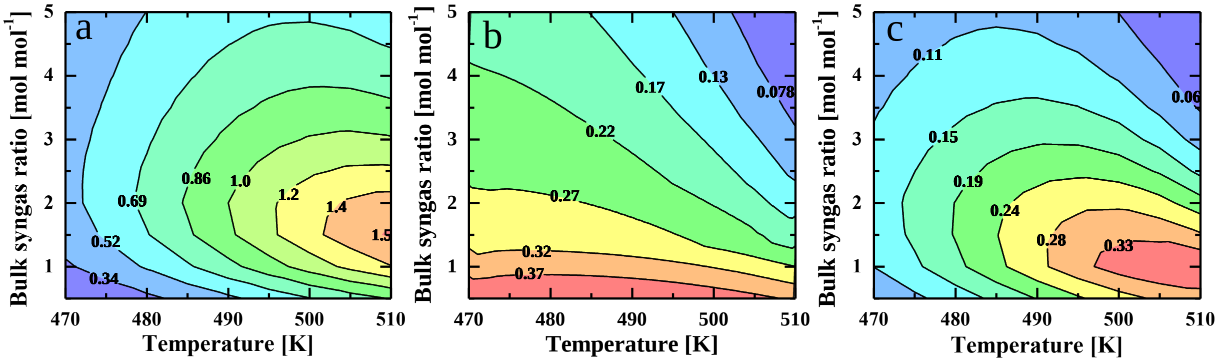

Figuur 8: Contourplot van (a): CO-verdwijnsnelheid [10^{-3}mol$_{CO}$ (kg$_{cat}$ s)$^{-1}$], (b): selectiviteit naar C_{5+} [mol mol^{-1}] and (c): C_{5+} productiviteit [10^{-3} mol (kg$_{cat}$s)$^{-1}$]. De totaaldruk was ingesteld op 2 MPa en de katalysatorkorreldiameter op 4 mm. De simulatieresultaten werden verkregen door integreren van verg. [6–1] en [6–2] met verg. [6–4] en [6–6] als randvoorwaarden door toepassen van de numerieke methodes uitgelegd in Sectie 6.3. De andere katalysatorkorrelspecificaties zijn opgenomen in Tabel 6-1. De diffusiecoëfficiënten, vloeistofeigenschappen, … zijn berekend zoals uitgelegd in Sectie 6.2.2.

Simulaties met het reactormodel tonen aan dat de fenomenen die zich afspelen in de katalysatorkorrel hoofdzakelijk het gedrag van de industriële reactor controleren. Een vloeistofstroom doorheen de reactor doet de warmteoverdrachtscoëfficiënt toenemen waardoor de maximumtemperatuur in de reactor verlaagt. Het in rekening brengen van radiale dispersie-effecten toont aan dat de zeer exotherme FTS-reacties effectief radiale temperatuursprofielen induceert in de reactor.

Een fundamenteel SEMK-model voor de Co-gekatalyseerde FTS-reactie werd ontwikkeld. Dit model werd uitgebreid zodat het ook kan worden gebruikt voor de simulatie van SITTKA-data. Hiervoor is er een specifieke combinatie vereist van numerieke methodes, supercomputers en een specifiek uitgedachte reactienetwerkgeneringsmethodologie die de grootte van het reactienetwerk limiteert. Het strategische voordeel van een multischaalmodel om bijkomende inzichten te verwerven in het complex samenspel van oppervlakreacties en transportfenomenen en het simultaan optimaliseren van de katalysator en de industriële reactor is ook aangetoond geweest.

1. Dry, M.E., *The Fischer-Tropsch process: 1950-2000.* Catalysis Today, 2002. **71**(3-4): p. 227-241.
2. Lozano-Blanco, G., J.W. Thybaut, K. Surla, P. Galtier, and G.B. Marin, *Single-event microkinetic model for Fischer-Tropsch synthesis on iron-based catalysts.* Industrial & Engineering Chemistry Research, 2008. **47**(16): p. 5879-5891.
3. Cheng, J., T. Song, P. Hu, C.M. Lok, P. Ellis, and S. French, *A density functional theory study of the a-olefin selectivity in Fischer-Tropsch synthesis.* Journal of Catalysis, 2008. **255**(1): p. 20-28.
4. Weststrate, C.J., P. van Helden, and J.W. Niemantsverdriet, *Reflections on the Fischer-Tropsch synthesis: Mechanistic issues from a surface science perspective.* Catalysis Today, In Press.
5. van Santen, R.A., A.J. Markvoort, I.A.W. Filot, M.M. Ghouri, and E.J.M. Hensen, *Mechanism and microkinetics of the Fischer-Tropsch reaction.* Physical Chemistry Chemical Physics, 2013. **15**(40): p. 17038-17063.
6. den Breejen, J.P., P.B. Radstake, G.L. Bezemer, J.H. Bitter, V. Froseth, A. Holmen, and K.P. de Jong, *On the Origin of the Cobalt Particle Size Effects in Fischer-Tropsch Catalysis.* Journal of the American Chemical Society, 2009. **131**(20): p. 7197-7203.
7. Shannon, S.L. and J.G. Goodwin, *Characterization of Catalytic Surfaces by Isotopic-Transient Kinetics during Steady-State Reaction.* Chemical Reviews, 1995. **95**(3): p. 677-695.
8. Ledesma, C., J. Yang, D. Chen, and A. Holmen, *Recent Approaches in Mechanistic and Kinetic Studies of Catalytic Reactions Using SSITKA Technique.* Acs Catalysis, 2014. **4**(12): p. 4527-4547.
9. Berger, R.J., F. Kapteijn, J.A. Moulijn, G.B. Marin, J. De Wilde, M. Olea, D. Chen, A. Holmen, L. Lietti, E. Tronconi, and Y. Schuurman, *Dynamic methods for catalytic kinetics.* Applied Catalysis a-General, 2008. **342**(1-2): p. 3-28.
10. van Dijk, H.A.J., J.H.B.J. Hoebink, and J.C. Schouten, *A mechanistic study of the Fischer-Tropsch synthesis using transient isotopic tracing. Part-1: Model identification and discrimination.* Topics in Catalysis, 2003. **26**(1-4): p. 111-119.
11. van Dijk, H.A.J., J.H.B.J. Hoebink, and J.C. Schouten, *A mechanistic study of the Fischer-Tropsch synthesis using transient isotopic tracing. Part 2: Model quantification.* Topics in Catalysis, 2003. **26**(1-4): p. 163-171.
12. Yang, J., Y. Qi, J. Zhu, Y.A. Zhu, D. Chen, and A. Holmen, *Reaction mechanism of CO activation and methane formation on Co Fischer-Tropsch catalyst: A combined DFT, transient, and steady-state kinetic modeling.* Journal of Catalysis, 2013. **308**: p. 37-49.

Chapter 1 Introduction

Our present economy strongly depends on the availability of crude oil as the major resource for the production of transportation fuels and chemicals. Although the crude oil price, see Figure 1-1, can vary strongly on a short term basis due to the geopolitical situation, a long term increase in crude oil price can be discerned. This goes hand in hand with the main idea of depleting natural crude oil resources which has never left the scene since the 1950s. Next to this, a stronger environmental awareness has led to more stringent environmental legislations around the globe with respect to the emission of NO_x, SO_x, soot and other detrimental products. Furthermore, the oil production is concentrated in a limited number of countries. These considerations have catalyzed the search for alternative production routes for fuels and chemicals starting from other carbon containing feedstocks such as natural gas, coal or biomass. Certainly the latter feedstock is important due to its renewable character.

Fischer-Tropsch Synthesis (FTS) is frequently envisaged as a promising process in the transition from an economy which strongly depends on crude oil towards a more sustainable one. In FTS, CO and H_2, also referred to as syngas, are converted into a hydrocarbon mixture, i.e., a synthetic crude. This hydrocarbon mixture can subsequently be processed into clean transportation fuels, base chemicals and high quality lubricants. The transportation fuels are free of sulfur, nitrogen and aromatics, hence, decreasing the emission of NO_x, SO_x and soot during their combustion. The CO and H_2 are obtained through gasification, partial oxidation or reforming of a carbon containing feedstock. FTS is, hence, capable of processing any carbonaceous feedstock into products which can be transported through, stored in and used by already existing infrastructures. This has resulted in a strong interest in FTS both in academia and industry. The former is illustrated by a strong increase in the annual number of research papers published on the topic, see Figure 1-1. The increased interest from industry has resulted in the installation of large-scale production facilities worldwide, see section 1.1.

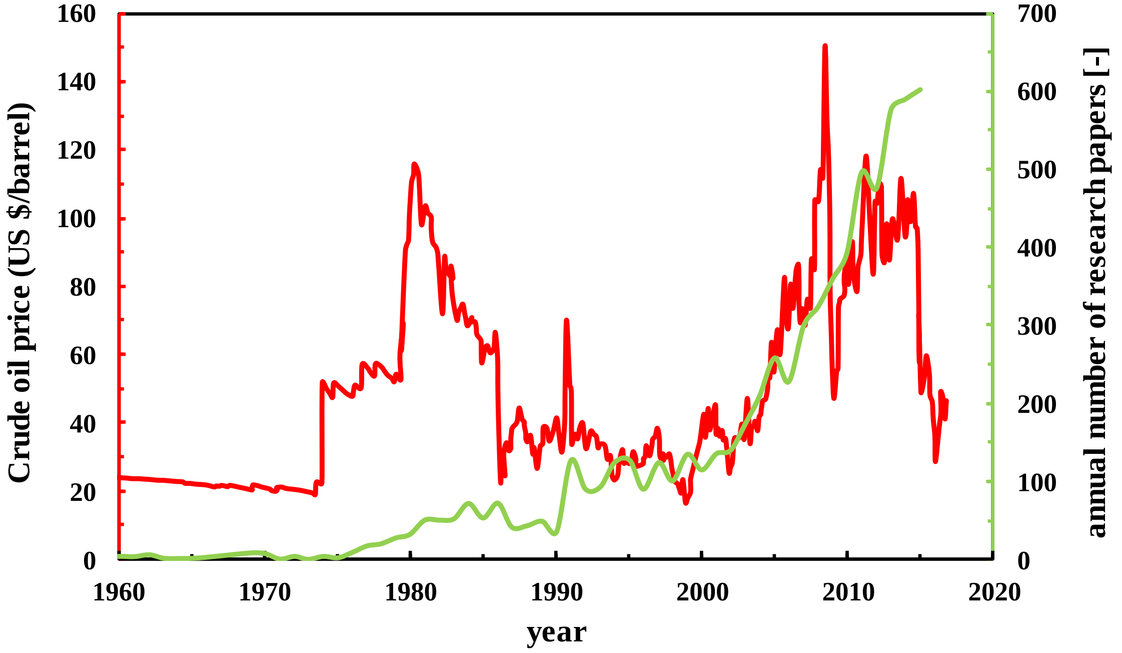

Figure 1-1: West Texas Intermediate crude oil price in US $ per barrel (red) [1] and the annual number of research papers published on the topic 'Fischer-Tropsch Synthesis' (green) [2]. The crude oil price is adjusted for inflation by means of the Consumer Price Index.

1.1 Feedstocks – Gas to Liquids, Coal to Liquids and Biomass to Liquids (GtL, CtL and BtL)

Natural gas, coal, biomass or very heavy crude oils can be converted into syngas and can subsequently be used as FTS reactants. Currently, the existing FTS production facilities are based on coal or natural gas.

1.1.1 Gas-to-Liquids (GtL) FTS

The natural gas reserves are much larger than the crude oil reserves. The cost to transport natural gas is, however, much higher than the transportation of crude oil. A significant amount of these natural gas reserves is present in so called 'stranded' fields which are too far away for the gas exploitation to be economically attractive with the currently available technologies. Converting the natural gas into liquid hydrocarbons can make the exploitation of these stranded fields economic viable, certainly when there is a large price difference between crude oil and natural gas.

The largest FTS production facilities are based on natural gas. Table 1-1 gives an overview of production facilities which were, are or will, in the near future, become operational together with the feedstock used, the location and the operating companies. From 1951 to 1957, a natural gas based production facility was operational in Brownsville (Texas) with an annual production capacity of 360 kt y^{-1} [3-5]. It was based on the Hydrocol Process [6] developed by Hydrocarbon Research Inc. A Fixed Fluidized Bed Reactor (FFBR) technology, see section 1.2.2, was applied at High Temperature Fischer-Tropsch (HTFT) conditions, see section 1.2.2, employing an Fe catalyst. This production facility ceased operation due to the low crude oil prices caused by the discovery of large oil reserves in the 1950’s in the Middle East

Table 1-1: Fischer-Tropsch Synthesis (FTS) production facilities [3-5, 7-9].

Year	Location	Production capacity	company	Catalyst
Gas based FTS production facilities				
1950	Brownsville	360 kt y^{-1}	Carthage Hydrocol Company	Fe
1992	South Africa	1000 kt y^{-1}	PetroSA	Fe
1993	Malaysia	500 kt y^{-1}	Shell	Co
2007	Qatar	1800 kt y^{-1}	Qatar Petroleum and Sasol	Co
2011	Qatar	7000 kt y^{-1}	Shell	Co
2014	Escravos	1800 kt y^{-1}	Chevron Nigeria	Co
Coal based FTS production facilities				
1938	Germany	660 kt y^{-1}	Ruhrchemie AG	Co
1955	South Africa	Combined: 6000 kt y^{-1}	Sasol	Fe
1980	South Africa			Fe
1982	South Africa			Fe

In 1992, a GtL FTS production facility was commissioned by the South African Government at Mossel Bay [3, 5, 10]. By 2002, PetroSA took over the operation of this production facility. It has 16 Circulating Fluidized Bed reactors (CFBRs), see also section 1.2.2, a reactor technology licensed by Sasol. The total production capacity amounts to 1000 kt y^{-1}. The natural gas is first reformed into CO, CO_2, H_2 and H_2O and subsequently converted into a synthetic crude. The CFBRs are operated at HTFT conditions. PetroSA has also demonstrated the use of a Low Temperature Fischer-Topsch Synthesis (LTFT) unit, see also section 1.2.2, and continues to invest intensively in research and development projects in the area of GtL technology.

Shell has two GtL production facilities, i.e., one in Malaysia [11, 12] and one in Qatar [13]. Both facilities are based on the proprietary Shell Middle Distillate Synthesis (SMDS) [12, 14] process filed in over 3500 patents. The syngas is produced by natural gas partial oxidation. Subsequently, impurities are removed from the syngas. The purified syngas is then reacted over Co catalysts in Multi-Tubular Trickle Bed Reactors (MTTBRs), see also section 1.2.2, at LTFT conditions. The resulting synthetic crude is further processed into marketable products such as high quality diesel fuel, kerosene and waxes by cracking and isomerization operations. The plant in Malaysia has a production capacity of 500 kt y^{-1} while the production facility in Qatar, the Pearl, has an annual production capacity of 7000 kt.

Another large-scale GtL production facility located in Qatar is the Oryx GtL [15] which is a joint venture between Qatar Petroleum and Sasol. The syngas is produced by natural gas reforming based on licensed technology of Haldor Topsøe while the FTS is performed in a slurry phase reactor, see also section 1.2.2, for which the technology was licensed by Sasol. The resulting synthetic crude is processed by isocracking operations based on technology of Chevron. The total production capacity amounts to 1800 kt y^{-1}. In Escravos (Nigeria), a FTS production facility is commissioned since 2014 based on the technology of Sasol and Chevron. Other projects based on the Sasol Slurry Phase Distillate (SPD) process are announced in Uzbekistan and North America. In North America, the shale gas revolution has increased the price difference between gas and crude oil opening up new opportunities for GtL production facilities.

Next to large scale production facilities which aim at producing 7000 kt y^{-1} of FTS liquids, technologies have also been developed recently which aim at the production of FTS liquids with a production capacity below 25 kt y^{-1}, e.g., INERATEC ReThink GtL process [16]. This has become possible by the development of microreactors.

1.1.2 Coal to Liquids (CtL) FTS

The first operational FTS production facilities were situated in Germany [4, 17]. In 1925, Franz Fischer and Hans Tropsch successfully synthesized hydrocarbons from syngas over Ni and Co catalysts. Their discovery was put into application in order to convert Germany's abundant coal reserves into liquid fuels. By 1938, nine plant were operational producing 600 kt y^{-1} [4]. Fixed Bed Reactors (FBR) loaded with Co based catalysts were employed to convert the syngas into synthetic fuels operated at temperatures between 180°C-200°C. Two modes of operation were employed, one at atmospheric pressures, i.e., 100 kPa, and one at higher pressures, i.e., 0.5-1.5 MPa.

Another coal based FTS production facility came on stream in 1955 in South Africa which was operated by Sasol, the so-called Sasol 1 [3, 5, 7, 8, 18]. Syngas is converted into a synthetic crude over promoted Fe based catalysts in FBRs or CFBRs. The FBRs are operated at LTFT conditions while the CFBRs are operated at HTFT conditions. The production of high quality waxes added to the economic viability of the Sasol 1. Sasol 2 and Sasol 3 came in operation in 1980 and 1982, respectively, converting coal based syngas into alkenes, gasoline, diesel fuel and waxes by converting syngas by means of Fe based catalysts in CFBRs [3, 5, 7, 8, 18].

The Sasol plants are, to date, still in operation but have seen a significant number of changes in the infrastructure. Major breakthroughs were obtained in the FTS reactor development which allowed to increase the reactor productivity significantly [7, 18]. The reactor technology in Sasol 2 and 3 was changed from CFBRs to Fixed Fluidized bed reactors (FFBRs) [18]. Further reactor engineering efforts lead to the development of the SPD process which replaced the CFBRs of the Sasol 1 [19] and is the leading reactor technology in the Oryx and Escravos plant.

1.1.3 Biomass to Liquids (BtL) FTS

The chemical and transportation sector strongly depend on the availability of crude oil. In order to reduce this dependency and meet the greenhouse gas emission reduction targets, biomass will have to be more extensively deployed. In the context of fuel and chemicals production from biomass, FTS can play a crucial role [20]. A FTS unit could be part of a biorefinery in which biomass is first treated to extract valuable products present in the biomass [21]. The remaining part of the biomass can subsequently be gasified and converted in chemicals or fuels over Fe or Co based catalysts. Alternatively, the full biomass could be gasified followed by a FTS conversion step.

1.2 Process overview

A FTS production facility comprises three main stages [8, 9], see Figure 1-2. The coal or natural gas first has to be converted to syngas. This syngas is subsequently converted into a synthetic crude. In the final stage, this synthetic crude is upgraded to marketable products.

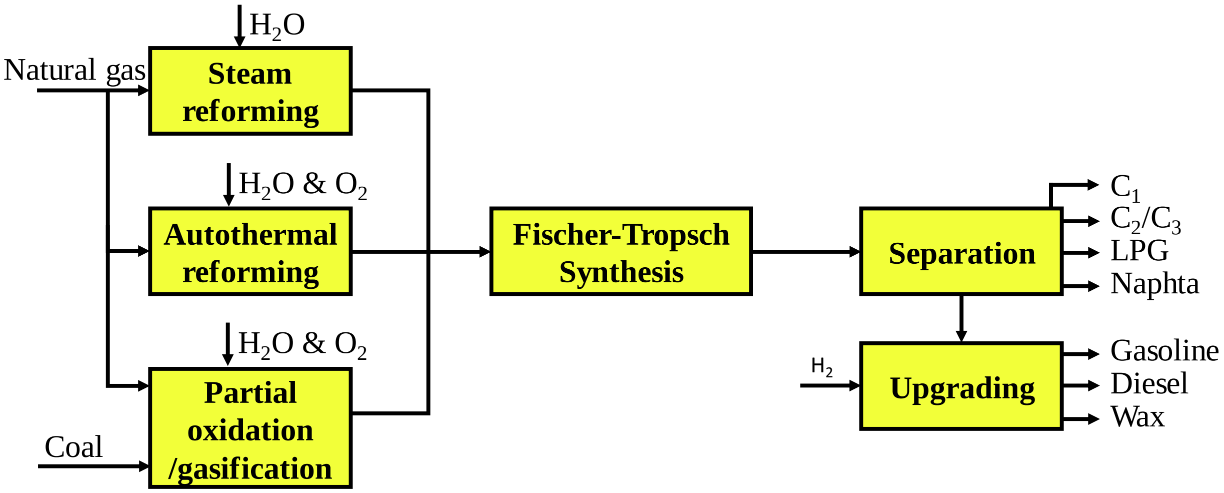

H_2O
Natural gas
Steam reforming
H_2O & O_2
Autothermal reforming
H_2O & O_2
Partial oxidation /gasification
Coal
Fischer-Tropsch Synthesis
Separation
C_1
C_2/C_3
LPG
Naphta
H_2
Upgrading
Gasoline
Diesel
Wax

Figure 1-2: Generalized overview of a Fischer-Tropsch Synthesis production facility [8].

1.2.1 Syngas production

Methane and light hydrocarbons can be converted into syngas by means of steam reforming, autothermal reforming or partial oxidation. In steam reforming, methane is mixed with water and reacted to CO and H_2 , see eq. [1-1]. The produced CO can react with H_2O to produce CO_2 and H_2 via the Water-Gas-Shift (WGS) reaction, see eq.[1-2].

$$CH_4 + H_2O \rightleftarrows CO + 3H_2 \qquad [1\text{-}1]$$

$$CO + H_2O \rightleftarrows CO_2 + H_2 \qquad [1\text{-}2]$$

Steam reforming is performed at high temperatures over, typically, a Ni catalyst. The catalyst is placed in a tube to obtain a FBR. The tubes are placed in furnaces to obtain the required temperatures. The plant in Mossel Bay is based on syngas obtained through steam reforming.

In autothermal reforming, methane is mixed with steam and oxygen in order to produce syngas:

$$4CH_4 + O_2 + 2H_2O \rightleftarrows 10H_2 + 4CO \qquad [1\text{-}3]$$

Methane is burnt with a substoichiometric amount of oxygen and the hot product gases are subsequently reacted over a catalyst bed. The Oryx GtL plant uses an autothermal reformer based on technology licensed by Haldor Topsøe.

A third way to produce syngas from methane or light hydrocarbons is by means of partial oxidation. This can be performed catalytically or non-catalytically, e.g., the Shell Gasification Process. The Shell FTS production facilities in Malaysia and Qatar produce syngas through methane partial oxidation.

Coal is non-catalytically gasified in fluidized or moving bed type reactors. The coal is reacted with oxygen and water vapor producing CO, H_2, CO_2 and CH_4. The produced methane by gasification can be further reformed to syngas together with the light hydrocarbons produced in the FTS step.

Overall methane reforming is, due to the higher hydrogen content, more efficient for the syngas production compared to coal gasification. Next to this, a methane based FTS production facility requires a lower capital investment, explaining the higher number of recent FTS production facilities based on methane rather than coal.

1.2.2 The FTS step

The syngas is converted in a FTS reactor to a hydrocarbon mixture. The composition of such a hydrocarbon mixture greatly depends on the applied technology. Two main categories exist in which the FTS technologies can be classified based on the operating temperature [5, 8, 9]. On the one hand, FTS can be operated between 270°C to 340°C which is classified as High Temperature

Fischer Tropsch (HTFT). The other operating mode is denoted as Low Temperature Fischer-Tropsch (LTFT) and is characterized by operating temperatures between 200°C and 240°C. At LTFT reaction conditions, the hydrocarbon mixture mainly consists of long chain hydrocarbons while at the HTFT operating conditions, shorter chain hydrocarbons in the naphtha to gasoline range are produced together with a higher fraction of oxygenates, see Figure 1-3. The significant difference in operating temperature and the resulting reaction products has a major impact on the applied reactor technologies. Overall, the reaction stoichiometry of the FTS reaction can be represented approximately as follows:

$$nCO + 2nH_2 \rightleftarrows (CH_2)_n + nH_2O \qquad [1\text{-}4]$$

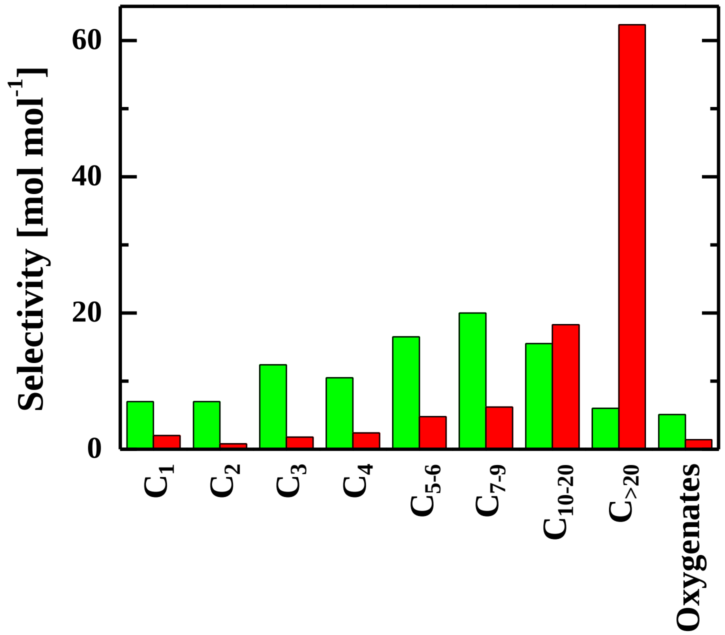

Figure 1-3: A typical obtained product distribution in commercial operation at High Temperature Fischer-Tropsch (green) and Low Temperature Fischer-Tropsch (red) conditions [8].

High Temperature Fischer-Tropsch (HTFT)

The major product yields are base chemicals such as 1-alkenes and gasoline [5]. The relatively low yield of high carbon number hydrocarbons together with the high temperatures prevents the formation of a liquid phase inside the reactor, i.e., only a gas phase is present in the reactor.

The operation of FTS reactors is complicated by a high heat production as the FTS is a highly exothermic reaction. Reactor technologies which can adequately handle this aspect are based on fluidized beds. A high velocity difference between the catalyst pellets and the gas phase in fluidized reactors ensures a high heat transfer coefficient. As a result, the produced reaction heat can be dissipated efficiently.

The first FTS production facilities, i.e., Sasol 1, 2 and 3, were based on the Circulating Fluidized Bed Reactor (CFBR) technology, see Figure 1-4-a [5, 7, 8, 18]. Syngas enters the reactor at the bottom together with catalyst pellets from the standpipe. The gas flows together with the catalyst pellets trough the reactor. Cyclones are used to separate the reactants and products from the catalyst pellets. As the catalyst pellets are circulated through the reactor, only a fraction of the total amount of catalyst loaded in the reactor is in contact with the syngas which is one of the major downsides of this reactor technology.

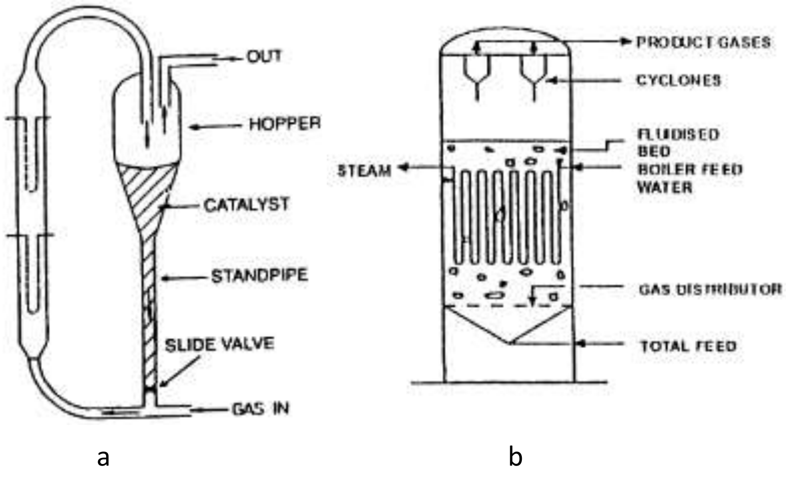

Figure 1-4: High Temperature Fischer-Tropsch (HTFT) reactor technologies. (a): Circulating Fluidized Bed Reactor (CFBR). (b): Fixed Fluidized Bed Reactor (FFBR). Adopted from [5].

An improvement to the CFBRs led to the Fixed Fluidized Bed Reactors (FFBR), see Figure 1-4-b [18]. The gas enters the reactor via a gas distributor at the bottom and flows through an entrained fluidized bed. Cooling coils are inserted in the fluidized bed to remove the produced reaction heat. This reactor technology replaced the CFBRs in the Sasol 2 and 3 plants [7, 18] due to a simpler operation and a lower capital investment of the FFBRs compared to the CFBRs [7].

Low Temperature Fischer-Tropsch (LTFT)

At LTFT conditions, the product distribution tends towards longer chain hydrocarbons compared to the product distribution obtained at the HTFT, see Figure 1-3. The major product yields are middle distillates and heavy waxes. The heavy products can be further processed to enhance the middle distillates yield. Due to the longer chain hydrocarbons and the lower temperature, a fraction of the products condenses. As a result, three phases occur in the reactor, i.e., a gas, a liquid and a solid phase. The liquid phase can also be present due to a liquid recycle. The presence of three phases necessitates the use of different reactor technologies compared to the ones used at the HTFT conditions. The two reactor technologies which are frequently applied in the large scale FTS production facilities are the Slurry Bubble Column Reactors (SBCRs) and the Multi-Tubular Trickle Bed Reactors (MTTBRs) [5, 9, 19]. The first technology has been developed by Sasol [19, 22] and is employed in, e.g., the Oryx GtL. The latter technology is mainly employed by Shell [12] in the FTS production facilities situated in Malaysia and the Pearl in Qatar.

The SBCR technology [19, 22] is schematically presented in Figure 1-5-a. The gas enters the reactor at the bottom and bubbles through a slurry phase to the top of the reactor. The slurry phase consists of long chain hydrocarbons and the suspended catalyst pellets. The gaseous products leave the reactor at the top while the slurry phase leaves the reactor from the side. Cooling coils are inserted in the slurry phase to remove the produced reaction heat.

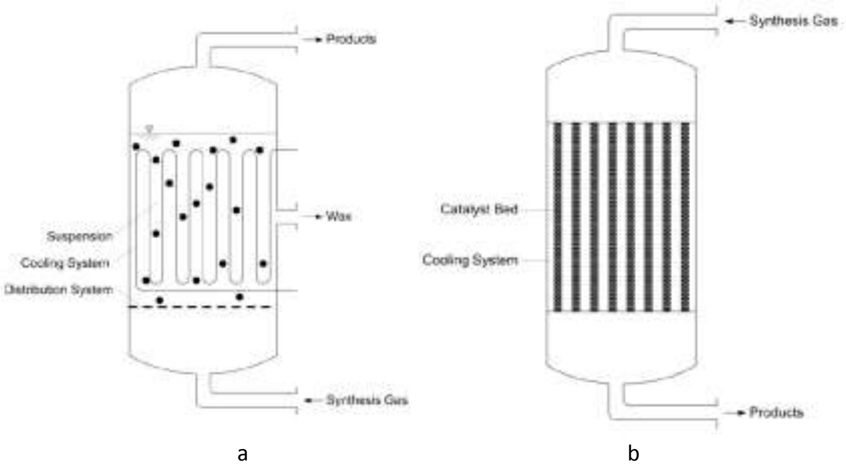

Figure 1-5: Low Temperature Fischer-Tropsch (LTFT) reactor technologies. (a): Slurry Bubble Column Reactor (SBCR). (B): Multi-Tubular Trickle Bed Reactor (MTTBR). Adopted from [9].

A schematic representation of the MTTBR technology is provided in Figure 1-5-b. The reactor is comparable to a shell and tube heat exchanger. The catalyst is present as a fixed bed in the tubes. A pressurized cooling medium flows around the tubes at the shell side to remove the produced reaction heat by evaporation. Syngas enters the reactor at the top and is distributed over the tubes. This reactor technology was the first one employed for the FTS during World War II in Germany. This technology was also implemented in the Sasol 1, i.e., the ARGE reactors, next to the CFBRs [7]. It is noted that these ARGE reactors are still in operation while the CFBRs were replaced by the SBCR technology.

Both reactor technologies have their advantages and disadvantages [7, 9]. Specific advantages of the SBCR are: a high catalyst effectiveness as much smaller catalyst pellets are used, the pressure drop is not determined by the catalyst pellet size and a high heat removal capacity allows to operate the reactor practically isothermal. A more efficient use of the reactor volume, absence of a difficult separation step of the catalyst pellets from the wax phase and much easier scale-up are characteristic for the MTTBR. It is noted that the specific choice of a reactor technology is also determined by the company's experience.

Next to these conventional reactor technologies, other, more advanced, reactor technologies have been investigated for FTS, i.e., monolith [23, 24], micro-structured and membrane reactors [25]. The development of micro-structured reactors made it possible to downscale FTS from large scale installation such as the Pearl to FTS facilities which fit the size of a trailer, e.g., the INERATEC ReThink GtL process [16].

1.3 FTS chemistry

1.3.1 Product distribution

The FTS results in a wide range of hydrocarbons, i.e., hydrocarbons ranging from methane to heavy waxes with carbon numbers exceeding one hundred. This hydrocarbon mixture consists mainly of linear alkanes and 1-alkenes. Oxygenates, monomethyl branched alkanes and internal alkenes are also observed under FTS conditions but are produced to a much lesser extent. The product distribution, furthermore, depends on the operating conditions and the employed catalyst [5, 26].

The product spectrum obtained via FTS can be approximated by an Anderson-Schulz-Flory (ASF) distribution [27]. This distribution is characterized by means of a single chain growth probability, α, defined as:

$$\alpha = \frac{r_p}{r_p + r_t} \tag{1-5}$$

With r_p the propagation rate and r_t the termination rate.

The mass fraction of the hydrocarbons with n carbon atoms, w_n, can be expressed as a function of this carbon number as follows:

$$w_n = n(1-\alpha)^2\alpha^{n-1} \tag{1-6}$$

The ASF distribution can, alternatively, also be expressed in terms of molar fractions. The molar fraction of the hydrocarbons with n carbon numbers, y_n, is obtained as follows:

$$y_n = (1-\alpha)\alpha^{n-1} \tag{1-7}$$

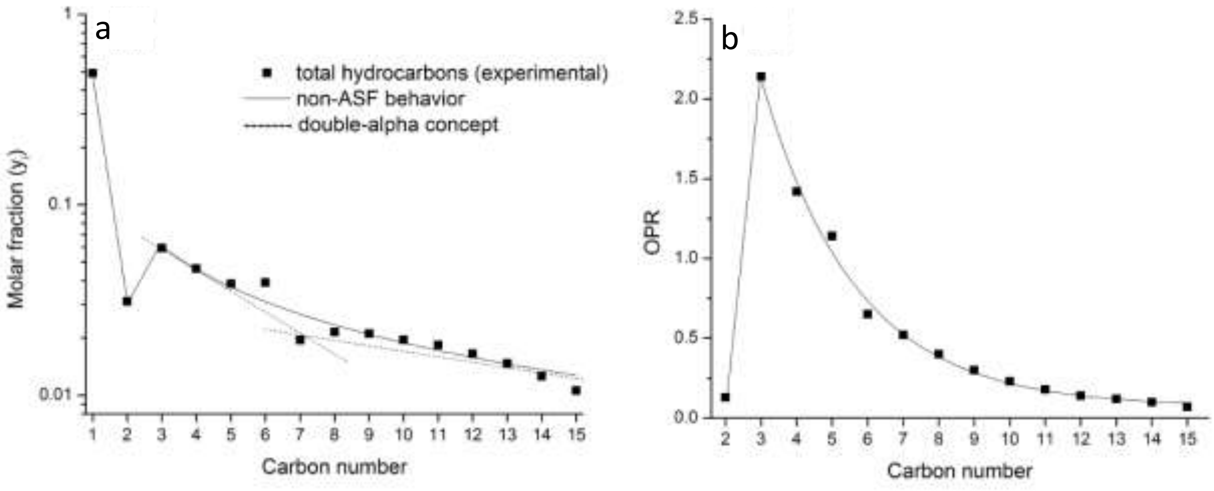

Figure 1-6: Typical product spectrum of the Co catalysed Fischer-Tropsch Synthesis. Adopted from [28]. (a): Molar fraction as function of the carbon number. (b): Alkene to alkane ratio as function of the carbon number.

Plotting the logarithm of the molar fraction as function of the carbon number should result in a straight line if the ASF distribution is exactly obtained. Although the major trend exhibited by the FTS product spectrum approaches the ASF distribution, systematic deviations have been observed [26]. This is illustrated in Figure 1-6-a. The methane yield exceeds the one expected based on the ASF distribution. Next to this, typically a minimum is observed at C_2 with a local maximum at C_3 or C_4. Furthermore, the chain growth probability increases at a higher carbon number, i.e., around a carbon number between 7 to 10. Another typically experimentally observed characteristic feature of the FTS product distribution is the maximum in the alkenes to alkanes ratio as a function of the carbon number at a carbon number of 3 or 4, see Figure 1-6-b.

The underlying phenomena responsible for these deviations have been a matter of controversy over the years. Several explanations for the different deviations have been proposed. One such explanation is based on the idea that the experimentally measured product distribution of the FTS is a mixture of freshly produced reaction products and products left in the reactor [29]. Another explanation is based on a superposition of two independent chain growth probabilities [30-32]. Next to this, the deviations have also been ascribed to secondary reactions of alkenes [33-45]. The readsorbed alkenes can be hydrogenated to the corresponding alkanes or participate in the chain growth process. Moreover, this effect is becoming more pronounced with increasing chain length of the alkenes. The latter is related to intraparticle diffusion [33, 40], solubility effects in the heavy wax phase [34, 42] or increasing interaction with the catalyst surface [38, 39, 41, 45]. Through microkinetic modeling, the deviations from ASF distribution for the small hydrocarbons, i.e., up to C_4, have been satisfactorily described by kinetic parameters which vary from C_1 to C_4 [28, 41, 43, 44, 46-51] indicative of (next) nearest neighbor effects on the rate coefficients belonging to the same reaction family.

1.3.2 Catalysts

FTS is a metal catalyzed process. The metals which are active for FTS are Group VIII metals. More precisely, Ru, Fe and Co are the most important metals with respect to FTS [5, 26]. Ni is also an active catalyst for CO hydrogenation leading to methane as the main reaction product under practical operating conditions [5].

Fe catalyst are very cheap in comparison to Co and Ru, i.e., the relative price difference amounts to 1000 and 50000 respectively [5]. This is one of the reasons for their common use in industrial FTS production facilities. Next to the activity for the FTS reaction, Fe catalysts also catalyze the WGS reaction [5, 26], see eq. [1-2]. This makes the Fe catalysts the preferred catalyst when the primary source of the syngas is coal [26], i.e., when the H_2/CO molar ratio is low. FTS on Fe based catalysts is inhibited by water [5, 19]. High water vapor pressures can also cause deactivation of the Fe catalyst by bulk phase oxidation [52]. At high temperatures, the catalyst can also be deactivated by the formation of aromatic coke and elemental carbon [5, 52]. Under FTS reaction conditions, Fe transforms into iron carbides which are more active than Fe in the metallic state [53-56]. The alkenes selectivity at low carbon numbers is high [5, 26], e.g., for C_3 and C_5-C_{12} the alkene content is typically 85% and 70% [5] and the chain growth probability is between 0.5 and 0.7 [26]. Fe based catalyst are, hence, ideally suited for the production of base chemicals and gasoline. Next to this, the changing chain growth probability with the carbon number is more strongly pronounced for Fe catalysts [26] and the minimum at C_2 and the maximum at C_3 or C_4 is less clearly pronounced compared to Co or Ru catalysts [26]. Fe based catalysts are the only catalysts used at HTFT conditions.

The other catalysts of industrial importance are Co based ones [5, 26]. These catalysts are inactive for WGS [26]. As such, Co catalysts are more suited for the conversion of natural gas derived syngas. Syngas derived from natural gas has a H_2/CO molar ratio close to 2 or higher, see section 1.2.1. Employing an active WGS catalyst would further increase this ratio and, hence, shift the H_2/CO molar ratio of the syngas away from the FTS stoichiometric H_2/CO molar ratio of 2, see eq. [1-4]. Furthermore, on Co based catalysts, FTS is not inhibited by the presence of water [5]. Consequently, higher conversions per pass can be achieved in reactors using Co based catalysts. The active state of the Co catalyst is in its metallic state but the exact nature of the active sites or the Co phase remains a matter of discussion as a Co catalyst reconstructs under FTS conditions [57]. Co catalysts are less sensitive to deactivation [5] which compensates for their higher cost. Co catalysts are preferably used at LTFT conditions as the methane selectivity rapidly increases with the temperature. The chain growth probability is typically higher than on Fe catalysts [5, 26] and mainly linear alkanes are produced. As a result, Co catalyzed FTS primarily leads to diesel with high cetane numbers and heavier components.

Ru catalysts are the most active ones for FTS [58] and selective towards high-molecular-weight waxes [26]. A significant WGS activity is not observed on ruthenium catalysts. Despite these interesting properties, the high price of Ru is prohibitive for its application in large scale installations [5].

In this thesis, the focus is on the Co catalyzed FTS. Therefore, the remaining part of the introduction is mainly dedicated to this specific combination of reaction and transition metal.

1.3.3 Reaction mechanism

The FTS reaction mechanism has, ever since its discovery, been a matter of controversy. All the mechanistic proposals agree that chain growth occurs by the step wise addition of a C_1 monomeric building block into a growing chain. This is widely accepted due to the ability of the ASF distribution in approximating the FTS product spectrum. The C_1 building blocks are produced on the metal catalyst surface. The nature of this C_1 building block is, however, unknown and at the origin of the various mechanistic proposals for FTS. Three main categories can be discerned [59], i.e., carbide mechanisms, CO insertion mechanisms and the hydroxycarbene mechanism. The former two classes of mechanistic proposals have drawn the major attention within the scientific community. Reviews on the mechanistic proposals of FTS have been widely published [7, 59-67] and, hence, this introductory chapter limits itself to the most important characteristic features governing the different reaction schemes.

Carbide mechanisms

In all the mechanistic proposals which belong to this class, CO is first dissociated to C and O. C is subsequently hydrogenated to a CH_x species which couples with other CH_y species to initiate the chain growth. Further chain growth occurs by step wise addition of CH_x species to CH_yCH_z species [59, 67]. This is illustrated in Figure 1-7 for the carbene insertion mechanism as originally proposed by Brady and Pettit [68, 69]. The surface carbon or carbide (C) is first hydrogenated to methylene (CH_2) (2 and 3) and metal methyl (CH_3) (4) surface species. Chain growth is initiated by coupling of the CH_2 and CH_3 species (5). Further chain growth occurs by the step wise insertion of CH_2 species into growing metal alkyl chains (6). Alkanes are produced by hydrogenation of the metal alkyl species (7). Alkenes are formed by desorption of the corresponding metal alkenes species (8), which are obtained by a beta hydride elimination of the corresponding metal alkyl species (9). This mechanism is sometimes also referred to as the alkyl mechanism. Variations to this mechanism based on CH_2 insertion have been proposed by Maitlis [70], i.e., the alkenyl mechanism, and by Gaube [31] which is referred to as the alkylidene mechanism.

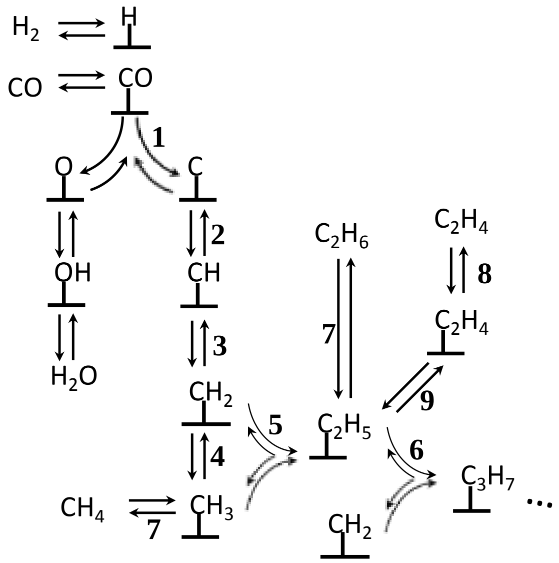

Figure 1-7: The carbene mechanism as proposed by Brady and Pettit [68, 69].

Next to the chain growth steps, the CO activation mechanism has also been extensively studied [71-80]. Two main reaction pathways are considered for CO activation, i.e., direct CO dissociation and hydrogen assisted CO dissociation. Based on ab initio calculations, hydrogen assisted CO dissociation is more likely on close packed facets of the Co catalyst than direct CO dissociation due to high activation barriers that were obtained for the latter [79-82]. The direct CO dissociation barrier is significantly reduced at step sites [74, 75, 77] of which the presence has been indicated by surface science techniques [57, 71, 83-85].

The side products, i.e., oxygenates, monobranched hydrocarbons and internal alkenes are explained by considering additional reaction steps in the mechanism. The formation of oxygenates is explained by CO insertion into a growing metal alkyl chain. This step is considered as a termination step, rather than a propagation step, in the carbide mechanisms [86]. The formation of internal alkenes and monobranched alkanes is based on secondary reactions of 1-alkenes [87]. The first step is a hydrogen addition to the ultimate CH_2 group of a RCH_2CHCH_2 metal alkenes species resulting in a RCH_2CHCH_3 metal alkyl species. This metal alkyl species can be subject to chain growth by CH_2 insertion. The hydrogenation of the resulting metal alkyl species leads to monobranched alkanes. A beta hydride abstraction of the CH_2 group in the RCH_2CHCH_3 metal alkyl species leads to an $RCHCHCH_3$ metal alkene species which, after desorption, yields an internal alkenes. The insertion of CH_2 into a RCH_2CHCH_3 metal alkyl species or a beta hydride elimination at the CH_2 group of the RCH_2CHCH_3 metal alkyl surface species are both sterically hindered. This explains why internal alkenes and monobranched alkanes are only observed in minor quantities.

CO insertion mechanisms

The CO insertion mechanism as originally proposed by Pichler and Schulz is illustrated in Figure 1-8. Chain growth proceeds by stepwise insertion of chemisorbed CO into growing metal alkyl chains (5). The resulting surface species undergoes an additional hydrogenation (6) before the C-O bond dissociates (7). The metal methyl, i.e., the first metal alkyl required to initiate the chain growth, is obtained from dissociation of a hydrogenated chemisorbed CO (1,2,3 and 4). The main difference between the CO insertion mechanisms and the carbide mechanisms is, hence, that the C-O bond dissociates only after CO has been inserted into a growing chain. This mechanism inherently explains the presence of alcohols in the FTS product mixture by hydrogenation of the O atom of an RCHO surface species (8). The formation of alkanes and alkenes is explained by considering the same elementary reactions as considered in the carbene mechanism (9, 10 and 11). It is noted that in the C-O bond dissociation of the chemisorbed CO

(1,2 and 3) and the growing chain (6 and 7) similar reaction steps take place. The production of long chain hydrocarbons, hence, critically depends on the relative rate between these reaction steps.

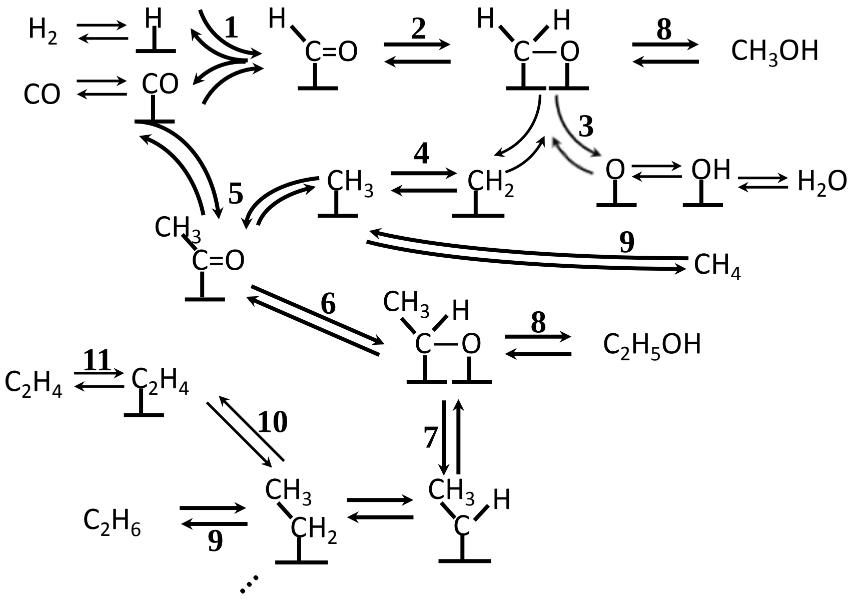

H_2
H
CO
CO
1
H
C=O
2
H
H
C—O
8
CH_3OH
3
4
CH_3
CH_2
O
OH
H_2O
5
CH_3
C=O
9
CH_4
6
CH_3
H
C—O
8
C_2H_5OH
11
C_2H_4
C_2H_4
10
7
CH_3
CH_2
CH_3
H
C
C_2H_6
9
...

Figure 1-8: The CO insertion mechanism as proposed by Pichler and Schulz [88].

Hydroxycarbene mechanism

This mechanism was originally proposed by Anderson et al [89] and is represented in Figure 1-9. In this mechanism, CO is first hydrogenated to hydroxycarbene surface species by the addition of a H to both the C and the O (1 and 2). Chain growth takes place by a condensation reaction of the hydroxycarbene species (3). This mechanism also immediately explains the formation of oxygenates in the product spectrum of the FTS. The major argument against this mechanism is that reaction has to take place between two electrophilic carbon atoms in the chain growth step [59].

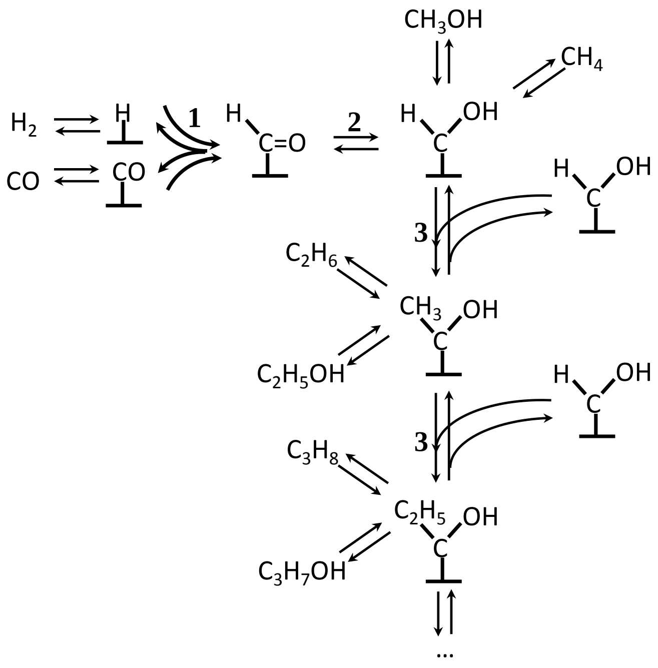

Figure 1-9: The hydroxycarbene mechanism [89].

1.3.4 Metal particle size effects

The dependence of activity and/or selectivity of a reaction on the metal particle size provides relevant information on the required configuration of surface atoms for the relevant elementary surface reaction steps to occur [90]. The requirement of a specific configuration of surface atoms is referred to as structure sensitivity. Van Santen identifies three types of structure sensitivity [90, 91], see also Figure 1-10. The first type, corresponding with an increasing turnover frequency (TOF), i.e., conversion rate normalized per exposed metal atom, with the metal particle size, is related to the cleavage or formation of molecular π-bonds present in, e.g., N_2 or CO. The activation of this type of molecular bonds requires a specific configuration of metal atoms and step-edge sites. Such unique configurations are not present on transition metal particles with particle sizes of less than 2 nm. Type II of structure sensitivity is characterized by an increasing TOF with decreasing metal particle size. This is related to reactions involving the activation of σ-bonds, e.g., cleavage of a CH bond, which only require a single metal atom. The rate of such reactions depends strongly on the coordinative unsaturation of surface atoms, e.g., surface atoms present at the particle edges. Type III of structure sensitivity corresponds with a TOF that is constant as a function of the metal particle size. Type III typically includes recombination reactions of adsorbed hydrogen with a surface alkyl as rate-determining step. Type II and Type III are, hence, complementary.

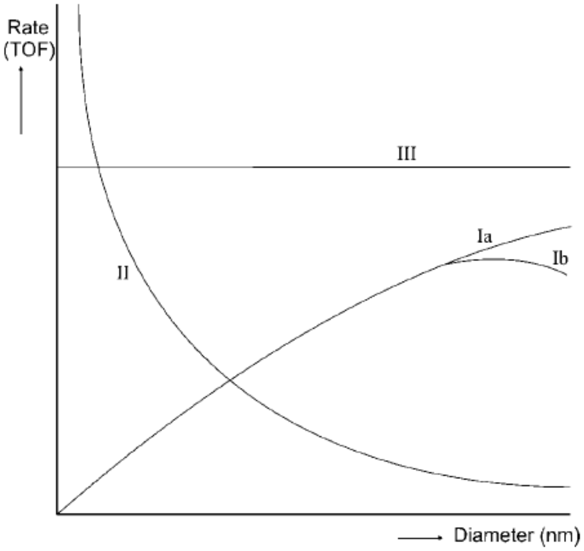

Figure 1-10: Structure sensitivity relationships. Adopted from [90].

Bezemer et al [92] investigated the TOF as function of the Co metal particle size for FTS, see Figure 1-11, and found that the TOF increases with the metal particle size up to a size of 8 nm. For larger metal particles, the TOF remained constant. This peculiar behavior of the TOF with the metal particle size is still a matter of debate and is strongly interrelated to the numerous mechanistic proposals for the FTS reaction. Bezemer et al [92] related the initial change in TOF with the metal particle size to blockage of edge/corner sites by irreversibly adsorbed CO and an increase in intrinsic activity of active sites with increasing metal particle size [92]. Van Santen explains the TOF dependency with the metal particle size via the structure sensitivity of the CO bond dissociation [62, 76, 90, 91, 93, 94]. Small metal particles with sizes below 8 nm follow a Type I structure sensitivity. Metal particles larger than 8 nm, would tend to reconstruct under FTS conditions and, hence, the specific configuration of the surface sites is formed in-situ. Evidence for the surface reconstruction of Co catalysts has been first reported by Wilson and de Groot [57] based on Scanning Tunneling Electron Microscopy. The structure sensitivity of the CO bond dissociation has been doubted by Salmeron and coworkers [72, 95]. Based on the observation that the apparent activation energy is constant as a function of the metal particle size, they conclude that the CO bond dissociation is not a structure sensitive reaction. According to these authors, the particle size dependency is related to hydrogen chemisorption [72, 95].

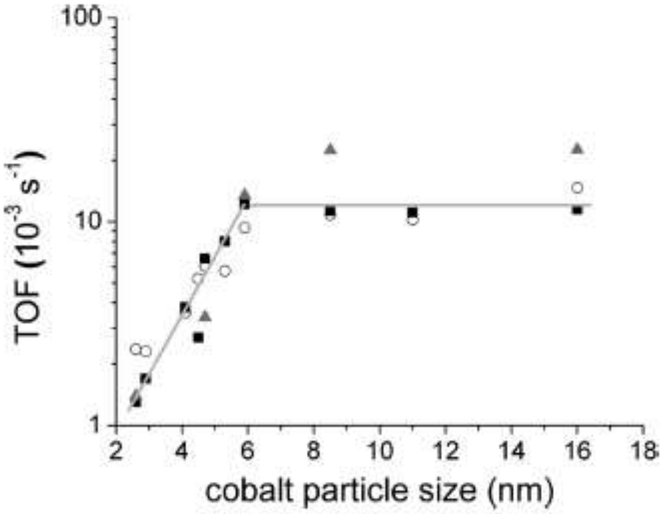

Figure 1-11: The Co particle size effect on the Turnover Frequency. Adopted from [92].

1.4 Multi-scale modelling

1.4.1 Microkinetic modeling

A kinetic model is used to mathematically relate experimentally observed conversions and selectivities to operating conditions such as, total pressure, reactant partial pressure, temperature,… Kinetic models of different levels of complexity are frequently encountered. The simplest kinetic models are based on power law rate expressions. The most comprehensive kinetic models are so-called microkinetic ones which are based on a detailed reaction mechanism in terms of elementary steps. The net production rate of a component is obtained by summation of the rates of all the steps involved in the production or consumption of that component. The effort to construct such detailed microkinetic models is, compared to the construction of a power law kinetic model, obviously, significantly higher.

A major advantage of these more fundamental models are the more reliable extrapolation capabilities outside the range of experimental conditions used to acquire the data against which the model has been validated. This is of strategic advantage for the design and optimization of industrial reactors. Next to this, a more detailed understanding of the underlying phenomena can be obtained thanks to such a model. By means of a reaction path analysis, the relative contribution of the elementary steps to the formation of the various products is quantified. The elementary steps which control the reactant conversion are identified via a degree of rate control analysis.

An adequate description of an experimental data set by a microkinetic model is not the final step in its construction. The kinetic parameters in the microkinetic model should have a physically interpretable meaning and more insight into the reaction mechanism can be obtained by a meticulous assessment of the model parameter estimates by comparing them with independently obtained insights, e.g., via quantum chemical calculations. The elementary steps controlling the activity and/or selectivity, as identified by a reaction path analysis or degree of rate control analysis, can be further investigated by means of ab initio calculations or dedicated experiments, e.g., co-feed experiments, transient experiments, … Next to this, if phenomenological models, such as the UBI-QEP method [96], are used in the microkinetic model construction, such phenomenological models can be further fine-tuned by means of ab initio calculations [97]. The additional information, which can be of experimental or fundamental nature, can in a next step be incorporated in the microkinetic model. As such, the construction of a microkinetic model is subject to a data-driven refinement methodology [98].

Microkinetic models constructed in such a way will probably result in even more reliable extrapolation capabilities. Such detailed microkinetic models can also be exploited in a model based catalyst design cycle by classifying the model parameters in catalyst descriptors and kinetic descriptors [99]. The former type of parameters are related to the catalyst properties while the latter are reaction specific and catalyst independent.

1.4.2 Steady State Isotopic Transient Kinetic Analysis (SSITKA)

The Steady State Isotopic Transient Kinetic Analysis (SSITKA) technique, originally developed by Happel [100], Bennet [101] and Biloen [102], is a powerful technique to study catalytic reactions. In a SSITKA experiment, the isotopic labels in reactants and products are monitored as a function of time after an abrupt switch from a reactant to an isotopic counterpart during steady state operation of the catalyst. The abrupt switch is performed by means of a valve switching between two feed lines that, apart from a different inert gas, differ only in the isotopic labeling of a reactant. It is important to note that the two feed lines are operated at identical concentration levels and other operating conditions such that the steady state operation of the catalyst is maintained. SSITKA experimentation, hence, offers the possibility of acquiring more information during steady state operation of the catalyst. This makes SSITKA a unique technique among all the transient techniques.

Two quantities which can be obtained from SSITKA experimentation without any assumption made with respect to the underlying mechanism are the surface mean residence time τ_p, and the surface concentration of adsorbed intermediates leading to a product P, L_p [103]. The surface mean residence time follows from the integration of the normalized transient response of product P:

$$\tau_p = \int_0^{+\infty} I_p(t)dt \qquad [1\text{-}8]$$

The steady state production rate of product p, R_p^{ss}, is related to τ_p as follows:

$$R_p^{ss} = \frac{L_p}{\tau_p} \qquad [1\text{-}9]$$

Additional assumptions with respect to the reaction mechanism allow relating the experimentally accessible quantities to reaction coefficients [103]. For example, for the reaction sequence of eq. [1-10], τ_p is equal to the inverse of the rate coefficient of the second step.

$$Reactant \rightarrow Surface\ Intermediate \rightarrow Product \qquad [1\text{-}10]$$

SSITKA studies of the Co catalyzed FTS

SSITKA has already been applied to a wide range of catalytic reactions [103, 104] such as the FTS [41, 105-111], ammonia synthesis [112], oxidative coupling of methane [113], …

The kinetic characterization capabilities of SSITKA are illustrated in what follows for the promoting effect of noble metals such as Pt [107] and Ru [114] on Co catalyzed FTS. Both noble metals typically increase the reaction rate, expressed on a catalyst mass basis, without significantly altering the selectivity. By decoupling the overall reaction rate into the surface coverage and the mean surface residence time, see eq. [1-9], the increase in overall reaction rate could be mainly related to an increase of the surface coverages. The intrinsic activity, expressed as the inverse of the mean surface residence time, see eq. [1-8], remained constant. This indicates that the intrinsic catalytic behavior of Co atoms is not significantly influenced by the presence of noble metal promoters. SSITKA studies of Co catalyzed FTS have also focused on other promoter effects [115], support effects [116], metal particle size effects [92].

As SSITKA data intrinsically decouples information on the surface concentration and activity of reactive intermediates, combination with kinetic modeling can help to further unravel some detailed aspects of the reaction mechanism [65, 104, 117]. Furthermore, kinetic modeling studies of SSITKA data acquired on Co catalysts for FTS indicated that parallel reaction paths are involved in the methane formation [41, 106, 117, 118].

1.4.3 Industrial reactor modeling

In a chemical reactor of an industrial production facility, such as the ones described in section 1.2.2, several phenomena take place at significantly different time and length scales [119]. The chemical reactions take place at metal particles with sizes of a few nanometers while the industrial reactor has dimension at the scale of meters. The construction of a mathematical model describing the industrial reactor can only be successful by combining models which accurately capture all the relevant phenomena occurring at these different scales and their possible interaction. Such a multi-scale reactor model can be used to better understand the behavior of an industrial unit, optimization of new and existing installations or extrapolation of catalyst improvements to the industrial scale.

1.5 Scope and outline of the thesis

The aim of this thesis is to study the Co catalyzed Fischer-Tropsch Synthesis by means of transient kinetics and multi-scale modeling. Co has been chosen as this is one of the two most important industrial FTS catalysts. Furthermore, as the recent industrial applications of FTS are in the exploitation of stranded gas fields, it can be expected that the importance of Co as an industrial FTS catalyst will further increase.

The starting point is the construction of a Single-Event MicroKinetic (SEMK) model which can adequately capture the effect of operating conditions on the reactant conversion and product selectivity (Chapter 3). This microkinetic model is subsequently exploited for the description of transient experiments obtained in a Steady State Isotopic Transient Kinetic Analysis (SSITKA) set-up (Chapter 4 and 5) and for the construction of a multi-scale model for a MTTBR (Chapter 6).

For the modeling of SSITKA data, a dedicated modeling procedure had to be devised (Chapter 4) which focuses on the one hand on the integration of the governing partial differential equations and on the other hand on reaction network generation accounting for the isotopic labeling of carbon atoms. Specific measures were taken to reduce the CPU time of a simulation as much as possible.

As SSITKA data intrinsically contains information with respect to the surface coverages of some of the kinetically relevant surface species and can, furthermore, potentially provide information on parallel reaction paths, it constitutes a severe test for the developed SEMK model and forms a second step in the data-driven model refinement methodology. This more fundamental model could be of high value for, e.g., a more profound interpretation of the metal particle size effects in FTS.

A multi-scale model is developed for the MTTBR technology as one of the most important Low Temperature Fischer-Tropsch reactor technologies. By means of a multi-scale model, the interaction between reaction and heat and mass transfer phenomena on different length and time scales can be better understood. Furthermore, the multi-scale model can be used to design new or optimize existing FTS production facilities.

1.6 References

1. *Crude oil prices - 70 Year Historical Chart*. 2016; Available from: http://www.macrotrends.net/1369/crude-oil-price-history-chart.
2. *ISI web of knowledge*. 2016; Available from: http://apps.webofknowledge.com.
3. Davis, B.H., *Fischer-Tropsch synthesis: Overview of reactor development and future potentialities.* Topics in Catalysis, 2005. **32**(3-4): p. 143-168.
4. Stranges, A.N., *A History of the Fischer-Tropsch Synthesis in Germany 1926-45.* Fischer-Tropsch Synthesis, Catalysts and Catalysis, 2006. **163**: p. 1-27.
5. Dry, M.E., *The Fischer-Tropsch process: 1950-2000.* Catalysis Today, 2002. **71**(3-4): p. 227-241.
6. Keith, P.C., *Gasoline from natural gas.* Oil Gas Journal, 1946(45): p. 102-112.
7. Dry, M.E., *Practical and theoretical aspects of the catalytic Fischer-Tropsch process.* Applied Catalysis a-General, 1996. **138**(2): p. 319-344.
8. Dry, M.E., *The fischer-tropsch process - commercial aspects.* Catalysis Today, 1990. **6**(3): p. 183-206.
9. Guettel, R., U. Kunz, and T. Turek, *Reactors for Fischer-Tropsch synthesis.* Chemical Engineering & Technology, 2008. **31**(5): p. 746-754.
10. Terblanche, K., *Value added synthetic fluids key to Mossgas' success.* Oil & Gas Journal, 1999. **97**(49): p. 48-52.
11. Hoek, A. *The Shell GTL process: Towards a World Scale Project in Qatar: the Pearl Project*. in *DGMK-Conference "Synthesis Gas Chemistry"*. 2006. Dresden.
12. Sie, S.T., *Process development and scale up: IV. Case history of the development of a Fischer-Tropsch synthesis process.* Reviews in Chemical Engineering, 1998. **14**(2): p. 109-157.
13. *Pearl GtL*. 2016; Available from: http://www.shell.com.qa/en_qa/projects-and-sites/pearl-gtl.html.
14. Eilers, J., S.A. Posthuma, and S.T. Sie, *The Shell Middle Distillate Synthesis Process (Smds).* Catalysis Letters, 1991. **7**(1-4): p. 253-269.
15. *Oryx GtL*. 2016; Available from: http://www.oryxgtl.com.qa/.
16. *Ineratec Rethink GtL Process*. 2016; Available from: http://www.ineratec.com/Technology/INERATEC-ReThink-GtL/.
17. Das, T.K., X.D. Zhan, J.L. Li, G. Jacobs, M.E. Dry, and B.H. Davis, *Fischer-Tropsch Synthesis: Kinetics and Effect of Water for a Co/Al(2)O(3) Catalyst.* Fischer-Tropsch Synthesis, Catalysts and Catalysis, 2006. **163**: p. 289-314.
18. Steynberg, A.P., R.L. Espinoza, B. Jager, and A.C. Vosloo, *High temperature Fischer-Tropsch synthesis in commercial practice.* Applied Catalysis a-General, 1999. **186**(1-2): p. 41-54.
19. Espinoza, R.L., A.P. Steynberg, B. Jager, and A.C. Vosloo, *Low temperature Fischer-Tropsch synthesis from a Sasol perspective.* Applied Catalysis A: General, 1999. **186**(1-2): p. 13-26.
20. Agathokles, D.E. and P. Capros, *Deliverable D3.2.2 BIOPOL - Report with results targeted scenario analysis concerning the implications of renewable policy, forestry policy, and agricultural policy for biorefinery viability*, 2009. p. 1-34.
21. Kamm, B., P.R. Gruber, and M. Kamm, - *Biorefineries – Industrial Processes and Products.* 2000.

22. Jager, B. and R. Espinoza, *Advances in Low-Temperature Fischer-Tropsch Synthesis.* Catalysis Today, 1995. **23**(1): p. 17-28.
23. Hilmen, A.M., E. Bergene, O.A. Lindvag, D. Schanke, S. Eri, and A. Holmen, *Fischer-Tropsch synthesis on monolithic catalysts of different materials.* Catalysis Today, 2001. **69**(1-4): p. 227-232.
24. de Deugd, R.M., F. Kapteijn, and J.A. Moulijn, *Trends in Fischer-Tropsch reactor technology - opportunities for structured reactors.* Topics in Catalysis, 2003. **26**(1-4): p. 29-39.
25. Rohde, M.P., D. Unruh, and G. Schaub, *Membrane application in Fischer–Tropsch synthesis reactors—Overview of concepts.* Catalysis Today, 2005. **106**(1–4): p. 143-148.
26. Van der Laan, G.P. and A. Beenackers, *Kinetics and selectivity of the Fischer-Tropsch synthesis: A literature review.* Catalysis Reviews-Science and Engineering, 1999. **41**(3-4): p. 255-318.
27. Anderson, R.B., R.A. Friedel, and H.H. Storch, *Fischer-Tropsch Reaction Mechanism Involving Stepwise Growth of Carbon Chain.* The Journal of Chemical Physics, 1951. **19**(3): p. 313-319.
28. Todic, B., W. Ma, G. Jacobs, B.H. Davis, and D.B. Bukur, *Effect of process conditions on the product distribution of Fischer–Tropsch synthesis over a Re-promoted cobalt-alumina catalyst using a stirred tank slurry reactor.* Journal of Catalysis, 2014. **311**: p. 325-338.
29. Shi, B.C. and B.H. Davis, *Fischer-Tropsch synthesis: accounting for chain-length related phenomena.* Applied Catalysis a-General, 2004. **277**(1-2): p. 61-69.
30. Dictor, R.A. and A.T. Bell, *Fischer-Tropsch Synthesis over Reduced and Unreduced Iron-Oxide Catalysts.* Journal of Catalysis, 1986. **97**(1): p. 121-136.
31. Gaube, J. and H.F. Klein, *Studies on the reaction mechanism of the Fischer-Tropsch synthesis on iron and cobalt.* Journal of Molecular Catalysis a-Chemical, 2008. **283**(1-2): p. 60-68.
32. Zhang, R.L., J. Chang, Y.Y. Xu, L.R. Cao, Y.W. Li, and J.L. Zhou, *Kinetic Model of Product Distribution over Fe Catalyst for Fischer-Tropsch Synthesis.* Energy & Fuels, 2009. **23**: p. 4740-4747.
33. Iglesia, E., S.C. Reyes, and R.J. Madon, *Transport-enhanced alpha-olefin readsorption pathways in Ru-catalyzed hydrocarbon synthesis.* Journal of Catalysis, 1991. **129**(1): p. 238-256.
34. Schulz, H. and M. Claeys, *Kinetic modelling of Fischer-Tropsch product distributions.* Applied Catalysis a-General, 1999. **186**(1-2): p. 91-107.
35. van der Laan, G.P. and A.A.C.M. Beenackers, *Hydrocarbon selectivity model for the gas-solid Fischer-Tropsch synthesis on precipitated iron catalysts.* Industrial & Engineering Chemistry Research, 1999. **38**(4): p. 1277-1290.
36. Zimmerman, W., D. Bukur, and S. Ledakowicz, *Kinetic-Model of Fischer-Tropsch Synthesis Selectivity in the Slurry Phase.* Chemical Engineering Science, 1992. **47**(9-11): p. 2707-2712.
37. Yan, F., W.X. Qian, Q.W. Sun, H.T. Zhang, W.Y. Ying, and D.Y. Fang, *Product distributions and olefin-to-paraffin ratio over an iron-based catalyst for Fischer-Tropsch synthesis.* Reaction Kinetics Mechanisms and Catalysis, 2014. **113**(2): p. 471-485.
38. Kuipers, E.W., C. Scheper, J.H. Wilson, I.H. Vinkenburg, and H. Oosterbeek, *Non-ASF product distributions due to secondary reactions during Fischer-Tropsch synthesis.* Journal of Catalysis, 1996. **158**(1): p. 288-300.

39. Kuipers, E.W., I.H. Vinkenburg, and H. Oosterbeek, *Chain-Length Dependence of Alpha-Olefin Readsorption in Fischer-Tropsch Synthesis.* Journal of Catalysis, 1995. **152**(1): p. 137-146.
40. Madon, R.J. and E. Iglesia, *The Importance of Olefin Readsorption and H2/Co Reactant Ratio for Hydrocarbon Chain Growth on Ruthenium Catalysts.* Journal of Catalysis, 1993. **139**(2): p. 576-590.
41. van Dijk, H.A.J., J.H.B.J. Hoebink, and J.C. Schouten, *A mechanistic study of the Fischer-Tropsch synthesis using transient isotopic tracing. Part 2: Model quantification.* Topics in Catalysis, 2003. **26**(1-4): p. 163-171.
42. van der Laan, G.P. and A. Beenackers, *alpha-Olefin readsorption product distribution model for the gas-solid Fischer-Tropsch synthesis*, in *Natural Gas Conversion V*, A. Parmaliana, D. Sanfilippo, F. Frusteri, A. Vaccari, and F. Arena, Editors. 1998, Elsevier Science Publ B V: Amsterdam. p. 179-184.
43. Todic, B., T. Bhatelia, G.F. Froment, W.P. Ma, G. Jacobs, B.H. Davis, and D.B. Bukur, *Kinetic Model of Fischer-Tropsch Synthesis in a Slurry Reactor on Co-Re/Al2O3 Catalyst.* Industrial & Engineering Chemistry Research, 2013. **52**(2): p. 669-679.
44. Todic, B., W.P. Ma, G. Jacobs, B.H. Davis, and D.B. Bukur, *CO-insertion mechanism based kinetic model of the Fischer-Tropsch synthesis reaction over Re-promoted Co catalyst.* Catalysis Today, 2014. **228**: p. 32-39.
45. Cheng, J., P. Hu, P. Ellis, S. French, G. Kelly, and C.M. Lok, *A DFT study of the chain growth probability in Fischer-Tropsch synthesis.* Journal of Catalysis, 2008. **257**(1): p. 221-228.
46. Visconti, C.G., E. Tronconi, L. Lietti, R. Zennaro, and P. Forzatti, *Development of a complete kinetic model for the Fischer-Tropsch synthesis over Co/Al2O3 catalysts.* Chemical Engineering Science, 2007. **62**(18-20): p. 5338-5343.
47. Visconti, C.G., E. Tronconi, L. Lietti, P. Forzatti, S. Rossini, and R. Zennaro, *Detailed Kinetics of the Fischer-Tropsch Synthesis on Cobalt Catalysts Based on H-Assisted CO Activation.* Topics in Catalysis, 2011. **54**(13-15): p. 786-800.
48. Bhatelia, T., C.E. Li, Y. Sun, P. Hazewinkel, N. Burke, and V. Sage, *Chain length dependent olefin re-adsorption model for Fischer-Tropsch synthesis over Co-Al2O3 catalyst.* Fuel Processing Technology, 2014. **125**: p. 277-289.
49. Qian, W.X., H.T. Zhang, W.Y. Ying, and D.Y. Fang, *The comprehensive kinetics of Fischer-Tropsch synthesis over a Co/AC catalyst on the basis of CO insertion mechanism.* Chemical Engineering Journal, 2013. **228**: p. 526-534.
50. Mosayebi, A. and A. Haghtalab, *The comprehensive kinetic modeling of the Fischer-Tropsch synthesis over Co@Ru/gamma-Al2O3 core-shell structure catalyst.* Chemical Engineering Journal, 2015. **259**: p. 191-204.
51. Azadi, P., G. Brownbridge, I. Kemp, S. Mosbach, J.S. Dennis, and M. Kraft, *Microkinetic Modeling of the Fischer-Tropsch Synthesis over Cobalt Catalysts.* Chemcatchem, 2015. **7**(1): p. 137-143.
52. Dry, M.E., *Fischer-Tropsch synthesis over iron catalysts.* Catalysis Letters, 1990. **7**(1): p. 241-251.
53. Lox, E.S., G.B. Marin, E. De Grave, and P. Bussière, *Characterization of a promoted precipitated iron catalyst for Fischer-Tropsch synthesis.* Applied Catalysis, 1988. **40**: p. 197-218.
54. Niemantsverdriet, J.W., A.M. Van der Kraan, W.L. Van Dijk, and H.S. Van der Baan, *Behavior of metallic iron catalysts during Fischer-Tropsch synthesis studied with*

Moessbauer spectroscopy, x-ray diffraction, carbon content determination, and reaction kinetic measurements. The Journal of Physical Chemistry, 1980. **84**(25): p. 3363-3370.

55. Cheng, J., P. Hu, P. Ellis, S. French, G. Kelly, and C.M. Lok, *Density Functional Theory Study of Iron and Cobalt Carbides for Fischer-Tropsch Synthesis.* Journal of Physical Chemistry C, 2010. **114**(2): p. 1085-1093.
56. Herranz, T., S. Rojas, F.J. Pérez-Alonso, M. Ojeda, P. Terreros, and J.L.G. Fierro, *Genesis of iron carbides and their role in the synthesis of hydrocarbons from synthesis gas.* Journal of Catalysis, 2006. **243**(1): p. 199-211.
57. Geerlings, J.J.C., M.C. Zonnevylle, and C.P.M. de Groot, *Structure sensitivity of the Fischer-Tropsch reaction on cobalt single crystals.* Surface Science, 1991. **241**(3): p. 315-324.
58. Filot, I.A.W., R.A. van Santen, and E.J.M. Hensen, *The Optimally Performing Fischer-Tropsch Catalyst.* Angewandte Chemie-International Edition, 2014. **53**(47): p. 12746-12750.
59. Hindermann, J.P., G.J. Hutchings, and A. Kiennemann, *Mechanistic Aspects of the Formation of Hydrocarbons and Alcohols from Co Hydrogenation.* Catalysis Reviews-Science and Engineering, 1993. **35**(1): p. 1-127.
60. Trimm, D.L. and A.A. Adesina, *Chemical Engineering and CatalysisHydrocarbon synthesis via Fischer-Tropsch reaction: travails and triumphs.* Applied Catalysis A: General, 1996. **138**(2): p. 345-367.
61. James, O.O., B. Chowdhury, M.A. Mesubi, and S. Maity, *Reflections on the chemistry of the Fischer-Tropsch synthesis.* RSC Advances, 2012. **2**(19): p. 7347-7366.
62. van Santen, R.A., I.M. Ciobica, E. van Steen, and M.M. Ghouri, *Mechanistic Issues in Fischer-Tropsch Catalysis.* Advances in Catalysis, Vol 54, 2011. **54**: p. 127-187.
63. Corral Valero, M. and P. Raybaud, *Cobalt Catalyzed Fischer–Tropsch Synthesis: Perspectives Opened by First Principles Calculations.* Catalysis Letters, 2013. **143**(1): p. 1-17.
64. Cheng, J., P. Hu, P. Ellis, S. French, G. Kelly, and C.M. Lok, *Some Understanding of Fischer-Tropsch Synthesis from Density Functional Theory Calculations.* Topics in Catalysis, 2010. **53**(5-6): p. 326-337.
65. Qi, Y., J. Yang, D. Chen, and A. Holmen, *Recent Progresses in Understanding of Co-Based Fischer–Tropsch Catalysis by Means of Transient Kinetic Studies and Theoretical Analysis.* Catalysis Letters, 2015. **145**(1): p. 145-161.
66. van Santen, R.A., A.J. Markvoort, I.A.W. Filot, M.M. Ghouri, and E.J.M. Hensen, *Mechanism and microkinetics of the Fischer-Tropsch reaction.* Physical Chemistry Chemical Physics, 2013. **15**(40): p. 17038-17063.
67. Biloen, P. and W.M.H. Sachtler, *MECHANISM OF HYDROCARBON SYNTHESIS OVER FISCHER-TROPSCH CATALYSTS.* Advances in Catalysis, 1981. **30**: p. 165-216.
68. Brady, R.C. and R. Pettit, *On the Mechanism of the Fischer-Tropsch Reaction - the Chain Propagation Step.* Journal of the American Chemical Society, 1981. **103**(5): p. 1287-1289.
69. Brady, R.C. and R. Pettit, *Reactions of Diazomethane on Transition-Metal Surfaces and Their Relationship to the Mechanism of the Fischer-Tropsch Reaction.* Journal of the American Chemical Society, 1980. **102**(19): p. 6181-6182.
70. Maitlis, P.M., H.C. Long, R. Quyoum, M.L. Turner, and Z.-Q. Wang, *Heterogeneous catalysis of C-C bond formation: black art or organometallic science?* Chemical Communications, 1996(1): p. 1-8.

71. Weststrate, C.J., P. van Helden, J. van de Loosdrecht, and J.W. Niemantsverdriet, *Elementary steps in Fischer–Tropsch synthesis: CO bond scission, CO oxidation and surface carbiding on Co(0001).* Surface Science, 2016. **648**: p. 60-66.
72. Tuxen, A., S. Carenco, M. Chintapalli, C.-H. Chuang, C. Escudero, E. Pach, P. Jiang, F. Borondics, B. Beberwyck, A.P. Alivisatos, G. Thornton, W.-F. Pong, J. Guo, R. Perez, F. Besenbacher, and M. Salmeron, *Size-Dependent Dissociation of Carbon Monoxide on Cobalt Nanoparticles.* Journal of the American Chemical Society, 2013. **135**(6): p. 2273-2278.
73. Böller, B., M. Ehrensperger, and J. Wintterlin, *In Situ Scanning Tunneling Microscopy of the Dissociation of CO on Co(0001).* ACS Catalysis, 2015. **5**(11): p. 6802-6806.
74. Shetty, S., A.P.J. Jansen, and R.A. van Santen, *Direct versus Hydrogen-Assisted CO Dissociation.* Journal of the American Chemical Society, 2009. **131**(36): p. 12874-+.
75. Shetty, S. and R.A. van Santen, *CO dissociation on Ru and Co surfaces: The initial step in the Fischer-Tropsch synthesis.* Catalysis Today, 2011. **171**(1): p. 168-173.
76. Shetty, S.G., I.M. Ciobica, E.J.M. Hensen, and R.A. van Santen, *Site regeneration in the Fischer-Tropsch synthesis reaction: a synchronized CO dissociation and C-C coupling pathway.* Chemical Communications, 2011. **47**(35): p. 9822-9824.
77. Liu, J.-X., H.-Y. Su, D.-P. Sun, B.-Y. Zhang, and W.-X. Li, *Crystallographic Dependence of CO Activation on Cobalt Catalysts: HCP versus FCC.* Journal of the American Chemical Society, 2013. **135**(44): p. 16284-16287.
78. Gong, X.-Q., R. Raval, and P. Hu, *CO dissociation and O removal on Co(0001): a density functional theory study.* Surface Science, 2004. **562**(1–3): p. 247-256.
79. Ojeda, M., R. Nabar, A.U. Nilekar, A. Ishikawa, M. Mavrikakis, and E. Iglesia, *CO activation pathways and the mechanism of Fischer-Tropsch synthesis.* Journal of Catalysis, 2010. **272**(2): p. 287-297.
80. Inderwildi, O.R., S.J. Jenkins, and D.A. King, *Fischer-tropsch mechanism revisited: Alternative pathways for the production of higher hydrocarbons from synthesis gas.* Journal of Physical Chemistry C, 2008. **112**(5): p. 1305-1307.
81. Liu, J.-X., H.-Y. Su, and W.-X. Li, *Structure sensitivity of CO methanation on Co (0 0 0 1), and surfaces: Density functional theory calculations.* Catalysis Today, 2013. **215**: p. 36-42.
82. Zhuo, M.K., K.F. Tan, A. Borgna, and M. Saeys, *Density Functional Theory Study of the CO Insertion Mechanism for Fischer-Tropsch Synthesis over Co Catalysts.* Journal of Physical Chemistry C, 2009. **113**(19): p. 8357-8365.
83. Papp, H., *Chemisorption and reactivity of carbon monoxide on a Co(11-20) single crystal surface; studied by LEED, UPS, EELS, AES and work function measurements.* Surface Science, 1985. **149**(2-3): p. 460-470.
84. Geerlings, J.J.C., J.H. Wilson, G.J. Kramer, H.P.C.E. Kuipers, A. Hoek, and H.M. Huisman, *Fischer-Tropsch technology - from active site to commercial process.* Applied Catalysis a-General, 1999. **186**(1-2): p. 27-40.
85. Weststrate, C.J., P. van Helden, and J.W. Niemantsverdriet, *Reflections on the Fischer-Tropsch synthesis: Mechanistic issues from a surface science perspective.* Catalysis Today, 2016. **275**: p. 100-110.
86. Cheng, J., P. Hu, P. Ellis, S. French, G. Kelly, and C.M. Lok, *First-principles study of oxygenates on Co surfaces in Fischer-Tropsch synthesis.* Journal of Physical Chemistry C, 2008. **112**(25): p. 9464-9473.

87. Schulz, H. and M. Claeys, *Reactions of α-olefins of different chain length added during Fischer–Tropsch synthesis on a cobalt catalyst in a slurry reactor.* Applied Catalysis A: General, 1999. **186**(1–2): p. 71-90.
88. Pichler, H. and H. Schulz, *Neuere Erkenntnisse auf Gebiet der Synthese von Kohlenwasserstoffen aus CO und* H_2. Chemie Ingenieur Technik, 1970. **42**: p. 12.
89. Storch, H., N.G. Golumbic, and R.B. Anderson, *The Fischer-Tropsch and Related Synthesis*. 1951, New York: Wiley.
90. Van Santen, R.A., *Complementary Structure Sensitive and Insensitive Catalytic Relationships.* Accounts of Chemical Research, 2009. **42**(1): p. 57-66.
91. van Santen, R.A., M. Neurock, and S.G. Shetty, *Reactivity Theory of Transition-Metal Surfaces: A Bronsted-Evans-Polanyi Linear Activation Energy-Free-Energy Analysis.* Chemical Reviews, 2010. **110**(4): p. 2005-2048.
92. den Breejen, J.P., P.B. Radstake, G.L. Bezemer, J.H. Bitter, V. Froseth, A. Holmen, and K.P. de Jong, *On the Origin of the Cobalt Particle Size Effects in Fischer-Tropsch Catalysis.* Journal of the American Chemical Society, 2009. **131**(20): p. 7197-7203.
93. van Santen, R.A., M.M. Ghouri, S. Shetty, and E.M.H. Hensen, *Structure sensitivity of the Fischer-Tropsch reaction; molecular kinetics simulations.* Catalysis Science & Technology, 2011. **1**(6): p. 891-911.
94. van Santen, R.A. and A.J. Markvoort, *Catalyst nano-particle size dependence of the Fischer-Tropsch reaction.* Faraday Discussions, 2013. **162**: p. 267-279.
95. Herranz, T., X. Deng, A. Cabot, J. Guo, and M. Salmeron, *Influence of the Cobalt Particle Size in the CO Hydrogenation Reaction Studied by In Situ X-Ray Absorption Spectroscopy*. Journal of Physical Chemistry B, 2009. **113**(31): p. 10721-10727.
96. Shustorovich, E. and H. Sellers, *The UBI-QEP method: a practical theoretical approach to understanding chemistry on transition metal surfaces.* Surface Science Reports, 1998. **31**(1-3): p. 5-119.
97. Maestri, M. and K. Reuter, *Semiempirical Rate Constants for Complex Chemical Kinetics: First-Principles Assessment and Rational Refinement.* Angewandte Chemie-International Edition, 2011. **50**(5): p. 1194-1197.
98. Maestri, M., D.G. Vlachos, A. Beretta, G. Groppi, and E. Rronconi, *A C-1 Microkinetic Model for Methane Conversion to Syngas on Rh/Al2O3.* Aiche Journal, 2009. **55**(4): p. 993-1008.
99. Thybaut, J.W. and G.B. Marin, *Single-Event MicroKinetics: Catalyst design for complex reaction networks.* Journal of Catalysis, 2013. **308**: p. 352-362.
100. Happel, J., *Transient tracing.* Chemical Engineering Science, 1978. **33**(11): p. 1567.
101. Bennett, C.O., *Understanding Heterogeneous Catalysis Through the Transient Method*, in *Catalysis Under Transient Conditions*, A.T. Bell and L.L. Hegedus, Editors. 1982, American Chemical Society: Washingon, DC. p. 1-32.
102. Biloen, P., *Transient kinetic methods.* Journal of Molecular Catalysis, 1983. **21**(1–3): p. 17-24.
103. Shannon, S.L. and J.G. Goodwin, *Characterization of Catalytic Surfaces by Isotopic-Transient Kinetics during Steady-State Reaction.* Chemical Reviews, 1995. **95**(3): p. 677-695.
104. Ledesma, C., J. Yang, D. Chen, and A. Holmen, *Recent Approaches in Mechanistic and Kinetic Studies of Catalytic Reactions Using SSITKA Technique.* Acs Catalysis, 2014. **4**(12): p. 4527-4547.

105. van Dijk, H.A.J., J.H.B. Hoebink, and J.C. Schouten, *Steady-state isotopic transient kinetic analysis of the Fischer-Tropsch synthesis reaction over cobalt-based catalysts.* Chemical Engineering Science, 2001. **56**(4): p. 1211-1219.
106. van Dijk, H.A.J., J.H.B.J. Hoebink, and J.C. Schouten, *A mechanistic study of the Fischer-Tropsch synthesis using transient isotopic tracing. Part-1: Model identification and discrimination.* Topics in Catalysis, 2003. **26**(1-4): p. 111-119.
107. Schanke, D., S. Vada, E.A. Blekkan, A.M. Hilmen, A. Hoff, and A. Holmen, *Study of Pt-Promoted Cobalt Co Hydrogenation Catalysts.* Journal of Catalysis, 1995. **156**(1): p. 85-95.
108. Rothaemel, M., K.F. Hanssen, E.A. Blekkan, D. Schanke, and A. Holmen, *The effect of water on cobalt Fischer-Tropsch catalysts studied by steady-state isotopic transient kinetic analysis (SSITKA).* Catalysis Today, 1997. **38**(1): p. 79-84.
109. Rothaemel, M., K.F. Hanssen, E.A. Blekkan, D. Schanke, and A. Holmen, *Determination of reactivity distributions from steady-state isotopic transient data: A model study.* Catalysis Today, 1998. **40**(2-3): p. 171-179.
110. Krishna, K.R., A.T. Bell, L. Zanderighi, D. Wang, R.W. Joyner, D. Bianchi, K. Klier, S.K. Ihm, J. Goodwin, H. Schulz, V. Ragaini, and A. Machocki, *Isotopic Tracer Studies of Chain Propagation and Termination during Fischer-Tropsch Synthesis over Ru Tio2.* Studies in Surface Science and Catalysis, 1993. **75**: p. 181-193.
111. Gao, J., X.H. Mo, and J.G. Goodwin, *Relationships between oxygenate and hydrocarbon formation during CO hydrogenation on Rh/SiO$_2$: Use of multiproduct SSITKA.* Journal of Catalysis, 2010. **275**(2): p. 211-217.
112. McClaine, B.C. and R.J. Davis, *Importance of product readsorption during isotopic transient analysis of ammonia synthesis on Ba-promoted Ru/BaX catalyst.* Journal of Catalysis, 2002. **211**(2): p. 379-386.
113. Nibbelke, R.H., J. Scheerova, M.H.J.M. de Croon, and G.B. Marin, *The Oxidative Coupling of Methane over Mgo-Based Catalysts - a Steady-State Isotope Transient Kinetic-Analysis.* Journal of Catalysis, 1995. **156**(1): p. 106-119.
114. Kogelbauer, A., J.G. Goodwin, and R. Oukaci, *Ruthenium promotion of Co/Al$_2$O$_3$ Fischer-Tropsch catalysts.* Journal of Catalysis, 1996. **160**(1): p. 125-133.
115. Vada, S., B. Chen, and J.G. Goodwin, *Isotopic Transient Study of La Promotion of Co/Al$_2$O$_3$ for CO Hydrogenation.* Journal of Catalysis, 1995. **153**(2): p. 224-231.
116. Borg, O., S. Erib, E.A. Blekkan, S. Storsaeter, H. Wigum, E. Rytter, and A. Holmen, *Fischer-Tropsch synthesis over gamma-alumina-supported cobalt catalysts: Effect of support variables.* Journal of Catalysis, 2007. **248**(1): p. 89-100.
117. Yang, J., Y. Qi, J. Zhu, Y.A. Zhu, D. Chen, and A. Holmen, *Reaction mechanism of CO activation and methane formation on Co Fischer-Tropsch catalyst: A combined DFT, transient, and steady-state kinetic modeling.* Journal of Catalysis, 2013. **308**: p. 37-49.
118. Rebmann, E., P. Fongarland, V. Lecocq, F. Diehl, and Y. Schuurman, *Kinetic modeling of transient Fischer–Tropsch experiments over Co/Al2O3 catalysts with different microstructures.* Catalysis Today, 2016. **275**: p. 20-26.
119. Salciccioli, M., M. Stamatakis, S. Caratzoulas, and D.G. Vlachos, *A review of multiscale modeling of metal-catalyzed reactions: Mechanism development for complexity and emergent behavior.* Chemical Engineering Science, 2011. **66**(19): p. 4319-4355.

Chapter 2 Methodology

In this chapter, both the experimental and modeling procedures used throughout this thesis are discussed. The first part (Section 2.1) deals with the experimental procedures. More precisely, the experimental set-up used to acquire the experimental data is explained (Section 2.1.1). Afterwards, the definitions of CO conversion and product selectivities are addressed (Section 2.1.2). The last paragraph of Section 2.1 (Section 2.1.3) provides more information on the catalyst and its activation and testing procedure.

The second part of this chapter (Section 2.2) discusses the modeling procedures in more detail. First of all, the methodology followed for the modeling of metal catalysis is discussed (section 2.2.1). In Section 2.2.2, the numerical settings for periodic DFT calculations are provided. The reaction network generation methodology is outlined in Section 2.2.3. The reactor equations which describe the experimental reactor are discussed next (Section 2.2.4). The following section (Section 2.2.5) provides more details on numerical solver packages typically used in chemical engineering problems. Subsequently, Section 2.2.6 explains the regression procedures used to find optimal values for the adjustable model parameters and the statistical tests used to verify the global statistical significance of the model and the statistical significance of the individual parameters. Section 2.2 ends with the definitions of differential disappearance and formation factor, affinity and degree of rate control analysis used for reaction path analysis.

2.1 Experimental procedures

2.1.1 Steady State Isotopic Transient Kinetic Analysis set-up

The experiments were performed on the Steady State Isotopic Transient Kinetic Analysis (SSITKA) set-up available at the Norwegian University for Science and Technology (NTNU) [1]. In a SSITKA experiment an isotopic label is monitored in the reactants and products as a function of time after an abrupt switch of a reactant by its isotopic counterpart [2-4]. As explained in Section 1.4.2, the transient responses allow to decouple the observed reaction rate into a rate coefficient and a surface concentration of the relevant species [5]. As, in addition to an alternative inert, the only difference between the feed lines is the isotopic labeling of a reactant, steady state operation of the catalyst is maintained.

The SSITKA set-up at NTNU consists of a feed, reactor and analysis section. Figure 2-1 gives a schematic representation of the set-up [1]. The feed section has a total of six lines. The first three lines are used to compose the original feed, the other three lines to compose the isotopically labelled one. Both the original and the isotopically labelled feed are connected to a switch valve. Each line is controlled individually by mass flow controllers to ensure an identical gas composition in both feeds, apart from the isotopic labelling, which is of high importance for SSITKA measurements in order to maintain steady state operation of the catalyst. The first feed comprises Ar, ^{12}CO and H_2, while the second one comprises Kr, ^{13}CO and H_2. Hence, it is the exchange of ^{12}C to ^{13}C which is monitored as a function of time. The change in inert, i.e., from Ar to Kr, is used to follow the gas holp-up in the reactor. Before switching, it is ensured that the pressure in both feed lines is equal by manually setting the pressure controllers.

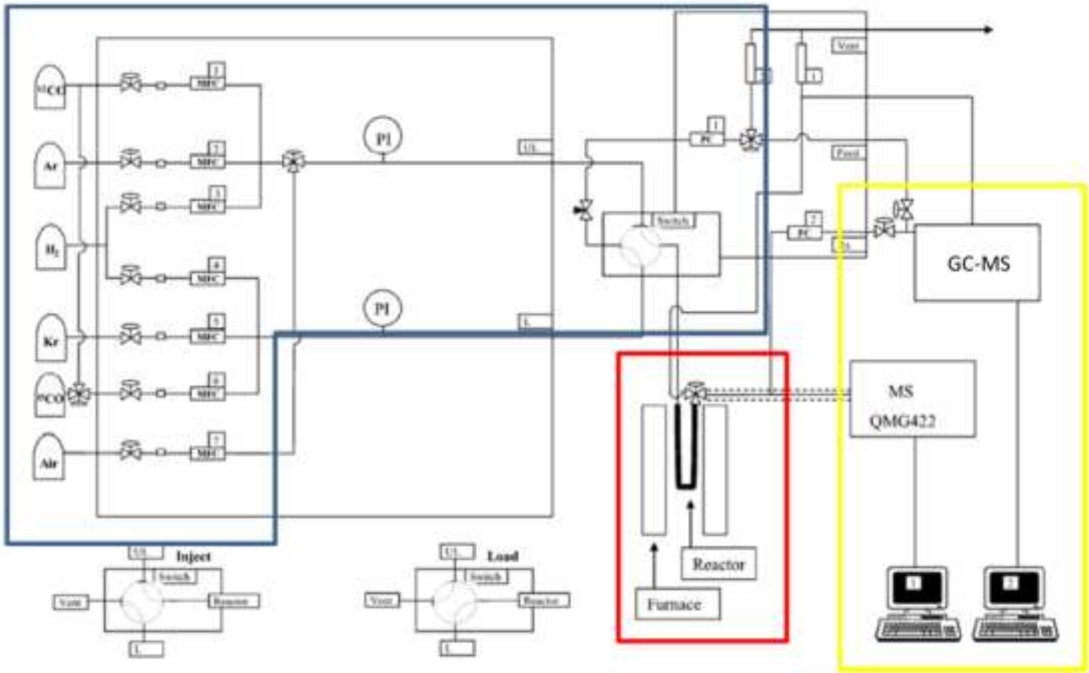

Figure 2-1: Schematic representation of the Steady State Isotopic Transient Kinetic Analysis set-up at NTNU. The blue lines enclose the feed section. The red rectangle encompasses the reactor section. The analysis section is indicated by the yellow rectangle [1].

The reactor is a U-shaped quartz reactor with an inner diameter of 4 mm. The temperature is measured with a thermocouple positioned outside next to the catalyst bed. The reactor is placed in an oven to obtain elevated temperatures. Quartz wool is used to keep the catalyst bed in place. The reactor was loaded with 8 to 100 mg of catalyst diluted with 32 to 400 mg inert silicon carbide to ensure isothermal operation of the catalyst bed. The catalyst was shaped into pellets with diameters ranging from 53 to 90 µm by sequential crushing and sieving to avoid internal diffusional limitations. The pellet diameter of the inert silicon carbide ranged from 75 to 150 µm.

The analysis section comprises a mass spectrometer (MS), i.e., a Balzers QMG 422 quadropole mass spectrometer, and a gas chromatograph – mass spectrometer (GC-MS), i.e., an Agilent technologies ® GC-MS 7890B-MSD5977. The MS monitors the reactants and products as a function of time which have a characteristic m/e value. For the present Fischer-Tropsch Synthesis (FTS) SSITKA experiments these components are H_2, ^{12}CO, ^{13}CO, $^{12}CH_4$, $^{13}CH_4$, Ar and Kr. The Agilent technologies ® GC-MS 7890B-MSD5977A is equipped with a Thermal Conductivity Detector (TCD), a Flame Ionization Detector (FID) and a Mass Selective Detector

(MSD) of which only the data recorded by the TCD and FID have been used. On the TCD, H_2, CO, Ar and CH_4 were measured. On the FID, the C_1 - C_6 alkanes and C_2 - C_5 alkenes were quantified. Hydrocarbons with more than six carbon atoms were not detected. In principle, the GC could measure hydrocarbons with more than 6 carbon atoms. This was verified by reference samples. However, at the reaction conditions, longer chain hydrocarbons were never detected. Even C_5 and C_6 species are merely produced in trace amounts. The formation of higher hydrocarbons is strongly suppressed by the applied reaction conditions, i.e., low CO partial pressures.

The data measured on the TCD and FID were converted into molar outlet flow rates by satisfying a 100% atomic carbon balance, see section 2.1.2. The latter was verified and was found to be within 5%. The outlet molar flow rates of iso-alkanes and iso-alkenes were added to the outlet molar flow rates of linear alkanes and 1-alkenes respectively.

An important characteristic of a SSITKA set-up is the time constant of the switch valve as this time constant determines the smallest time constant of the kinetic phenomena of which information can be obtained [6]. In Table 2-1 the switch time constant of the SSITKA set-up at NTNU [1] is compared to the switch time constant of other SSITKA/Step-response set-ups which have been used for kinetic studies.

Table 2-1: The switch time constant of various SSITKA/Step-response set-ups.

a_2 [s]	University/Lab
7.9	Clemson University [7]
5.4	Akron University [8]
3.7	Institut de Recherches sur la Catalyse - CNRS[9]
8.8	Université libre de Bruxelles [10]
0.7	Eindhoven University of Technology (1995) [11]
4.1	University of Pitssburgh [12]
0.3	Eindhoven University of Technology (2001) [6]
0.9	Norwegian University of Science and Technology

The switch time constants of the various SSITKA/Step-response set-ups can differ considerably. The switch time constant of the SSITKA set-up at NTNU is in the low range of switch time constants which have been used for kinetic studies of FTS.

2.1.2 Experimental data treatment

The raw GC data was converted to outlet molar flow rates. The composition of the reactor effluent can be determined as follows:

$$y_k = \frac{\frac{A_k^i CF_k}{A_{ref}^i CF_{ref}}}{\sum_{j=1}^{n_{comp}} \frac{A_j^i CF_j}{A_{ref}^i CF_{ref}}} \qquad [2\text{-}1]$$

Where y_k is the molar fraction of component k in the mixture, A_k^i is the peak area of component k on detector i, CF_k the calibration factor of component k, A_{ref}^i the peak area of a reference component measured on both the FID and TCD which is in this case CH_4. It is noted that in the summation of the denominator each component should be considered only once.

Ar was used as an internal standard to obtain the flow rates of each component:

$$F_k = \frac{F_{Ar,0}}{y_{Ar}} y_k \qquad [2\text{-}2]$$

Where F_k represents the outlet molar flow rate of component k $[mol\, s^{-1}]$ and $F_{Ar,0}$ the inlet molar flow rate of Ar $[mol\, s^{-1}]$.

The flow rates of all the components calculated with eq. [2-2] can be used to verify the carbon balance. Once the carbon balance is verified, the outlet molar flow rates are rescaled to satisfy a 100% carbon balance:

$$F_{tot} = \frac{F_{CO,0}}{\sum_{i=1}^{n_{comp}} a_{C,i} y_i} \qquad [2\text{-}3]$$

Where $F_{CO,0}$ represents the CO inlet molar flow rate $[mol\ s^{-1}]$, $a_{C,i}$ the number of carbon atoms in component i. Combining eq. [2-1] and eq. [2-3] yields the outlet molar flow rates used for the determination of conversion and selectivity.

The conversion and selectivity have been assessed on a carbon basis. The conversion $[mol\, mol^{-1}]$, X_{CO}, is defined as the ratio of the number of moles of CO which have reacted to the number of moles of CO which have entered the reactor, eq [2-4].

$$X_{CO} = \frac{F_{CO,0} - F_{CO}}{F_{CO,0}} \qquad [2\text{-}4]$$

The selectivity toward a gas phase component i $[mol\, mol^{-1}]$, S_i , is defined as follows:

$$S_i = \frac{a_{C,i} F_i}{F_{CO,0} - F_{CO}} \qquad [2\text{-}5]$$

The normalized response of component i, $I_i(t)$, measured on the MS is defined as:

$$I_i(t) = \frac{\varphi(t) - \varphi_{min}}{\varphi_{max} - \varphi_{min}} \qquad [2\text{-}6]$$

Where t is time $[s]$, φ represents the measured signal on the MS, and φ_{min} and φ_{max} the minimum and maximum of the MS signal measured during the transient response.

The surface residence time of a component i $[s]$, τ_i, is calculated from the normalized transient response:

$$\tau_i = \int_0^{+\infty} (I_i(t) - I_{inert}(t))dt \qquad [2\text{-}7]$$

2.1.3 Catalyst preparation, characterization, activation and testing

The catalyst synthesis and characterization have been thoroughly discussed by Yang et al [13] and are briefly summarized here. A 20 wt% Co on carbon nanotubes catalyst (Co/CNT) was used and obtained by incipient wetness impregnation of an aqueous solution of cobalt nitrate hexahydrate on CNT purchased from Chengdu Organic Chemicals [13]. An average Co metal particle size of 12.5 nm was determined by electron microscopy [13]. This is considered sufficiently large not to have any metal particle size effect on the turnover-frequency (TOF) or selectivity [14]. More detailed information on the catalyst preparation and characterization, e.g., transmission electron microscopy (TEM) images, has been provided by Yang et al [13].

The catalyst was activated prior to the experimentation by reduction under flowing H_2 (6.8 µmol s^{-1}) at atmospheric pressure. The temperature during this reduction was increased from room temperature to 623 K at a rate of 1 K min^{-1}, after which the catalyst was maintained for 16 hours at this final temperature under the same H_2 flow. After reduction, the temperature was lowered to 463 K and a mixture of CO (1.0 µmol s^{-1}), H_2 (10.0 µmol s^{-1}) and Ar (22.8 µmol s^{-1}) was fed to the reactor. The pressure was increased from atmospheric pressure to 185 kPa. The temperature was increased from 463 K to 483 K at a rate of 1 K min^{-1}. The catalyst was kept at these reaction conditions for at least 12 hours for lining-out purposes. After this period, the reaction conditions were adjusted to retrieve experimental data at the desired operating conditions. After a change in the reaction conditions, typically 3 GC samples were analyzed. In total, the catalyst was under the investigated conditions for typically 1.5 h. The reaction conditions were frequently changed back to the reference conditions to assess potential changes in catalyst activity or selectivity. Overnight, the catalyst was kept under the same reference conditions. As such typically 10 to 15 experiments could be performed prior to significant changes in observed catalyst activity or selectivity covering a time period of 48 to 72 h.

After taking the 3 GC samples at the adjusted operating conditions, transient responses of ^{12}CO and $^{12}CH_4$ were also acquired. The flow of Kr, ^{13}CO and H_2 and the pressure controller were set to match the composition and operating pressure of the other feed line. Once identical operating conditions in both feed lines were established, the switch of $Ar/^{12}CO/H_2$ to $Kr/^{13}CO/H_2$ was performed. On the MS, the transient responses of ^{12}CO and $^{12}CH_4$ were followed and the switch back to the original feed line was only performed after no noticeable changes occurred in the MS signals of ^{12}CO and $^{12}CH_4$. This back switch was typically performed after 2 to 3 minutes.

The total site concentration has been determined by means of ^{12}CO-^{13}CO isotopic switch experiments in the absence of reaction. The total number of adsorbed CO was multiplied with 2 in order to obtain the total site concentration [15]. The total site concentration based on this experiment amounted to 0.179 mol kg_{cat}^{-1}.

2.2 Modeling procedures

2.2.1 Mircokinetic modeling of metal catalysis

2.2.1.1 Single-Event MicroKinetics (SEMK) methodology

For the determination of the rate coefficients, k, the single-event methodology is applied [16]. The various components present in a complex reaction network can typically be grouped into a limited set of homologous series. Thanks to this, the elementary steps in the reaction network can be classified into reaction families. Differences in rate coefficients belonging to the same reaction family are taken into account by differences in symmetry as assessed by the global symmetry number σ_{gl}:

$$k = \frac{\sigma_{gl,reactant}}{\sigma_{gl,\ddagger}} \tilde{k} \qquad [2\text{-}8]$$

Where ‡ represents the transition state and ~ refers to single-event.

As such, a single rate coefficient, i.e., the single-event rate coefficient, $\tilde{k}$, eq [2-9], together with the a priori determined symmetry numbers suffices to calculate the rate coefficients of all elementary steps within a reaction family.

$$\tilde{k} = \frac{k_B T}{h} \exp\left(\frac{\Delta \tilde{S}^{0,\ddagger}}{R}\right) \exp\left(-\frac{\Delta H^{0,\ddagger}}{RT}\right) \qquad [2\text{-}9]$$

Where $\Delta \tilde{S}^{0,\ddagger}$ is the single-event standard activation entropy [$J\ (K\ mol)^{-1}$] and $\Delta H^{0,\ddagger}$ the standard activation enthalpy [$J\ mol^{-1}$].

2.2.1.2 Rate expression of an elementary step

For an elementary reaction to occur, the reactants must be in the direct vicinity of each other. This can for example be illustrated for the dissociative chemisorption of M_2 on two free sites:

$$M_2 + ** \rightleftarrows M ** M \qquad [2\text{-}10]$$

In order for the elementary reaction to proceed, two free sites adjacent to each other are required. The rate expression for the forward reaction of this elementary step is, based on the law of mass action, given by:

$$r_{ads} = k_{ads} p_{M_2} L_{**} \qquad [2\text{-}11]$$

Where r_{ads} is the rate of adsorption $[mol\ (kg_{cat}\ s)^{-1}]$, p_{M_2} the partial pressure of M_2 [Pa] and L_{**} the total concentration of two free sites adjacent to each other $[mol\ (kg_{cat}\ s)^{-1}]$.

If a dynamic equilibrium is considered between the total concentration of adjacent free sites, L_{**}, an occupied site adjacent to a free site, L_{*M}, and adjacent occupied sites , L_{MM}, and if no interaction energy is considered in this equilibrium, the total concentration of two adjacent free sites can be expressed in terms of the surface fraction of free sites [17]:

$$L_{**} = \frac{1}{2} z L_{tot} \theta_*^2 \qquad [2\text{-}12]$$

Where z represents the number of nearest neighbors [-] which depends on the crystallographic structure of the metal, L_{tot} the total concentration of sites $[mol\ kg_{cat}^{-1}]$ and θ_* the surface fraction of free sites $[-]$ defined as:

$$\theta_* = \frac{L_*}{L_{tot}} \qquad [2\text{-}13]$$

Where L_* is the total concentration of free sites $[mol\ kg_{cat}^{-1}]$.

As such the reaction rate expression for the adsorption step becomes:

$$r_{ads} = \frac{1}{2} z L_{tot} p_{M_2} \theta_*^2 \qquad [2\text{-}14]$$

A more intuitive reasoning can also be applied which states that the concentration of two adjacent free sites is equal to the concentration of one free, L_*, site multiplied with the probability that one of the nearest neighbors is also a free site, $1/2\, z\, L_*/L_{tot}$. The factor $1/2$ is required to avoid a double counting. This reasoning implies that there is no interaction between the chemisorbed species.

In case an elementary reaction takes place between an adsorbed species and two or more free metal sites, e.g., in case of CH_2 dehydrogenation, see Table 3-1, the rate expression for such an elementary step is obtained by first expressing the probability of two free sites being adjacent to each other as $1/2\, z\, {L_*}^2/L_{tot}$ and multiplying this with the probability of these two sites being adjacent to CH_2 which results in $(1/2\, z)^2 L_{CH_2} (L_*/L_{tot})^2$.

The rate expressions for all the elementary steps together with the number of metal sites to which a surface species binds are listed in Section 3.2.2.3 and Section 5.3.1. The number of metal sites occupied by a surface species was determined by ensuring that a carbon atom has 4 σ-bonds with a maximum of 3 bonds with the metal surface, an oxygen atom has 2 σ-bonds and a hydrogen atom has a single σ-bond. Changing the number of sites to which a surface species binds is anticipated to have an impact on the model parameter estimates, i.e., the activation energies and atomic chemisorption enthalpies, see Section 2.2.1.4. However, the generic conclusions such as which elementary reactions are rate limiting, relative reaction rates of elementary steps, etc… are expected to remain valid upon changing the number of metal sites to which a surface species binds.

The net rates of formation of the gas phase components and surface species are obtained by summation of all the rates of the elementary steps in which this respective gas phase component or surface species is involved:

$$R_j = \sum_{i=1}^{n_{reactions}} \left(\nu_{i,j}^f + \nu_{i,j}^r\right) r_i \qquad [2\text{-}15]$$

Where R_j represents the net formation rate of the jth gas phase component or surface species $[mol\ (kg_{cat}\ s)^{-1}]$, $n_{reaction}$ the number of elementary reactions considered in the reaction network, $\nu_{i,j}^{f}$ the forward stoichiometric coefficient of the ith elementary step belonging to the jth gas phase component or surface species which is by convention negative, $\nu_{i,j}^{r}$ the reverse stoichiometric coefficients of the ith elementary reaction belonging to the jth gas phase component or surface species which is by convention positive.

2.2.1.3 Pre-exponential factors and reaction entropies

The single-event rate coefficient, eq [2-9], is expressed according to the Arrhenius relationship. The single-event pre-exponential factor, $\tilde{A}$, hence, becomes [18]:

$$\tilde{A} = \frac{k_B T}{h} \exp\left(\frac{\Delta\tilde{S}^{0,\ddagger}}{R}\right) \qquad [2\text{-}16]$$

The single-event standard activation entropy $[J\ (mol\ K)^{-1}]$, $\Delta\tilde{S}^{0,\neq}$, of an elementary step is the entropy difference between the single-event entropy of the transition state, $\tilde{S}^{0,\ddagger}$, and the single-event entropy of the reactants, $\tilde{S}_{surf,i}^{0}$:

$$\Delta\tilde{S}^{0,\neq} = \tilde{S}^{0,\ddagger} - \sum_{i=1}^{n_{react}} \nu_i \tilde{S}_{surf,i}^{0} \qquad [2\text{-}17]$$

The single-event entropies of both the transition state and the surface species are calculated from single-event entropies of the equivalent gas phase components and the single-event standard entropy change related to the chemisorption step [18, 19]. The standard single-event entropies of the equivalent gas phase components can be determined from open databases [20] or group additvity methods [21, 22]. The entropy change related to the chemisorption step is calculated based on the idea that it is primarily dominated by a loss of translational entropy [23].

The translational entropy of a gas phase component is calculated with the Sackur-Tetrode equation [24]:

$$S^0_{trans} = Rln\left(\frac{RT}{p^0 N_A}\left(\frac{2\pi(M_i/N_A)k_B T}{h^2}\right)^{3/2}\right) + \frac{5}{2}R \qquad [2\text{-}18]$$

Where p^0 is the standard pressure $[Pa]$ and M_i the molecular mass of component i $[kg\ mol^{-1}]$.

The loss of a translational degree of freedom upon chemisorption is approximated by 1/3 of the full translational entropy.

The number of degrees of freedom being lost upon chemisorption has to be determined in correspondence with the state of the chemisorbed layer. High surface coverages, such as encountered in FTS, will tend to reduce the mobility of the chemisorbed species. Therefore, in general the loss of two to three degrees of freedom upon chemisorption has been assumed.

The pre-exponential factor for an adsorption step obtained by employing eq. [2-18] is obtained in $(bar\ s)^{-1}$ and has to be modified according to the units used in the microkinetic model for the pressure of the gas phase components.

The reverse pre-exponential factors, $\tilde{A}^r$, are calculated by applying the principle of microscopic reversibility at the elementary step level:

$$\ln(\tilde{A}^r) = \ln(\tilde{A}^f) - \frac{\Delta\tilde{S}^0_r}{R} \qquad [2\text{-}19]$$

The standard surface reaction entropy, $\Delta\tilde{S}^0_r$, is calculated from the entropy of the reactant and product surface species.

2.2.1.4 Activation energies and reaction enthalpies

The forward activation energies are considered as the adjustable model parameters. The reverse activation energies, E^r_a are also calculated by applying the principle of microscopic reversibility:

$$E^r_a = E^f_a - \Delta H^0_r \qquad [2\text{-}20]$$

The standard surface reaction enthalpy , ΔH^0_r, is calculated from the enthalpy of the reactant and product surface species. The enthalpy of the surface species is obtained in a similar way as the entropy of the surface species, i.e., by considering the enthalpy of the corresponding gas phase components and the enthalpy change related to the chemisorption step. These chemisorption enthalpies are calculated via the UBI-QEP method [25-27], which is widely used in fundamental microkinetic modeling studies [28-35].

UBI-QEP

The UBI-QEP (Unity Bond Idex – Quadratic Exponential Potential) method is a phenomenological method devised by Shustorovich et al. [25-27]. The method relates the chemisorption enthalpy of a gas phase species to a limited set of parameters, i.e., gas phase molecular bond energies, D_{AB}, and atomic chemisorption enthalpies, Q_A. The first set of parameters can be readily obtained from open databases [20] or group additivity methods [21, 22] for a large group of frequently encountered surface species. In absence of such information, an accurate estimate can be made with ab initio calculations for gas phase molecules. The UBI-QEP method can also be used to calculate activation energies but this was merely done to obtain initial estimates.

The second set of parameters, i.e., Q_A, can also be estimated from experimental observations [36] or solid state ab initio calculations. The presence of surface defects, e.g., step sites, or the surface coverage of the various surface species can have a significant impact on the atomic chemisorption enthalpies [37, 38]. Therefore, the values from experimental observations or solid state ab initio calculations typically require further fine-tuning by regression to experimental data.

In the UBI-QEP method the atomic chemisorption enthalpy on an n fold coordination site is related to the atomic chemisorption enthalpy on the top site as follows:

$$Q_A = Q_{0A}\left(2 - \frac{1}{n}\right) \tag{2-21}$$

Where Q_A is the atomic chemisorption enthalpy on a n fold coordination site [kJ mol^{-1}], Q_{0A} the atomic chemisorption enthalpy on the top site [kJ mol^{-1}] and n the coordination number [-].

The atomic chemisorption enthalpies which were considered as adjustable model parameters are the atomic chemisorption enthalpies assuming three coordinations (n=3).

Depending on the nature of the surface species, a distinction is made in the UBI-QEP method to derive relations for weak, intermediate and strong chemisorption.

Weak bonding

For an AB molecule chemisorbed in an n fold coordination site through the A atom, the UBI-QEP method relates the chemisorption enthalpy of an AB gas phase component, Q_{AB}, to the atomic chemisorption enthalpy of A, Q_A, and the gas phase molecular bond energy, D_{AB}, as follows:

$$Q_{AB} = \frac{{Q_{0A}}^2}{\frac{Q_{0A}}{n} + D_{AB}} \qquad [2\text{-}22]$$

This equation is typically employed to calculate the chemisorption enthalpy of gas phase components with no or strongly delocalized unpaired electrons, e.g., CO.

Strong bonding

In this case, the atomic chemisorption enthalpy on the on top site in eq. [2-8] is replaced by the atomic chemisorption enthalpy on an n fold coordination site:

$$Q_{AB} = \frac{{Q_A}^2}{Q_A + D_{AB}} \qquad [2\text{-}23]$$

Gas phase components which typically strongly bind to a metal surface are components with localized unpaired electrons, e.g., hydroxyl, methylidene and methylene species.

Intermediate bonding

For some of the gas phase components, the chemisorption enthalpy is obtained by considering a superposition of weak and strong bonding:

$$Q_{AB} = (1 - \alpha)\frac{{Q_{0A}}^2}{\frac{Q_{0A}}{n} + D_{AB}} + \alpha\frac{{Q_A}^2}{Q_A + D_{AB}} \qquad [2\text{-}24]$$

Where α is a superposition constant [-].

This formula is, for example, used to calculate the atomic chemisorption enthalpy of alkyl radicals. For alkyl radicals, the α is typically set to 0.5 [25]. It is noted that for polyatomic species such as alkyl radicals, the D_{AB} is calculated by considering the C atom to be in contact with the surface and B representing any molecular fragment. The D_{AB} used for the calculation of the chemisorption energy of a methyl radical, hence, considers three H atoms as molecular fragments while for larger alkyl radicals, the D_{AB} is calculated by considering 2 H atoms and the remaining alkyl chain as molecular fragments.

It is noted that AB molecules can also interact with the metal surface through the A and B atom. In this case, the chemisorption enthalpy is obtained as follows:

$$Q_{AB} = \frac{ab(a+b) + D_{AB}(a-b)^2}{ab + D_{ab}(a+b)} \qquad [2\text{-}25]$$

With

$$\begin{aligned} a &= \frac{{Q_A}^2(Q_A + 2Q_B)}{(Q_A + Q_B)^2} \\ b &= \frac{{Q_B}^2(Q_B + 2Q_A)}{(Q_A + Q_B)^2} \end{aligned} \qquad [2\text{-}26]$$

Eqs. [2-25] and [2-26] can be used for the calculation of the chemisorption enthalpy of, e.g., alkenes.

It is noted with respect to the forward activation energies that, for an endothermic elementary reaction, the standard reaction enthalpy is the lower limit for the forward activation energy of that elementary reaction. Consequently, if, during the course of the regression the value for the forward activation energy becomes smaller than the standard reaction enthalpy of such an endothermic elementary reaction, this activation energy was set equal to the standard reaction enthalpy.

The increasing availability of ab initio techniques makes it possible to compare UBI-QEP calculated values with ab initio determined ones. As such, the formulas, eq [2-22] to eq [2-26], can be assessed a priori to match the values from ab initio calculations. Furthermore, ab initio calculations can also reveal important differences between surface species of homologous series. For example, ab initio calculations have shown that a difference in chemisorption enthalpy is to be expected between a methyl radical and radicals with more than 1 carbon atom [39]. As such, α in eq [2-24] can be set equal to 0.5 for the heavier alkyl radicals [25] while it can be increased for the methyl radical, see also Chapter 3 and Chapter 5.

In conclusion, the kinetic parameters are determined via the SEMK methodology. The single-event pre-exponential factors are calculated by means of the Sackur-Tetrode equation, eq. [2-18], and considerations with respect to the degrees of freedom being lost or gained. The activation energies of the forward elementary steps are considered as adjustable model parameters. The reverse activation energies are obtained by applying the principle of microscopic reversibility. For this, the chemisorption enthalpy of the surface species is calculated by means of the UBI-QEP method. The atomic chemisorption enthalpy of H, C and O required in the latter method are also considered as adjustable model parameters.

2.2.2 Vienna Ab Initio Simulation Package (VASP)

As already mentioned in the previous section, ab initio calculation can be used to obtain initial estimates for the atomic chemisorption enthalpies. Furthermore, ab initio calculations can also be applied to construct correlations between these atomic chemisorption energies and the adsorption energies of other surface species. As such, the results from ab initio calculations can be used to fine tune the UBI-QEP method, e.g., by determining the superposition constant of eq [2-24].

Periodic DFT calculations were performed with the Vienna Ab Initio Simulation Package (VASP) [40-43]. The calculations make use of the projector augmented wave (PAW) pseudopotentials [44, 45] and plane-wave basis sets with a kinetic energy cut-off value of 450 eV. A smearing method, i.e., the method of Methfessel and Paxton, is used for the calculation of the integrals close to the *Fermi surface* with a smearing value of 0.1. The k point sampling of the Brillouin-zone is done by means of the Monkhorst-Pack method [46] and depends on the size of the unit cell considered. Only the Γ point is considered for gas phase calculations. As calculations were performed for Co, spin-polarized calculations had to be performed. The solution of the Kohn-Sham equations is obtained iteratively by using a robust mixture of the blocked Davidson iteration method and the quasi-Newton RMM-DIIS method until the energy convergence criterion of 10^{-6} eV is satisfied. The generalized gradient PBE functional [47] was applied as the DFT functional. An artificial dipole correction was used to avoid interaction between the periodic images in the z-direction.

The unit cells were 3×3 or 3×6 atoms large, four layers of Co metals thick and a vacuum spacing of 20 Å was employed. The 3×3 unit cell was used to model the Co(0001) surface while the 3×6 unit cell was used to model a stepped Co(0001) surface. The Monkhorst-Pack mesh was 5×5×1 and 5×3×1 for the 3×3 and 3×6 unit cell respectively. The step was obtained by removing Co atoms from the top layer. For geometry optimization, the conjugate-gradient method is applied with a force convergence criterion of 0.01 eV/ Å. During the geometry optimization, the Co atoms in the two top layers were allowed to relax.

2.2.3 Reaction network generation

Several methodologies for automated reaction network generation for FTS have been developed [18, 48-50]. The ones outlined by Klinke et al. [48] and Lozano-Blanco et al. [18] have been successfully applied in the development of a microkinetic model for the FTS. Both methodologies are based on a matrix representation of molecules and reactions are implemented by operation on these matrices. More precisely, Klinke et al. [48] used the bond-electron matrix representation [51] with modifications to extend this to heterogeneous catalysis. Chemical reactions were generated by summation of the bond-electron matrix of the reactants and a matrix representing the reaction [48]. In the approach discussed by Lozano-Blanco et al. [18], the chemical species are represented by standardized labels [52] and Boolean matrices [53]. As the latter approach has typically been discussed in conjunction with the development of SEMK models [54], this approach was adopted here.

The species representation by means of a Boolean matrix [53] or a standardized label [52] is illustrated in Figure 2-2. A bond between 2 atoms is represented in the Boolean matrix by the element on the corresponding row and column being equal to one. To distinguish between different type of atoms, the first column of the Boolean matrix stores the atomic number of the corresponding atom. Hydrogen atoms are not explicitly accounted for in this representation. Hence, an additional information vector is employed to distinguish saturated from unsaturated atoms. [18]

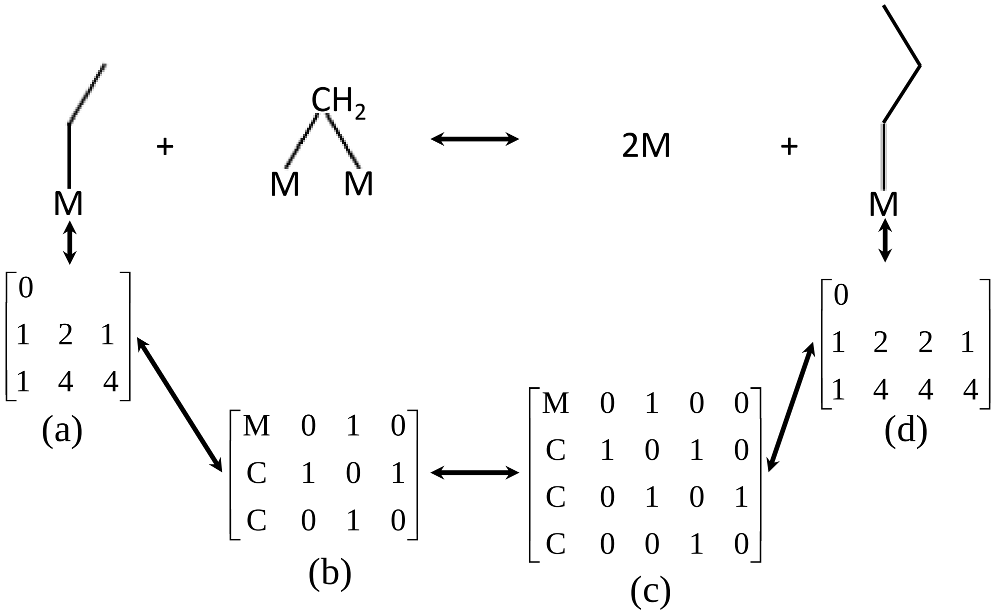

Figure 2-2: Automated reaction network generation. (a) and (d) Standardized label representation of metal ethyl and metal propyl respectively. (b) and (c) Boolean matrix representation of metal ethyl and metal propyl respectively. Adapted from Lozano-Blanco et al. [18].

The standardized labels are a more compact and, hence, memory saving representation of the species, especially for larger ones. The elements of this vector are organized in three rows. The first element of the standardized label indicates the position of a charge on the hydrocarbon chain, if any. The second row elements indicate the degree of substitution, e.g., a ‘2’ means that the atom on that position is a secondary atom. The elements of the third row are used to designate the nature of the atoms.

The generation of an elementary step, including the corresponding reaction products, is also represented in Figure 2-2 for a methylene insertion. The generation of such an elementary step is generally more easily performed by operations on the Boolean matrices compared to the standardized labels. Once the elementary step has been generated, the Boolean matrix representation of the product(s) is converted to the standardized label. For each reaction family a specific operation on the Boolean matrix has to be included in the reaction network generation program. A counter based while loop is used to guarantee the generation of every possible intermediate species and reaction. [18]

2.2.4 Reactor equations

The experiments were performed in a fixed bed reactor. The absence of pressure and temperature gradients on the reactor scale was verified via adequate correlations [55], see also Table 2-2. This implies that only mass balances for the various components have to be considered. The flow regime can be approximated by plug flow as the ratio of the bed height and bed diameter to the diameter of the catalyst pellet amount to 140 and 40 respectively. Furthermore, significant external and internal concentration gradients could also be ruled out based on the proper correlations [55], see also Table 2-2.

Table 2-2: Summary of criteria to assess the presence of intrinsic kinetic conditions.

Plug-flow regime	
Bed height/d_p > 0.97	140
Bed diameter/d_p > 8	40
Mass transport limitations	
External (Ca < 0.05)	$1.3\ 10^{-5}$
Internal (Wheeler – Weisz < 0.08)	$3\ 10^{-4}$
Heat transport limitations	
Internal (< 0.92 K)	$1\ 10^{-4}$ K
External (<0.92 K)	0.004 K
Radial (<0.92 K)	0.09 K
Axial (<0.92 K)	0.77 K

If only the steady state GC measurements acquired with the SSITKA set-up are to be simulated, the reactor can, hence, be simulated using a 1-dimensional, pseudo-homogeneous reactor model. Flow rate profiles for the gas phase components along the axial direction of the catalyst bed are obtained by solving a set of ordinary differential equations (ODEs), eq [2-27]. For the surface species the pseudo steady state approximation is applied, resulting in a set of algebraic equations (AEs), eq [2-28], which have to be solved simultaneously with the ODEs. This results in a set of differential algebraic equations (DAEs), eq. [2-27] and eq. [2-28].

$$\frac{dF_i}{dW} = R_i \quad i = 1, n_{gas\ phase\ components} \tag{2-27}$$

$$R_j = 0 \quad j = 1, n_{surface\ species} \tag{2-28}$$

Where W represents the catalyst mass [kg$_{\text{cat}}$], R_i the net formation rate of the ith gas phase component $[mol\ (kg_{cat}\ s)^{-1}]$ and R_j the net formation rates of surface species j.

This set of DAEs is complemented with a set of initial conditions:.

$$F_i(0) = F_{i,0} \tag{2-29}$$

Where $F_{i,0}$ represents the inlet molar rate of the ith gas phase component $[mol\ s^{-1}]$.

If the transient responses have to simulated, the evolution of the concentration of the isotopically labeled gas phase species, i', and labeled surface species, j', with the time is calculated by integrating a set of partial differential equations (PDEs), eq. [2-30] and eq. [2-31] respectively, with initial conditions, eq. [2-32], and boundary conditions, eq. [2-33] [56, 57].

$$\frac{\partial C_{i'}(x,t)}{\partial t} + \frac{1}{\tau_b}\frac{\partial C_{i'}(x,t)}{\partial x} = \frac{\rho_b}{\varepsilon_b} R_{i'}(x,t) \tag{2-30}$$

$$\frac{\partial L_{j'}(x,t)}{\partial t} = R_{j'}(x,t) \tag{2-31}$$

$$C_{i'}(x,0) = L_{j'}(x,0) = 0 \tag{2-32}$$

$$C_{i'}(0,t) = C_{i',0}(t) \tag{2-33}$$

Where $C_{i'}$ is the gas phase concentration of gas phase component $i'[mol\ m^{-3}]$, $L_{j'}$ the surface concentration of surface species $j'[mol\ kg_{cat}^{-1}]$, ρ_b the bed density $[kg_{cat}\ m_r^{-3}]$, ε_b the bed porosity $[m_f^3\ m_r^{-3}]$, x the dimensionless reactor coordinate varying between 0 and 1, τ_b the bed residence time $[s]$ calculated as $\tau_b = (\varepsilon_b W)/(\rho_b F_{tot} V_{mol})$ with F_{tot} the total molar flow rate,

V_{mol} the molar volume of the gas phase at the reactor conditions and $C_{i',0}$ the gas phase concentration of gas phase component i' at the reactor entrance. It is noted that, in the derivation of eq. [2-30], it is assumed that the superficial gas velocity is constant along the axial direction of the reactor. Given the typically high dilutions that are used and that relatively low conversions are aimed at, this assumption is quite reasonable.

The shape of the input signal is taken from Govender et al. [57]:

$$C_{i',0}(t) = C_{i,0}^{SS}\left(\frac{1}{1+e^{-\frac{t-a_1}{a_2}}}\right)^{a_3} \qquad [2\text{-}34]$$

Where $C_{i,0}^{SS}$ is the steady state concentration of gas phase component i at the reactor entrance.

There are three parameters which control the shape of the input signal, i.e., a_1, a_2 and a_3. a_2 is related to the inertia of the switch valve and should be as small as possible. This parameter will be referred to as the switch time constant. Parameters a_1 and a_3 do not have a physically interpretable meaning. These three parameters are determined experimentally and are set-up specific. It is noted that the input signal of eq. [2-34] is, in the limit of t approaching zero, algebraically not equal to zero. Numerically calculating the value of the input signal at time zero using typical values for a_1, a_2 and a_3 results in a value for the input signal practically equal to zero.

As the steady state is maintained, the sum of the concentrations of both unlabeled, i, and labeled, i', gas phase species and unlabeled, j, and labeled, j', surface species are modeled by a set of DAEs [11, 56, 57]:

$$\frac{dC_{i+i'}(x)}{dx} = \frac{\tau_b \rho_b}{\varepsilon_b} R_{i+i'}(x)$$

$$R_{j+j'} = 0 \qquad [2\text{-}35]$$

2.2.5 Numerical routines

Frequently encountered problems in chemical engineering can be described by a set of first ODEs, e.g., eq [2-27], and is more generally defined in eq [2-36].

$$\frac{d\underline{y}(t)}{dt} = \underline{f}(t, \underline{y}(t)) \qquad [2\text{-}36]$$

Where $\underline{y}(t)$is the vector of dependent variables, t is the independent variable and $\underline{f}(t, \underline{y}(t))$ the function defining the set of ODEs. $\underline{f}(t, \underline{y}(t))$ is also referred to as the right hand side (RHS) of the set of ODEs.

Due to the complexity of the problem, the solution of the resulting set of equations can only rarely be found analytically. In order to obtain values for the dependent variables at different positions of the independent variable, a large variety of numerical methods have been developed which are typically classified into two major groups, i.e., the linear multistep methods (LMMs) and the Runge-Kutta methods.

Linear multistep Methods

The general definition of LMMs is:

$$\sum_{j=0}^{k} \alpha_j \underline{y}_{n+j} = h \sum_{j=0}^{k} \beta_j \underline{f}\left(t_{n+j}, \underline{y}_{n+j}\right)$$

$$\alpha_k = 1 \; and \; |\alpha_0| + |\beta_0| \neq 0 \qquad [2\text{-}37]$$

Where y_i is the numerical approximation of the vector of dependent variables at the independent variable t_i, h the step size and α_i and β_i coefficients belonging to a specific LMM.

The coefficients α_i and β_i are determined by interpolating $\underline{f}(t, \underline{y})$ or $\underline{y}$ on several discretization points. An example of a class of LMMs based on interpolation of $\underline{f}(t, \underline{y})$ are the so-called Adams-Bashfort formulas which can be obtained as follows. By integrating eq. [2-36] from $[t_n, t_{n+1}]$, eq. [2-38] is obtained:

$$\underline{y}(t_{n+1}) - \underline{y}(t_n) = \int_{t_n}^{t_{n+1}} \underline{f}\left(t, \underline{y}(t)\right) dt \tag{2-38}$$

The integral of eq. [2-38] is subsequently calculated by considering a Lagrange polynomial of degree m, $\underline{P_m}(t)$, on the interval $[t_{n-m}, t_n]$:

$$\underline{y}_{n+1} = \underline{y}_n + \int_{t_n}^{t_{n+1}} \underline{P_m}(t)$$

$$\underline{P_m}(t) = \sum_{j=0}^{m} \underline{f}\left(t_{n-j}, \underline{y}_{n-j}\right) \prod_{\substack{l=0 \\ l\neq j}}^{m} \frac{t - t_{n-l}}{t_{n-j} - t_{n-l}} \tag{2-39}$$

An important class of LMMs obtained by interpolating $\underline{y}$ are the so-called Backward Differentiation Formulas (BDFs). The formulas are obtained by interpolating $\underline{y}$ by a Langrange polynomial of degree m, $\underline{P_m}(t)$, on $[t_{n-m+1}, \dots, t_{n+1}]$ and equating the derivative to the dependent variable in t_{n+1} to an evaluation of the RHS at t_{n+1}:

$$\frac{d\underline{P_m}(t_{n+1})}{dt} = \underline{f}\left(t_{n+1}, \underline{y}_{n+1}\right) \tag{2-40}$$

A distinction has to be made between explicit and implicit schemes. In the former, the numerical solution of the dependent variables is obtained at the independent variable t_{n+1} by considering only evaluations of the RHS of the ODEs at points $[t_{n-m}, t_n]$. For implicit schemes, the linear multistep formula contains $\underline{y}_{n+1}$ and an evaluation of the RHS at t_{n+1}. The Adams-Bashfort fomulas are an example of explicit schemes while the BDFs are an example of implicit schemes.

Runge-Kutta methods

The general definition of the Runge-Kutta methods is:

$$\underline{y}_{n+1} = \underline{y}_n + h \sum_{i=1}^{s} b_i \underline{k}_i \tag{2-41}$$

$$\underline{k}_i = \underline{f}\left(t_n + c_i h, \underline{y}_n + h\sum_{j=1}^{s} a_{ij}\underline{k}_j\right)$$

Formulas can be obtained by integrating both the left hand side and right hand side of eq. [2-36] between t_n and t_{n+1}:

$$\underline{y}(t_{n+1}) - \underline{y}(t_n) = \int_{t_n}^{t_{n+1}} \underline{f}\left(t, \underline{y}(t)\right) dt \qquad [2\text{-}42]$$

And evaluating the integral of the RHS by means of quadrature formulas on internal point of $[t_n, t_{n+1}]$.

Also for the Runge-Kutta methods, explicit and implicit discretization schemes have been constructed.

Stiff solvers

The set of ODEs encountered in chemical engineering problems frequently suffer from stiffness. Stiffness originates from large differences in the time scales present in the set of ODEs. Employing an explicit scheme to a stiff set of ODEs would force the stepsize to become excessively small compared to the differentiability of the solution. This is because explicit schemes only have limited areas of absolute stability compared to implicit schemes. Stiff ODEs, hence, force explicit schemes to use small stepsizes for stability reasons. In order to avoid these small stepsizes, stiff ODEs are solved by implicit schemes.

The major downside of an implicit scheme is that at each step a set of algebraic equations has to be solved, e.g., for the linear multistep methods:

$$\alpha_k \underline{y}_{n+k} - h\beta_k \underline{f}\left(t_{n+k}, \underline{y}_{n+k}\right) = \sum_{j=0}^{k-1}\left(h\beta_j \underline{f}_{n+j} - \alpha_j \underline{y}_{n+j}\right) \qquad [2\text{-}43]$$

The solution of this set of AEs is obtained via Newton’s iterative method:

$$\underline{y}_{n+k}^{s+1} = \underline{y}_{n+k}^{s} - \left[\underline{\underline{I}} - h\beta_k \frac{\partial \underline{f}}{\partial \underline{y}}\left(t_{n+k}, \underline{y}_{n+k}^{s}\right)\right]^{-1} \dots$$

$$\dots \left[\underline{y}_{n+k}^{s} - h\beta_k \underline{f}\left(t_{n+k}, \underline{y}_{n+k}^{s}\right) + \sum_{j=0}^{k-1} \alpha_j \underline{y}_{n+j}\right] \qquad [2\text{-}44]$$

Where the superscript s indicates the number of interation and $\frac{\partial \underline{f}}{\partial \underline{y}}$, is called the Jacobian matrix.

To reduce the number of iterations, $\underline{y}_{n+k}$, is first approximated by an explicit scheme (predictor). The implicit scheme is called the corrector.

The calculation of the Jacobian matrix and the subsequent inversion are two time consuming steps. Therefore, numerical solver packages, such as DASPK [58] or LSODE [59], provide options to provide the numerical solver package with more information on the Jacobian matrix, e.g., a banded structure, or allow the user to provide the Jacobian matrix analytically.

2.2.6 Regression

The adjustable model parameters, i.e., the activation energies of the forward reactions and the atomic chemisorption enthalpies, are estimated by an iteratively reweighted least squares (IRLS) optimization in which the following objective function is applied:

$$SSQ(\underline{b}) = \sum_{i=1}^{n_{exp}} \sum_{j=1}^{n_{resp}} w_j (y_{ij} - \hat{y}_{ij})^2 \xrightarrow{\underline{b}} min \qquad [2\text{-}45]$$

Where $\underline{b}$ represents the vector of adjustable model parameters, n_{exp} the number of experiments, n_{resp} the number of responses in each experiment, w_j the statistical weight corresponding to response j, y_{ij} the experimental response j in experiment i, $\hat{y}_{ij}$ the model simulated value for response j in experiment i. The statistical weights, w_j, are calculated from the inverse of the covariance of the experimental errors:

$$w_j = \left[\frac{\sum_{i=1}^{n_{exp}}\left(y_{ij} - \hat{y}_{ij}\right)^2}{n_{exp}n_{resp} - n_{par}}\right]^{-1} \qquad [2\text{-}46]$$

Where n_{par} represents the number of adjustable model parameters. The statistical weights, w_j, are determined via an iterative procedure in which updates for w_j are determined from the model responses obtained with values for w_j from the last iteration. This is repeated until convergence, typically requiring only 2 or 3 iterations. Initial estimates for the w_j can be determined from the inverse of the experimental error if repeat experiments are available.

The minimization is performed in two steps. In a first step, the multiresponse Rosenbrock [60] optimization algorithm has been applied to bring the initial parameter estimates towards the possible region of the global optimum. This algorithm is implemented in an in-house developed computer code in Fortran. Subsequently, the multireponse Levenberg-Marquardt [61] algorithm as implemented in ODRPACK [62] has been used to find the actual minimum of the objective function. Some complementary code was added to ODRPACK to retrieve additional information on the regression, i.e., the total, regression and residual sum of squares, t values of the individual parameter estimates, the F value for the global significance of the regression, the correlation matrix of the parameters and the multiple correlation coefficient, see also Section 2.2.6.1.

2.2.6.1 Statistical tests

The global regression significance was assessed via an F test [63]. This test verifies the null hypothesis that all model parameters in the model would simultaneously equal zero. The F value is calculated as the ratio of the mean regression sum of squares to the mean residual sum of squares:

$$F_c = \frac{\dfrac{\sum_i^{n_{exp}}\sum_j^{n_{resp}} w_j \hat{y}_{i,j}^2}{n_{par}}}{\dfrac{\sum_i^{n_{exp}}\sum_j^{n_{resp}} w_j\left(\hat{y}_{i,j}^2 - y_{i,j}^2\right)}{n_{exp}n_{resp} - n_{par}}} \qquad [2\text{-}47]$$

If the null hypothesis is valid, the value calculated by eq. [2-47] should follow an F distribution. In case the calculated F value exceeds the tabulated 95% confidence F value, the null hypothesis can be rejected and the regression can be considered as globally, statistically significant. In practice, the calculated F value significanty exceeds the tabulated value and, hence, the null hypothesis is easily rejected. Therefore, for the regression to have any practical meaning, the calculated F value should be at least 100 or higher.

The statistical significance of each individual parameter estimate is also assessed. This is done by a t test [63]. In this test, it is verified whether the parameter is statistically significantly different from a postulated value, typically zero. The t value of a parameter in this case is calculated as given by:

$$t_c = \frac{|b_i|}{\sqrt{\left[V(\underline{b})\right]_{ii}}} \qquad [2\text{-}48]$$

Where t_c represents the calculated t value, b_i the parameter estimate and $\left[V(\underline{b})\right]_{ii}$ the ith diagonal element of the variance-covariance matrix.

If t_c exceeds the 95 % confidence tabulated t value, the parameter estimate is significantly different from zero and, as a consequence, the corresponding confidence interval will not include zero.

The binary correlation coefficient between parameter i and parameter j, ρ_{ij}, is calculated by means of the variance-covariance matrix of the parameters:

$$\rho_{ij} = \frac{\left[V(\underline{b})\right]_{ij}}{\sqrt{\left[V(\underline{b})\right]_{ii}\left[V(\underline{b})\right]_{jj}}} \qquad [2\text{-}49]$$

Parameters are considered to be correlated if $\left|\rho_{ij}\right| > 0.95$.

Next to the statistical assessment of the global regression significance and the individual parameter significance, it is also important to verify the model’s ability to predict physically acceptable trends as a function of the reaction conditions and the physicochemical meaning of the parameters such as positive activation energies.

2.2.7 Reaction path analysis

Once the microkinetic model is constructed and the adjustable model parameters have been determined by regression to the experimental data, the model can be exploited to get more insight in the reaction mechanism and the impact of the model parameters on the model performance via a so-called reaction path analysis. To this purpose, the differential disappearance and formation factor and the affinity of an elementary step are combined with a degree of rate control analysis.

The differential disappearance factor, $\varphi_{i,j}^{d}$, of a component i leading to a component j is obtained by dividing the corresponding reaction rate, $r_{i,j}$, by the sum of all the reaction rates of all the elementary steps in which component i is consumed:

$$\varphi_{i,j}^{d} = \frac{r_{i,j}}{\sum_k r_{i,k}} \tag{2-50}$$

Similarly, the differential formation factor of a component i, $\varphi_{j,i}^{f}$, is defined as the ratio of the formation rate of component i starting from component j, $r_{j,i}$, and the sum of all the reactions producing component i:

$$\varphi_{j,i}^{f} = \frac{r_{j,i}}{\sum_k r_{k,i}} \tag{2-51}$$

The affinity of an elementary reaction i, A_i, indicates if an elementary reaction is quasi-equilibrated. The affinity of an elementary reaction $aA + bB \rightleftarrows cC + dD$ is calculated as follows:

$$A_i = RTln\left(\mathrm{K}\frac{A^a B^b}{C^c D^d}\right) \tag{2-52}$$

If the affinity is close to zero, i.e., $|A_i| < 1000\, J\, mol^{-1}$ corresponding to r_i^f / r_i^r = 1.27 at 493 K, the elementary reaction is assumed to be at quasi-equilibrium.

Affinity calculations are useful to identify the steps in the reaction mechanism which are kinetically relevant, i.e., not quasi-equilibrated. If more than one elementary reaction is not quasi-equilibrated, the reaction steps which ultimately control the reactant conversion can be identified by means of a degree of rate control analysis [64, 65]. In a degree of rate control analysis [65], the relative change in a net formation rate of a component i with a relative change in the rate coefficient of an elementary step is determined:

$$\chi_{RC,i} = \frac{\partial \ln(R_i)}{\partial \ln(k_i)} = \frac{k_i}{R}\left(\frac{\partial R_i}{\partial k_i}\right)_{k_{j\neq i},K_i} \qquad [2\text{-}53]$$

As no analytical rate expressions in terms of observable species are available, this partial derivative is determined by increasing both the forward and reverse rate coefficients of the elementary step i with one percent and numerically determine the effect of this change on the net formation rate R_i.

2.3 References

1. Froseth, V., S. Storsaeter, O. Borg, E.A. Blekkan, M. Ronning, and A. Holmen, *Steady state isotopic transient kinetic analysis (SSITKA) of CO hydrogenation on different Co catalysts.* Applied Catalysis A: General, 2005. **289**(1): p. 10-15.
2. Happel, J., *Transient tracing.* Chemical Engineering Science, 1978. **33**(11): p. 1567.
3. Bennett, C.O., *Understanding Heterogeneous Catalysis Through the Transient Method*, in *Catalysis Under Transient Conditions*, A.T. Bell and L.L. Hegedus, Editors. 1982, American Chemical Society: Washingon, DC. p. 1-32.
4. Biloen, P., *Transient kinetic methods.* Journal of Molecular Catalysis, 1983. **21**(1–3): p. 17-24.
5. Shannon, S.L. and J.G. Goodwin, *Characterization of Catalytic Surfaces by Isotopic-Transient Kinetics during Steady-State Reaction.* Chemical Reviews, 1995. **95**(3): p. 677-695.
6. van Dijk, H.A.J., *The Fischer-Tropsch synthesis: A mechanistic study using transient isotopic tracing*, TU Eindhoven, Department: Chemical Engineering and Chemistry, *PhD Thesis*, p. 174
7. Gao, J., X.H. Mo, and J.G. Goodwin, *Relationships between oxygenate and hydrocarbon formation during CO hydrogenation on Rh/SiO_2: Use of multiproduct SSITKA.* Journal of Catalysis, 2010. **275**(2): p. 211-217.
8. Balakos, M.W., S.S.C. Chuang, G. Srinivas, and M.A. Brundage, *Infrared Study of the Dynamics of Adsorbed Species during Co Hydrogenation.* Journal of Catalysis, 1995. **157**(1): p. 51-65.
9. Agnelli, M., H.M. Swaan, C. Marquez-Alvarez, G.A. Martin, and C. Mirodatos, *CO hydrogenation on a nickel catalyst - II. A mechanistic study by transient kinetics and infrared spectroscopy.* Journal of Catalysis, 1998. **175**(1): p. 117-128.
10. Schweicher, J., A. Bundhoo, and N. Kruse, *Hydrocarbon Chain Lengthening in Catalytic CO Hydrogenation: Evidence for a CO-Insertion Mechanism.* Journal of the American Chemical Society, 2012. **134**(39): p. 16135-16138.
11. Nibbelke, R.H., J. Scheerova, M.H.J.M. de Croon, and G.B. Marin, *The Oxidative Coupling of Methane over Mgo-Based Catalysts - a Steady-State Isotope Transient Kinetic-Analysis.* Journal of Catalysis, 1995. **156**(1): p. 106-119.
12. Zhang, X.H. and P. Biloen, *A Transient Kinetic Observation of Chain Growth in the Fischer-Tropsch Synthesis.* Journal of Catalysis, 1986. **98**(2): p. 468-476.
13. Yang, J., Y. Qi, J. Zhu, Y.A. Zhu, D. Chen, and A. Holmen, *Reaction mechanism of CO activation and methane formation on Co Fischer-Tropsch catalyst: A combined DFT, transient, and steady-state kinetic modeling.* Journal of Catalysis, 2013. **308**: p. 37-49.
14. den Breejen, J.P., P.B. Radstake, G.L. Bezemer, J.H. Bitter, V. Froseth, A. Holmen, and K.P. de Jong, *On the Origin of the Cobalt Particle Size Effects in Fischer-Tropsch Catalysis.* Journal of the American Chemical Society, 2009. **131**(20): p. 7197-7203.
15. Yang, J., V. Froseth, D. Chen, and A. Holmen, *Particle size effect for cobalt Fischer-Tropsch catalysts based on in situ CO chemisorption.* Surface Science, 2016. **648**: p. 67-73.
16. Thybaut, J.W. and G.B. Marin, *Single-Event MicroKinetics: Catalyst design for complex reaction networks.* Journal of Catalysis, 2013. **308**: p. 352-362.

17. Boudart, M. and G. Djéga-Mariadassou, *Kinetics of heterogeneous catalytic reactions*. 1984, New Jersey: Princeton University Press.
18. Lozano-Blanco, G., J.W. Thybaut, K. Surla, P. Galtier, and G.B. Marin, *Fischer-Tropsch synthesis: Development of a microkinetic model for metal catalysis.* Oil & Gas Science and Technology-Revue D Ifp Energies Nouvelles, 2006. **61**(4): p. 489-496.
19. Lozano-Blanco, G., J.W. Thybaut, K. Surla, P. Galtier, and G.B. Marin, *Single-event microkinetic model for Fischer-Tropsch synthesis on iron-based catalysts.* Industrial & Engineering Chemistry Research, 2008. **47**(16): p. 5879-5891.
20. *NIST Chemistry WebBook - NIST Standard Reference Database Number 69*. Available from: http://webbook.nist.gov/chemistry.
21. Cohen, N., *Thermochemistry of alkyl free-radicals.* Journal of Physical Chemistry, 1992. **96**(22): p. 9052-9058.
22. Cohen, N., *Revised group additivity values for enthalpies of formation (at 298 K) of carbon-hydrogen and carbon-hydrogen-oxygen compounds.* Journal of Physical and Chemical Reference Data, 1996. **25**(6): p. 1411-1481.
23. Dumesic, J.A., D.F. Rudd, L.M. Aparicio, J.E. Rekoske, and A.A. Treviño, *The microkinetics of heterogeneous catalysis.* ACS Professional Reference Book. 1993: American Chemical Society. 315.
24. Atkins, P. and J. De Paula, *Atkins' Physical Chemistry*. eighth ed. 2006, New York: Oxford University Press. 1100.
25. Shustorovich, E. and H. Sellers, *The UBI-QEP method: a practical theoretical approach to understanding chemistry on transition metal surfaces.* Surface Science Reports, 1998. **31**(1-3): p. 5-119.
26. Shustorovich, E. and A.V. Zeigarnik, *The UBI-QEP method: Basic formalism and applications to chemisorption phenomena on transition metal surfaces.* Russian Journal of Physical Chemistry, 2006. **80**(4): p. 665-666.
27. Zeigarnik, A.V. and E. Shustorovich, *The UBI-QEP method: Mechanistic and kinetic studies of heterogeneous catalytic reactions.* Russian Journal of Physical Chemistry B, 2007. **1**(4): p. 330-356.
28. Maestri, M., D. Livio, A. Beretta, and G. Groppi, *Hierarchical Refinement of Microkinetic Models: Assessment of the Role of the WGS and r-WGS Pathways in CH4 Partial Oxidation on Rh.* Industrial & Engineering Chemistry Research, 2014. **53**(27): p. 10914-10928.
29. Maestri, M., D.G. Vlachos, A. Beretta, G. Groppi, and E. Tronconi, *Steam and dry reforming of methane on Rh: Microkinetic analysis and hierarchy of kinetic models.* Journal of Catalysis, 2008. **259**(2): p. 211-222.
30. Maestri, M. and K. Reuter, *Molecular-level understanding of WGS and reverse WGS reactions on Rh through hierarchical multiscale approach.* Chemical Engineering Science, 2012. **74**: p. 296-299.
31. Sharma, H. and A. Mhadeshwar, *A detailed microkinetic model for diesel engine emissions oxidation on platinum based diesel oxidation catalysts (DOC).* Applied Catalysis B-Environmental, 2012. **127**: p. 190-204.
32. Maestri, M., D.G. Vlachos, A. Beretta, G. Groppi, and E. Rronconi, *A C-1 Microkinetic Model for Methane Conversion to Syngas on Rh/Al2O3.* Aiche Journal, 2009. **55**(4): p. 993-1008.

33. Karakaya, C., R. Otterstätter, L. Maier, and O. Deutschmann, *Kinetics of the water-gas shift reaction over Rh/Al2O3 catalysts.* Applied Catalysis A: General, 2014. **470**: p. 31-44.
34. Appari, S., V.M. Janardhanan, R. Bauri, S. Jayanti, and O. Deutschmann, *A detailed kinetic model for biogas steam reforming on Ni and catalyst deactivation due to sulfur poisoning.* Applied Catalysis A: General, 2014. **471**: p. 118-125.
35. Essmann, C., L. Maier, A.J. Li, S. Tischer, and O. Deutschmann, *Natural Gas Steam Reforming over Rhodium/Alumina Catalysts: Experimental and Numerical Study of the Carbon Deposition from Ethylene and Carbon Monoxide.* Industrial & Engineering Chemistry Research, 2014. **53**(31): p. 12270-12278.
36. Benziger, J.B., *Thermochemical methods for reaction energetics on metal surfaces.* ChemInform, 1992. **23**(41).
37. Ojeda, M., R. Nabar, A.U. Nilekar, A. Ishikawa, M. Mavrikakis, and E. Iglesia, *CO activation pathways and the mechanism of Fischer-Tropsch synthesis.* Journal of Catalysis, 2010. **272**(2): p. 287-297.
38. Liu, J.-X., H.-Y. Su, D.-P. Sun, B.-Y. Zhang, and W.-X. Li, *Crystallographic Dependence of CO Activation on Cobalt Catalysts: HCP versus FCC.* Journal of the American Chemical Society, 2013. **135**(44): p. 16284-16287.
39. Cheng, J., T. Song, P. Hu, C.M. Lok, P. Ellis, and S. French, *A density functional theory study of the a-olefin selectivity in Fischer-Tropsch synthesis.* Journal of Catalysis, 2008. **255**(1): p. 20-28.
40. Kresse, G., *Structure of Non-Crystalline Materials 6Ab initio molecular dynamics for liquid metals.* Journal of Non-Crystalline Solids, 1995. **192**: p. 222-229.
41. Kresse, G. and J. Furthmüller, *Efficiency of ab-initio total energy calculations for metals and semiconductors using a plane-wave basis set.* Computational Materials Science, 1996. **6**(1): p. 15-50.
42. Kresse, G. and J. Furthmüller, *Efficient iterative schemes for \textit{ab initio} total-energy calculations using a plane-wave basis set.* Physical Review B, 1996. **54**(16): p. 11169-11186.
43. Kresse, G. and J. Hafner, *\textit{Ab initio} molecular-dynamics simulation of the liquid-metal\char21{}amorphous-semiconductor transition in germanium.* Physical Review B, 1994. **49**(20): p. 14251-14269.
44. Blöchl, P.E., *Projector augmented-wave method.* Physical Review B, 1994. **50**(24): p. 17953-17979.
45. Kresse, G. and D. Joubert, *From ultrasoft pseudopotentials to the projector augmented-wave method.* Physical Review B, 1999. **59**(3): p. 1758-1775.
46. Monkhorst, H.J. and J.D. Pack, *Special points for Brillouin-zone integrations.* Physical Review B, 1976. **13**(12): p. 5188-5192.
47. Perdew, J.P., K. Burke, and M. Ernzerhof, *Generalized Gradient Approximation Made Simple.* Physical Review Letters, 1996. **77**(18): p. 3865-3868.
48. Klinke, D.J. and L.J. Broadbelt, *Construction of a mechanistic model of Fischer-Tropsch synthesis on Ni(111) and Co(0001) surfaces.* Chemical Engineering Science, 1999. **54**(15-16): p. 3379-3389.
49. Temkin, O.N., A.V. Zeigarnik, A.E. Kuz"min, L.G. Bruk, and E.V. Slivinskii, *Construction of the reaction networks for heterogeneous catalytic reactions: Fischer—Tropsch synthesis and related reactions.* Russian Chemical Bulletin, 2002. **51**(1): p. 1-36.

50. Lin, Y.-C., L.T. Fan, S. Shafie, B. Bertók, and F. Friedler, *Generation of light hydrocarbons through Fischer–Tropsch synthesis: Identification of potentially dominant catalytic pathways via the graph–theoretic method and energetic analysis.* Computers & Chemical Engineering, 2009. **33**(6): p. 1182-1186.
51. Ugi, I., J. Bauer, K. Bley, A. Dengler, A. Dietz, E. Fontain, B. Gruber, R. Herges, M. Knauer, K. Reitsam, and N. Stein, *Computer-Assisted Solution of Chemical Problems - The Historical Development and the present State of the Art of a New Discipline of Chemistry.* Angewandte Chemie-International Edition in English, 1993. **32**(2): p. 201-227.
52. Vynckier, E. and G.F. Froment, *Modeling of the kinetics of complex processes based upon elementary steps*, in *Kinetic and Thermodynamic Lumping of Multicomponent Mixtures*, G.A.I. Sandler, Editor. 1991, Elsevier: Amsterdam. p. 131-161.
53. Clymans, P.J. and G.F. Froment, *Computer-generation of reaction paths and rate-equations in the thermal-cracking of normal and branched paraffins.* Computers & Chemical Engineering, 1984. **8**(2): p. 137-142.
54. Cochegrue, H., P. Gauthier, J.J. Verstraete, K. Surla, D. Guillaume, P. Galtier, and J. Barbier, *Reduction of Single Event Kinetic Models by Rigorous Relumping: Application to Catalytic Reforming.* Oil & Gas Science and Technology-Revue D Ifp Energies Nouvelles, 2011. **66**(3): p. 367-397.
55. Berger, R.J., E.H. Stitt, G. Marin, F. Kapteijn, and J. Moulijn, *Eurokin. Chemical Reaction Kinetics in Practice.* CATTECH, 2001. **5**(1): p. 36-60.
56. van Dijk, H.A.J., J.H.B.J. Hoebink, and J.C. Schouten, *A mechanistic study of the Fischer-Tropsch synthesis using transient isotopic tracing. Part-1: Model identification and discrimination.* Topics in Catalysis, 2003. **26**(1-4): p. 111-119.
57. Govender, N.S., F.G. Botes, M.H.J.M. de Croon, and J.C. Schouten, *Mechanistic pathway for methane formation over an iron-based catalyst.* Journal of Catalysis, 2008. **260**(2): p. 254-261.
58. Brown, P.N., A.C. Hindmarsh, and L.R. Petzold, *Using krylov methods in the solution of large-scale differential-algebraic systems.* Siam Journal on Scientific Computing, 1994. **15**(6): p. 1467-1488.
59. Hindmarsh, A.C., *ODEPACK, A Systematized Collection of ODE Solvers.* IMACS Transactions on Scientific Computation, 1983. **1**: p. 55-64.
60. Rosenbrock, H.H., *An automatic method for finding the greatest or least value of a function.* Computer Journal, 1960. **3**(3): p. 175-184.
61. Marquardt, D.W., *An algorithm for least-squares estimation of nonlinear parameters.* Journal of the Society for Industrial and Applied Mathematics, 1963. **11**(2): p. 431-441.
62. Boggs, P.T., J.R. Donaldson, R.h. Byrd, and R.B. Schnabel, *Algorithm 676: ODRPACK: software for weighted orthogonal distance regression.* ACM Trans. Math. Softw., 1989. **15**(4): p. 348-364.
63. Toch, K., J.W. Thybaut, and G.B. Marin, *A Systematic Methodology for Kinetic Modeling of Chemical Reactions Applied to n-Hexane Hydroisomerization.* Aiche Journal, 2015. **61**(3): p. 880-892.
64. Campbell, C.T., *Finding the Rate-Determining Step in a Mechanism: Comparing DeDonder Relations with the “Degree of Rate Control”.* Journal of Catalysis, 2001. **204**(2): p. 520-524.

65. Stegelmann, C., A. Andreasen, and C.T. Campbell, *Degree of Rate Control: How Much the Energies of Intermediates and Transition States Control Rates.* Journal of the American Chemical Society, 2009. **131**(23): p. 8077-8082.

Chapter 3 A Single-Event MicroKinetic Model for the Cobalt Catalyzed Fischer-Tropsch Synthesis*

The Single-Event MicroKinetic (SEMK) methodology has been successfully extended from Fe to Co catalyzed Fischer-Tropsch Synthesis (FTS) by regression to experimental data. A total of 82 experiments were performed in a plug flow reactor with a H_2 to CO molar inlet ratio between 3 and 10, a temperature range from 483 – 503 K, CO inlet partial pressures from 3.7 to 16.7 kPa and space times, i.e., $W/F_{CO,0}$, varying between 7.2 and 36.3 $(kg_{cat}\ s)\ mol_{CO}^{-1}$. Via regression, statistically significant and physicochemically meaningful estimates were obtained for the activation energies in the model and the H, C and O atomic chemisorption enthalpies as required for the UBI-QEP method. A reaction path analysis allowed relating the observed deviations from the Anderson-Schulz-Flory distribution, i.e., a high methane and low ethene selectivity, to the symmetry numbers involved and a higher chemisorption enthalpy of the metal methyl species compared to the other metal alkyl species. Simulations at industrially relevant conditions show that, as a catalyst descriptor, the H atomic chemisorption enthalpy crucially determines both the CO conversion and the C_{5+} selectivity. The higher FTS activity of Co compared to Fe is explained via the higher oxygen atomic chemisorption enthalpy on the latter compared to the former.

---

*A modified version of this Chapter has been published in Applied Catalysis A: General: Van Belleghem, J., et al., A Single-Event MicroKinetic model for the cobalt catalyzed Fischer-Tropsch Synthesis. Applied Catalysis A: General, 2016. **524**: p. 149-162.

3.1 Introduction

Microkinetic simulations of Fischer-Tropsch Synthesis (FTS) are of key importance to acquire fundamental insight that can be exploited for process design, optimization and simulation [1] as well as for rational catalyst development [2-5]. Certainly when considering the scale of the industrial application, an improved design, even if it only leads to a minor enhancement of the desired product selectivity, can have a major impact on the process economics. A microkinetic model may assist in unraveling the complex reaction chemistry by quantifying the observed experimental trends in terms of adsorption enthalpies and activation energies and the resulting surface coverages of the various species involved [2-4].

The detailed FTS mechanism is still a matter of debate [6-10]. There is a general consensus that the reaction proceeds through a polymerization-like scheme where the monomeric building block is formed on the catalyst surface and is inserted in a growing chain [10]. Nevertheless, considering FTS as a pure polymerization reaction would be an oversimplification as this would result in a product distribution characterized by a single chain growth probability, while distinct deviations in the product spectrum have been systematically observed [6], i.e., a high methane selectivity, a low ethene selectivity and an alkene to alkane ratio decreasing with increasing carbon number.

This has led to the development of various microkinetic models for Co catalyzed FTS [5, 11-21]. Klinke et al [11] developed a microkinetic model based on direct CO dissociation and chain growth by inserting CH_x species. A bond additivity model was employed to determine chemisorption enthalpies and reduce the number of adjustable model parameters [11]. Storsaeter et al. [12] developed a microkinetic model for the reactant conversion and C_1 and C_2 selectivity by considering both CO and CH_x insertion steps. The UBI-QEP [22-24] method was applied for the calculation of chemisorption enthalpies and activation energies [12]. The CO dissociation has been assessed by Visconti et al [13, 14] in two consecutive papers and these authors showed that CO dissociation is, most probably, H assisted [14]. In both models, chain growth was considered to proceed via CH_2 insertion in metal alkyl species. Azadi et al [5] developed a detailed microkinetic model based on similar considerations for the reaction mechanism as Visconti et al [14]. The aspect of a decreasing alkene to alkane ratio with the carbon number has been specifically addressed by Todic et al [17, 18] in two consecutive papers and by Bhatelia et al

[19]. In these three papers the alkene desorption energy was considered to be chain length dependent, based on the idea of Botes [25].

FTS has also been extensively studied via first principle calculations [7, 8, 26, 27]. As such, the physical significance of the estimates for the adjustable model parameters can be assessed by comparing them with the corresponding activation barriers and chemisorption enthalpies calculated from first principles. Furthermore, as illustrated in this chapter, ab initio calculated trends in chemisorption enthalpies can help in the model construction, see also Section 3.3.1.

In this chapter, a Single-Event MicroKinetic (SEMK) model constructed for Fe catalyzed FTS is extended to Co catalyzed FTS. The SEMK methodology is ideally suited to describe the conversion of complex reaction mixtures [2, 28-31]. All the elementary reaction steps are grouped into a limited set of reaction families for which a single-event rate coefficient is considered. The differences in rate coefficients within the same reaction family are a priori accounted for by the symmetry numbers of the reactants and corresponding transition state. For an Fe catalyst the inclusion of the symmetry numbers was sufficient to explain the typical deviations from the Anderson-Schulz-Flory (ASF) distribution [30]. All the elementary steps are considered to be reversible and the rate of every elementary step is accounted for. Thermodynamic consistency is explicitly implemented by considering a Born-Haber cycle for each elementary step. As in the model of Storsaeter et al [12], the UBI-QEP [22-24] method is applied to calculate the adsorption enthalpies of the various surface species. An extensive experimental data set comprising 82 experiments was used for the model regression. The data was measured at low reactant partial pressures to avoid wax phase formation in the reactor or in the catalyst pellet. Therefore, the measured yields of the products are not influenced by secondary effects such as a chain length dependent diffusivities [32, 33].

3.2 Procedures

3.2.1 Experimental data

The experimental dataset was acquired on the Co/CNT catalyst described in section 2.1.3 employing the SSITKA set-up explained in section 2.1.1. A CO inlet partial pressure ranging from 3.7 to 16.7 kPa was used with H_2 to CO molar inlet ratios between 3 and 10 mol mol^{-1} in a temperature range from 483 to 503 K. In total 82 experiments were acquired out of which 66 were measured at different reaction conditions.

3.2.2 Modeling procedures

3.2.2.1 Reactor model

As explained in section 2.2.4, the reactor can be considered as an ideal plug flow reactor and, hence, a set of differential algebraic equations (DAEs), eq. [2–27] to eq. [2–28], is employed to determine the molar flow rates along the axial direction of the catalyst bed. The DASPK solver [34] has been used to solve this set of DAEs. When DASPK is used, an initial guess for the surface species concentrations at the reactor entrance, from which the solution of the subset of AEs starts, has to be supplied. This may not be straightforward for a set of DAEs, particularly when the AEs involved are nonlinear. Despite the options provided by DASPK to obtain a consistent set of initial guesses, convergence was rarely obtained. Another strategy was, hence, developed to acquire such a consistent set of initial estimates, i.e., a time dependent mass balance for the surface species is solved at the initial conditions corresponding with the reactor entrance, eq. [3-1].

$$\frac{dL_j(t)}{dt} = R_j \qquad [3\text{-}1]$$

Where L_j is the surface concentration of surface species j $[mol\ kg_{cat}^{-1}]$, t is time $[s]$ and R_j the net production rate of surface species j $[mol\ (kg_{cat}\ s)^{-1}]$

Eq. [3-1] is integrated as a function of time until the surface species concentrations are a solution of the set of AEs at the reactor entrance. The surface species concentrations are subsequently provided to DASPK. In this way, a stable integration procedure was obtained.

3.2.2.2 Regression analysis

The adjustable model parameters, i.e., the activation energies of the forward reactions and the atomic chemisorption enthalpies, see also section 2.2.1.4, are estimated by an iteratively reweighted least squares (IRLS) optimization, see section 2.2.6. The outlet molar flow rates of C_1 to C_6 n-alkanes and C_2 to C_5 1-alkenes were used as responses in eq. [2–45].

3.2.2.3 The Single-Event Microkinetic (SEMK) model for FTS

Reaction mechanism

The elementary steps considered in the reaction network together with the number of metal sites to which a surface species binds have been adopted from the originally developed SEMK model for Fe catalyzed FTS [30, 35] without any adjustments and are summarized in Table 3-1. CO is assumed to chemisorb molecularly on the surface while dissociative H_2 chemisorption is assumed. The reaction is initiated by CO dissociation to surface C and O. The C on the surface is hydrogenated in consecutive steps to CH, CH_2 and CH_3. The chain growth is considered to occur by CH_2 insertion in metal alkyl species. Hydrogenation of a metal alkyl species leads to alkanes. Alkenes are produced via a beta hydride elimination step of the same metal alkyl species and subsequent desorption. H_2O formation is taken into account by two consecutive hydrogenations of the O species on the surface. The reaction network corresponding to these reactions is generated using ReNGeP [35]. The number of metal sites occupied by a surface species was determined by assuming that the preferred binding site on the metal surface for, e.g., CH_x-species is such that the carbon atom has 4 σ-bonds [35, 36].

The CO activation mechanism and the nature of the propagating species are strongly debated in the literature for FTS and particularly for the Co catalyzed variant. Certainly with respect to CO activation, considerable efforts have been undertaken to elucidate the mechanism and explain the observed structure sensitivity of the FTS reaction [26, 27, 37-46]. In principle, two mechanisms are considered, i.e., direct CO dissociation and H assisted CO dissociation. Ab initio calculations have pointed out that, on close packed surfaces, CO activation is most likely H assisted and that close packed Co(0001) surfaces are not capable to dissociate CO directly [43, 45, 47-49]. In contrast, direct CO dissociation was found to proceed with lower activation energies than hydrogen assisted CO dissociation on corrugated surfaces [40, 41]. Surface science studies, furthermore, confirm that under-coordinated sites are active for direct CO dissociation [37, 50-52]. With respect to the structure sensitivity of the FTS reaction, ab initio calculated activation energies for both the direct or the H assisted CO dissociation depend on the type of active site. Besides, the structure sensitivity is also attributed to the ability to dissociate hydrogen [38, 53]. Visconti et al [13, 14] compared both CO dissociation mechanisms via microkinetic model regression and found that the model based on the H assisted CO dissociation performed best [14].

It should be noted that other modifications, such as the description of the reactant adsorption, may also have contributed to the improved model performance. A general consensus with respect to the CO activation mechanism has, hence, not been reached and it is possible that, depending on the operating conditions used, both reaction pathways contribute to the CO dissociation to a higher or lesser extent. A direct observation of the surface species is lacking and changes in reaction conditions can initiate changes in the surface structure which, in turn, affect the local reactivity of the surface [54]. The use of direct CO dissociation as a possible CO activation step is, hence, a viable option [3, 8, 11, 16, 20, 55-57]. With respect to the chain growth step, it is noted that several microkinetic models have already adopted the carbene mechanism considering CH_2 as the propagating species on Co [5, 13, 14, 16, 17, 20]. It is, furthermore, noted that the inclusion of parallel reaction paths for, e.g., the CO dissociation, would increase the number of adjustable model parameters considerably. These will be mathematically correlated and compensate for each other such that they would make the regression of the SEMK model to the experimental data difficult. By considering the same elementary steps on Co and Fe catalysts, a more straightforward comparison can be made, see section 3.8, which can provide useful information for the incorporation of additional elementary steps in the FTS reaction network in a later stage, e.g., based on an ab initio assessment of the various elementary steps and reaction pathways.

Table 3-1: Elementary reactions and reaction families considered in the reaction network [35].

Elementary reactions	
	Reactant adsorption
$r_{H_2 chem,des}$	$H_{2,(g)} + 2* \leftrightarrows 2H^*$
$r_{CO\ chem,des}$	$CO_{(g)} + 2* \leftrightarrows CO^{**}$
	Initiation reactions
$r_{CO\ diss,ass}$	$CO^{**} + 3* \rightleftarrows C^{***} + O^{**}$
$r_{C\ hyd,dehyd}$	$C^{***} + H^* \rightleftarrows CH^{***} + *$
$r_{CH\ hyd,dehyd}$	$CH^{***} + H^* \rightleftarrows CH_2^{**} + 2*$
$r_{CH_2\ hyd,dehyd}$	$CH_2^{**} + H^* \rightleftarrows CH_3^* + 2*$
	Water formation
$r_{O\ hyd,dehyd}$	$O^{**} + H^* \rightleftarrows OH^* + 2*$
$r_{OH\ hyd,dehyd}$	$OH^* + H^* \rightleftarrows H_2O_{(g)} + 2*$
Reaction families	
Chain growth	
$r_{C_nH_{2n+1}\ mi,md}$	$C_nH_{2n+1}^* + CH_2^{**} \rightleftarrows C_{n+1}H_{2n+3}^* + 2*$
Alkanes formation	
$r_{C_nH_{2n+1}\ hyd,dehyd}$	$C_nH_{2n+1}^* + H^* \rightleftarrows C_nH_{2n+2,(g)} + 2*$
Metal alkenes formations	
$r_{C_nH_{2n+1}\ be,ba}$	$C_nH_{2n+1}^* + * \rightleftarrows C_nH_{2n}^* + H^*$
Alkenes desorption	
$r_{C_nH_{2n}\ des,chem}$	$C_nH_{2n}^* \rightleftarrows C_nH_{2n,(g)} + *$

Rate expressions

In this microkinetic model none of the elementary reactions is considered to be quasi-equilibrated, i.e., the rate of every elementary step is accounted for. The rate expressions for all the elementary reactions are listed in Table 3-2. It was assumed that the Co surface is a Co(0001) surface. As such, the number of nearest neighbors, z, was set equal to 6. These expressions are obtained by applying the law of mass action and the mean field approximation. Particularly the probability of two surface species being adjacent to each other is accounted for, see section 2.2.1.2. The net production rates of the various gas phase components and surface species as required by eq. [2–27] and eq. [2–28] are obtained from the rates of the elementary reactions as explained by eq. [2–15] and are provided in Table 3-3. A site balance is used to find the free site concentration:

$$
\begin{aligned}
L_{tot} = {} & L_{H^*} + 2L_{CO^{**}} + 3L_{C^{***}} + 3L_{CH^{***}} + 2L_{CH_2^{**}} + \sum_{i=1}^{10} L_{C_iH_{2i+1}^*} + \sum_{i=2}^{10} L_{C_iH_{2i}^*} \\
& + 2L_{O^{**}} + L_{OH^*}
\end{aligned}
\qquad [3\text{-}2]
$$

To the forward rate coefficients, the single-event methodology [2] is applied, see section 2.2.1.1. The reverse rate coefficient is obtained by applying the principle of microscopic reversibility at the elementary step level. Chemisorption enthalpies for the various surface species are calculated via the UBI-QEP method [22-24], see section 2.2.1.4, which is widely used in fundamental microkinetic modeling studies [58-65]. This method relates the chemisorption enthalpy of a species to the atomic chemisorption enthalpies of H, C and O. These atomic chemisorption enthalpies are three additional adjustable model parameters. Chemisorption entropies of the various surface species are obtained via the Sackur-Tetrode equation [66] and considerations about the number of degrees of freedom being lost or gained, see also section 2.2.1.3.

Table 3-2: Rate expression for the elementary steps considered in the reaction network.

Reaction		**Rate expression**
Elementary reaction		
Reactant adsorption		
$r_{H_2\ chem,des}$	$H_{2,(g)} + 2\,* \leftrightarrows 2H^*$	$r_{H_2\ chem,des} = \frac{z}{2}\frac{\sigma_r}{\sigma_\ddagger}\tilde{k}_{H_2\ chem}p_{H_2}\frac{L_*^2}{L_{tot}} - \frac{z}{2}\frac{\sigma_r}{\sigma_\ddagger}\tilde{k}_{H_2\ des}\frac{L_{H^*}^2}{L_{tot}}$
$r_{CO\ chem,des}$	$CO_{(g)} + 2\,* \leftrightarrows CO^{**}$	$r_{CO\ chem,des} = \frac{z}{2}\frac{\sigma_r}{\sigma_\ddagger}\tilde{k}_{CO\ chem}p_{CO}\frac{L_*^2}{L_{tot}} - \frac{\sigma_r}{\sigma_\ddagger}\tilde{k}_{CO\ des}L_{CO^{**}}$
Initiation reactions		
$r_{CO\ diss,ass}$	$CO^{**} + 3\,* \rightleftarrows C^{***} + O^{**}$	$r_{CO\ diss,ass} = \left(\frac{z}{2}\right)^3\frac{\sigma_r}{\sigma_\ddagger}\tilde{k}_{CO\ diss}L_{CO^{**}}\left(\frac{L_*}{L_{tot}}\right)^3 - \frac{z}{2}\frac{\sigma_r}{\sigma_\ddagger}\tilde{k}_{CO\ ass}L_{C^{***}}\frac{L_{O^{**}}}{L_{tot}}$
$r_{C\ hyd,dehyd}$	$C^{***} + H^* \rightleftarrows CH^{***} + *$	$r_{C\ hyd,dehyd} = \frac{z}{2}\frac{\sigma_r}{\sigma_\ddagger}\tilde{k}_{Cre}L_{C^{***}}\frac{L_{H*}}{L_{tot}} - \frac{z}{2}\frac{\sigma_r}{\sigma_\ddagger}\tilde{k}_{CHoa}L_{CH^{***}}\frac{L_*}{L_{tot}}$
$r_{CH\ hyd,dehyd}$	$CH^{***} + H^* \rightleftarrows CH_2^{**} + 2\,*$	$r_{CH\ hyd,dehyd} = \frac{z}{2}\frac{\sigma_r}{\sigma_\ddagger}\tilde{k}_{CHre}L_{CH^{***}}\frac{L_{H^*}}{L_{tot}} - \left(\frac{z}{2}\right)^2\frac{\sigma_r}{\sigma_\ddagger}\tilde{k}_{CH_2oa}L_{CH_2^{**}}\left(\frac{L_*}{L_{tot}}\right)^2$
$r_{CH_2\ hyd,dehyd}$	$CH_2^{**} + H^* \rightleftarrows CH_3^* + 2\,*$	$r_{CH_2\ hyd,dehyd} = \frac{z}{2}\frac{\sigma_r}{\sigma_\ddagger}\tilde{k}_{CH_2re}L_{CH_2^{**}}\frac{L_{H*}}{L_{tot}} - \left(\frac{z}{2}\right)^2\frac{\sigma_r}{\sigma_\ddagger}\tilde{k}_{CH_3oa}L_{CH_3^*}\left(\frac{L_*}{L_{tot}}\right)^2$
Water formation		
$r_{O\ hyd,dehyd}$	$O^{**} + H^* \rightleftarrows OH^* + 2\,*$	$r_{O\ hyd,dehyd} = \frac{z}{2}\frac{\sigma_r}{\sigma_\ddagger}\tilde{k}_{O\ re}L_{O^{**}}\frac{L_{H*}}{L_{tot}} - \left(\frac{z}{2}\right)^2\frac{\sigma_r}{\sigma_\ddagger}\tilde{k}_{OH\ oa}L_{OH^*}\left(\frac{L_*}{L_{tot}}\right)^2$
$r_{OH\ hyd,dehyd}$	$OH^* + H^* \rightleftarrows H_2O_{(g)} + 2\,*$	$r_{OH\ hyd,dehyd} = \frac{z}{2}\frac{\sigma_r}{\sigma_\ddagger}\tilde{k}_{OH\ re}L_{OH^*}\frac{L_{H*}}{L_{tot}} - \frac{z}{2}\frac{\sigma_r}{\sigma_\ddagger}\tilde{k}_{H_2O\ oa}p_{H_2O}\left(\frac{L_*^2}{L_{tot}}\right)$

Table 3–2: continued

Reaction		Rate expression
Reaction family		
Chain growth		
$r_{C_nH_{2n+1}\,mi,md}$	$C_nH^*_{2n+1} + CH_2^{**} \rightleftarrows C_{n+1}H^*_{2n+3} +**$	$r_{C_nH_{2n+1}mi,md} = \frac{z}{2}\frac{\sigma_r}{\sigma_\ddagger}\tilde{k}_{mi}L_{CH_2^{**}}\frac{L_{C_nH^*_{2n+1}}}{L_{tot}} - \left(\frac{z}{2}\right)^2\frac{\sigma_r}{\sigma_\ddagger}\tilde{k}_{md}L_{C_{n+1}H^*_{2n+3}}\left(\frac{L_*}{L_{tot}}\right)^2$
Alkanes formation		
$r_{C_nH_{2n+1}\,hyd,dehyd}$	$C_nH^*_{2n+1} + H^* \rightleftarrows C_nH_{2n+2,(g)} + 2\,*$	$r_{C_nH_{2n+1}\,hyd,dehyd} = \frac{z}{2}\frac{\sigma_r}{\sigma_\ddagger}\tilde{k}_{C_nH_{2n+1}\,re}L_{H^*}\frac{L_{C_nH^*_{2n+1}}}{L_{tot}} - \frac{z}{2}\frac{\sigma_r}{\sigma_\ddagger}\tilde{k}_{C_nH_{2n+2}\,oa}p_{C_nH_{2n+2}}\frac{L_*^2}{L_{tot}}$
Metal alkenes formations		
$r_{C_nH_{2n+1}\,be,ba}$	$C_nH^*_{2n+1} +* \rightleftarrows C_nH^*_{2n} + H^*$	$r_{C_nH_{2n+1}\,be,ba} = \frac{z}{2}\frac{\sigma_r}{\sigma_\ddagger}\tilde{k}_{C_nH_{2n+1}\,be}L_{C_nH^*_{2n+1}}\frac{L_*}{L_{tot}} - \frac{z}{2}\frac{\sigma_r}{\sigma_\ddagger}\tilde{k}_{C_nH_{2n}\,ba}L_{C_nH^*_{2n}}\frac{L_{H^*}}{L_{tot}}$
Alkenes desorption		
$r_{C_nH_{2n}\,des,chem}$	$C_nH^*_{2n} \rightleftarrows C_nH_{2n,(g)} +*$	$r_{C_nH_{2n}\,des,chem} = \frac{\sigma_r}{\sigma_\ddagger}\tilde{k}_{C_nH_{2n}\,des}L_{C_nH^*_{2n+1}} - \frac{\sigma_r}{\sigma_\ddagger}\tilde{k}_{C_nH_{2n}\,chem}p_{C_nH_{2n}}L_*$

Table 3-3: The net rate of formation of the various gas phase components and surface species.

Species	**Net rate of formation [mol (kg_{cat} s)$^{-1}$]**
	Gas phase components
H_2	$R_{H_2} = -r_{H_2\ chem,des}$
CO	$R_{CO} = -r_{CO\ chem,des}$
C_nH_{2n+2}	$R_{C_nH_{2n+2}} = r_{C_nH_{2n+1}\ hyd,dehyd}$
C_nH_{2n}	$R_{C_nH_{2n}} = r_{C_nH_n des,chem}$
H_2O	$R_{H_2O} = r_{OH\ hyd,dehyd}$
	Surface species
H^*	$R_{H^*} = 2r_{H_2\ chem,des} - r_{C\ hyd,dehyd} - r_{CH\ hyd,dehyd} - r_{CH_2\ hyd,dehyd} - \sum_{i=1}^{CN} r_{C_iH_{2i+1}\ hyd,dehyd} + \sum_{i=2}^{CN} r_{C_iH_{2i+1}\ be,ba} - r_{O\ hyd,dehyd} - r_{OH\ hyd,dehyd}$
CO^{**}	$R_{CO^{**}} = r_{CO\ chem,des} - r_{CO\ diss,ass}$
C^{***}	$R_{C^{***}} = r_{CO\ diss,ass} - r_{C\ re,oa}$
CH^{***}	$R_{CH^{***}} = r_{C\ hyd,dehyd} - r_{CH\ hyd,dehyd}$
CH_2^{**}	$R_{CH_2^{**}} = r_{CH\ hyd,dehyd} - r_{CH_2\ hyd,dehyd}$
CH_3^*	$R_{CH_3^*} = r_{CH_2\ hyd,dehyd} - r_{CH_3\ hyd,dehyd} - r_{CH_3\ mi,md}$
$C_nH_{2n+1}^*$	$R_{C_nH_{2n+1}^*} = r_{C_{n-1}H_{2n-1}\ mi,md} - r_{C_nH_{2n+1}\ mi,md} - r_{C_nH_{2n+1}\ hyd,dehyd} - r_{C_nH_{2n+1}\ be,ba} \quad (n > 1)$
$C_nH_{2n}^*$	$R_{C_nH_{2n}^*} = r_{C_nH_{2n+1}\ be,ba} - r_{C_nH_{2n}\ des,chem} \quad (n > 1)$
O^{**}	$R_{O^{**}} = r_{CO\ diss,ass} - r_{O\ hyd,dehyd}$
OH^*	$R_{OH^*} = r_{O\ hyd,dehyd} - r_{OH\ hyd,dehyd}$

3.3 Results and discussion

3.3.1 Experimental data

The temperature effect on the CO conversion is presented in Figure 3-1. With increasing temperature from 483 K to 503 K the CO conversion increases strongly, e.g., at a space time of 20 (kg_{cat} s) mol^{-1} the CO conversion increases from 4% at 483 K to 15% at 503K. The corresponding apparent activation energy amounts to 115 kJ mol^{-1} which is at the higher end of the range of apparent activation energies reported in the FTS literature, i.e., from 80 to 120 kJ mol^{-1} [67]. The temperature effect on the product selectivity is depicted in Figure 3-2 at 6% CO conversion. A temperature increase results in an enhanced methane selectivity and a correspondingly lower selectivity to the other reaction products. This is in agreement with other experimental studies on the product selectivity for Co catalysts [14, 17]. It indicates that the hydrogenation of the metal methyl species is more strongly activated than methylene insertion. Furthermore, a decrease in chain growth probability, calculated from C_3 onwards, was observed with increasing temperature, see Section 5.3.1, indicating that also the activation energy for the hydrogenation of the heavier alkyl species is higher than the activation energy for methylene insertion.

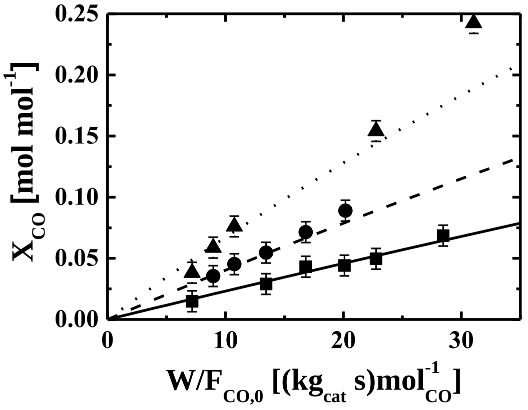

Figure 3-1: CO conversion, X_{CO}, as a function of space time, $W/F_{CO,0}$, at a H_2/CO molar inlet ratio of 10, a CO inlet partial pressure of 5.5 kPa, a total pressure of 185 kPa and different temperatures: ■, full line: 483K; ●, dashed line: 493 K; ▲, dotted line: 503K. The symbols correspond to the experimental observations, the lines correspond to the model simulations obtained by integrating eq. [2–27] and eq. [2–28] in which the net production rates are calculated as explained by eq. [2–15] and using the set of parameters of Table 3-4.

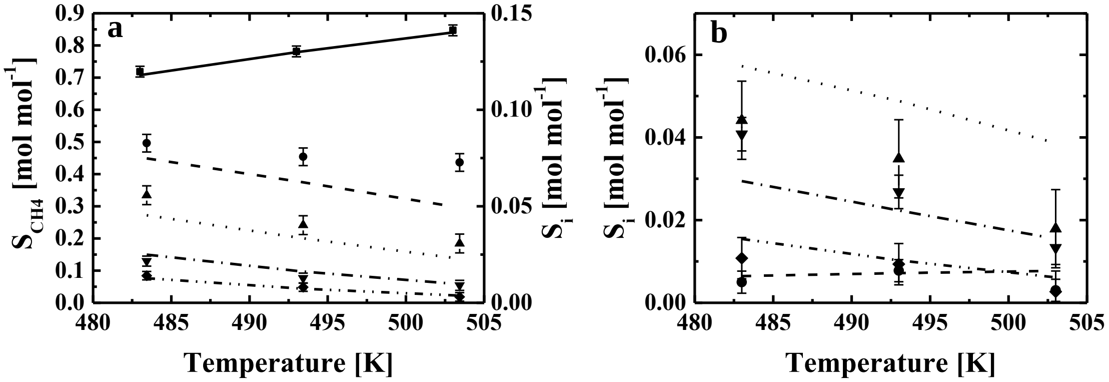

Figure 3-2: Selectivity, S_i, toward the different observed *n*-alkanes (a) and 1-alkenes (b) as a function of the temperature at H_2/CO molar inlet ratio of 10, a CO inlet partial pressure of 5.5 kPa and a total pressure of 185 kPa at 6 % CO conversion. The symbols correspond to the experimental observations, the lines to the model simulations obtained by integrating eq. [2-27] and eq. [2–28] in which the net production rates are calculated as explained by eq. [2–15] and using the set of parameters of Table 3-4. ■, full line: C_1; ●, dashed line: C_2; ▲, dotted line: C_3; ▼, dash dotted line: C_4; ♦ , dash dot dotted line: C_5.

The effect of the H_2 to CO molar inlet ratio on the conversion is presented in Figure 3-3. An increasing H_2 to CO molar inlet ratio increases the CO conversion as has been found by other experimental studies [15]. Within the investigated range of operating conditions, there is no pronounced effect of the H_2 to CO molar inlet ratio on the alkanes and alkenes selectivities at isoconversion. In principle, an increase in methane selectivity would be expected as an increased hydrogen surface coverage would increase the hydrogenation rate of the metal methyl species which would be accompanied by a decreased selectivity to the heavier reaction products. The hydrogen coverage will, however, also impact on the CH_2 surface coverage and, as a such, the change in hydrogen coverage on the hydrogenation rate of the metal methyl can be counteracted by the change in CH_2 surface coverage, see section 3.3.4.

The alkenes to alkanes ratio in the experimental data can be deduced from Figure 3-2. It is clear that the ethene selectivity is much lower compared to the ethane selectivity as typically observed in FTS. The ratio of alkenes to alkanes as a function of the carbon number exhibits a maximum at C_4 at the experimental conditions corresponding with Figure 3-2. Typically a maximum in the alkenes to alkanes ratio is observed already at C_3 [17, 18, 68]. This discrepancy can most probably be attributed to the high H_2/CO molar inlet ratio, amounting to 10, used in the present experimentation. A less pronounced maximum in alkenes to alkanes ratio at C_3 was also observed by van Dijk et al [69] at a H_2/CO molar inlet ratio of 5 compared to a clear maximum in the alkenes to alkanes ratio at C_3 at a H_2/CO molar inlet ratio of 1. Higher H_2/CO molar inlet ratios can, hence, be expected to enhance this effect. The exact position and the manifestation of the maximum, hence, depends on the operating conditions.

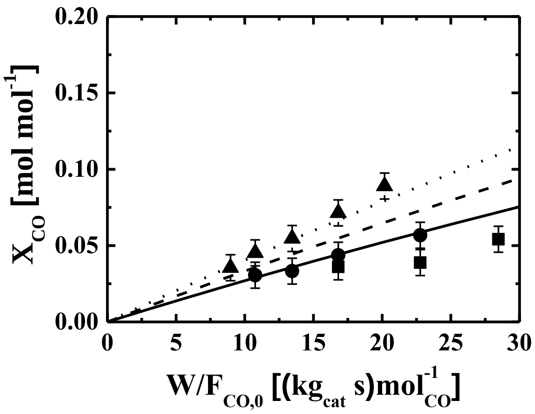

Figure 3-3: CO conversion, X_{CO}, as function of space time, $W/F_{CO,0}$, at a temperature of 493 K, a CO inlet partial pressure of 5.5 kPa, a total pressure of 185 kPa and different H_2/CO molar inlet ratios: ■, full line: 5 ●, dashed line: 7; ▲ and dotted line: 10. The symbols correspond to the experimental observations, the lines correspond to the model simulations obtained by integrating eq. [2–27] and eq. [2–28] in which the net production rates are calculated as explained by eq. [2–15] and using the set of parameters of Table 3-4.

3.3.2 Regression results

In total, 12 adjustable model parameters were identified and had to be estimated by model regression to the experimental data. This set of 12 parameters comprises 9 activation energies, as indicated in Table 3-4, complemented by the three atomic chemisorption enthalpies of hydrogen, Q_H, carbon, Q_C, and oxygen, Q_O. The resulting parameter estimates along with their 95% confidence interval are listed in Table 3-4 in bold font. The single-event pre-exponential factors and single-event reaction entropies, a priori determined via statistical thermodynamic considerations, see also section 2.2.1.3, of all the elementary steps are also included in Table 3-4 in plain font. The reaction enthalpies calculated from the three atomic chemisorption enthalpies via the UBI-QEP method, see also section 2.2.1.4, are provided in Table 3-4 in italic font.

All the parameters are estimated significantly different from zero as none of the 95% confidence intervals includes zero. The lowest t value, see eq. [2–48], equals 23.0. Furthermore, the estimates are in line with the general, physicochemical constraints such as positive activation energies. The F value for the global significance of the regression, see eq. [2–47], amounts to 1025 which considerably exceeds the tabulated one, i.e., 2.8. Equivalently, an R^2 value of 0.92 was obtained. No strong correlation was observed between the estimated parameters, i.e., all the binary correlation coefficients, see eq. [2–49] were found to be in the range from -0.45 to 0.73. The full binary correlation matrix is provided in Table 3-5.

The parity diagrams for the alkanes and alkenes outlet molar flow rates are presented in Figure 3-4. Residual figures for CO conversion and alkanes and alkenes outlet molar flow rates are presented in Figure 3-5 as a function of the inlet CO partial pressure, H_2 to CO molar inlet ratio and temperature. No trends are observed in the residual plots as a function of the experimental settings. The model performance is also indicated in Figure 3-1 to Figure 3-3, from which it is clear that the model is capable to accurately describe the conversion and product selectivities.

Table 3-4: Forward single-event pre-exponential factors, $\tilde{A}^{f}$, activation energies, E_a^{f}, atomic chemisorption enthalpies of hydrogen, Q_H, carbon, Q_C, and oxygen, Q_O, surface reaction enthalpies, ΔH_r^0, and single-event surface reaction entropies, $\Delta\tilde{S}_r^0$ *a*t 493 K. The values in plain font are determined a priori from open source data bases and statistical thermodynamic considerations, see section 2.2.1.3. The values indicated in bold font are estimated by non-linear regression of the model to the experimental data in which the responses are simulated by integrating eq. [2–27] and eq. [2–28] in which the net production rates are calculated as explained by eq. [2-15]. The values in italic font are derived from the ones obtained from the non-linear regression, see section 2.2.1.4.

Reaction	**$\tilde{A}^{f}$ [s^{-1} or (Mpa s)$^{-1}$]**	**E_a^{f} [kJ mol^{-1}]**	**ΔH_r^0 [kJ mol^{-1}]**	**$\Delta\tilde{S}_r^0$ [J (K mol)$^{-1}$]**
Elementary reaction				
Reactant adsorption				
$H_{2,(g)} + 2 * \leftrightarrows 2H^*$	3.6 10^{9}	0.0	*-63.6*	-60.0
$CO_{(g)} + 2 * \leftrightarrows CO^{**}$	2.6 10^{8}	0.0	*-114.2*	-160.9
Initiation reactions				
$CO^{**} + 3 * \rightleftarrows C^{***} + O^{**}$	1.0 10^{13}	**52.0±1.0**	*15.9*	-15.2
$C^{***} + H^* \rightleftarrows CH^{***} + *$	5.5 10^{14}	**79.5±3.5**	*79.4*	33.2
$CH^{***} + H^* \rightleftarrows CH_2^{**} + 2 *$	4.4 10^{11}	**10.4±0.2**	*-25.3*	-26.2
$CH_2^{**} + H^* \rightleftarrows CH_3^{*} + 2 *$	1.7 10^{11}	**63.4±0.02**	*-115.1*	-33.9
Water formation				
$O^{**} + H^* \rightleftarrows OH^* + 2 *$	9.8 10^{11}	**99.2±3.5**	*59.6*	32.0
$OH^* + H^* \rightleftarrows H_2O_{(g)}$	2.0 10^{11}	**96.0±0.2**	*51.3*	70.7
Reaction family				
Chain growth				
$C_nH_{2n+1}^{*} + CH_2^{**}$ $\rightleftarrows C_{n+1}H_{2n+3}^{*} + **$	4.6 10^{9}	**21.2±0.2**	*-57.3 (n=1)* *-99.1 (n=2)* *-98.3 (n>2)*	-63.4
Alkanes formation				
$C_nH_{2n+1}^{*} + H^*$ $\rightleftarrows C_nH_{2n+2,(g)} + 2 *$	2.9 10^{10} (n=1) 1.6 10^{10} (n>2)	**88.7±0.2**	*23.6 (n=1)* *-6.3 (n=2)* *-5.5 (n>2)*	61.1

Table 3–4: continued

Reaction	$\mathbf{\tilde{A}^f}$ **[s^{-1} or (Mpa s)$^{-1}$]**	$\mathbf{E_a^f}$ **[kJ mol^{-1}]**	$\mathbf{\Delta H_r^0}$ **[kJ mol^{-1}]**	$\mathbf{\Delta \tilde{S}_r^0}$ **[J (K mol)$^{-1}$]**
Metal alkenes formation				
$C_nH_{2n+1}^* + * \rightleftarrows C_nH_{2n}^* + H^*$	1.0 10^{10}	**69.2±0.3**	*8.27 (n=2)* *0.78 (n=3)* *1.42 (n>3)*	13.5
Alkenes desorption				
$C_nH_{2n}^* \rightleftarrows C_nH_{2n,(g)} + *$	1.0 10^{13}	61.1 (n=2) 57.6 (n=3) 57.8 (n>3)	*61.1 (n=2)* *57.6 (n=3)* *57.8 (n>3)*	115.5

Atomic chemisorption enthalpy [kJ mol-1]	
Q_H	**251.0±0.2**
Q_C	**633.9±0.5**
Q_O	**543.3±0.3**

Table 3-5: Binary correlation coefficients, eq. [2–49], between the parameter estimates reported in Table 3-4 as determined by non-linear regression of the model to the experimental data. The model responses are obtained by integrating eq. [2–27] and eq. [2–28] in which the net production rates are calculated as explained by eq. [2–15]. 1, 2 and 3: the atomic chemisorption enthalpies of hydrogen, carbon and oxygen respectively; 4, 5, 6, 7, 8, 9, 10, 11 and 12: activation energy of CO^{**} dissociation, C^{***} hydrogenation, CH^{***} hydrogenation, CH_2^{**} hydrogenation, CH_2^{**} insertion, $C_nH_{2n+1}^{*}$ hydrogenation, $C_nH_{2n+1}^{*}$ beta hydride elimination, O^{**} hydrogenation and OH^{*} hydrogenation respectively

	1	2	3	4	5	6	7	8	9	10	11	12
1	1.00											
2	0.67	1.00										
3	0.08	0.28	1.00									
4	0.11	0.08	0.04	1.00								
5	0.28	0.18	0.23	0.64	1.00							
6	0.06	0.02	0.07	0.64	0.65	1.00						
7	0.11	0.11	0.02	0.06	0.00	0.01	1.00					
8	0.04	0.55	0.34	0.04	0.17	0.23	0.10	1.00				
9	0.61	0.71	0.38	0.11	0.06	0.16	0.068	0.58	1.00			
10	0.05	0.01	0.37	0.18	0.18	0.26	-0.22	0.44	0.42	1.00		
11	0.18	0.04	0.38	0.08	0.66	0.12	0.02	0.49	-0.20	-0.45	1.00	
12	0.05	0.06	0.73	0.04	0.00	0.04	-0.12	0.11	-0.12	-0.13	0.03	1.00

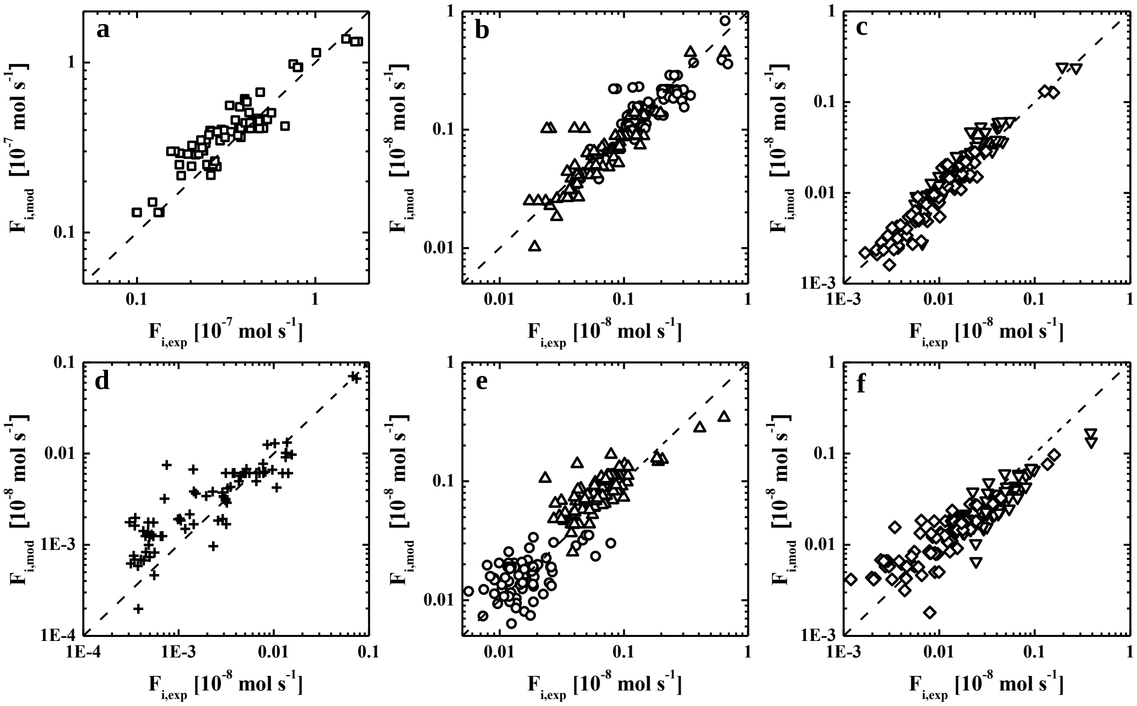

Figure 3-4: Experimental and model calculated outlet molar flow rates, F_i, at 3 - 10 H_2/CO molar inlet ratios, 483 K-503 K temperature range, 3.7 kPa-16.7 kPa CO inlet partial pressure, 7.2 - 36.3 $(kg_{cat}s)mol_{CO}^{-1}$ space time, $W/F_{CO,0}$, and 185 kPa total pressure. The calculated outlet molar flow rates are obtained by integrating eq. [2–27] and eq. [2–28] in which the net production rates are calculated as explained by eq. [2–15] and using the set of parameters given in Table 3-4. (a): methane; (b): ethane (○) and propane (△); (c): *n*-butane (▽) and *n*-pentane (◇); (d): *n*-hexane (✚); (e): ethene (○) and propene (△) and (f): 1-butene (▽) and 1-pentene (◇).

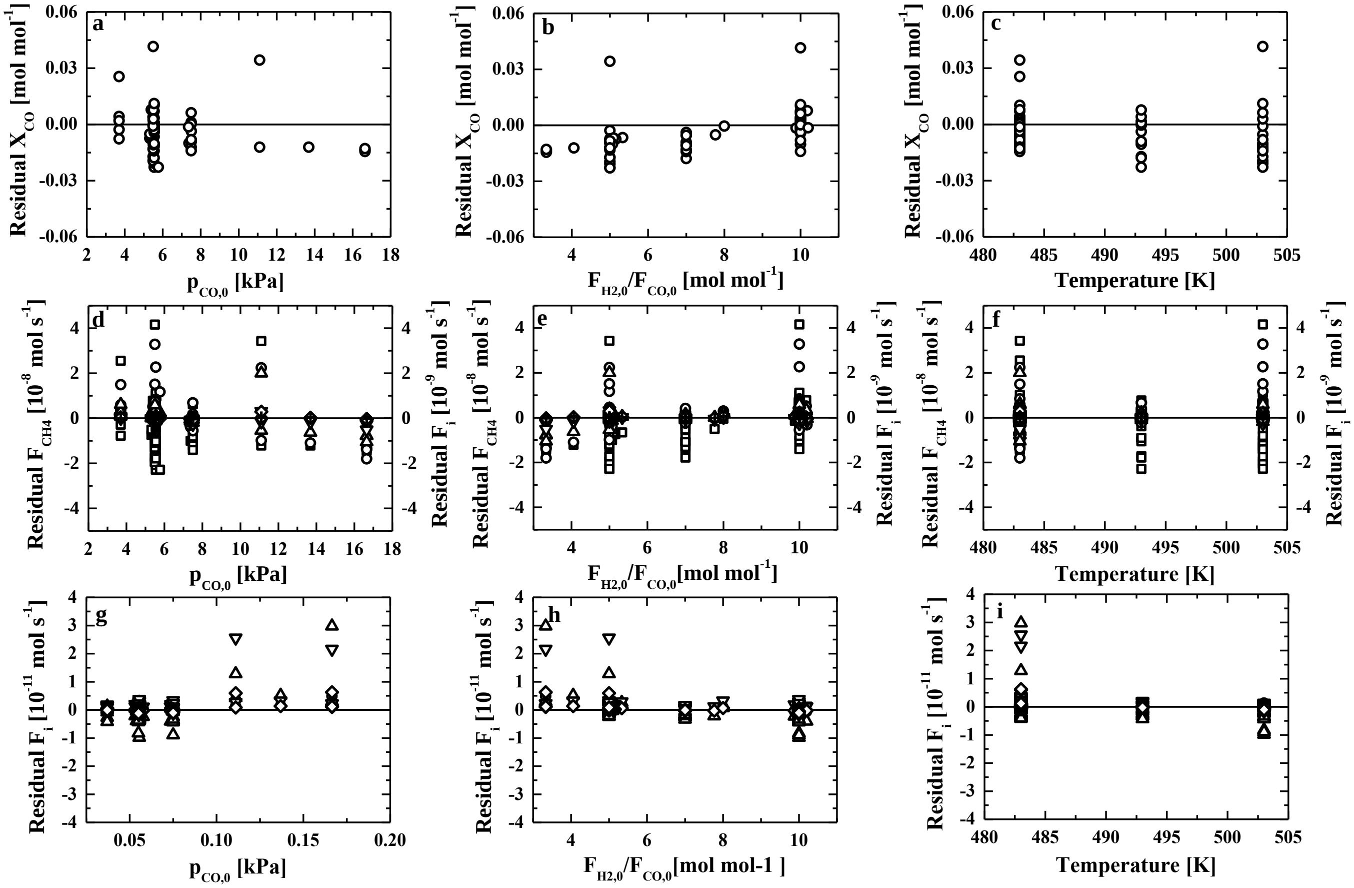

Figure 3-5: Residual diagrams for the CO conversion, X_{CO}, and outlet molar flow rates, F_i, of *n*-alkanes and 1-alkenes as a function of CO inlet partial pressure (a, d and g respectively), H_2/CO molar inlet ratio (b, e and h respectively) and temperature (c, f and i respectively) at 3 – 10 H_2/CO molar inlet ratio, 483 K – 503 K temperature range, 3.7 kPa – 16.7 kPa CO inlet partial pressure, 7.2 – 36.3 $(kg_{cat}s)mol_{CO}^{-1}$ space time, $W/F_{CO,0}$, and 185 kPa total pressure. Residuals are determined by the difference between the calculated value obtained by integrating eq. [2–27] and eq. [2–28] in which the net production rates are calculated as explained by eq. [2–15] and using the set of parameters given in Table 3-4 and the experimentally observed value. For d – i: □: C_1; ○: C_2, △: C_3, ▽: C_4, ◇:C_5 , ✚:C_6.

3.3.3 Assessment of the model parameters

3.3.3.1 Chemisorption enthalpies

The estimate for the H atomic chemisorption enthalpy, Q_H, as obtained in this chapter, i.e., 251.0 ± 0.2 kJ mol^{-1}, is close to the experimentally determined one, i.e., 251 kJ mol^{-1} [70], and in the center of the range determined by ab initio calculations, i.e., from 221 kJ mol^{-1} to 282 kJ mol^{-1}, depending on the CO coverage [43]. The H atomic chemisorption enthalpy is not significantly influenced by the type of site on which the H atom adsorbs, e.g., ab initio calculations on corrugated HCP or FCC Co surfaces result in a difference of only 7 kJ mol^{-1} [41]. The ab initio calculated C atomic chemisorption enthalpy, Q_C, on the contrary, is reported to vary from 541 kJ mol^{-1} to 647 kJ mol^{-1} on the Co(0001) plane depending on the CO coverage [43]. Moving from the adsorption site on the Co(0001) plane to a so called step-corner site enhances Q_C to 723 kJ mol^{-1} [71]. This illustrates that Q_C is very sensitive to the type of site on which carbon atoms bind. Calculations on corrugated HCP Co surfaces show that the adsorption enthalpy can be as high as 782.4 kJ mol^{-1} [41]. The O atomic chemisorption enthalpy, Q_O, determined by ab initio calculation is found to be in the range from 419 kJ mol^{-1} to 524 kJ mol^{-1} on the Co(0001) plane depending on the CO coverage [43]. The effect of a different type of site on the Q_O is less pronounced as compared to that on Q_C, i.e., in the range of 40 kJ mol^{-1} [41]. Estimates for the Q_C and Q_O have also been reported based on experimentally determined formation enthalpies of the bulk structures [70] resulting in 678 kJ mol^{-1} and 485.6 kJ mol^{-1} respectively for Q_C and Q_O. The Q_C and Q_O obtained in this chapter are, hence, close to the ab initio determined values on a clean Co(0001) surface. Taking into account that these values depend on the surface coverage of the various species and that different type of sites are present on the Co catalyst surface under FTS conditions, it can be concluded that reasonable values have been obtained for the three atomic chemisorption enthalpies.

The corresponding chemisorption enthalpies of the reactants are 64 kJ mol^{-1} for H_2 and 114 kJ mol^{-1} for CO. A wide variety of reactant adsorption enthalpies has been reported. The following H_2 chemisorption enthalpies can be found; 70 kJ mol^{-1} [12], 54.0 kJ mol^{-1} [11], 48.1 kJ mol^{-1} [5], 9.4 kJ mol^{-1} [18] and 2 kJ mol^{-1} [19]. For the CO chemisorption enthalpy, the following values have been reported: 111.6 kJ mol^{-1} [12], 85.2 kJ mol^{-1} to 37.3 kJ mol^{-1} depending on the number of metal atoms considered in the adsorption [11], 86.7 kJ mol^{-1} [5] and 48.9 kJ mol^{-1} [18]. Ab initio calculated values for CO chemisorption vary between 181.0 kJ mol^{-1} to 75.0 kJ mol^{-1} depending on the CO coverage [43]. The chemisorption enthalpies of the reactants obtained in this microkinetic modeling study are in the middle of the range of reported values.

The UBI-QEP method, see section 2.2.1.4, results in an adsorption enthalpy for the methyl radical amounting to 216 kJ mol^{-1} and to 167 kJ mol^{-1} for the heavier alkyl radicals. The stronger adsorption of the methyl radical was obtained by describing its adsorption as a linear superposition of strong and weak adsorption strength within the UBI-QEP methodology, see eq [2–24]. The α in eq. [2–24] was first considered as a model parameter. Regression including this parameter always resulted in values close to 1.0 and very narrow confidence intervals. Therefore, the chemisorption enthalpy of metal methyl was set equal to the strong adsorption part of the linear interpolation of eq. [2–24]. This significantly increased the performance of the model for describing the ethene yields, see also section 3.4.

A higher chemisorption for the methyl radical compared to the heavier alkyl radicals is also found via ab initio calculations [72]. The chemisorption enthalpy of the methyl radical [71, 72] is reported in the range from 224 kJ mol^{-1} to 190 kJ mol^{-1} depending on the surface site whereas for heavier alkyl radicals, the chemisorption enthalpy was found to be around 160 kJ mol^{-1} [72]. Hence, a difference in chemisorption enthalpy for the metal methyl species compared to the other metal alkyl species of about 50 kJ mol^{-1} is an acceptable value. Note that such a difference in chemisorption enthalpy is not contradictory with the SEMK methodology and be compared to a difference in stability level of a primary and a secondary carbenium ion [73].

The alkene chemisorption enthalpies amount to approximately 58 kJ mol^{-1}. This value is lower than the ab initio calculated value, i.e., 75 kJ mol^{-1} [72]. Alkene chemisorption was only considered as an elementary step by Azadi et al. [5]. These authors considered the possibility of activated desorption in their model and distinguished between the chemisorption of ethene, propene and higher alkenes. The chemisorption enthalpies for the alkenes obtained in this work are in the middle of the range reported by Azadi et al. [5].

3.3.3.2 Activation energies

The CO dissociation mechanism is strongly debated. Despite the importance of this reaction, the corresponding activation energy is rarely estimated in kinetic modeling studies which also consider direct CO dissociation [11, 20]. Klinke et al. [11] reported an activation energy for this reaction amounting to 72 kJ mol^{-1}. Ab initio calculations have been performed on different Co surfaces [40-42] and showed that to obtain low activation energies for direct CO dissociation, the Co surface sites should have a low coordination, e.g., it should concern step sites or corrugated sites. On a Co($10\bar{1}0$) the activation energy for direct CO dissociation has been reported to amount to 68 kJ mol^{-1} [40]. With a value amounting to 52 kJ mol^{-1}, the CO dissociation activation energy obtained in this microkinetic modeling study is, hence, reasonable.

In general, the activation energies estimated for the carbon hydrogenation reactions up to CH_3 follow the trend obtained from ab initio calculations [48, 71]. For the low CO coverage limit, e.g., Gong et al [71] calculated 81.6 kJ mol^{-1}, 63 kJ mol^{-1} and 60 kJ mol^{-1} for $E_{a,Cre}$, $E_{a,CHre}$ and E_{a,CH_2re} compared to 79.5 kJ mol^{-1}, 10.4 kJ mol^{-1} and 63.4 kJ mol^{-1} obtained by regression. These values have also been calculated on corrugated Co surfaces and are found to be significantly less sensitive to coordination of the Co metal atoms [48, 71] compared to CO dissociation. This can be related to the structure insensitivity of the Q_H. Higher CO coverages tend to decrease the activation barriers [43, 74]. The major difference in the regressed values obtained in the present chapter compared to the ab initio calculated values is situated in the CH hydrogenation reaction. The UBI-QEP chemisorption enthalpy of CH^{***} is considerably lower compared to the CH^{***} chemisorption enthalpy obtained via DFT calculations. This increases the endothermicity of the C^{***} hydrogenation reaction and correspondingly decreases the activation energy of the subsequent CH^{***} hydrogenation reaction. A reaction energy diagram for the formation of CH_4 and H_2O starting from CO and H_2 is shown in Figure 3-6 to illustrate this more clearly.

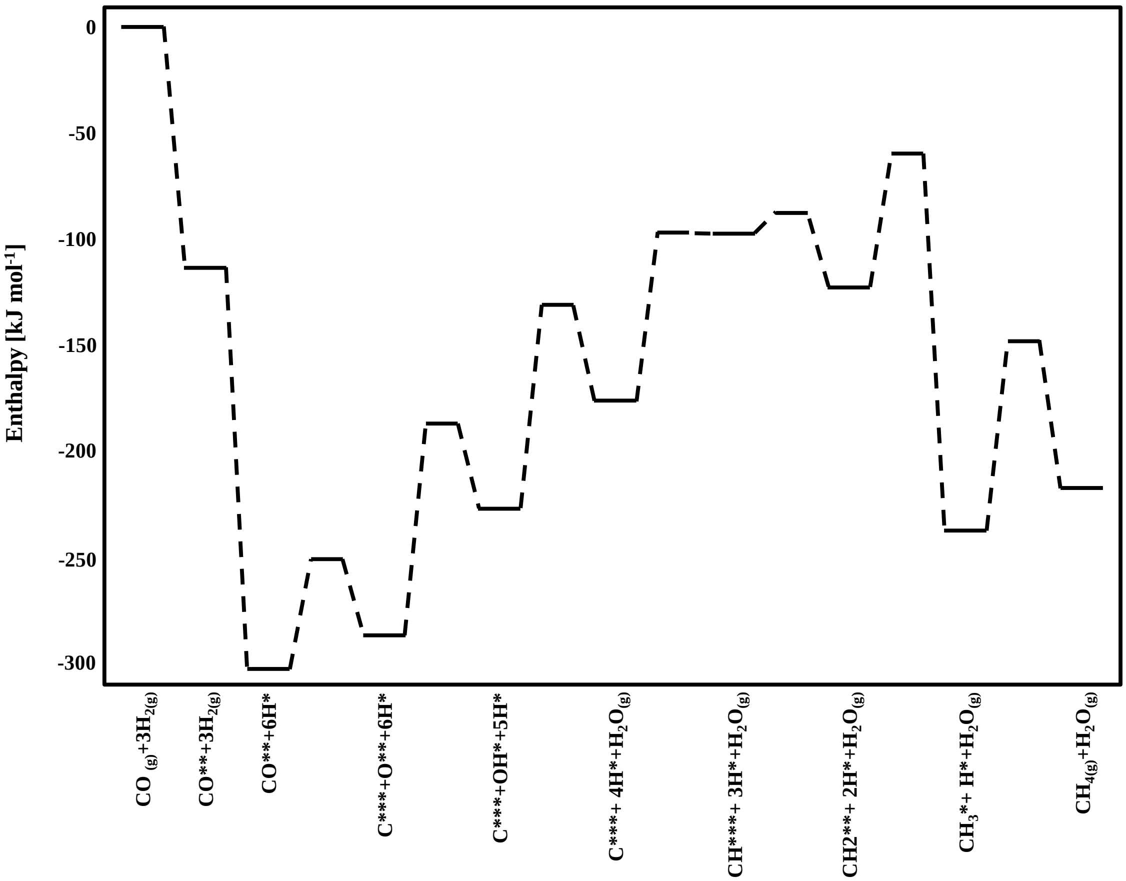

Figure 3-6: The reaction energy diagram for methane and water formation starting from CO and 3 H_2.

The methylene insertion, metal alkyl hydrogenation and beta hydride elimination activation energies determine the product selectivities. Only a few microkinetic modeling studies report the activation energy for the ‘propagation’ reaction, i.e., methylene insertion. The literature reported values vary between 5.4 kJ mol^{-1} [12] to 108 kJ mol^{-1} [20]. The estimated value for the propagation step in this work is at the lower end of this range. The activation energy for the alkane formation exceeds that for metal alkenes formation and the methylene insertion step. This stems from the experimentally observed trends of an increasing methane selectivity with the temperature, see Figure 3-2. This trend in activation energies is confirmed by another kinetic modeling study [5] as well as by ab initio calculations [72]. The estimate for the metal alkyl hydrogenation activation energy is lower than the one reported by Azadi et al. [5], while that for the metal alkenes formation is much closer to the value reported by Azadi et al. [5] for the higher alkenes (n>3). Other kinetic modeling studies typically report a reverse order for the activation energies, i.e., the activation energy for the hydrogenation of metal alkyl species is lower than the activation energy to go from a metal alkyl to the corresponding alkene in the gas phase [17-21]. This is related to the reaction mechanism considered for the simulation of the alkanes and alkenes formation. A metal alkyl species is susceptible to hydrogenation to the corresponding alkanes or beta hydride elimination to the corresponding metal alkenes. In our work the beta hydride elimination step is assumed to require a free site while this is not a prerequisite in other microkinetic models [17-21]. Due to the high chemisorption enthalpies of the reactants, the free surface site concentration as calculated by our model is low, see Table 3-6. Hence, the beta hydride elimination reaction is considerably suppressed. In other microkinetic modeling studies not requiring a free site as required in the alkene formation step, a comparatively higher activation energy ensures that the selectivity to alkenes does not exceed the selectivity to alkanes.

The O and OH hydrogenation steps are found to have high activation energies. Transient experiments have shown that water formation is, indeed, slower than methane formation [75]. The activation energies involved in water formation are, hence, higher than the activation energy of metal alkyl hydrogenation. High activation energies for the two elementary steps involved in water formation are also obtained via ab initio studies [42].

In general it can be concluded that the chemisorption enthalpies and activation energies obtained in this work are in line with ab initio and experimentally determined ones.

3.3.4 Surface coverages

The surface species coverages at X_{CO} = 5%, corresponding to a space time of 20 (kg_{cat} s)mol^{-1}, a CO inlet partial pressure of 5.5 kPa, a temperature of 483 K, a H_2/CO molar inlet ratio of 10 and a total pressure of 185 kPa are presented in Table 3-6. The surface species coverages were found to vary only to a limited extent as a function of the space time, see Figure 3-7. At the aforementioned reaction conditions, the surface is covered for 73% with H and 24% with CO. Comparable results, i.e., $\theta_H = 59\%$ and $\theta_{CO} = 32\%$, were obtained by Storsaeter et al. [12] who developed a microkinetic model for FTS at similar methanation conditions. Other kinetic modeling studies for Co catalyzed FTS report CO surface coverages varying between 10% [17] and 65% [18] but are performed at higher pressures and lower H_2/CO molar ratios. The H surface coverage as found by microkinetic modeling studies at higher pressures is typically much lower, i.e., from less than 1% [18] to 4% [17] and is attributed to the coverage dependence of the H chemisorption enthalpy [43]. Based on ab initio calculations [43], the H atomic chemisorption enthalpy at a CO coverage of 50% can vary from 278 kJ mol^{-1} to 221 kJ mol^{-1} corresponding with molecular H_2 adsorption enthalpies between 120 kJ mol^{-1} and 6 kJ mol^{-1}. This indicates that at higher total pressures, the higher CO coverage results in a decrease of the H coverage by a reduction in the H_2 adsorption enthalpy. This explains why at much lower pressures, the chain growth probability is strongly reduced, see also section 3.6. A decreased H coverage will, hence, result in longer chain hydrocarbons as the hydrogenation of the methylene surface species and metal alkyls is suppressed. Suppressing the former reaction reduces the number of growing chains on the surface as less metal methyl species are formed. A lower hydrogenation rate of the metal alkyls causes the metal alkyls to stay relatively longer on the surface enhancing the chain growth probability.

Table 3-6: The surface coverages of the various surface species at a CO inlet partial pressure of 5.5 kPa, a H_2/CO molar inlet ratio of 10, temperature of 483 K, a total pressure of 185 kPa and 5 % CO conversion. The surface coverages are obtained by integrating eq. [2–27] and eq. [2–28] in which the net production rates are calculated as explained by eq [2–15] using the set of parameters of Table 3-4.

Surface species	Surface coverage
H^*	0.73
CO^{**}	0.24
C^{***}	8.86 10^{-7}
CH^{***}	9.11 10^{-12}
CH_2^{**}	1.94 10^{-7}
O^{**}	1.75 10^{-2}
$\sum_{i=1}^{10} C_iH_{2i+1}^*$	2.79 10^{-4}
$\sum_{i=2}^{10} C_iH_{2i}^*$	3.19 10^{-6}
OH^*	6.96 10^{-4}
$*$	9.07 10^{-3}

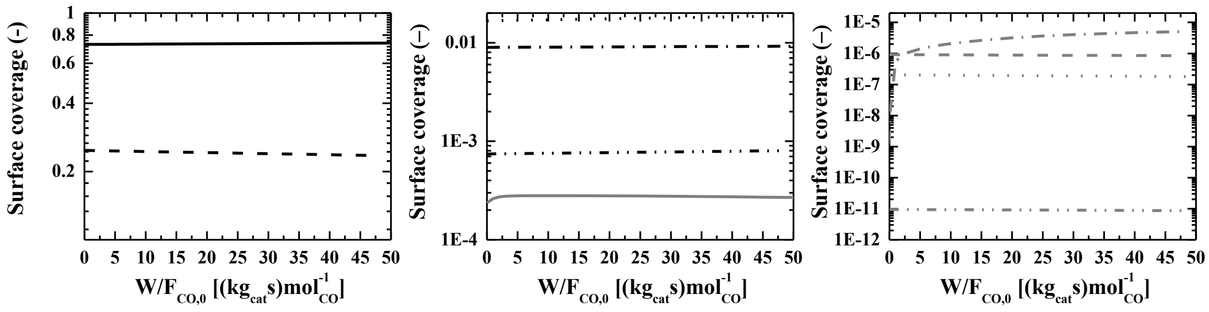

Figure 3-7: The surface coverage as function of space time, $W/F_{CO,0}$. The simulation results are obtained by integrating eq. [2–27] and eq. [2–28] in which the net production rates are calculated as explained by eq. [2–15] using the set of parameters of Table 3-4. The inlet conditions for the simulations are a CO inlet partial pressure of 5.5 kPa, a H_2/CO molar inlet ratio of 10, a temperature of 483 K and a total pressure of 185 kPa. Full line – black: H^*, dashed line – black: CO^{**}, dotted line – black: O^{**}, dash dotted line – black: *, dash dot dotted line – black: OH^*, full line – grey: $C_nH_{2n+1}{}^*$, dashed line – grey: C^{***}, dotted line – grey: $CH_2{}^{**}$, dash dotted line – grey: $C_nH_{2n}{}^*$, dash dot dotted line – grey: CH^{***}.

The temperature effect on the selectivity, see Figure 3-2, is explained by the H_2 and CO chemisorption enthalpies and the activation energies of the elementary steps which control the product selectivity, i.e., methylene insertion and metal alkyl hydrogenation and dehydrogenation. A higher temperature will more strongly impact on the CO coverage due to the much higher chemisorption enthalpy. As a consequence the H coverage will increase. Additionally, the hydrogenation of metal alkyl species has a higher activation energy compared to the other reactions involved in the hydrocarbon formation. Due to this, an increase in temperature will selectively increase metal alkyl hydrogenation reaction rates, increasing the selectivity to methane.

Table 3-7 represents the effect of H_2/CO molar inlet ratio at CO conversion of 5% on the surface coverages of H^*, CH_2^{**} and CH_3^*. A lower H_2/CO molar inlet ratio decreases the H^*, coverage. This decreases the surface coverage of CH_3^* and CH_2^{**}. However, the relative decrease in CH_2^{**} is more pronounced compared to that in H^*. As a consequence CH_3^* species are comparatively more consumed by hydrogenation than by chain growth reactions explaining that for the same conversion and, hence, the same amount of converted carbon, a higher selectivity to methane is simulated.

Table 3-7: The effect of the H_2/CO molar inlet ratio, $F_{H2,0}/F_{CO,0}$, on the relative surface coverages of H^*, CH_2^{**} and CH_3^* at a CO inlet partial pressure of 5.5 kPa, a total pressure of 185 kPa, a temperature of 493 K and 5% CO conversion. The simulation results are obtained by integrating eq. [2–27] and eq. [2–28] in which the net production rates are calculated as explained by eq. [2–15] and using the set of parameters given in Table 3-4. The relative surface coverages are obtained by dividing the surface coverage of surface species *i* at a $F_{H2,0}/F_{CO,0}$ by the maximum surface coverage of surface species *i* found at the different $F_{H2,0}/F_{CO,0}$.

Surface species	**Relative surface coverage [-]**		
	$F_{H_2,0}/F_{CO,0}$ = 5	$F_{H_2,0}/F_{CO,0}$ = 7	$F_{H_2,0}/F_{CO,0}$ = 10
H^*	0.86	0.93	1.0
CH_2^{**}	0.77	0.90	1.0
CH_3^*	0.80	0.91	1.0

3.4 Deviations from the ASF distribution: methane and ethene selectivity

A reaction path analysis at H_2/CO molar inlet ratio of 10, a temperature of 483 K, a CO inlet partial pressure of 5.5 kPa, a total pressure of 185 kPa and space time of 20 $(kg_{cat}s)mol^{-1}$ is presented in Figure 3-8 and allows quantifying the surface reactions which ultimately determine the product selectivities. The elementary surface reactions which are at quasi-equilibrium as determined from their affinity, see eq. [2–52] and Table 3-8, at the considered operating conditions are represented by the black arrows. The chemisorption of H_2, CO and alkenes were found to be in quasi-equilibrium. Other reactions which are at quasi-equilibrium are the CO dissociation and the hydrogenation of carbide, methylidene and surface oxygen. The other reactions considered in the reaction mechanism are identified as kinetically relevant and are indicated in Figure 3-8 by colored arrows of which the thickness is scaled logarithmically to the reaction rate, the slowest elementary steps being represented by dotted arrows. The various reaction families considered in the SEMK model have been assigned a separate color. At the tip of each arrow the differential formation factor, eq. [2–51], and at the tail of each arrow the differential disappearance factor, eq. [2–50], is indicated. It is noted that in a large reaction network, elementary steps can reach quasi-equilibrium even though the rates of these elementary steps are not excessively high compared to the rates of the other reaction steps present in the reaction network. This is illustrated for the beta hydride elimination/addition reactions.

The reaction path analysis clearly shows that, at the investigated operating conditions, the reversibility of the methylene insertion step is kinetically relevant, i.e., the differential disappearance factor of metal ethyl to metal methyl amounts to 32% which is in fact higher than the differential disappearance factor to higher metal alkyl species. This can be attributed to the higher adsorption enthalpy of the metal methyl compared to the other metal alkyl species. The higher adsorption enthalpy reduces the activation energy of the reverse deinsertion reaction. Note that the other methylene insertions are practically irreversible.

The combination of the reaction path analysis and the affinity calculations also explains how a stronger chemisorption enthalpy of the metal methyl species is responsible for a lower ethene production than would be expected from the ASF distribution. The elementary surface reactions involved in the ethene formation from metal ethyl reach quasi-equilibrium in the beginning of the catalyst bed and, hence, the following relation between the ethene partial pressure and the surface coverage of metal ethyl can be considered:

$$K = \frac{L_{H^*} p_{C_2H_4}}{L_{C_2H_5^*}} \qquad [3\text{-}3]$$

Due to the increased disappearance rate of metal ethyl to metal methyl caused by the increased methylene deinsertion rate of metal ethyl, the surface coverage of metal ethyl decreases which subsequently also decreases the partial pressure of ethene.

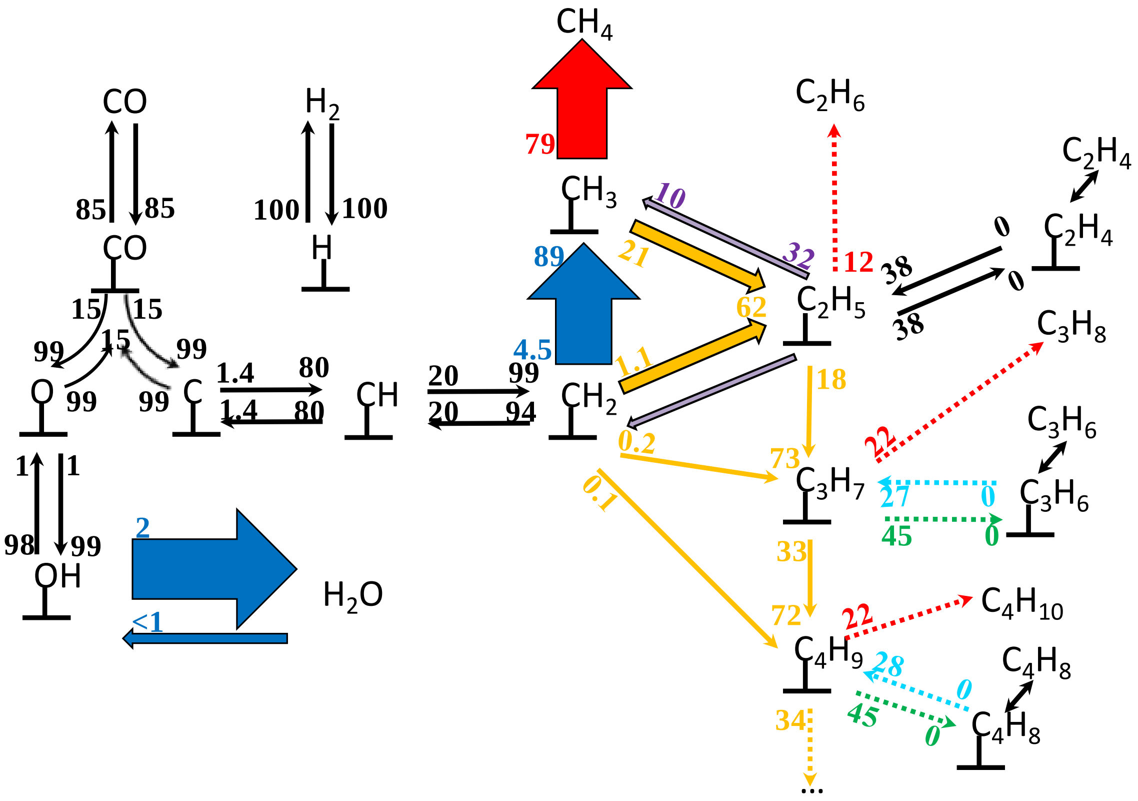
CH_4
CO
H_2
C_2H_6
C_2H_4
79
CH_3
10
85
85
100
100
CO
H
89
21
32
12
38
0
C_2H_4
0
38
C_2H_5
62
15
15
15
99
99
99
99
O
C
1.4
80
1.4
80
CH
20
99
20
94
4.5
1.1
CH_2
0.2
18
C_3H_8
22
C_3H_6
1
1
98
99
OH
73
C_3H_7
27
0
C_3H_6
45
0
0.1
2
H_2O
<1
33
72
22
C_4H_{10}
C_4H_9
28
C_4H_8
0
45
0
C_4H_8
34
...

Figure 3-8: Reaction path analysis at a H_2/CO molar inlet ratio of 10, a temperature of 483 K, a CO inlet partial pressure of 5.5 kPa, a total pressure of 185 kPa and space time, $W/F_{CO,0}$, 20 $(kg_{cat}s)mol_{CO}^{-1}$. The simulation is performed by integrating eq. [2–27] and eq. [2–28] in which the net production rates are calculated as explained by eq. [2–15] and using the parameters of Table 3-4. The elementary reactions indicated by black arrows are at quasi-equilibrium as confirmed by affinity calculations, see Table 3-8. The reactions which are not at quasi-equilibrium are presented by the colored arrows. The thickness of these arrows are scaled to the reaction rate. The reaction families considered in the SEMK model are assigned a separate color, i.e., CH_2^{**} insertion/deinsertion (yellow – purple), $C_nH_{2n+1}^{*}$ hydrogenation (red), beta hydride elimination/ addition (green/cyan). The other elementary steps are indicated in blue. The number indicated at the tail of an arrow is the differential disappearance factor, eq. [2–50]. The number indicated at the tip of an arrow is the differential formation factors, eq.[2–51]. H_2 has not been included not to overload the figure.

Table 3-8: The affinity [kJ mol^{-1}] of the various elementary surface reactions considered in the reaction network calculated as explained by eq. [2–52] at a CO inlet partial pressure of 5.5 kPa, a H_2/CO molar inlet ratio of 10, a total pressure of 185 kPa, a temperature of 483 K and 2 values for the space time, W/$F_{CO,0}$. The required surface coverages are obtained by integrating eq. [2–27] and eq. [2–28] in which the net production rates are calculated as explained by eq. [2–15] and using the set of parameters given in Table 3-4.

	$\mathbf{W}/F_{CO,0}$ $[(\mathbf{kg_{cat}s})\ mol_{CO}^{-1}]$	
	0.01	20.0
Elementary reaction		
Reactant adsorption		
$H_{2,(g)} + 2* \leftrightarrows 2H^*$	0.0	0.0
$CO_{(g)} + 2* \leftrightarrows CO^{**}$	0.0	0.0
Initiation reactions		
$CO^{**} + 3* \rightleftarrows C^{***} + O^{**}$	0.0	0.0
$C^{***} + H^* \rightleftarrows CH^{***} + *$	0.0	0.0
$CH^{***} + H^* \rightleftarrows CH_2^{**} + 2*$	0.2	0.2
$CH_2^{**} + H^* \rightleftarrows CH_3^* + 2*$	99.3	99.0
Water formation		
$O^{**} + H^* \rightleftarrows OH^* + 2*$	0.1	0.1
$OH^* + H^* \rightleftarrows H_2O_{(g)}$	40.2	9.9
reaction family		
Chain growth		
$C_nH_{2n+1}^* + CH_2^{**} \rightleftarrows C_{n+1}H_{2n+3}^*$	72.7 (n=1) 112.3 (n=2) 111.5 (n>2)	70.7 (n=1) 110.9 (n=2) 110.0 (n>2)
Alkanes formation		
$C_nH_{2n+1}^* + H^* \rightleftarrows C_nH_{2n+2,(g)} + 2*$	58.0 (n=1) 93.4 (n=2) 92.7 (n>2)	27.3 (n=1) 62.7 (n=2) 62.4 (n>2)
Metal alkenes formation		
$C_nH_{2n+1}^* + * \rightleftarrows C_nH_{2n}^* + H^*$	16.7 (n=2) 30.2 (n=3) 29.3 (n>3)	0.0 (n=2) 2.1 (n=3) 2.0 (n>3)

Table 3–8: continued

	$\mathbf{W}/\boldsymbol{F_{CO,0}}$ $[(\mathbf{kg_{cat}s})\ \boldsymbol{mol_{CO}^{-1}}]$ 0.01	20.0
reaction family		
Alkenes desorption		
$C_nH_{2n}^{*} \rightleftarrows C_nH_{2n,(g)} + *$	0.2 (n=2) 0.4 (n>2)	0.0 (n≥2)

$$\frac{r_i^f}{r_i^r} = exp\left(\frac{A_i}{RT}\right)$$

Methane and ethene formation could be satisfactorily described even with a single activation energy, i.e., independent of the carbon number, for the hydrogenation of a metal alkyl to the corresponding alkanes and for beta hydride elimination of a metal alkyl to the corresponding metal alkene. In other microkinetic modeling studies, a separate activation energy is typically estimated for methane and ethene formation of [5, 13, 14, 16-21, 76]. A single activation energy for the beta hydride eliminations is confirmed by an ab initio study [72]. For the hydrogenation of metal alkyl species, ab initio studies are less conclusive [71, 77]. Specifically taking the symmetry numbers into account, as is done in this chapter and in previous work [30] by using the SEMK concept, the methane formation rate increases by a factor of 3 and the ethene readsorption rate by a factor of 2, increasing the selectivity to methane and decreasing the selectivity to ethene. Next to this, the effect of a stronger chemisorption enthalpy of the metal methyl also increased the selectivity to methane and decreased the selectivity to ethene.

3.5 Degree of rate control analysis

A degree of rate control analysis was performed to asses which elementary surface reactions control the CO conversion. Affinity calculations are useful to identify the steps in the reaction mechanism which are far from equilibrium. To identify the reaction steps which ultimately control the CO conversion, a more generalized approach is required which incorporates more than only considerations about the thermodynamic driving force of an elementary surface reaction [78]. In Figure 3-9 the results of the degree of rate control analysis are presented. The degree of rate control analysis shows that for changes in temperature or H_2/CO molar inlet ratio the OH hydrogenation and CH_2 hydrogenation control the observed reaction rate. This corresponds to the elementary steps in the reaction path analysis which have the highest rate but are not in quasi-equilibrium, see Figure 3-8. The temperature effect on the CO conversion can, hence, be attributed to the activation energy of the OH hydrogenation and to the difference in the adsorption enthalpy of H_2 and CO. The effect of H_2/CO molar inlet ratio is also related to the H surface coverage. A larger H_2/CO molar inlet ratio increases the H coverage, enhancing the reaction rate of the rate controlling reactions. The OH hydrogenation, hence, controls the activity while the CH_2 hydrogenation determines the activity as well as the selectivity. Water formation as rate-controlling step for the CO conversion rate has also been suggested by Weststrate et al [37] based on surface science studies.

The reaction orders according to the model with respect to the partial pressure of CO and H_2 have been determined to be equal to -1.0 and 0.6 respectively. Based on the degree of rate control analysis, the rate limiting steps in the model involve hydrogenation steps. An increasing partial pressure of CO at a constant partial pressure of H_2 decreases the reaction rate as a higher CO partial pressure will suppress the hydrogen surface coverage. Similarly, increasing the H_2 partial pressure increases the hydrogen coverage and, hence, increases the rate of the rate-limiting steps.

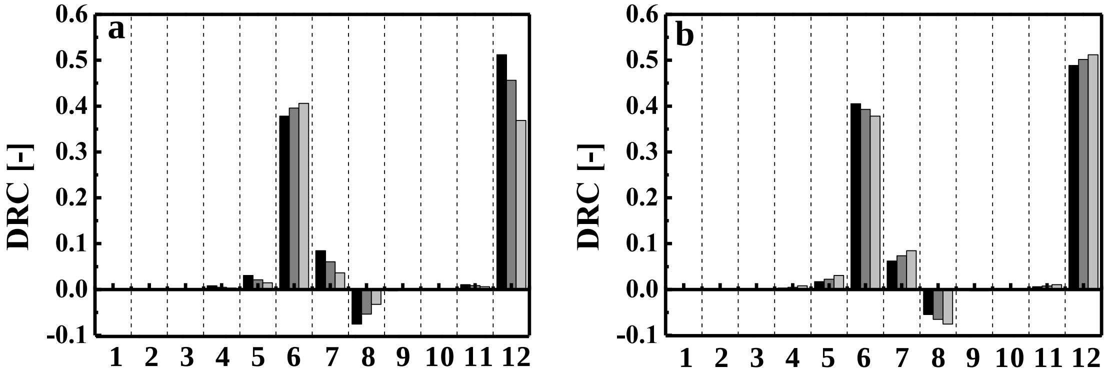

Figure 3-9: The degree of rate control, eq. [2–53], at (a) different temperatures (black: 483K; dark grey: 493 K; light grey: 503 K) and a H_2/CO molar inlet ratio of 10 and (b) different H_2/CO molar inlet ratios (black: 5; dark grey: 7; light grey 10) and a temperature of 483 K. The other conditions for the simulations were a CO inlet partial pressure of 5.5 kPa a total pressure of 185 kPa and a space time, $W/F_{CO,0}$, of 20 (kg_{cat} s) mol_{CO}^{-1}. The simulations are performed by integrating eq. [2–27] and eq. [2–28] in which the net production rates are calculated as explained by eq [2–15] and using the set of parameters given in Table 3-4. 1: H_2 chemisorption, 2: CO chemisorption, 3: CO^{**} dissociation, 4: C^{***} hydrogenation, 5: CH^{***} hydrogenation, 6: CH_2^{**} hydrogenation, 7: CH_2^{**} insertion, 8: $C_nH_{2n+1}^{*}$ hydrogenation, 9: beta hydride elimination, 10: C_nH_{2n} chemisorption, 11: O^{**} hydrogenation and 12: OH^{*} hydrogenation.

3.6 Impact of atomic chemisorption enthalpies on catalyst performance

The hydrogen, Q_H, carbon, Q_C, and oxygen, Q_O, atomic chemisorption enthalpies have been varied to investigate the effect of these parameters on the reactant conversion and product selectivity. The simulations have been performed at industrially more relevant operating conditions, i.e., a total pressure of 2.0 MPa, a H_2/CO molar inlet ratio of 2, a temperature of 493 K and a space time of 50 (kg_{cat}s) mol_{CO}^{-1}. Figure 3-10 displays the results of varying Q_H , Q_C and Q_O on the CO conversion and C_{5+} selectivity. As a function of Q_H, the CO conversion follows a volcano curve according to the Sabatier principle [79]. A too low Q_H results in a lower hydrogen surface coverage which reduces the rate of the rate controlling steps, see also section 3.5. A too high Q_H, on the other hand, results in a higher H coverage and, hence, a lower CO coverage resulting in a decreasing CO conversion. A maximum conversion at intermediate Q_H is, hence, observed. Furthermore, the C_{5+} selectivity is strongly determined by the Q_H. At a low Q_H, the C_{5+} selectivity is high. In the range of 245 kJ mol^{-1} to 255 kJ mol^{-1} the C_{5+} selectivity strongly decreases. A higher Q_H enhances the hydrogenation of the metal alkyl species which, hence, become less susceptible to chain growth. As a function of Q_C and Q_O, the CO conversion follows again the Sabatier principle, although the maximum in the CO conversion is more pronounced for variations in Q_O. For the C_{5+} selectivity an opposite trend as a function of Q_C and Q_O is observed compared to that with Q_H, i.e., the C_{5+} selectivity increases with increasing Q_C and Q_O. Furthermore, a maximum in the C_{5+} selectivity is observed as function of Q_C and Q_O. To obtain high C_{5+} selectivities, the Q_H should be decreased, and the accompanying decrease in CO conversion can be compensated by an increased Q_C and Q_O.

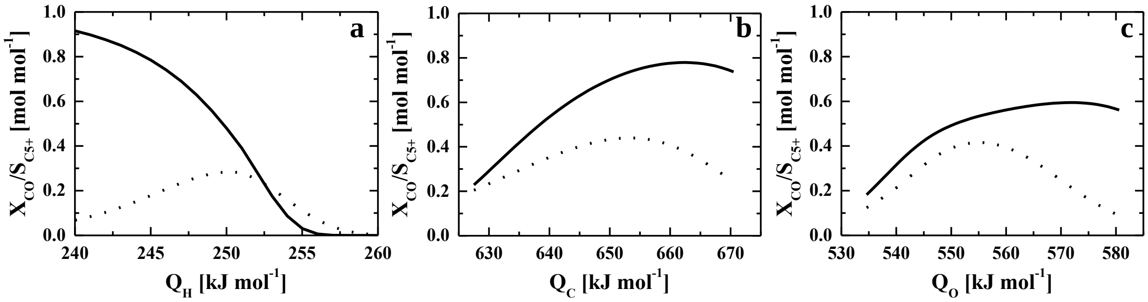

Figure 3-10: The CO conversion, X_{CO}, (dotted line) and C_{5+} selectivity, S_{C5+}, (full line) as a function of the hydrogen atomic chemisorption enthalpy, Q_H, (a), the carbon atomic chemisorption enthalpy, Q_C, (b) and oxygen atomic chemisorption enthalpy, Q_O, (c) at a temperature of 493 K, a H_2/CO molar inlet ratio of 2, a total pressure of 2.0 MPa and a space time, $W/F_{CO,0}$, of 50 $(kg_{cat}s)mol_{CO}^{-1}$. The results are obtained by integrating eq. [2–27] and eq. [2–28] in which the net production rates are calculated as explained by eq [2–15] and using the set of parameters given in Table 3-4.

Using the model parameters reported in Table 3-4 at a total pressure of 2.0 MPa, a H_2/CO molar inlet ratio of 2, a temperature of 493 K and a space time of 50 $(kg_{cat}s)$ mol_{CO}^{-1} results in a CO conversion of 0.25 and a C_{5+} selectivity of 0.35, see Figure 3-10. For the C_{5+} selectivity this is a low value for a Co catalyst. For densely covered surfaces, the adsorption enthalpy can change with changing surface coverages of the most abundant species [80]. By increasing the total pressure, the CO coverage will increase and, as a consequence, the Q_H value is expected to decrease. Decreasing the Q_H by 5 kJ mol^{-1} results in CO conversion of 0.19 and a more realistic C_{5+} selectivity of 0.80. These values are close to those reported by Visconti et al. [14], i.e., there a CO conversion of 0.15 and a C_{5+} selectivity of 0.75 was found at total pressure of 2.0 MPa, a

H_2/CO molar inlet ratio of 2.1, a temperature of 493 K and a space time of 54 (kg_{cat}s) mol_{CO}^{-1}. This illustrates that for microkinetic models to be valid over a wide range of operating conditions, a coverage dependent adsorption enthalpy of some key species is of primary importance. It is noted that, although the experimental data was measured at low CO partial pressures, the extrapolation capabilities of the SEMK model are demonstrated. This illustrates the advantages of a fundamental microkinetic model compared to power law kinetic models.

3.7 Comparison between Fe and Co catalysts.

A comparison between the activation energies and atomic chemisorption enthalpies obtained for the SEMK model validated for Co catalyzed and Fe catalyzed FTS is reported in Table 3-9. The most significant differences between the activation energies are related to those of the elementary steps which control the product selectivity, i.e., the activation energy for methylene insertion, metal alkyl hydrogenation and beta hydride elimination of a metal alkyl. The activation energies involved in the initiation reactions and the water formation differ only slightly from each other. With respect to the atomic chemisorption enthalpies, the most significant difference is found for the Q_O which has a high impact on the kinetic significance of the elementary steps involving O and OH.

Table 3-9: Comparison between the activation energies, E_a, and atomic chemisorption enthalpy, Q_i, for Co and Fe catalyzed FTS. The values for Co are taken from Table 3-4. The values for Fe are adopted from Lozano et al [30].

Reaction	E_a [$kJ\ mol^{-1}$]	
	Co	**Fe**
Elementary reactions		
Initiation reactions		
$CO^{**} + 3* \rightleftarrows C^{***} + O^{**}$	52.02±1.00	56.8±0.5
$C^{***} + H^{*} \rightleftarrows CH^{***} + *$	79.53±3.46	77.7±0.7
$CH^{***} + H^{*} \rightleftarrows CH_2^{**} + 2*$	10.42±0.16	11.9±0.1
$CH_2^{**} + H^{*} \rightleftarrows CH_3^{*} + 2*$	63.40±0.02	61.9±0.5
Water formation		
$O^{**} + H^{*} \rightleftarrows OH^{*} + 2*$	99.24±3.45	103.8±1.0
$OH^{*} + H^{*} \rightleftarrows H_2O_{(g)}$	95.95±0.17	86.2±0.6
Reaction family		
Chain growth		
$C_nH_{2n+1}^{*} + CH_2^{**} \rightleftarrows C_{n+1}H_{2n+3}^{*}$	21.21±0.18	44.8±0.4
Alkanes formation		
$C_nH_{2n+1}^{*} + H^{*} \rightleftarrows C_nH_{2n+2,(g)} + 2*$	88.68±0.23	117.8±0.7
Metal alkenes formation		
$C_nH_{2n+1}^{*} + * \rightleftarrows C_nH_{2n}^{*} + H^{*}$	69.17±0.29	96.3±0.5
Atomic chemisorption enthalpies [$kJ\ mol^{-1}$]		
Q_H	251.0±0.2	249.2±0.6
Q_C	633.9±0.5	639.5±2.1
Q_O	543.3±0.3	578.8±0.9

In general the atomic chemisorption enthalpies should be lower for Co catalysts than for Fe catalysts [81], even if the latter is present as a carbide. This trend is also confirmed here for the atomic chemisorption enthalpy of C and O, i.e., Q_C = 633.9 kJ mol^{-1} and Q_O = 543.3 kJ mol^{-1} for the Co catalyst against Q_C = 639.5 kJ mol^{-1} and Q_O = 578.8 kJ mol^{-1} for the Fe catalyst. For the hydrogen atomic chemisorption enthalpy, i.e., 250.0 kJ mol^{-1} for Co and 249.2 kJ mol^{-1} for Fe, it is noted that the experiments were performed at stronger hydrogenation conditions compared to the experiments used for the validation for Fe catalyzed FTS [30]. Furthermore, it is anticipated that the atomic chemisorption enthalpies obtained here for the Co catalyst would become lower at higher CO partial pressures due to the coverage effect.

The comparison between the Fe catalyzed FTS and the Co catalyzed FTS in terms of CO conversion is shown in Figure 3-11 as a function of space time at industrially more relevant operating conditions, i.e., a temperature of 493 K, a H_2/CO molar inlet ratio of 2 and a total pressure of 2.0 MPa. For the simulations, the parameters of Table 3-4 and the parameters of Table 3-9 have been used for Co and Fe respectively. Fe catalysts are known to be active water gas shift (WGS) catalysts. Therefore, in the SEMK model for the Fe catalyst, the WGS reaction was specifically taken into account [30]. More precisely, the reaction steps involved in the WGS reaction were considered to take place on magnetite (Fe_3O_4) while the FTS reactions were considered to take place on iron carbides [30]. It is noted that no WGS reaction was taken into account for the Co catalyst as Co catalyst are practically inactive for the WGS reaction. More detailed information on the Fe catalyst, catalyst characterization and procedures to obtain the kinetic data have been reported by Lox et al [82, 83]. The Co catalyst is found to be more active than the Fe catalyst. For the Fe catalyst, the water formation reactions are found to be quasi-equilibrated from the reactor entrance. This is caused by the higher oxygen atomic chemisorption enthalpy on Fe catalysts compared to Co catalysts which increases the endothermicity of these two elementary surface reactions and decreases the activation energy of the reverse reaction, see eq. [2–20], which results in increasing surface coverages of the oxygen containing species with space time or equivalently with increasing partial pressure of H_2O as one of the major FTS products. As a consequence, the CO surface coverage and the number of free sites decreases as a function of space time. This causes the CO dissociation reaction to become one of the kinetically relevant reaction steps. Hence, water has an inhibiting effect on the activity of an Fe catalyst explaining the typically observed rapid decrease of the initial disappearance rate of CO with increasing space time compared to the Co catalysts on which the initial CO consumption rate is maintained for a much larger part of the catalyst bed [84]. It is noted that for the Fe catalyst, the water partial pressure is partly reduced due to the WGS activity of the Fe catalyst. The pernicious effect of a too high Q_O can also be observed in Figure 3-10-c, i.e., Co is on the left and much closer to the maximum of the Sabatier curve as function of the Q_O, while Fe is much further to the right of the maximum.

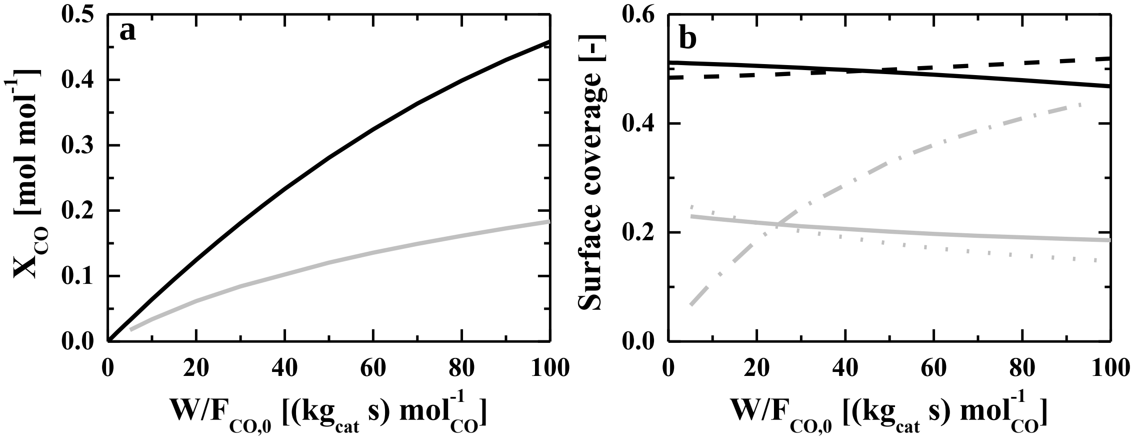

Figure 3-11: Comparison of Co to Fe catalysts. a: CO conversion, X_{CO}, as function of space time, W/$F_{CO,0}$, for Co (black) and Fe (grey) catalysts. b: surface coverage of H^* (full line), CO^{**} (dashed line) and OH^*+O^{**} (dash dotted line) for Co (black) and Fe (grey) catalysts as function of space time. The results are obtained by integrating eq. [2–27] and eq. [2–28] in which the net production rates are calculated as explained by eq. [2–15]. For the simulations for the Co catalyst, the parameters of Table 3-4 are used. For the simulations of the Fe catalyst, the parameters reported by Lozano et al. [30] are employed. The reaction conditions were a temperature of 493 K, a H_2/CO molar inlet ratio of 2 and a total pressure of 2.0 MPa.

3.8 Conclusions

The Single-Event MicroKinetic model developed for Fe catalyzed Fischer-Tropsch Synthesis (FTS) has been successfully applied to an extensive experimental data set acquired for Co catalyzed FTS. For both catalysts, the same reaction network for FTS reaction has been considered and the most significant changes were situated in the three atomic chemisorption enthalpies, the activation energies for methylene insertion, hydrogenation and beta hydride elimination and a higher chemisorption enthalpy of the metal methyl species compared to the higher metal alkyl species. It is stressed that the latter, together with the symmetry numbers of reactants and transition states and single activation energies for the hydrogenation and beta hydride elimination, allow adequately reproducing the deviations from the Anderson-Schulz-Flory distribution.

The positive effect of the H_2/CO molar inlet ratio on the CO conversion was found to be related to the hydrogenation of the hydroxyl and methylene surface species. These have been identified as the rate-controlling steps in the reaction mechanism.

The hydrogen atomic chemisorption enthalpy is the catalyst descriptor with the most significant impact on both the maximum obtainable CO conversion and C_{5+} selectivity. The significant difference in activity as a function of the space time between Co and Fe catalysts is related to the higher surface coverage of oxygen containing compounds, i.e., O and OH, on the Fe catalyst surface which stems from the much higher oxygen atomic chemisorption enthalpy on Fe catalysts compared to Co catalysts. The higher oxygen atomic chemisorption enthalpy on Fe catalysts causes the water formation reactions to be in quasi-equilibrium. As such, water acts as an inhibitor for Fe catalysts but not for Co catalysts.

3.9 References

1. Toch, K., J.W. Thybaut, and G.B. Marin, *A Systematic Methodology for Kinetic Modeling of Chemical Reactions Applied to n-Hexane Hydroisomerization.* Aiche Journal, 2015. **61**(3): p. 880-892.
2. Thybaut, J.W. and G.B. Marin, *Single-Event MicroKinetics: Catalyst design for complex reaction networks.* Journal of Catalysis, 2013. **308**: p. 352-362.
3. Filot, I.A.W., R.A. van Santen, and E.J.M. Hensen, *The Optimally Performing Fischer-Tropsch Catalyst.* Angewandte Chemie-International Edition, 2014. **53**(47): p. 12746-12750.
4. Cheng, J. and P. Hu, *Utilization of the three-dimensional volcano surface to understand the chemistry of multiphase systems in heterogeneous catalysis.* Journal of the American Chemical Society, 2008. **130**(33): p. 10868-+.
5. Azadi, P., G. Brownbridge, I. Kemp, S. Mosbach, J.S. Dennis, and M. Kraft, *Microkinetic Modeling of the Fischer-Tropsch Synthesis over Cobalt Catalysts.* Chemcatchem, 2015. **7**(1): p. 137-143.
6. Van der Laan, G.P. and A. Beenackers, *Kinetics and selectivity of the Fischer-Tropsch synthesis: A literature review.* Catalysis Reviews-Science and Engineering, 1999. **41**(3-4): p. 255-318.
7. van Santen, R.A., I.M. Ciobica, E. van Steen, and M.M. Ghouri, *Mechanistic Issues in Fischer-Tropsch Catalysis.* Advances in Catalysis, Vol 54, 2011. **54**: p. 127-187.
8. van Santen, R.A., A.J. Markvoort, I.A.W. Filot, M.M. Ghouri, and E.J.M. Hensen, *Mechanism and microkinetics of the Fischer-Tropsch reaction.* Physical Chemistry Chemical Physics, 2013. **15**(40): p. 17038-17063.
9. Biloen, P. and W.M.H. Sachtler, *MECHANISM OF HYDROCARBON SYNTHESIS OVER FISCHER-TROPSCH CATALYSTS.* Advances in Catalysis, 1981. **30**: p. 165-216.
10. Dry, M.E., *The Fischer-Tropsch process: 1950-2000.* Catalysis Today, 2002. **71**(3-4): p. 227-241.
11. Klinke, D.J. and L.J. Broadbelt, *Construction of a mechanistic model of Fischer-Tropsch synthesis on Ni(111) and Co(0001) surfaces.* Chemical Engineering Science, 1999. **54**(15-16): p. 3379-3389.
12. Storsaeter, S., D. Chen, and A. Holmen, *Microkinetic modelling of the formation of C-1 and C-2 products in the Fischer-Tropsch synthesis over cobalt catalysts.* Surface Science, 2006. **600**(10): p. 2051-2063.
13. Visconti, C.G., E. Tronconi, L. Lietti, R. Zennaro, and P. Forzatti, *Development of a complete kinetic model for the Fischer-Tropsch synthesis over Co/Al2O3 catalysts.* Chemical Engineering Science, 2007. **62**(18-20): p. 5338-5343.
14. Visconti, C.G., E. Tronconi, L. Lietti, P. Forzatti, S. Rossini, and R. Zennaro, *Detailed Kinetics of the Fischer-Tropsch Synthesis on Cobalt Catalysts Based on H-Assisted CO Activation.* Topics in Catalysis, 2011. **54**(13-15): p. 786-800.
15. Kwack, S.H., J.W. Bae, M.J. Park, S.M. Kim, K.S. Ha, and K.W. Jun, *Reaction modeling on the phosphorous-treated Ru/Co/Zr/SiO2 Fischer-Tropsch catalyst with the estimation of kinetic parameters and hydrocarbon distribution.* Fuel, 2011. **90**(4): p. 1383-1394.
16. Kwack, S.H., M.J. Park, J.W. Bae, S.J. Park, K.S. Ha, and K.W. Jun, *Modeling a slurry CSTR with Co/P-Al2O3 catalyst for Fischer-Tropsch synthesis.* Fuel Processing Technology, 2011. **92**(12): p. 2264-2271.

17. Todic, B., T. Bhatelia, G.F. Froment, W.P. Ma, G. Jacobs, B.H. Davis, and D.B. Bukur, *Kinetic Model of Fischer-Tropsch Synthesis in a Slurry Reactor on Co-Re/Al2O3 Catalyst.* Industrial & Engineering Chemistry Research, 2013. **52**(2): p. 669-679.
18. Todic, B., W.P. Ma, G. Jacobs, B.H. Davis, and D.B. Bukur, *CO-insertion mechanism based kinetic model of the Fischer-Tropsch synthesis reaction over Re-promoted Co catalyst.* Catalysis Today, 2014. **228**: p. 32-39.
19. Bhatelia, T., C.E. Li, Y. Sun, P. Hazewinkel, N. Burke, and V. Sage, *Chain length dependent olefin re-adsorption model for Fischer-Tropsch synthesis over Co-Al2O3 catalyst.* Fuel Processing Technology, 2014. **125**: p. 277-289.
20. Mosayebi, A. and A. Haghtalab, *The comprehensive kinetic modeling of the Fischer-Tropsch synthesis over Co@Ru/gamma-Al2O3 core-shell structure catalyst.* Chemical Engineering Journal, 2015. **259**: p. 191-204.
21. Qian, W.X., H.T. Zhang, W.Y. Ying, and D.Y. Fang, *The comprehensive kinetics of Fischer-Tropsch synthesis over a Co/AC catalyst on the basis of CO insertion mechanism.* Chemical Engineering Journal, 2013. **228**: p. 526-534.
22. Shustorovich, E. and H. Sellers, *The UBI-QEP method: a practical theoretical approach to understanding chemistry on transition metal surfaces.* Surface Science Reports, 1998. **31**(1-3): p. 5-119.
23. Shustorovich, E. and A.V. Zeigarnik, *The UBI-QEP method: Basic formalism and applications to chemisorption phenomena on transition metal surfaces.* Russian Journal of Physical Chemistry, 2006. **80**(4): p. 665-666.
24. Zeigarnik, A.V. and E. Shustorovich, *The UBI-QEP method: Mechanistic and kinetic studies of heterogeneous catalytic reactions.* Russian Journal of Physical Chemistry B, 2007. **1**(4): p. 330-356.
25. Botes, F.G., *Proposal of a new product characterization model for the iron-based low-temperature Fischer-Tropsch synthesis.* Energy & Fuels, 2007. **21**(3): p. 1379-1389.
26. Corral Valero, M. and P. Raybaud, *Cobalt Catalyzed Fischer–Tropsch Synthesis: Perspectives Opened by First Principles Calculations.* Catalysis Letters, 2013. **143**(1): p. 1-17.
27. Qi, Y., J. Yang, D. Chen, and A. Holmen, *Recent Progresses in Understanding of Co-Based Fischer–Tropsch Catalysis by Means of Transient Kinetic Studies and Theoretical Analysis.* Catalysis Letters, 2015. **145**(1): p. 145-161.
28. Bera, T., J.W. Thybaut, and G.B. Marin, *Single-Event MicroKinetics of Aromatics Hydrogenation on Pt/H-ZSM22.* Industrial & Engineering Chemistry Research, 2011. **50**(23): p. 12933-12945.
29. Froment, G.F., *Kinetic modeling of acid-catalyzed oil refining processes.* Catalysis Today, 1999. **52**(2-3): p. 153-163.
30. Lozano-Blanco, G., J.W. Thybaut, K. Surla, P. Galtier, and G.B. Marin, *Single-event microkinetic model for Fischer-Tropsch synthesis on iron-based catalysts.* Industrial & Engineering Chemistry Research, 2008. **47**(16): p. 5879-5891.
31. Martinis, J.M. and G.F. Froment, *Alkylation on solid acids. Part 2. Single-event kinetic modeling.* Industrial & Engineering Chemistry Research, 2006. **45**(3): p. 954-967.
32. Iglesia, E., S.C. Reyes, and R.J. Madon, *Transport-enhanced alpha-olefin readsorption pathways in Ru-catalyzed hydrocarbon synthesis.* Journal of Catalysis, 1991. **129**(1): p. 238-256.

33. Glasser, D., D. Hildebrandt, X. Liu, X. Lu, and C.M. Masuku, *Recent advances in understanding the Fischer–Tropsch synthesis (FTS) reaction.* Current Opinion in Chemical Engineering, 2012. **1**(3): p. 296-302.
34. Brown, P.N., A.C. Hindmarsh, and L.R. Petzold, *Using krylov methods in the solution of large-scale differential-algebraic systems.* Siam Journal on Scientific Computing, 1994. **15**(6): p. 1467-1488.
35. Lozano-Blanco, G., J.W. Thybaut, K. Surla, P. Galtier, and G.B. Marin, *Fischer-Tropsch synthesis: Development of a microkinetic model for metal catalysis.* Oil & Gas Science and Technology-Revue D Ifp Energies Nouvelles, 2006. **61**(4): p. 489-496.
36. Kua, J., F. Faglioni, and W.A. Goddard, *Thermochemistry for hydrocarbon intermediates chemisorbed on metal surfaces: CHn-m(CH3)(m) with n=1, 2, 3 and m <= n on Pt, Ir, Os, Pd, Ph, and Ru.* Journal of the American Chemical Society, 2000. **122**(10): p. 2309-2321.
37. Weststrate, C.J., P. van Helden, and J.W. Niemantsverdriet, *Reflections on the Fischer-Tropsch synthesis: Mechanistic issues from a surface science perspective.* Catalysis Today, In Press.
38. Tuxen, A., S. Carenco, M. Chintapalli, C.-H. Chuang, C. Escudero, E. Pach, P. Jiang, F. Borondics, B. Beberwyck, A.P. Alivisatos, G. Thornton, W.-F. Pong, J. Guo, R. Perez, F. Besenbacher, and M. Salmeron, *Size-Dependent Dissociation of Carbon Monoxide on Cobalt Nanoparticles.* Journal of the American Chemical Society, 2013. **135**(6): p. 2273-2278.
39. Böller, B., M. Ehrensperger, and J. Wintterlin, *In Situ Scanning Tunneling Microscopy of the Dissociation of CO on Co(0001).* ACS Catalysis, 2015. **5**(11): p. 6802-6806.
40. Shetty, S. and R.A. van Santen, *CO dissociation on Ru and Co surfaces: The initial step in the Fischer-Tropsch synthesis.* Catalysis Today, 2011. **171**(1): p. 168-173.
41. Liu, J.-X., H.-Y. Su, D.-P. Sun, B.-Y. Zhang, and W.-X. Li, *Crystallographic Dependence of CO Activation on Cobalt Catalysts: HCP versus FCC.* Journal of the American Chemical Society, 2013. **135**(44): p. 16284-16287.
42. Gong, X.-Q., R. Raval, and P. Hu, *CO dissociation and O removal on Co(0001): a density functional theory study.* Surface Science, 2004. **562**(1–3): p. 247-256.
43. Ojeda, M., R. Nabar, A.U. Nilekar, A. Ishikawa, M. Mavrikakis, and E. Iglesia, *CO activation pathways and the mechanism of Fischer-Tropsch synthesis.* Journal of Catalysis, 2010. **272**(2): p. 287-297.
44. Chen, C., Q. Wang, G. Wang, B. Hou, L. Jia, and D. Li, *Mechanistic Insight into the C2 Hydrocarbons Formation from Syngas on fcc-Co(111) Surface: A DFT Study.* Journal of Physical Chemistry C, 2016. **120**(17): p. 9132-9147.
45. Inderwildi, O.R., S.J. Jenkins, and D.A. King, *Fischer-tropsch mechanism revisited: Alternative pathways for the production of higher hydrocarbons from synthesis gas.* Journal of Physical Chemistry C, 2008. **112**(5): p. 1305-1307.
46. den Breejen, J.P., P.B. Radstake, G.L. Bezemer, J.H. Bitter, V. Froseth, A. Holmen, and K.P. de Jong, *On the Origin of the Cobalt Particle Size Effects in Fischer-Tropsch Catalysis.* Journal of the American Chemical Society, 2009. **131**(20): p. 7197-7203.
47. Yang, J., Y. Qi, J. Zhu, Y.A. Zhu, D. Chen, and A. Holmen, *Reaction mechanism of CO activation and methane formation on Co Fischer-Tropsch catalyst: A combined DFT, transient, and steady-state kinetic modeling.* Journal of Catalysis, 2013. **308**: p. 37-49.

48. Liu, J.-X., H.-Y. Su, and W.-X. Li, *Structure sensitivity of CO methanation on Co (0 0 0 1), and surfaces: Density functional theory calculations.* Catalysis Today, 2013. **215**: p. 36-42.
49. Zhuo, M.K., K.F. Tan, A. Borgna, and M. Saeys, *Density Functional Theory Study of the CO Insertion Mechanism for Fischer-Tropsch Synthesis over Co Catalysts.* Journal of Physical Chemistry C, 2009. **113**(19): p. 8357-8365.
50. Papp, H., *Chemisorption and reactivity of carbon monoxide on a Co(11-20) single crystal surface; studied by LEED, UPS, EELS, AES and work function measurements.* Surface Science, 1985. **149**(2-3): p. 460-470.
51. Geerlings, J.J.C., M.C. Zonnevylle, and C.P.M. de Groot, *Structure sensitivity of the Fischer-Tropsch reaction on cobalt single crystals.* Surface Science, 1991. **241**(3): p. 315-324.
52. Weststrate, C.J., P. van Helden, J. van de Loosdrecht, and J.W. Niemantsverdriet, *Elementary steps in Fischer–Tropsch synthesis: CO bond scission, CO oxidation and surface carbiding on Co(0001).* Surface Science, 2016. **648**: p. 60-66.
53. Herranz, T., X. Deng, A. Cabot, J. Guo, and M. Salmeron, *Influence of the Cobalt Particle Size in the CO Hydrogenation Reaction Studied by In Situ X-Ray Absorption Spectroscopy.* Journal of Physical Chemistry B, 2009. **113**(31): p. 10721-10727.
54. Wilson, J. and C. Degroot, *Atomic-Scale Restructuring in High-Pressure Catalysis.* Journal of Physical Chemistry, 1995. **99**(20): p. 7860-7866.
55. Markvoort, A.J., R.A. van Santen, P.A.J. Hilbers, and E.J.M. Hensen, *Kinetics of the Fischer-Tropsch Reaction.* Angewandte Chemie-International Edition, 2012. **51**(36): p. 9015-9019.
56. van Santen, R.A. and A.J. Markvoort, *Catalyst nano-particle size dependence of the Fischer-Tropsch reaction.* Faraday Discussions, 2013. **162**: p. 267-279.
57. van Santen, R.A. and A.J. Markvoort, *Chain Growth by CO Insertion in the Fischer-Tropsch Reaction.* Chemcatchem, 2013. **5**(11): p. 3384-3397.
58. Maestri, M., D. Livio, A. Beretta, and G. Groppi, *Hierarchical Refinement of Microkinetic Models: Assessment of the Role of the WGS and r-WGS Pathways in CH4 Partial Oxidation on Rh.* Industrial & Engineering Chemistry Research, 2014. **53**(27): p. 10914-10928.
59. Maestri, M., D.G. Vlachos, A. Beretta, G. Groppi, and E. Tronconi, *Steam and dry reforming of methane on Rh: Microkinetic analysis and hierarchy of kinetic models.* Journal of Catalysis, 2008. **259**(2): p. 211-222.
60. Maestri, M. and K. Reuter, *Molecular-level understanding of WGS and reverse WGS reactions on Rh through hierarchical multiscale approach.* Chemical Engineering Science, 2012. **74**: p. 296-299.
61. Sharma, H. and A. Mhadeshwar, *A detailed microkinetic model for diesel engine emissions oxidation on platinum based diesel oxidation catalysts (DOC).* Applied Catalysis B-Environmental, 2012. **127**: p. 190-204.
62. Maestri, M., D.G. Vlachos, A. Beretta, G. Groppi, and E. Rronconi, *A C-1 Microkinetic Model for Methane Conversion to Syngas on Rh/Al2O3.* Aiche Journal, 2009. **55**(4): p. 993-1008.
63. Karakaya, C., R. Otterstätter, L. Maier, and O. Deutschmann, *Kinetics of the water-gas shift reaction over Rh/Al2O3 catalysts.* Applied Catalysis A: General, 2014. **470**: p. 31-44.

64. Appari, S., V.M. Janardhanan, R. Bauri, S. Jayanti, and O. Deutschmann, *A detailed kinetic model for biogas steam reforming on Ni and catalyst deactivation due to sulfur poisoning.* Applied Catalysis A: General, 2014. **471**: p. 118-125.
65. Essmann, C., L. Maier, A.J. Li, S. Tischer, and O. Deutschmann, *Natural Gas Steam Reforming over Rhodium/Alumina Catalysts: Experimental and Numerical Study of the Carbon Deposition from Ethylene and Carbon Monoxide.* Industrial & Engineering Chemistry Research, 2014. **53**(31): p. 12270-12278.
66. Atkins, P. and J. De Paula, *Atkins' Physical Chemistry*. eighth ed. 2006, New York: Oxford University Press. 1100.
67. Bartholomew, C.H. and R.J. Farrauto, *Hydrogen Production and Synthesis Gas Reactions*, in *Fundamentals of Industrial Catalytic Processes*. 2005, John Wiley & Sons, Inc. p. 339-486.
68. Todic, B., W. Ma, G. Jacobs, B.H. Davis, and D.B. Bukur, *Effect of process conditions on the product distribution of Fischer–Tropsch synthesis over a Re-promoted cobalt-alumina catalyst using a stirred tank slurry reactor.* Journal of Catalysis, 2014. **311**: p. 325-338.
69. van Dijk, H.A.J., J.H.B. Hoebink, and J.C. Schouten, *Steady-state isotopic transient kinetic analysis of the Fischer-Tropsch synthesis reaction over cobalt-based catalysts.* Chemical Engineering Science, 2001. **56**(4): p. 1211-1219.
70. Benziger, J.B., *Thermochemical methods for reaction energetics on metal surfaces.* ChemInform, 1992. **23**(41).
71. Gong, X.Q., R. Raval, and P. Hu, *CHx hydrogenation on Co(0001): A density functional theory study*. Journal of Chemical Physics, 2005. **122**(2).
72. Cheng, J., T. Song, P. Hu, C.M. Lok, P. Ellis, and S. French, *A density functional theory study of the a-olefin selectivity in Fischer-Tropsch synthesis.* Journal of Catalysis, 2008. **255**(1): p. 20-28.
73. Kumar, P., J.W. Thybaut, S. Svelle, U. Olsbye, and G.B. Marin, *Single-Event Microkinetics for Methanol to Olefins on H-ZSM-5.* Industrial & Engineering Chemistry Research, 2013. **52**(4): p. 1491-1507.
74. Zhuo, M.K., A. Borgna, and M. Saeys, *Effect of the CO coverage on the Fischer-Tropsch synthesis mechanism on cobalt catalysts.* Journal of Catalysis, 2013. **297**: p. 217-226.
75. Khodakov, A.Y., B. Peregryn, A.S. Lermontov, J.S. Girardon, and S. Pietrzyk, *Transient studies of the elementary steps of Fischer-Tropsch synthesis.* Catalysis Today, 2005. **106**(1-4): p. 132-136.
76. Anfray, J., M. Bremaud, P. Fongarland, A. Khodakov, S. Jallais, and D. Schweich, *Kinetic study and modeling of Fischer-Tropsch reaction over a Co/Al2O3 catalyst in a slurry reactor.* Chemical Engineering Science, 2007. **62**(18-20): p. 5353-5356.
77. Cheng, J., P. Hu, P. Ellis, S. French, G. Kelly, and C.M. Lok, *A DFT study of the chain growth probability in Fischer-Tropsch synthesis.* Journal of Catalysis, 2008. **257**(1): p. 221-228.
78. Campbell, C.T., *Finding the Rate-Determining Step in a Mechanism: Comparing DeDonder Relations with the "Degree of Rate Control".* Journal of Catalysis, 2001. **204**(2): p. 520-524.
79. Deutschmann, O., H. Knözinger, K. Kochloefl, and T. Turek, *Heterogeneous Catalysis and Solid Catalysts*, in *Ullmann's Encyclopedia of Industrial Chemistry*. 2000, Wiley-VCH Verlag GmbH & Co. KGaA.
80. Lausche, A.C., A.J. Medford, T.S. Khan, Y. Xu, T. Bligaard, F. Abild-Pedersen, J.K. Norskov, and F. Studt, *On the effect of coverage-dependent adsorbate-adsorbate*

interactions for CO methanation on transition metal surfaces. Journal of Catalysis, 2013. **307**: p. 275-282.

81. Cheng, J., P. Hu, P. Ellis, S. French, G. Kelly, and C.M. Lok, *Density Functional Theory Study of Iron and Cobalt Carbides for Fischer-Tropsch Synthesis.* Journal of Physical Chemistry C, 2010. **114**(2): p. 1085-1093.
82. Lox, E.S., G.B. Marin, E. De Grave, and P. Bussière, *Characterization of a promoted precipitated iron catalyst for Fischer-Tropsch synthesis.* Applied Catalysis, 1988. **40**: p. 197-218.
83. Lox, E.S. and G.F. Froment, *Kinetics of the Fischer-Tropsch reaction on a precipitated promoted iron catalyst. 1. Experimental procedure and results.* Industrial & Engineering Chemistry Research, 1993. **32**(1): p. 61-70.
84. Espinoza, R.L., A.P. Steynberg, B. Jager, and A.C. Vosloo, *Low temperature Fischer-Tropsch synthesis from a Sasol perspective.* Applied Catalysis A: General, 1999. **186**(1-2): p. 13-26.

Chapter 4 Numerical Methods and Complex Reaction Network Generation for Steady State Isotopic Transient Kinetic Analysis*

A versatile modeling strategy for Steady State Isotopic Transient Kinetic Analysis (SSITKA) data, acquired in a plug flow reactor, is elaborated with particular attention to complex reaction networks such as encountered in Fischer-Tropsch Synthesis (FTS). A spatial discretization scheme optimizing numerical accuracy and CPU time is developed. In case of a low switch time constant in the SSITKA set-up used, the van Leer and van Albada flux limiter functions used in conjunction with the DASPK solver yield the lowest CPU time for the integration of the resulting ordinary differential equations (ODEs). For larger switch time constants, conventional central differencing can be applied. A dedicated network generation methodology is implemented accounting for the isotopic labeling. It limits the dependence of the number of considered species on the carbon number to a quadratic one. For a reaction network allowing a maximum chain length of 5 carbon atoms a gain in CPU time up to a factor of 10 can be achieved.

A modified version of this Chapter has been published in Computer and Chemical Engineering: Van Belleghem, J., et al., *Numerical methods and Fischer-Tropsch complex reaction network generation for steady state isotopic transient kinetic analysis.* Computers & Chemical Engineering (In Press).

4.1 Introduction

Heterogeneous catalysis is of key importance to the chemical process industry [1]. A fundamental understanding of the intrinsic reaction kinetics is of great importance aiming at improving and innovating these catalytic processes. As explained in Section 1.4.2, a very powerful technique to investigate catalysts at steady state conditions is the Steady State Isotopic Transient Kinetic Analysis (SSITKA) technique originally developed by Happel [2], Bennett [3] and Biloen [4]. Numerous reactions such as Fischer-Tropsch Synthesis (FTS), methane coupling, ammonia synthesis, etc. have been studied using this technique since its conception [5, 6].

In a SSITKA experiment, isotopically labeled atoms in the reactants and products are monitored as a function of the time after an abrupt switch of a reactant by an isotopically labeled counterpart while preserving the overall steady state operation of the catalyst. The transient responses are particularly useful to assess adsorbed intermediates surface life times and concentrations [6], see also eqs. [1–6] and [1–7]. While these quantities have already provided specific information with respect to metal particle size effects [7-9], promoter effects [10-18] as well as support effects [19-23], additional insights about the reaction pathway and how the aforementioned phenomena affect the catalyst activity and product selectivity can be obtained by combining SSITKA with kinetic modeling in a regression analysis [5]. These additional insights, which are quantified in terms of kinetic and catalyst descriptors, can further shorten the catalyst design cycle via a more rational model-guided design procedure [24, 25].

The present chapter focuses on the simulation of SSITKA data acquired for complex reactions in a plug flow reactor (PFR) as this is the preferred reactor configuration for SSITKA experiments [6]. The simulation of SSITKA data requires to focus on two aspects. On the one hand specific attention has to be paid to the stable and fast integration of the conservation equations involved. More specifically, due to convective nature of the conservation equations, a thorough assessment of different numerical methods is essential [26-30] and is discussed for the first time in the framework of SSITKA data modeling. More precisely, a case study has been performed in order to assess the performance of 14 flux limiter (FL) functions compared to higher order linear discretization schemes which can be prone to physically irrelevant oscillations in the numerical solution. Next to this, the impact on the CPU time of an adaptive moving grid method [31-33] has been assessed. A further reduction in CPU time can be obtained by an assessment of several stiff solvers and a semi-analytical treatment of the Jacobian matrix required by these solvers [34].

The other important aspect is the development of strategies to efficiently cope with the drastic increase in the number of species present in the reaction network due to the inclusion of an isotope. FTS has been selected to illustrate the impact of this on the reaction network generation and the microkinetic model, as it is one of the most actively investigated reactions with SSITKA [5] and is of a challenging complexity. The Single-Event MicroKinetic (SEMK) methodology is selected as modeling strategy as it is ideally suited to describe the conversion of complex reaction mixtures [35-40]. The combination of SEMK and a reaction network generation algorithm which takes the isotopic labeling into account is reported in this chapter for the first time. The number of species in the resulting reaction network literally explodes upon an increase in the carbon number of the longest hydrocarbon chain considered in this network. The strategy devised in the present chapter is a particularly suited trade-off between the required number of species to retrieve sufficient information with the model and the level of detail that can be obtained with the current experimental techniques.

4.2 Modeling procedures

4.2.1 Numerical integration

The concentration of the various gas phase components and surface species as a function of space and time is obtained by integrating a set of partial differential equations (PDEs), eq. [2–30] and eq. [2–31]. The integration of this set of equations is done by means of ‘the method of lines’ (MOL) [41]. The numerical domain is discretized in the direction of the spatial variable, see Figure 4-1. A control volume ranging from x_e to x_w is considered around a discretization point. Both points, x_e and x_w, are located halfway two discretization points. Eq. [2–30] and eq. [2-31] are integrated in space from x_e to x_w, which gives after integration:

$$\begin{gathered}\frac{dC_{i'}}{dt} = \frac{\rho_b}{\varepsilon_b} R_{i'}\left(x_j, t\right) - \frac{1}{\tau_b \Delta x}\left(C_{i'}(x_w, t) - C_{i'}(x_e, t)\right) \\ \frac{dL_{j'}}{dt} = R_{j'}\left(x_j, t\right)\end{gathered} \qquad [4\text{-}1]$$

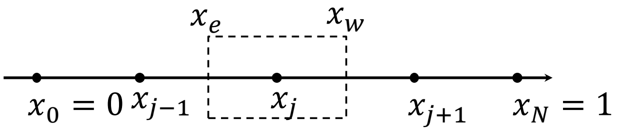

Figure 4-1: Discretization of the spatial domain. A control volume is centered around grid point x_j ranging from x_w to x_e which are points located halfway the discretization points.

A specific discretization scheme is obtained by the corresponding approximation of the concentration at the boundaries of the control volume. For example, approximating the concentration at x_e by the concentration at x_{j-1} and x_w by the concentration at x_j results in the First Order Upwind (FOU) discretization scheme.

The convective nature of the PDEs calls for specific attention in the selection of an appropriate discretization scheme [26-30]. Sharp gradients will result in spurious oscillations in the numerical solution when linear discretization schemes are employed except in the case of the FOU scheme which is unconditionally stable but of low accuracy. Therefore, so-called non-linear discretization schemes have been developed for the approximation of the concentration at the boundaries of the control volume.

As the CPU time can vary drastically depending on the considered discretization scheme, a case study has been performed in which the performance of several linear and non-linear discretization schemes is assessed for variations in space time, i.e., from 4 (kg_{cat} s)mol_{CO}^{-1} to 400 (kg_{cat} s)mol_{CO}^{-1}, and switch time constant, a_2 in eq. [2–34], in the SSITKA set-up, i.e., from 0.01 s to 1.0 s. The reaction conditions, properties of the catalyst pellets and dilution material and reactor characteristic are provided in Table 4-1.

Table 4-1: Reaction conditions and properties of the catalyst pellets, dilution material and reactor characteristics.

Quantity	
Temperature $[K]$	553
Pressure $[MPa]$	0.2
Catalyst mass $[kg]$	0.011
Mass of dilution material $[kg]$	0.022
Density catalyst particle $[kg\ m^{-3}]$	3000.0
Density dilution material $[kg\ m^{-3}]$	3200.0
Reactor diameter $[m]$	0.01
Reactor length $[m]$	0.25
Porosity catalyst particle $[-]$	0.40
Bed density $[kg\ m^{-3}]$	573
Bed porosity $[-]$	0.53
$F_{H2,0}/F_{CO,0}$ $[mol\ mol^{-1}]$	5
$F_{inert,0}/F_{CO,0}$ $[mol\ mol^{-1}]$	10

Linear discretization schemes considered in the case study

For the linear discretization schemes, second order central differencing (SOCD) [41], eq. [4-2] , and second order upwinding (SOU) [29], eq. [4-3], have been selected. The latter was also considered as upwinding can improve the integration stability [29].

$$\frac{dC_{i'}}{dt} = \frac{\rho_b}{\varepsilon_b} R_{i'}\left(x_j, t\right) - \frac{1}{\tau_b \Delta x}\left(C_{i'}\left(x_{j+1}, t\right) - C_{i'}\left(x_{j-1}, t\right)\right) \qquad [4\text{-}2]$$

$$\frac{dC_{i'}}{dt} = \frac{\rho_b}{\varepsilon_b} R_{i'}\left(x_j, t\right) - \frac{1}{\tau_b 2\Delta x}\left(3C_{i'}\left(x_j, t\right) - 4C_{i'}\left(x_{j-1}, t\right) + C_{i'}\left(x_{j-2}, t\right)\right) \qquad [4\text{-}3]$$

Non-linear discretization schemes considered in the case study

The approximation of the concentrations at the boundaries of the control volume, i.e., $C_{i'}(x_e, t)$ and $C_{i'}(x_w, t)$ of eq. [4-1], in case the non-linear discretization schemes are used, are obtained by applying the flux limiter (FL) approach, eq. [4-4] to eq. [4-6] [28], which also covers the normalized variable approach [30]:

$$C_{i'}(x_w, t) = C_{i'}\left(x_j, t\right) + \frac{\varphi\left(r_{j+1}\right)}{2}\left(C_{i'}\left(x_{j+1}, t\right) - C_{i'}\left(x_j, t\right)\right) \qquad [4\text{-}4]$$

$$C_{i'}(x_e, t) = C_{i'}\left(x_{j-1}, t\right) + \frac{\varphi\left(r_j\right)}{2}\left(C_{i'}\left(x_j, t\right) - C_{i'}\left(x_{j-1}, t\right)\right) \qquad [4\text{-}5]$$

Where φ is a flux limiter function, which depends on the ratio, r_j, of the concentration gradient of the upstream control volume boundary to that of the downstream control volume boundary:

$$r_j = \frac{C_{i'}\left(x_{j-1}, t\right) - C_{i'}\left(x_{j-2}, t\right)}{C_{i'}\left(x_j, t\right) - C_{i'}\left(x_{j-1}, t\right)} \qquad [4\text{-}6]$$

The ratio of the concentration gradients use two upwind points and one downwind point. Hence, for the discretization points located near the boundaries of the domain FOU is used to ensure the discretization scheme is unconditionally stable.

The FL function, φ, is designed to adapt the discretization scheme based on the local gradient of the solution. Where possible, higher-order discretization schemes are used while in the case of a steep gradient the FL function reduces the discretization scheme to lower-order discretization schemes to ensure that a boundedness criterion is fulfilled [30]. For example, Sweby [42] showed that to fulfill the Total Variation Diminishing, TVD, criterion, the FL function should be within the grey area indicated in Figure 4-2. For small values of r_j and, hence, a steep gradient, the FL function should have a low value, bringing in a large contribution of the first order upwind scheme, see eq. [4-4] to eq. [4-6]. If the solution shows a smooth variation, i.e., r_j close to one, the TVD criterion allows to reduce the contribution from the FOU scheme increasing the order of approximation.

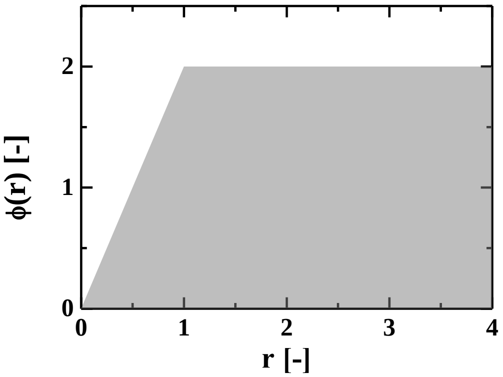

Figure 4-2: The Total Variation Diminishing area in the flux limiter diagram [42].

Many FL functions have been proposed in literature and can be classified according to their mathematical expression [30]. In total, 4 classes have been defined, i.e., symmetric piecewise linear (SPL) schemes, generalized piecewise-linear (GPL) schemes, smooth, continuous polynomial-ratio (PR) schemes and discontinuous PR schemes [30]. Next to this, four design principles are derived for FL functions which can give an indication about the convergence behavior of FL functions. According to the design principles, it is expected that the FL functions which (1) are symmetric, (2) do not switch around $r_j = 1$, (3) follow Fromm's scheme [43] around $r_j = 1$ and (4) have a moderate value for the maximum bound, i.e., between 1 and 4, should show acceptable convergence behavior [30].

14 candidate FL functions have been considered covering all classes of FL functions. The function prescription of these FL functions are listed in Table 4-2 together with the design principles [30] of the FL functions. Based on these design principles, Koren, MUSCL, van Leer, van Albada, OSPRE, GPR-1/2 and GVA-1/2 are expected to give the best performance.

Table 4-2: The flux limiter functions considered in the case study. κ indicates the behavior of the FL function around r_j=1. Two values means that 2 linear schemes are mixed around r_j=1, one value indicates which linear κ scheme is followed around r_j=1. M indicates the maximum bound. [26, 28, 30, 44-50]

Flux limiter	Function prescription	Symmetric	κ	M
Minmod [44]	$\varphi(r) = \max(0, \min(r, 1))$	✔	1,-1	1
Superbee [45]	$\varphi(r) = \max(0, \min(2r, 1), \min(r, 2))$	✔	1,-1	2
Koren [46]	$\varphi(r) = max\left[0, min\left(2r, \frac{2r}{3} + \frac{1}{3}, 2\right)\right]$	✔	1/3	2
MUSCL [47]	$\varphi(r) = \max\left[0, \min\left(2r, \frac{r}{2} + \frac{1}{2}, 2\right)\right]$	✔	0	2
van Leer [48]	$\varphi(r) = \frac{r + \lvert r \rvert}{r + 1}$	✔	0	2
SPL-1/3 [30]	$\varphi(r) = max\left[0, min\left(2r, \frac{2r}{3} + \frac{1}{3}, \frac{2}{3} + \frac{1}{3}r, 2\right)\right]$	✔	1/3,-1/3	2
SMART [49]	$\varphi(r) = \max\left[0, \min\left(2r, \frac{3r}{4} + \frac{1}{4}, 4\right)\right]$	X	1/2	4
van Albada [50]	$\varphi(r) = \frac{r(r + 1)}{r^2 + 1}$	✔	0	1
OSPRE [30]	$\varphi(r) = \frac{3r(r + 1)}{2(r^2 + r + 1)}$	✔	0	1.5
H-CUI [30]	$\varphi(r) = \frac{3(r + \lvert r \rvert)}{2(r + 2)}$	X	1/3	3

Table 4-2: continued

Flux limiter	Function prescription	Symmetric	κ	M
H-QUICK [30]	$\varphi(r) = \frac{4(r+\lvert r\rvert)}{2(r+3)}$	X	1/2	4
SMARTER [51]	$\varphi(r) = \frac{(r+\lvert r\rvert)(3r+1)}{2(r+1)^2}$	X	1/2	3
GPR-1/2 [30]	$\varphi(r) = \frac{2r(r+1)}{r^2+r+2}$	X	1/2	2
GVA-1/2 [30]	$\varphi(r) = \frac{r(r+3)}{r^2+3}$	X	1/2	1

4.2.2 Moving grid

A moving grid method allows to reduce the number of grid points compared to a simulation performed on a fixed grid [32, 33]. As such, the required CPU time to perform a simulation can potentially be reduced. In this chapter, the number of grid points during a simulation with a moving grid is kept constant but the location of these grid points changes during the simulation. This in contrast to other adaptive grid methods which locally increase the grid resolution by adding grid points [33].

The location of the moving grid points is determined by simultaneously solving a time dependent equation for each grid point. The implementation of the grid point equations has been taken from Algorithm 731 [52]. As the grid points are now moving as a function of time eq. [2–30] and eq. [2–31] have to be formulated in Lagrange form [33]:

$$\begin{gathered}\frac{\partial C_{i'}(x,t)}{\partial t}-\frac{\partial x}{\partial t}\frac{\partial C_{i'}(x,t)}{\partial x}+\frac{1}{\tau_b}\frac{\partial C_{i'}(x,t)}{\partial x}=\frac{\rho_b}{\varepsilon_b}R_{i'}(x,t)\\ \frac{\partial L_{j'}(x,t)}{\partial t}-\frac{\partial x}{\partial t}\frac{\partial L_{j'}(x,t)}{\partial x}=R_{j'}(x,t)\end{gathered} \qquad [4\text{-}7]$$

The additional term from the Lagrange transformation has been discretized by using SOCD. This was found to be sufficient for convection-dominated PDEs [33].

4.2.3 Error analysis

As an analytical solution was lacking, numerical solutions were first obtained using the FOU scheme. The number of grid points was gradually increased until there were no significant differences between two simulations. The error was calculated as follows:

$$error(n_{gp})=\sqrt{\sum_{i=1}^{n_{gas\,comp}}\sum_{j=1}^{n_{time\,steps}}\left(\frac{C_{i',n_{gp}}(1,j\Delta t)}{C_i^{ss}}-\frac{C_{i',n_{gp,max}}(1,j\Delta t)}{C_i^{ss}}\right)^2} \qquad [4\text{-}8]$$

Where, n_{gp} is the number of grid points, $n_{gas\,comp}$ is the number of gas phase components for which eq. [2–30] is solved, $n_{time\,steps}$ is the number of time steps, $n_{gp,max}$ is the maximum number of grid points, $C_{i',n_{gp}}(1, j\Delta t)$ is the concentration of gas phase species i' at the exit of the reactor for n_{gp} number of grid points at time step j, C_i^{ss} is the steady state concentration of gas phase components i.

The deviation between the simulation results obtained with a discretization scheme and the simulation results obtained for the converged solution with FOU discretization scheme is defined as:

$$error(n_{gp}) = \sqrt{\sum_{i=1}^{n_{gas\ comp}} \sum_{j=1}^{n_{time\ steps}} \left(\frac{C_{i',n_{gp}}^{DS}(1, j\Delta t)}{C_i^{ss}} - \frac{C_{i'}^{FOU}(1, j\Delta t)}{C_i^{ss}} \right)^2} \qquad [4\text{-}9]$$

Where, $C_{i',n_{gp}}^{DS}(1, j\Delta t)$ is the concentration of gas phase components i' at the reactor outlet for n_{gp} number of grid points at time step j obtained with a discretization scheme and $C_{i'}^{FOU}(1, j\Delta t)$ is the concentration of gas phase species i' at reactor outlet of the converged solution obtained with FOU discretization at time step j.

4.2.4 The Jacobian Matrix

The differences in time scale between reaction and convection can be quite large. Moreover, significant differences may also exist in the time scales among the various elementary steps in the network. This necessitates the use of solvers which can adequately handle the stiffness originating from these large differences. An important matrix during the numerical integration when using such solvers is the so called Jacobian matrix, see also section 2.2.5.

The Jacobian matrix originating from a set of ODEs after applying the MOL to a set of PDEs has a banded structure. Explicitly accounting for the banded structure of the Jacobian matrix in the numerical routines used for solving the set of equations describing the SSITKA reactor limits the increase in required CPU time for calculating the Jacobian matrix from a quadratic dependence on the number of equations to a linear one with a proportionality constant equal to the band width. The structure of the Jacobian matrix in case the discretization is carried out with a FL function is illustrated in Figure 4-3. The two lines to left and the one line to the right of the main diagonal come from the discretized convective terms of eq. [4-1]. Only the parts of these three lines indicated by the dashed lines are different from zero as only the gas phase components can be transported by convection. The derivatives of these flux terms are approximated by finite differences as most of the flux limiters are piecewise functions. The numerical formulas of the finite differences have been taken from the source code of the different backward differentiation solvers, i.e. VODE [53], DASPK [54], LSODE [55] and LSODA [55].

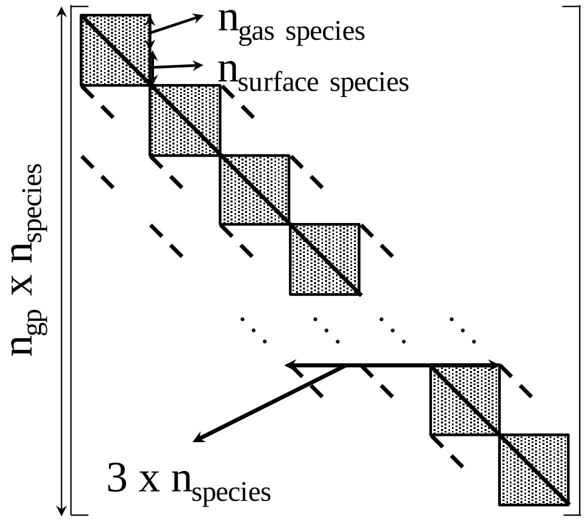

Figure 4-3: Graphical representation of the Jacobian matrix. Full line: Main diagonal. Squares: derivatives of the net production rate terms, i.e., the first terms of the right hand side of eq. [4-1]. Dashed lines: derivatives of the discretized convective terms of the right hand side of eq. [4-1] when using flux limiter functions, eq. [4-4] to eq. [4-6].

The derivatives of the net production rate terms, eq. [2–15], of the gas phase and surface species are only different from zero in the squares indicated in Figure 4-3 and can be determined analytically [34]:

$$\frac{dR_i}{dC_j} = \sum_{k=1}^{n_{reactions}} \left(\nu_{k,i}^{f} + \nu_{k,i}^{r}\right) \frac{dr_k}{dC_j} \qquad [4\text{-}10]$$

With,

$$\frac{dr_k}{dC_j} = k_k^f \left(\prod_{\substack{i=l \\ i \neq j}}^{n_{species}} C_i^{-\nu_{k,i}^f} \right) \left(-\nu_{k,j}^f\right) C_j^{\left(-\nu_{k,j}^f - 1\right)} - k_k^r \left(\prod_{\substack{i=l \\ i \neq j}}^{n_{species}} C_i^{\nu_{k,i}^r} \right) \left(\nu_{k,i}^r\right) C_j^{\left(\nu_{k,i}^r - 1\right)} \qquad [4\text{-}11]$$

Where $\nu_{k,i}^f$ the forward stoichiometric coefficient of the kth elementary step belonging to the ith gas phase component or surface species which is by convention negative, $\nu_{k,i}^r$ the reverse stoichiometric coefficients of the kth elementary reaction belonging to the ith gas phase component or surface species which is by convention positive and r_k the rate of the kth elementary reaction step.

The analytical treatment of the derivatives of the net production rate terms can considerably speed up the simulations as typically only a limited number of positions within the blocks on the main diagonal of the banded matrix will be different from zero for large reaction networks.

4.2.5 Microkinetic model

The carbene insertion mechanism, see also Section 1.3.3 and Section 3.2.2.3, [56] has been considered to simulate the FTS reaction. According to this mechanism [57], CO is first dissociated in C and O. C subsequently undergoes hydrogenation steps to a CH_2 species which is then incorporated in a growing metal alkyl chain. Alkane formation is described by hydrogenation of a metal alkyl chain. Metal alkenes are produced by a beta hydride elimination of a metal alkyl chain which can desorb as alkenes.

The forward rate coefficients are calculated based on the SEMK methodology, see section 2.2.1.1. The reverse rate coefficients are obtained by applying the concept of thermodynamic consistency at the elementary step level, see section 2.2.1.3 and section 2.2.1.4. The forward activation energies and UBI-QEP parameters used in this modeling study are listed in Table 3–9.

4.3 Reaction network generation accounting for isotopes

4.3.1 Impact on reaction network generation

The standardized label, see section 2.2.3, is extended with an additional row to track the isotopic labeling of the carbon atoms. On each position of this additional row a ‘12’ or a ‘13’ is stored if it corresponds to a carbon atom. The Boolean matrix representation, see section 2.2.3, remains unchanged as only the connectivity between atoms is indicated in this matrix. The additional information is stored in a complementary vector. Hence, the operations on the Boolean matrices to generate the elementary steps and the corresponding reaction products do not need any modification. With respect to the elementary steps, methylene insertion can now occur both via $^{12}CH_2^{**}$ and $^{13}CH_2^{**}$ species. Furthermore, it is noted that care has to be taken to avoid certain species to occur more than once in the final reaction network. For example, in a first step, eight propane molecules will be generated while only 6 isotopically labeled propane molecules are unique. This is illustrated in Figure 4-4. The isotopically labeled propane molecules in the dashed rectangles are generated twice in first instance. This is recognized by the network generation algorithm and for each of the two ‘pairs’, only a single species is kept by the program.

The symmetry numbers of the isotopically labeled species are calculated during the network generation. The isotopic labeling will typically diminish the external symmetry of the species. This is illustrated also in Figure 4-4 for propane. Unlabeled propane has a global symmetry number of 18. From the six possible isotopically labeled propane molecules, two loose the C_2 external symmetry axis compared to unlabeled propane. This reduces the global symmetry number for these two species to 9, i.e., the product of the symmetry number related to the methyl rotors. The other four molecules keep the global symmetry number of 18.

In Table 4-3 the total number of species in the reaction network accounting for isotopic labeling is calculated as a function of the carbon number of the longest hydrocarbon chain, CN_{max}, considered in the network. It is clear that the number of species increases dramatically with this carbon number. For a carbon number equal to 10, the number of species equals 8190 making this description of the kinetics computationally too demanding for regression to experimental data. Moreover, it is impossible to experimentally observe all these species.

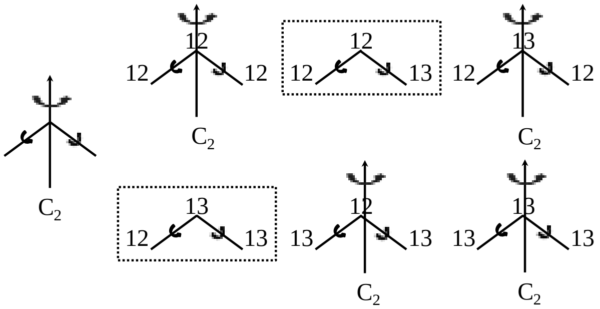

Figure 4-4: Global symmetry numbers of unlabeled and labeled propane.

Table 4-3: Number of species in the reaction network as a function of the carbon number of the longest hydrocarbon considered in the reaction network (CN_{max}). CN_{det}: the maximum chain length of hydrocarbons for which all isotopologues and for each isotopologue all isotopomers are accounted for in a reaction network.

$\boldsymbol{CN_{max}}$	$\boldsymbol{CN_{det} = CN_{max}}$	$\boldsymbol{CN_{det} = 2}$
5	254	123
6	510	171
7	1022	227
8	2046	291
9	4094	363
10	8190	443

4.3.2 Reducing the number of species and elementary steps

As the number of species and elementary steps increases sharply with the carbon number of the longest hydrocarbon chain that is considered in the network, a strategy is required to reduce these numbers. The CPU time required to perform the simulation of a single experiment would become excessively high if the full, detailed network would be employed. Moreover, the experimental detail that can reasonably be acquired with respect to labeling is limited to the fraction of ^{12}C in the hydrocarbon chain [58]. Only for the smaller molecules, it may be possible to track the intermediate isotopically labeled hydrocarbons, e.g., the transient response of ethane with only ^{12}C atoms, ethane with one ^{12}C atom and ethane with only ^{13}C atoms [59].

The level of detail in the considered reaction network should, hence, match the information that is acquired experimentally. To this purpose, two types of information need to be followed. As explained by van Santen et al. [9], the isotopic fraction at each position in the chain has to be followed due to the potential reversibility of the chain growth process [60]. This information, i.e., the isotopic fraction at each position in the chain, can be used to generate the total isotopic fraction of ^{12}C or ^{13}C in the hydrocarbon chain. To simulate the transient responses of specific isotopically labeled hydrocarbons with a smaller carbon number than the longest hydrocarbon for which experimental data are available, a reaction network as described in Section 4.3.1 considering all isotopologues and all isotopomers for at least this smaller set of hydrocarbons will have to be used. A methodology to track this latter type of information on top of the isotopic fraction at each position in the chain of the longer hydrocarbons for which no intermediate isotopically labeled experimental data are available, is outlined in the following paragraphs for isotopically labeled metal alkyls. Its extension to isotopically labeled metal alkenes, alkanes and alkenes is straightforward and was implemented as well.

The species considered in a reaction network limited to hydrocarbons with maximum carbon atom CN_{max} are split into two groups. This is illustrated on the left of Figure 4-5. A first group comprises those species with a maximum carbon number, CN_{det}, for which all possible isotopologues and isotopomers are followed. This group is indicated in Figure 4-5 by '1'. The second group, indicated by '2' in Figure 4-5, comprises all other species from which only subsets are followed. Two types of subsets are defined as illustrated on the right of Figure 4-5, and implemented per carbon number.

The first type of subset is defined to follow the total concentration of species with a ^{12}C or ^{13}C at a specific position i in the alkyl chain with $1 \leq i < CN_{max} - CN_{det}$, irrespective of the labeling of the other carbon atoms. The two subsets corresponding to a position i cover all species of a specific carbon number and are mutually exclusive. These subsets are illustrated in Figure 4-5 by 'a' and 'b' for $i = 1$. Subsets corresponding to different positions, e.g., for longer chains than metal propyls with $CN_{det} = 2$, would be indicated by 'a'' and 'b'', etc… and are no longer mutually exclusive. These subsets follow the total concentration of ^{12}C or ^{13}C at a position i with

$2 \leq i \leq CN_{max} - CN_{det}$ corresponding with positions in the hydrocarbon chain different from carbon atoms directly attached to the surface or carbon atoms present in the last CN_{det} carbon atoms in the hydrocarbon chain. The second type of subset is defined to follow the concentration of species with the specific labeling of the CN_{det} last carbon atoms in the hydrocarbon chain, irrespective of the labeling of the other carbon atoms in the chain. All these latter subsets are also mutually exclusive and cover all species of the considered carbon atom. These subsets are illustrated in Figure 4-5 by 'c' – 'f'. The gain in terms of the number of species that needs to be monitored is illustrated in Table 4-3 as a function of CN_{max} with CN_{det} equal to 2. The total number of species if CN_{max} is equal to 10 is reduced to 443 compared to 8190 if all the isotopically labeled species are considered.

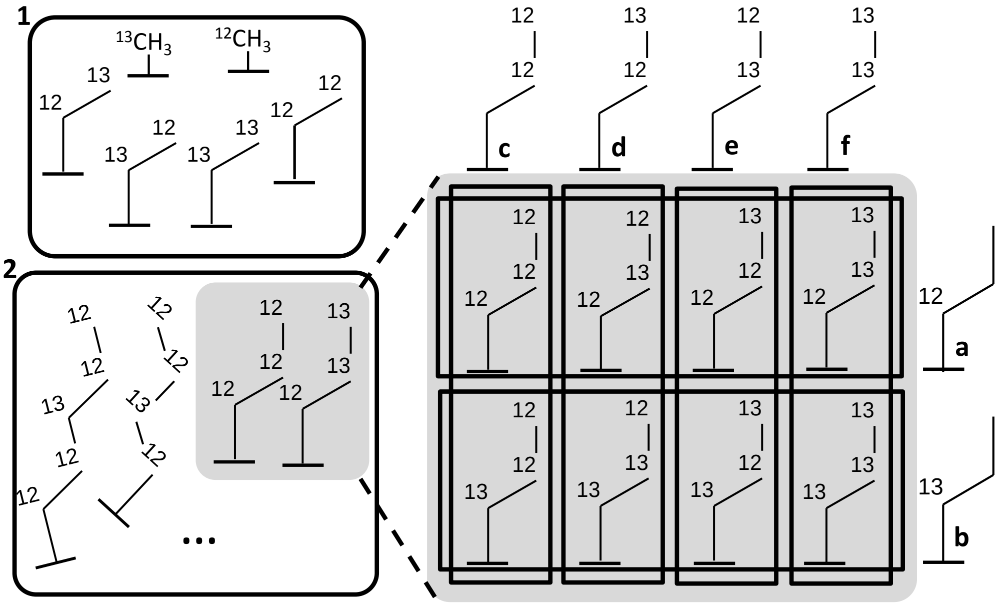

Figure 4-5: Graphical representation of the different type of subsets introduced in the reaction network. 1: group comprising those species with a maximum carbon number, CN_{det} for which all possible isotopologues and isotopomers are followed. 2: complement of group 1 for which subsets are introduced. These subsets are illustrated for the isotopic labeled metal propyl species and is done on the basis of the labeling of the carbon atom on a position *i* in the chain with $1 \leq i \leq CN_{max} - CN_{det}$ (a and b) or the isotopic labeling of the penultimate and ultimate carbon atom (c –f).

The total concentration of ^{12}C atoms in an alkane or alkene can then be calculated:

$$\begin{aligned} C^{^{12}C}_{C_iH_{2i+2}} = & \sum_{j=1}^{CN_{max}-CN_{det}} C^{j,^{12}C}_{C_iH_{2i+2}} \\ & + \sum_{j=1}^{2^{CN_{det}}} \left(N_{^{12}C}\left(\left\{ {}^{*}C_{i-CN_{det}} \dots {}^{*}C_i \right\}_j\right) C^{\left\{ {}^{*}C_{i-CN_{det}} \dots {}^{*}C_i \right\}_j}_{C_iH_{2i+2}} \right) \end{aligned} \qquad [4\text{-}12]$$

Where, $C^{^{12}C}_{C_iH_{2i+2}}$ is the gas phase concentration of the alkanes with i carbon atoms and a ^{12}C at a position in the chain, $C^{j,^{12}C}_{C_iH_{2i+2}}$ is the gas phase concentration of the alkanes with i carbon atoms and a ^{12}C at the jth position in the chain, $N_{^{12}C}(\cdot)$ stands for an operator which determines the number of ^{12}C atoms in element $\left\{ {}^{*}C_{i-CN_{det}} \dots {}^{*}C_i \right\}_j$ and $\left\{ {}^{*}C_{i-CN_{det}} \dots {}^{*}C_i \right\}_j$ is the jth element among all possible isotopologues and isotopomers which can be formed with the last CN_{det} carbon atoms of an alkanes with i carbon atoms. The '*' indicates that the carbon atom has a specific isotopic label, i.e., '12' or '13'.

4.3.3 Expression for the net production rates

Figure 4-6 illustrates the methylene insertion and deinsertion step. The formation rate of metal alkyl chains with $i+1$ carbon atoms that are bonded to the metal atom via a ^{12}C via methylene insertion is found by considering the steady state concentration of the metal alkyl chain with i carbon atoms and the concentration of the ^{12}C labeled monomer. This is indicated in Figure 4-6 by the dotted line.

The formation rate of metal alkyl chains with $i+1$ carbon atoms and a ^{12}C at a position $j+1$ in the chain is found by considering the methylene insertion between the metal alkyl chains with i carbon atoms and ^{12}C at the jth position in the chain with the $CH_2^{**,ss}$ concentration. This is illustrated by the dashed line in Figure 4-6.

The formation rate of the metal alkyl species with a detailed tail and $i+1$ carbon atoms is found by considering the methylene insertion between the steady state monomer concentration and the corresponding metal alkyl chain with the same tail but with i carbon atoms. This is illustrated in Figure 4-6 by the dash-dot-dotted line.

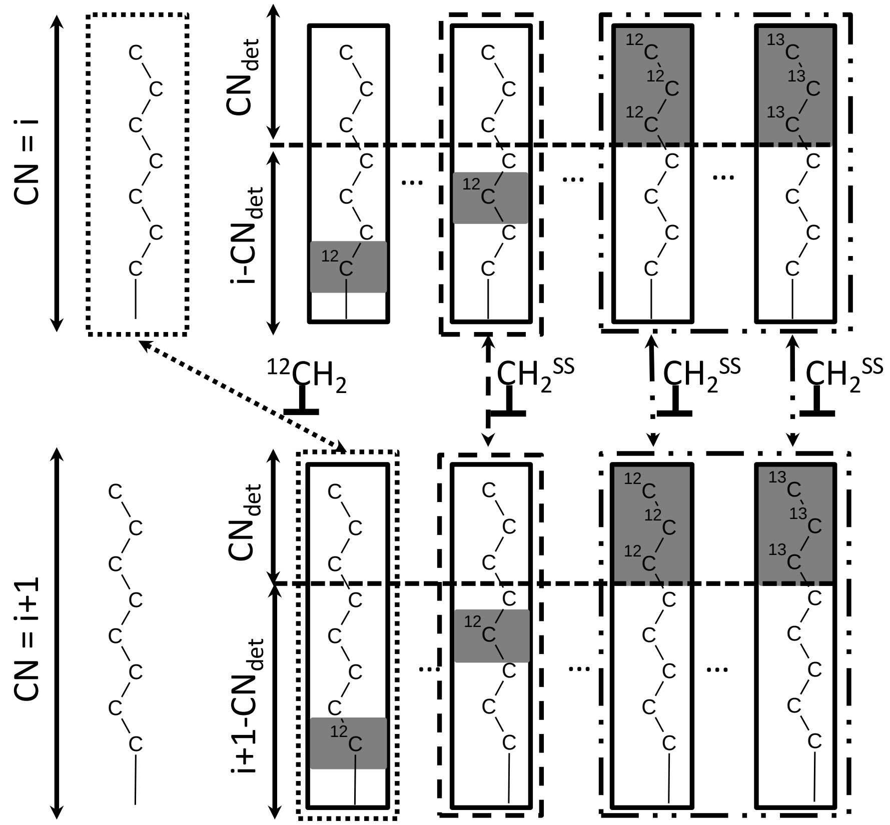
CN = i
CN_det
i-CN_det
12
13
...
12CH2
CH2SS
CH2SS
CH2SS
CN = i+1
CN_det
i+1-CN_det

Figure 4-6: Illustration of the methylene insertion and methylene deinsertion step between the two types of subsets introduced in the metal alkyl species.

The expression for the net production rate of ${}^{12}CH_2^{**}$ is given by eq. [4-13]. These methylene species are consumed by methylene insertions, hydrogenation to metal methyl species and dehydrogenation to ${}^{12}CH^{***}$. The production of the ${}^{12}CH_2^{**}$ species follows from hydrogenation of ${}^{12}CH^{***}$, by methylene deinsertion steps and dehydrogenation of ${}^{12}CH_3^{*}$.

$$\begin{aligned} R_{L^{^{12}C}_{CH_2}} = {} & \frac{z}{2}\frac{\sigma_r}{\sigma_\ddagger}\tilde{k}_{CHhyd}L^{^{12}C}_{CH}\frac{L_H}{L_{tot}} - \left(\frac{z}{2}\right)^2\frac{\sigma_r}{\sigma_\ddagger}\tilde{k}_{CH_2dehyd}L^{^{12}C}_{CH_2}\left(\frac{L_*}{L_{tot}}\right)^2 \\ & - \frac{z}{2}\frac{\sigma_r}{\sigma_\ddagger}\tilde{k}_{CH_2hyd}L^{^{12}C}_{CH_2}\frac{L_H}{L_{tot}} + \left(\frac{z}{2}\right)^2\frac{\sigma_r}{\sigma_\ddagger}\tilde{k}_{CH_3dehyd}L^{^{12}C}_{CH_3}\left(\frac{L_*}{L_{tot}}\right)^2 \\ & - \frac{z}{2}\frac{\sigma_r}{\sigma_\ddagger}\tilde{k}_{mi}L^{^{12}C}_{CH_2}\sum_{i=1}^{CN_{max}}\frac{L^{SS}_{C_iH_{2i+1}}}{L_{tot}} \\ & + \left(\frac{z}{2}\right)^2\frac{\sigma_r}{\sigma_\ddagger}\tilde{k}_{md}\left(\frac{L_*}{L_{tot}}\right)^2\left(\sum_{i=2}^{CN_{\mathrm{det}}}\left(\sum_{j=1}^{2^{i-1}}L^{\{^{12}C_1\ ^*C_2\ldots\ ^*C_i\}_j}_{C_iH_{2i+1}}\right)\right. \\ & \left. + \sum_{i=CN_{det}+1}^{CN_{max}}L^{1,^{12}C}_{C_iH_{2i+1}}\right) \end{aligned} \qquad [4\text{-}13]$$

Where $L^{^{12}C}_{CH_2}$ represents the methylene surface concentration with a ^{12}C atom, $L^{^{12}C}_{CH}$ the methylidyne surface concentration with a ^{12}C atom, $L^{^{12}C}_{CH_3}$ the metal methyl surface concentration with a ^{12}C atom, $L^{\{^{12}C_1\ ^*C_2\ldots\ ^*C_i\}_j}_{C_iH_{2i+1}}$ the surface concentration of metal alkyl species j of the set of all the metal alkyl species with in total i carbon atoms of which the carbon attached to the metal surface is a ^{12}C and $L^{1,^{12}C}_{C_iH_{2i+1}}$ the surface concentration of metal alkyl species with i carbon atoms and a ^{12}C atom attached to the metal surface.

The net production rate of the metal alkyl species with carbon number i and a ^{12}C atom bonded to the metal atom is obtained from eq. [4-14]. These species are produced by methylene insertion of a $^{12}CH_2^{**}$ into a metal alkyl species with $i-1$ carbon atoms, methylene deinsertion of a metal alkyl species with $i+1$ carbon atoms and a ^{12}C at the second position with respect to the metal atom, dehydrogenation of the corresponding alkane and beta hydride addition to the corresponding metal alkene species. The consumption of metal alkyl species with i carbon atoms and a ^{12}C bonded to the metal atom occurs via methylene insertion by a $^{12}CH_2^{**}$ or $^{13}CH_2^{**}$, methylene deinsertion, hydrogenation to the corresponding alkane and beta hydride elimination to the corresponding metal alkene.

$$\begin{aligned}R_{L^{1,{}^{12}C}_{C_iH_{2i+1}}} &= \frac{z}{2}\frac{\sigma_r}{\sigma_\ddagger}\tilde{k}_{mi}L^{{}^{12}C}_{CH_2}\frac{L^{SS}_{C_{i-1}H_{2i-1}}}{L_{tot}} - \frac{z}{2}\frac{\sigma_r}{\sigma_\ddagger}\tilde{k}_{mi}L^{SS}_{CH_2}\frac{L^{1,{}^{12}C}_{C_iH_{2i-1}}}{L_{tot}} \\ &\quad + \left(\frac{z}{2}\right)^2\frac{\sigma_r}{\sigma_\ddagger}\tilde{k}_{md}L^{2,{}^{12}C}_{C_{i+1}H_{2i+3}}\left(\frac{L_*}{L_{tot}}\right)^2 - \left(\frac{z}{2}\right)^2\frac{\sigma_r}{\sigma_\ddagger}\tilde{k}_{md}L^{1,{}^{12}C}_{C_iH_{2i+1}}\left(\frac{L_*}{L_{tot}}\right)^2 \\ &\quad - \frac{z}{2}\frac{\sigma_r}{\sigma_\ddagger}\tilde{k}_{C_nH_{2n+1}hyd}L^{1,{}^{12}C}_{C_iH_{2i+1}}\frac{L_H}{L_{tot}} \\ &\quad + \frac{z}{2}\frac{\sigma_r}{\sigma_\ddagger}\tilde{k}_{C_nH_{2n+2}dehyd}RTC^{1,{}^{12}C}_{C_iH_{2i+1}}\left(\frac{L_*}{L_{tot}}\right)^2 \\ &\quad - \frac{z}{2}\frac{\sigma_r}{\sigma_\ddagger}\tilde{k}_{C_nH_{2n+1}be}L^{1,{}^{12}C}_{C_iH_{2i+1}}\frac{L_*}{L_{tot}} + \frac{z}{2}\frac{\sigma_r}{\sigma_\ddagger}\tilde{k}_{C_nH_{2n}ba}L^{1,{}^{12}C}_{C_iH_{2i}}\frac{L_H}{L_{tot}}\end{aligned} \tag{4-14}$$

$CN_{det} + 1 \le i \le CN_{max}$

The net production rate of the metal alkyl species with i carbon atoms and a ^{12}C at a position j is obtained from eq. [4-15]. The production of these species occurs via methylene insertion of $^{12}CH_2^{**}$ or $^{13}CH_2^{**}$ into a metal alkyl chain with $i-1$ carbon atoms and a ^{12}C at the $j-1$ position, by methylene deinsertion of a metal alkyl chain with $i+1$ carbon atoms and at the $j+1$ position a ^{12}C, by dehydrogenation of the corresponding alkane or by beta hydride addition to the corresponding metal alkene species. The metal alkyl species with i carbon atoms and a ^{12}C at the jth position are consumed by methylene insertion of a $^{12}CH_2^{**}$ or $^{13}CH_2^{**}$, methylene deinsertion, hydrogenation to the corresponding alkane or beta hydride elimination to the corresponding metal alkene species.

$$\begin{aligned}R_{L^{j,{}^{12}C}_{C_iH_{2i+1}}} &= \frac{z}{2}\frac{\sigma_r}{\sigma_\ddagger}\tilde{k}_{mi}L^{SS}_{CH_2}L^{j-1,{}^{12}C}_{C_{i-1}H_{2i-1}} - \frac{z}{2}\frac{\sigma_r}{\sigma_\ddagger}\tilde{k}_{mi}L^{SS}_{CH_2}L^{j,{}^{12}C}_{C_iH_{2i+1}} \\ &\quad + \left(\frac{z}{2}\right)^2\frac{\sigma_r}{\sigma_\ddagger}\tilde{k}_{md}L^{j+1,{}^{12}C}_{C_{i+1}H_{2i+3}}\left(\frac{L_*}{L_{tot}}\right)^2 - \left(\frac{z}{2}\right)^2\frac{\sigma_r}{\sigma_\ddagger}\tilde{k}_{md}L^{j,{}^{12}C}_{C_iH_{2i+1}}\left(\frac{L_*}{L_{tot}}\right)^2 \\ &\quad - \frac{z}{2}\frac{\sigma_r}{\sigma_\ddagger}\tilde{k}_{C_iH_{2i+1}hyd}L^{j,{}^{12}C}_{C_iH_{2i+1}}\frac{L_H}{L_{tot}} \\ &\quad + \frac{z}{2}\frac{\sigma_r}{\sigma_\ddagger}\tilde{k}_{C_nH_{2n+2}dehyd}RTC^{j,{}^{12}C}_{C_iH_{2i+1}}\left(\frac{L_*}{L_{tot}}\right)^2 \\ &\quad - \frac{z}{2}\frac{\sigma_r}{\sigma_\ddagger}\tilde{k}_{C_nH_{2n+1}be}L^{j,{}^{12}C}_{C_iH_{2i+1}}\frac{L_*}{L_{tot}} + \frac{z}{2}\frac{\sigma_r}{\sigma_\ddagger}\tilde{k}_{C_nH_{2n}ba}L^{j,{}^{12}C}_{C_iH_{2i}}\frac{L_H}{L_{tot}}\end{aligned} \tag{4-15}$$

$CN_{det} + 2 \le i \le CN_{max}$ and $2 \le j \le i - CN_{det}$

The rate expression for the net production rate of a metal alkyl chain with i carbon atoms and a detailed tail is given by eq. [4-16]. Methylene insertion of ${}^{12}CH_2^{**}$ or ${}^{13}CH_2^{**}$ into a metal alkyl chain with $i-1$ carbon atoms, methylene deinsertion of a metal alkyl with $i+1$ carbon atoms, dehydrogenation of an alkane with i carbon atoms and beta hydride addition to the corresponding metal alkene all with the same detailed tail increase the surface concentration of this type of metal alkyl species. The metal alkyl chains with i carbon atoms and a detailed tail are consumed by methylene insertion of a ${}^{12}CH_2^{**}$ or a ${}^{13}CH_2^{**}$, methylene deinsertion, hydrogenation to the corresponding alkane and beta hydride elimination to the corresponding metal alkene species.

$$
\begin{aligned}
&R_{L_{C_iH_{2i+1}}^{\{{}^*C_{i-CN_{det}}\cdots{}^*C_i\}_j}} \\
&\quad= \frac{z}{2}\frac{\sigma_r}{\sigma_\ddagger}\tilde{k}_{mi}L_{C_{i-1}H_{2i-3}}^{\exists!k:\{{}^*C_{i-1-CN_{det}}\cdots{}^*C_{i-1}\}_k=\{{}^*C_{i-CN_{det}}\cdots{}^*C_i\}_j}\frac{L_{CH_2}^{SS}}{L_{tot}} \\
&\quad- \frac{z}{2}\frac{\sigma_r}{\sigma_\ddagger}\tilde{k}_{mi}L_{C_iH_{2i+1}}^{\{{}^*C_{i-CN_{det}}\cdots{}^*C_i\}_j}\frac{L_{CH_2}^{SS}}{L_{tot}} \\
&\quad+ \left(\frac{z}{2}\right)^2\frac{\sigma_r}{\sigma_\ddagger}\tilde{k}_{md}L_{C_{i+1}H_{2(i+1)+1}}^{\exists!k:\{{}^*C_{i+1-CN_{det}}\cdots{}^*C_{i+1}\}_k=\{{}^*C_{i-CN_{det}}\cdots{}^*C_i\}_j}\left(\frac{L_*}{L_{tot}}\right)^2 \\
&\quad- \left(\frac{z}{2}\right)^2\frac{\sigma_r}{\sigma_\ddagger}\tilde{k}_{md}L_{C_iH_{2i+1}}^{\{{}^*C_{i-CN_{det}}\cdots{}^*C_i\}_j}\left(\frac{L_*}{L_{tot}}\right)^2 \qquad [4\text{-}16] \\
&\quad- \frac{z}{2}\frac{\sigma_r}{\sigma_\ddagger}\tilde{k}_{C_nH_{2n+1}hyd}L_{C_iH_{2i+1}}^{\{{}^*C_{i-CN_{det}}\cdots{}^*C_i\}_j}\frac{L_H}{L_{tot}} \\
&\quad+ \frac{z}{2}\frac{\sigma_r}{\sigma_\ddagger}\tilde{k}_{C_nH_{2n+2}dehyd}RTC_{C_iH_{2i+2}}^{\{{}^*C_{i-CN_{det}}\cdots{}^*C_i\}_j}\left(\frac{L_*}{L_{tot}}\right)^2 \\
&\quad- \frac{z}{2}\frac{\sigma_r}{\sigma_\ddagger}\tilde{k}_{C_nH_{2i+1}be}L_{C_iH_{2i+1}}^{\{{}^*C_{i-CN_{det}}\cdots{}^*C_i\}_j}\frac{L_*}{L_{tot}} \\
&\quad+ \frac{z}{2}\frac{\sigma_r}{\sigma_\ddagger}\tilde{k}_{C_nH_{2n}ba}L_{C_iH_{2i}}^{\{{}^*C_{i-CN_{det}}\cdots{}^*C_i\}_j}
\end{aligned}
$$

$CN_{det}+1 \le i \le CN_{max}$ and $j = 1, \dots, 2^{CN_{det}}$

Where, $L_{C_iH_{2i+1}}^{\left\{{}^*C_{i-CN_{det}}\cdots{}^*C_i\right\}_j}$ represents the surface concentration of the set of metal alkyl species with in total i carbon atoms of which the tail, consisting of CN_{det} carbon atoms, has a specific isotopic labeling represented by $\left\{{}^{*}C_{i-CN_{det}}\dots{}^{*}C_{i}\right\}_{j}$ and $L_{C_{i+1}H_{2i+3}}^{\exists!k:\left\{{}^{*}C_{i+1-CN_{det}}\dots{}^{*}C_{i+1}\right\}_{k}=\left\{{}^{*}C_{i-CN_{det}}\dots{}^{*}C_{i}\right\}_{j}}$ represents the surface concentration of the set of metal alkyl species with in total $i+1$ carbon atoms of which the tail, consisting of CN_{det} carbon atoms, has the corresponding isotopic labeling.

4.4 Effect of numerical methods on the required CPU time

The required CPU time as a function of the selected numerical discretization scheme, the implementation of a semi-analytical treatment of the Jacobian matrix and the numerical integration routine is discussed in the following sections. First the selection of an adequate numerical discretization scheme is discussed. In a second step, the effect of a semi-analytical treatment of the Jacobian matrix on the CPU time is reported. Also the effect of this treatment on the ranking of the best performing discretization scheme was considered. The ranking of the best performing discretization scheme potentially depends on to the interplay between the number of steps taken by the solver and the number of Jacobian matrix updates. In the assessment of the different solvers, a semi-analytical treatment of the Jacobian matrix was immediately considered. All the simulations were performed on 2 × 4-core Intel L5520 (Nehalem) processors which have access to 12 GB of RAM memory and local disk space of 90 GB. The simulation results discussed in the following sections, i.e., Section 4.4.1 – Section 4.4.3, were obtained with a reaction network of which the longest hydrocarbon chain has 5 carbon atoms, i.e., $CN_{max} = 5$, unless it is specifically mentioned otherwise.

4.4.1 Selection of a numerical discretization scheme

The convergence of the various FL functions has been assessed for the methanation reaction, i.e., $CN_{max} = 1$. The DASPK solver was used to perform the integration. The convergence to the benchmark solutions exhibited a comparable behavior for all the studied combinations of space times and switch time constants, a_2, as illustrated in Figure 4-7. The error obtained with the various FL functions as a function of the number of grid points is similar. This is illustrated by the grey band in Figure 4-7. There is one exception, i.e. the GPR-1/2 FL functions, which showed a slower convergence with respect to the number of grid points for all the studied combinations of space times and switch time constants.

All the FL functions, except for GPR-1/2, converge to the benchmark solution in a practically identical manner as a function of the number of grid points. As there is only a very small difference between the numerical solutions obtained with the FL functions and the benchmark solutions, the numerical solutions obtained with the flux limiter functions are considered accurate. It is, hence, anticipated that simulation results obtained with a FL function will not be altered by changing the employed FL function by another FL function. Therefore, the selection of a FL function for the simulation of SSITKA data is focused on the CPU time required to perform a single simulation. The latter was plotted for a specific value of the switch time constant as a function of the number of grid points from which convergence was obtained for the different space times. This is illustrated in Figure 4-8 for an a_2 value of 0.01 s. The simulation results clearly illustrate that a careful selection of a proper FL function can considerably reduce the CPU time, e.g., the Superbee FL function requires up to 9.6 h for the simulation with 500 grid points while the van Albada FL function reaches the same result in only 51 s. The CPU time for the 4 least time consuming FL functions is illustrated on the right part of Figure 4-8.

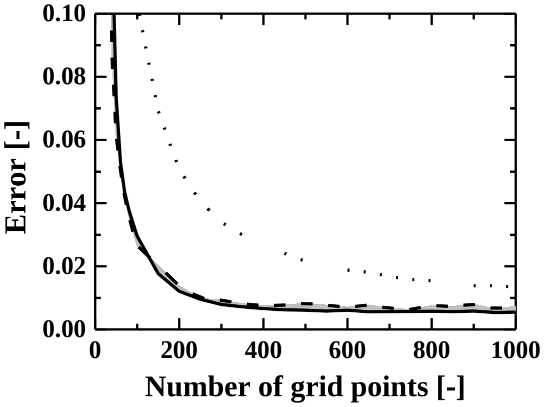

Figure 4-7: Deviation, eq. [4-9], of the simulation results obtained with the various Flux Limiter (FL) functions from the benchmark solution as function of the number of grid points. a_2= 0.1 s. $W/F_{CO,0}$ = 40 (kg_{cat} s) mol_{CO}^{-1}. Dotted line: GPR-1/2, dashed line: Superbee, full line: MUSCL, grey band: other FL functions. The simulations were performed for the methanation reaction. The results were obtained by integrating eq. [4-1] with the DASPK solver.

The best FL functions which were common for each value of a_2 were van Albada, van Leer, GVA-1/2 and OSPRE. These four FL functions are among the ones which were expected to perform the best based on the performance indicators outlined in Section 4.2.1 and are all members of the class of PR FL functions. Nevertheless, the difference in required CPU time can still exceed 25 %, e.g., 80 s are required by van Albada compared to 108 s required by OSPRE for one simulation at a space time of 40 (kg_{cat} s)mol_{CO}^{-1} s and 1000 grid points. The van Leer and van Albada FL function were found to perform equally well in terms of CPU time.

Simulations have also been performed for the same variation in space times and switch time constants by using the SOCD, eq. [4-2], and SOU, eq. [4-3], scheme. For the SOCD scheme, no numerical oscillations were observed, irrespective of the space time used at a switch time constant of 1 s. For an a_2 value of 0.1 s, the appearance of numerical oscillations depended on the space time. When the SOU scheme was employed, numerical oscillations were not observed for an a_2 equal to 0.1 s and 1 s. Nevertheless, the SOU scheme may lead to numerical difficulties at an a_2 value of 0.1s at the beginning of the step resulting in an increased CPU time. At an a_2 of 0.01 s numerical instabilities were observed for practically all simulations with both discretization schemes. The error, eq. [4-9], as a function of the number of grid points decreases at the same rate as observed for the van Albada Flux Limiter function for both discretization schemes. These linear discretization schemes require considerably less CPU time compared to the van Albada FL function, e.g., for a space time of 40 $(kg_{cat}s)mol_{CO}^{-1}$ and 500 grid points, the van Albada FL function requires 72 s while the simulation using the SOCD scheme achieves convergence within 6.7 s and the simulation using the SOU scheme within 7.6 s. Overall, the performance of these two linear discretization schemes in terms of CPU time were found to be comparable. Hence, when the input signal has a relatively low switch time constant, i.e., $a_2 \leq 0.1$ s, the van Albada or van Leer FL function has to be considered. If, on the other hand, the input signal has a smooth variation, i.e., $a_2 \geq 1$s, the second-order linear discretization schemes can be applied.

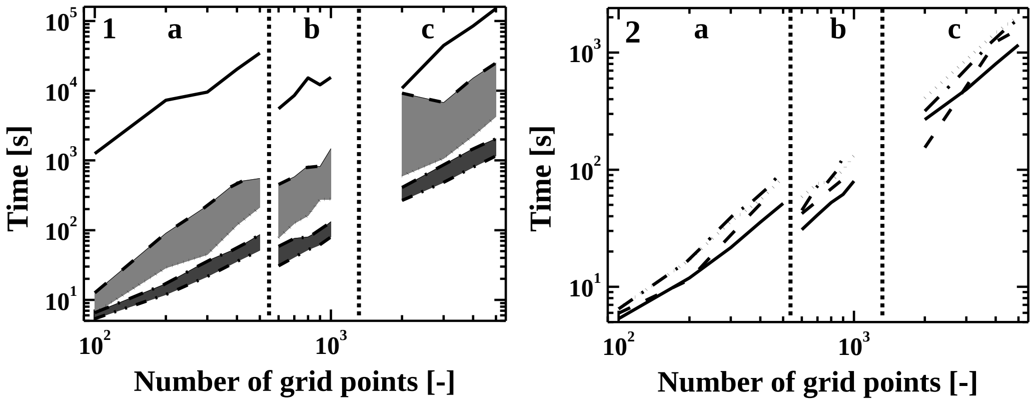

Figure 4-8: CPU time as function of the number of grid points. $a_2 = 0.01$ s. a: $W/F_{CO,0} = 4$ $(kg_{cat}\ s)mol_{CO}^{-1}$. b: $W/F_{CO,0} = 40$ $(kg_{cat}\ s)mol_{CO}^{-1}$. c: $W/F_{CO,0} = 400$ $(kg_{cat}\ s)mol_{CO}^{-1}$. 1: Full line: Superbee, dashed line: SMART, dotted line: SPL-1/3, dash dotted line: GVA-1/2, dash dot dotted line: van Albada, grey band: MUSCL, Koren, Minmod, H-CUI, H-QUICK, SMARTER and GPR-1/2, dark grey band OSPRE and van Leer. 2: Full line: van Albada, dashed line: van Leer, dotted line: OSPRE and dash dotted line: GVA-1/2. The simulations were performed for the methanation reaction. The results were obtained by integrating eq. [4-1] with the DASPK solver.

The moving grid implementation used here did not allow to reduce the required CPU time. On the contrary, the introduction of the term because of the Lagrange transformation and the additional equations related to the mobility of the grid points even resulted in an increase of the required CPU time, e.g., for a space time of 4 $(kg_{cat}s)mol_{CO}^{-1}$ and 100 grid points, the required CPU time increases from 6 s without a moving grid to 16 s with moving grid points. The increase in required CPU time is also related to the fact that the steady state, eq. [2–32], has to be recalculated each time the location of the grid points changes. In the simulations, the grid points were found to concentrate in the region where steep gradients were present. This reduces, however, the accuracy of the methane response at the reactor outlet. For the simulations of SSITKA experiment it is, hence, sufficient to use a fixed grid.

4.4.2 CPU time reduction by semi-analytical treatment of the Jacobian matrix

Table 4-4 quantifies the effect on the required CPU time by calculating the Jacobian matrix via finite differences or semi-analytically. In these simulations, a reaction network that accounts for all isotopologues and isotopomers is considered. The space time is varied from 4 $(kg_{cat}\ s)mol_{CO}^{-1}$

to 40 $(kg_{cat}\ s)mol_{CO}^{-1}$ and a_2 was set at 0.01 s, 0.1 s and 1.0 s. The number of grid points used for a space time of 4 $(kg_{cat}\ s)mol_{CO}^{-1}$ amounts to 100 and for a space time of 40 $(kg_{cat}\ s)mol_{CO}^{-1}$ to 500. The DASPK solver was used to perform the integration. The discretization was carried out by using the van Albada FL function. The effect of a semi-analytical treatment of the Jacobian matrix on the ranking of the FL functions was found to be minor. The gain in required CPU time by calculating the Jacobian matrix semi-analytically is around a factor 2. This is at the low end of the range which has been found by Perini et al. [34].

Table 4-4: The CPU time in minutes for different space times ($W/F_{CO,0}$) and different switch time constants (a_2). The Jacobian matrix was calculated by finite differences (FD) or semi-analytically (SA). The simulation results were obtained by integrating eq. [4-1] with the DASPK solver. For the reaction network $CN_{max} = CN_{det} = 5$.

$W/F_{CO,0}$ $[(kg_{cat}s)\ mol_{CO}^{-1}]$	4			40		
n_{gp}	100			500		
a_2 [s]	0.01	0.1	1	0.01	0.1	1
FD	114	260	498	1051	1720	3587
SA	76	157	350	676	999	2114
Ratio	1.5	1.7	1.4	1.6	1.7	1.7

It is noted that in Table 4-4 the CPU time increases with the switch time constant, i.e., the more smooth the input function behaves, the more difficult the calculations become. This apparently contradictory result is in line with the good performance of more simple discretization schemes such as second-order central difference discretization when smoother input functions are to be simulated. The benefits of the more advanced FL functions for the steeper input functions are not only lost, but even result in additionally required CPU time. Of course, a small a_2 value is desired in SSITKA and, hence, a_2 should not be increased in favor of the CPU time.

4.4.3 Selection of a backward differentiation solver

Several stiff ODE solvers such as LSODA [55], LSODE [55], VODE [53] and DASPK [54], are available as open source codes. LSODA and LSODE are similar to each other except that LSODA can switch between non-stiff and stiff methods. VODE uses variable-coefficient Adams-

Moulton and backward differentiation methods. DAPSK uses variable-order variable-step size backward differentiation. Hence, all these solvers employ a backward differentiation technique to integrate a set of stiff ODEs. Although similar mathematical methods are used, small differences exist in the implementation, e.g., the criteria to update the Jacobian matrix and, hence, a difference in performance can be expected [34].

The four abovementioned solvers were compared to each other for the simulation of the transient responses of all the isotopologues and all isotopomers. The space time was set at 4 $(kg_{cat}\ s)mol_{CO}^{-1}$ and 40 $(kg_{cat}\ s)mol_{CO}^{-1}$ with 100 and 500 number of grid points respectively and the switch time constant, a_2, was varied at 0.01 s, 0.1 s and 1.0 s. The van Albada flux limiter is used as discretization scheme. The results of these simulations in terms of required CPU time are illustrated in Table 4-5. For each space time and each value of a_2, the DASPK solver outperforms the other 3 solvers in terms of required CPU time. The second best performing solver is LSODE. The LSODA solver requires the longest time. This can probably be attributed to the fact that the LSODA solver switches between non-stiff and stiff methods and always starts from the non-stiff methods.

Table 4-5: CPU time in minutes required by the different solvers for different space times ($W/F_{CO,0}$) and different switch time constants (a_2). The simulation results were obtained by integrating eq. [4-1]. For the reaction network $CN_{max} = CN_{det} = 5$. (*) exceeds the wall time limit of 4320 minutes.

$W/F_{CO,0}$ [$(kg_{cat}s)\ mol_{CO}^{-1}$]	4			40		
n_{gp}	100			500		
a_2 [s]	0.01	0.1	1	0.01	0.1	1
DASPK	76	157	346	676	999	2114
VODE	509	583	703	*	*	*
LSODE	305	323	569	2803	2839	3544
LSODA	799	821	821	*	*	*

4.5 Effect of the level of detail accounted for in the reaction network

Simulations were performed with reaction networks with 3 different levels of detail. The most detailed reaction network describes the transient responses of all the isotopologues and isotopomers of each hydrocarbon present in the reaction network, i.e., $CN_{max} = CN_{det}$. The reaction network of intermediate degree of detail accounts for all the isotopologues and isotopomers of each hydrocarbon with a maximum chain length of 2, i.e. $CN_{det} = 2$. The least detailed reaction network only simulates the total fraction of ^{12}C in a hydrocarbon species, which is equivalent with $CN_{det} = 1$. The latter network is equivalent to that used by van Santen and Markvoort [9]. In the simulations, the space time was varied between 4 (kg$_{cat}$ s)mol$_{CO}^{-1}$ and 40 (kg$_{cat}$ s)mol$_{CO}^{-1}$. a_2 was set at 0.01 s, 0.1s and 1 s. The van Albada FL function was used for the discretization. The integration was performed with the DASPK solver.

The simulation results obtained with the three different reaction networks for a space time of 4 (kg$_{cat}$ s)mol$_{CO}^{-1}$ and switch time constant a_2= 0.01s are depicted in Figure 4-9. I-a to I-c illustrate the simulation results obtained with the most detailed reaction network. II-a to II-c illustrate the simulation results obtained with the reaction network of intermediate degree of detail. III-a to III-c illustrate the simulation results obtained with the least detailed reaction network. The simulations clearly illustrate the difference in information which can be acquired from the different reaction networks. With the most detailed reaction network, all the normalized concentrations, i.e., $C_i/C^{SS}_{C_nH_{2n+2}}$, for the intermediate isotopically labeled alkanes can be simulated. The reaction network of intermediate degree of detail only provides the normalized concentration of the intermediate isotopically labeled alkanes up to $CN_{det} = 2$. For the longer hydrocarbon chains, only the total fraction of ^{12}C can be simulated. If the least detailed reaction network is used, only the total fraction of ^{12}C in the hydrocarbon chains can be retrieved from the simulations. Figure 4-9 clearly shows that for the three different reaction networks the same normalized methane concentration and total fraction of ^{12}C in ethane and propane is achieved, i.e., identical kinetics are simulated. The only difference between the three reaction networks is related to the information which can be acquired with respect to individually labeled species.

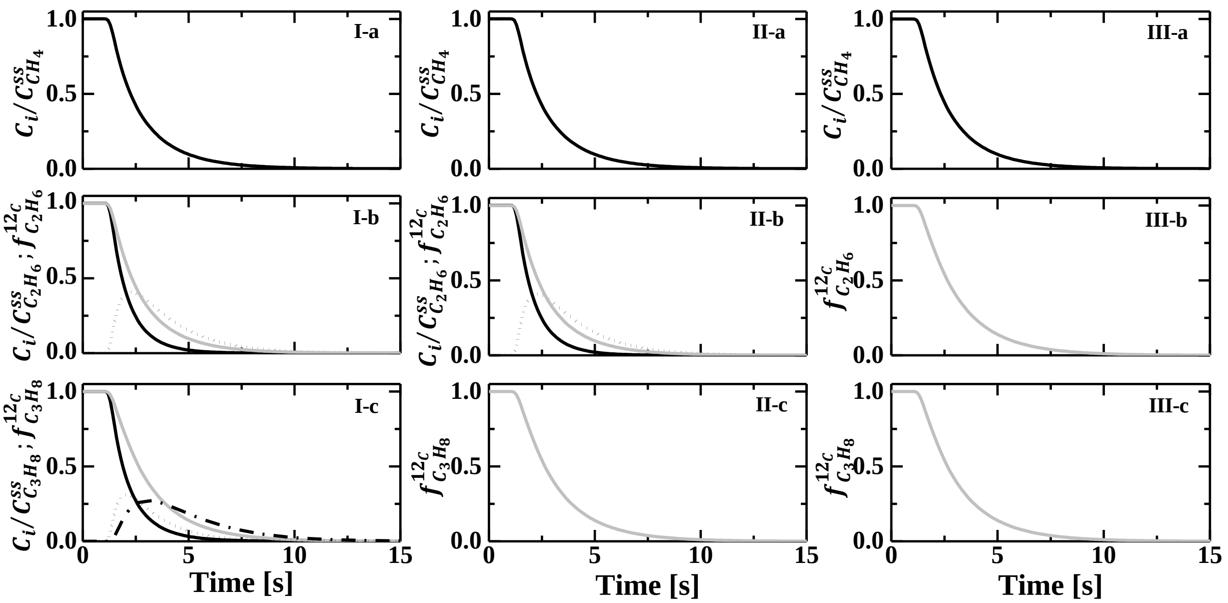

Figure 4-9: Transient responses of isotopically labeled alkanes obtained with reaction networks with 3 different levels of detail (I, II and III) as function of time. I: $CN_{max} = CN_{det} = 5$. II: $CN_{max} = 5$ and $CN_{det} = 2$. III: $CN_{max} = 5$ and $CN_{det} = 1$ with (a) methane, (b) ethane and (c) propane. Black lines: normalized concentrations (full line: alkane with only ^{12}C, dotted line: alkane with only one ^{12}C and dash-dotted line: alkane with two ^{12}C atoms). Grey line: the total fraction of ^{12}C. $W/F_{CO,0} = 4\ (kg_{cat}s)mol_{CO}^{-1}$. $a_2 = 0.01$ s. $n_{gp} = 100$. The results were obtained by integrating eq. [4-1] with DASPK.

The transient responses of the alkanes are essentially determined by the kinetics of the propagation and termination elementary steps as considered in the reaction network, i.e., the kinetic parameters and the corresponding surface coverages. Detailed information on the isotopic exchange as in I-b, I-c and II-b of Figure 4-9 will contain more information on these kinetic parameters compared to the case if only the total fraction of ^{12}C in the alkanes can be measured.

Furthermore, the simulation results obtained with the detailed reaction network can, e.g., be used to better understand which metal propyl species with two ^{12}C atoms on the surface finally contributes the most to the concentration of propane with two ^{12}C atoms. This is illustrated in Figure 4-10. There are two propane molecules with two ^{12}C atoms which can contribute to the final lumped concentration of propane with two ^{12}C atoms, see also Figure 4-4. Figure 4-10 clearly shows that the largest contribution comes from the metal propyl species with the ^{13}C atoms attached to surface and two ^{12}C atoms for the penultimate and ultimate carbon atoms. This detailed information cannot be withdrawn from a simulation in which only one lumped metal propyl species is considered for metal propyl species with two ^{12}C atoms [61]. The largest contribution to the concentration of propane molecules with one ^{12}C atom comes from the metal propyl surface species with a ^{13}C atom attached to the surface and as penultimate carbon atom and a ^{12}C atom as the ultimate carbon atom. It is noted that the kinetic parameters used for these simulations predict a low contribution from the other two metal propyl species with two ^{12}C atoms to the final concentration of propane with two ^{12}C atoms and that changes in these kinetic parameters might increase these contributions.

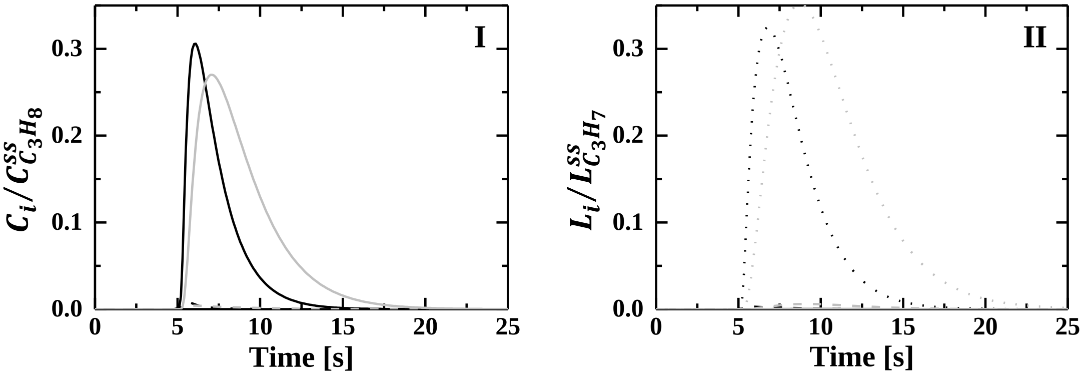

Figure 4-10: Normalized transient responses of propane (I) and metal propyl (II). I: Full black line: $^{12}CH_3{}^{12}CH_2{}^{13}CH_3$, dashed black line: $^{12}CH_3{}^{13}CH_2{}^{12}CH_3$, full grey line: $^{12}CH_3{}^{13}CH_2{}^{13}CH_3$, dashed grey line: $^{13}CH_3{}^{12}CH_2{}^{13}CH_3$. II: Full black line: $M^{12}CH_2{}^{12}CH_2{}^{13}CH_3$, dashed black line: $M^{12}CH_2{}^{13}CH_2{}^{12}CH_3$, dotted black line: $M^{13}CH_2{}^{12}CH_2{}^{12}CH_3$, full grey line: $M^{12}CH_2{}^{13}CH_2{}^{13}CH_3$, dashed grey line: $M^{13}CH_2{}^{12}CH_2{}^{13}CH_3$, dotted grey line: $M^{13}CH_2{}^{13}CH_2{}^{12}CH_3$. $W/F_{CO,0}$ = 4 $(kg_{cat}s)mol_{CO}^{-1}$. a_2 = 0.01 s. n_{gp} = 100. The results were obtained by integrating eq. [4-1] with DASPK.

The simulation results in terms of CPU time between the different reaction networks are given in Table 4-6. The gain in CPU time by using a less detailed reaction network can be considerable. For example, the CPU time is reduced by a factor 6 if the simulations are run with the reaction network of intermediate degree of detail compared to the case for which the simulations are run with the most detailed reaction network. Furthermore, the additional information acquired by the reaction network of intermediate degree of detail does not come with an excessive penalty in the required CPU time compared to the least detailed reaction network.

Table 4-6: The required CPU time in minutes for different space times ($W/F_{CO,0}$) and different switch time constants (a_2) obtained with reaction networks with 3 different levels of detail (I, II and III). I: $CN_{max} = CN_{det} = 5$. II: $CN_{max} = 5$, $CN_{det} = 2$. III: $CN_{max} = 5$ and $CN_{det} = 1$. The results were obtained by integrating eq. [4-1] with DASPK.

$W/F_{CO,0}$ [(kg_{cat}s) mol_{CO}^{-1}]	n_{gp}	a_2 [s]	I	II	III
4	100	0.01	76	13	10
	100	0.1	157	25	17
	100	1	346	50	35
40	500	0.01	676	125	88
	500	0.1	999	193	122
	500	1	2114	374	248

4.6 Kinetic simulations

The detailed reaction network results in simulations which yield information on the intermediate labeled alkanes and alkenes gas phase components, see Figure 4-9 – I. A qualitative comparison to reported experimental data [61] shows that the model correctly simulates the transient response of propane with two ^{12}C atoms. These species exhibit a stronger initial increase with the time compared to the transient response of propane with only one ^{12}C atom.

The effect of the operating conditions, i.e., H_2/CO molar inlet ratio, the temperature and total pressure on the transient responses of the alkanes and alkenes is briefly addressed in what follows. For these simulations, a reaction network is used which is limited to the description of the fraction of ^{12}C in the hydrocarbons. The maximum size of the hydrocarbon was limited to 5. The results are summarized in Table 4-7 as surface residence times of the different alkanes and alkenes and were calculated according to eq. [2–7].

Table 4-7: Effect of operating conditions on the surface residence time, eq. [2–7], of the different alkanes and alkenes. The CO conversion amounts to 0.11 for all the simulations. The simulation results are obtained by integrating eq. [4-1] with the DASPK solver.

H_2/CO [-]	T [K]	p_{tot} [Mpa]	τ_{CH4}	τ_{C2H6}	τ_{C3H8}	τ_{C4H10}	τ_{C2H4}	τ_{C3H6}	τ_{C4H8}
5	553	0.2	3.06	2.71	2.95	2.98	3.19	2.97	2.99
10	553	0.2	1.22	1.41	1.84	2.19	1.42	1.85	2.20
5	553	0.3	2.21	1.94	2.68	2.93	2.26	2.69	2.94
5	563	0.2	1.88	1.60	1.71	1.70	1.62	1.72	1.70

Increasing the H_2/CO molar inlet ratio from 5 to 10 reduces the time during which isotopic scrambling occurs. At the higher H_2/CO molar inlet ratio, the hydrogen coverage increased by a factor of 1.7 along the reactor coordinate. The higher hydrogen coverage increases the rate of the hydrogenation reactions which are the termination steps in the reaction mechanism. Hence, the total amount of species which contain ^{12}C will be removed faster from the surface, decreasing the surface residence time of these species. This illustrates the need to account for hydrogenation steps in the modeling of SSITKA experiments of FTS which is rarely done, i.e., typically the adjustable parameters in a global model are re-estimated at other H_2/CO molar inlet ratios [61]. As such, an increasing trend in the rate coefficients for the termination towards alkanes with an increasing H_2/CO molar inlet ratio was found which qualitatively correspondence with the effect of a changing H_2/CO molar inlet ratio predicted by the model.

An increase in the total pressure decreases the surface residence time of the hydrocarbon species slightly. For the alkanes, the readsorption only contributes to the net production rate to a minor extent. Hence, the net production rate is determined by the product of the hydrogen and metal alkyl surface coverages. An increase in total pressure, increases both surface coverages of metal alkyl and hydrogen surface species. As the surface residence time of the alkanes is determined by the ratio of the surface coverage of the equivalent metal alkyl species divided by the net production rate, the decreased surface residence time of the alkanes is due to the increased H surface coverage. It is noted that the increase in metal alkyl surface coverages is higher compared to the increase in H surface coverage resulting in an increasing selectivity to longer chain hydrocarbons. For the alkenes, the decreased residence time at higher pressures is related to the decrease in free surface sites, decreasing the contribution of alkenes readsorption.

Increasing the temperature reduces the time period during which isotopic scrambling can occur. In the microkinetic model, the hydrogenation steps have the highest activation energy. Hence, increasing the temperature will have the strongest effect on the hydrogenation reactions. As a consequence, the species which contain ^{12}C atoms are depleted much faster at a higher temperature.

4.7 Conclusions

The simulation of Steady State Isotopic Transient Kinetic Analysis (SSITKA) experiments requires a judicious selection of techniques to devise a methodology for integrating the set of time dependent partial differential equations. The method of lines is generally applied to obtain a set of first order nonlinear ordinary differential equations for which dedicated solvers exist. An adequate discretization technique is a prerequisite for a smooth and efficient simulation of the transient phenomena. At low switch time constants, i.e., ≤ 0.1 s, the van Leer and van Albada flux limiter functions were selected as the best discretization schemes for the simulation of SSITKA data. At higher values of the switch time constant, i.e., ≥ 1.0 s, conventional, linear second-order discretization schemes suffice despite the convective nature of the time dependent partial differential equations but these higher switch time constants should, of course, be avoided in SSITKA experimentation.

Given the comprehensive set of equations as a result of the transient nature of SSITKA data and the extent of the considered reaction network, further opportunities to reduce the CPU time have been evaluated. First, simulations showed that the semi-analytical calculation of the Jacobian matrix is an effective way to reduce the CPU time. Next, from 4 publicly available ordinary differential equation solvers, the DASPK implementation was found to outperform the other three. The third exploited opportunity is limiting the number of species and elementary reactions in the reaction network. To this end, a methodology has been devised such that the level of detail generated by the simulations can be matched to that available in the experimental data. In addition to monitoring the detailed labeling of short hydrocarbons and the end of growing alkyl chains, this methodology allows tracking the fraction of ^{12}C and ^{13}C atoms at a given position in the produced hydrocarbon chains. Simulations have shown that the CPU time can be reduced up to a factor of 5 without losing critical information on the labeling of the carbon atoms, if not up to a factor of 10. It is anticipated that SSITKA of other complex reactions can be modeled with the tools presented here.

The simulated transient responses of intermediate isotopically labeled alkanes and alkenes are in qualitative correspondence with experimental observations. Furthermore, including the surface coverage of important surface species in the Fischer-Tropsch Synthesis in the kinetic model allows to capture the effect of changing reaction conditions more straightforwardly .

4.8 References

1. Marin, G.B. and G.S. Yablonsky, *Kinetics of Chemical Reactions*. 2011: WILEY-VCH.
2. Happel, J., *Transient tracing.* Chemical Engineering Science, 1978. **33**(11): p. 1567.
3. Bennett, C.O., *Understanding Heterogeneous Catalysis Through the Transient Method*, in *Catalysis Under Transient Conditions*, A.T. Bell and L.L. Hegedus, Editors. 1982, American Chemical Society: Washingon, DC. p. 1-32.
4. Biloen, P., *Transient kinetic methods.* Journal of Molecular Catalysis, 1983. **21**(1–3): p. 17-24.
5. Ledesma, C., J. Yang, D. Chen, and A. Holmen, *Recent Approaches in Mechanistic and Kinetic Studies of Catalytic Reactions Using SSITKA Technique.* Acs Catalysis, 2014. **4**(12): p. 4527-4547.
6. Shannon, S.L. and J.G. Goodwin, *Characterization of Catalytic Surfaces by Isotopic-Transient Kinetics during Steady-State Reaction.* Chemical Reviews, 1995. **95**(3): p. 677-695.
7. den Breejen, J.P., P.B. Radstake, G.L. Bezemer, J.H. Bitter, V. Froseth, A. Holmen, and K.P. de Jong, *On the Origin of the Cobalt Particle Size Effects in Fischer-Tropsch Catalysis.* Journal of the American Chemical Society, 2009. **131**(20): p. 7197-7203.
8. Yang, J., E.Z. Tveten, D. Chen, and A. Holmen, *Understanding the Effect of Cobalt Particle Size on Fischer-Tropsch Synthesis: Surface Species and Mechanistic Studies by SSITKA and Kinetic Isotope Effect.* Langmuir, 2010. **26**(21): p. 16558-16567.
9. van Santen, R.A. and A.J. Markvoort, *Catalyst nano-particle size dependence of the Fischer-Tropsch reaction.* Faraday Discussions, 2013. **162**: p. 267-279.
10. Lohitharn, N. and J.G. Goodwin, *Effect of K promotion of Fe and FeMn Fischer-Tropsch synthesis catalysts: Analysis at the site level using SSITKA.* Journal of Catalysis, 2008. **260**(1): p. 7-16.
11. Haddad, G.J., B. Chen, and J.G. Goodwin, *Effect of* La^{3+} *promotion of* Co/SiO_2 *on CO hydrogenation.* Journal of Catalysis, 1996. **161**(1): p. 274-281.
12. Lohitharn, N. and J.G. Goodwin, *Impact of Cr, Mn and Zr addition on Fe Fischer-Tropsch synthesis catalysis: Investigation at the active site level using SSITKA.* Journal of Catalysis, 2008. **257**(1): p. 142-151.
13. Vada, S., B. Chen, and J.G. Goodwin, *Isotopic Transient Study of La Promotion of* Co/Al_2O_3 *for CO Hydrogenation.* Journal of Catalysis, 1995. **153**(2): p. 224-231.
14. Hoost, T.E. and J.G. Goodwin, *Reaction Analysis of Potassium Promotion of Ru-Catalyzed Co Hydrogenation Using Steady-State Isotopic Transients.* Journal of Catalysis, 1992. **137**(1): p. 22-35.
15. Kogelbauer, A., J.G. Goodwin, and R. Oukaci, *Ruthenium promotion of* Co/Al_2O_3 *Fischer-Tropsch catalysts.* Journal of Catalysis, 1996. **160**(1): p. 125-133.
16. Enger, B.C., V. Froseth, J. Yang, E. Rytter, and A. Holmen, *SSITKA analysis of CO hydrogenation on Zn modified cobalt catalysts.* Journal of Catalysis, 2013. **297**: p. 187-192.
17. Schanke, D., S. Vada, E.A. Blekkan, A.M. Hilmen, A. Hoff, and A. Holmen, *Study of Pt-Promoted Cobalt Co Hydrogenation Catalysts.* Journal of Catalysis, 1995. **156**(1): p. 85-95.

18. Yang, J., D. Chen, and A. Holmen, *Understanding the kinetics and Re promotion of carbon nanotube supported cobalt catalysts by SSITKA.* Catalysis Today, 2012. **186**(1): p. 99-108.
19. Rane, S., O. Borg, J. Yang, E. Rytter, and A. Holmen, *Effect of alumina phases on hydrocarbon selectivity in Fischer-Tropsch synthesis.* Applied Catalysis a-General, 2010. **388**(1-2): p. 160-167.
20. Gao, J., X.H. Mo, and J.G. Goodwin, *Evidence of strong metal-oxide interactions in promoted Rh/*SiO_2 *on CO hydrogenation: Analysis at the site level using SSITKA.* Catalysis Today, 2011. **160**(1): p. 44-49.
21. Rohr, F., O.A. Lindvag, A. Holmen, and E.A. Blekkan, *Fischer-Tropsch synthesis over cobalt catalysts supported on zirconia-modified alumina.* Catalysis Today, 2000. **58**(4): p. 247-254.
22. den Breejen, J.P., A.M. Frey, J. Yang, A. Holmen, M.M. van Schooneveld, F.M.F. de Groot, O. Stephan, J.H. Bitter, and K.P. de Jong, *A Highly Active and Selective Manganese Oxide Promoted Cobalt-on-Silica Fischer-Tropsch Catalyst.* Topics in Catalysis, 2011. **54**(13-15): p. 768-777.
23. Phan, X.K., J. Yang, H. Bakhtiary-Davijnay, R. Myrstad, H.J. Venvik, and A. Holmen, *Studies of Macroporous Structured Alumina Based Cobalt Catalysts for Fischer-Tropsch Synthesis.* Catalysis Letters, 2011. **141**(12): p. 1739-1745.
24. Thybaut, J.W., I.R. Choudhury, J.F. Denayer, G.V. Baron, P.A. Jacobs, J.A. Martens, and G.B. Marin, *Design of Optimum Zeolite Pore System for Central Hydrocracking of Long-Chain n-Alkanes based on a Single-Event Microkinetic Model.* Topics in Catalysis, 2009. **52**(9): p. 1251-1260.
25. Filot, I.A.W., R.A. van Santen, and E.J.M. Hensen, *The Optimally Performing Fischer-Tropsch Catalyst.* Angewandte Chemie-International Edition, 2014. **53**(47): p. 12746-12750.
26. Alhumaizi, K., *Flux-limiting solution techniques for simulation of reaction-diffusion-convection system.* Communications in Nonlinear Science and Numerical Simulation, 2007. **12**(6): p. 953-965.
27. Alhumaizi, K., R. Henda, and M. Soliman, *Numerical analysis of a reaction–diffusion–convection system.* Computers & Chemical Engineering, 2003. **27**(4): p. 579-594.
28. Hassanzadeh, H., J. Abedi, and M. Pooladi-Darvish, *A comparative study of flux-limiting methods for numerical simulation of gas–solid reactions with Arrhenius type reaction kinetics.* Computers & Chemical Engineering, 2009. **33**(1): p. 133-143.
29. Saucez, P., W.E. Schiesser, and A. Vande Wouwer, *Upwinding in the method of lines.* Mathematics and Computers in Simulation, 2001. **56**(2): p. 171-185.
30. Waterson, N.P. and H. Deconinck, *Design principles for bounded higher-order convection schemes - a unified approach.* Journal of Computational Physics, 2007. **224**(1): p. 182-207.
31. Nibbelke, R.H., J. Scheerova, M.H.J.M. de Croon, and G.B. Marin, *The Oxidative Coupling of Methane over Mgo-Based Catalysts - a Steady-State Isotope Transient Kinetic-Analysis.* Journal of Catalysis, 1995. **156**(1): p. 106-119.
32. Verwer, J.G., J.G. Blom, R.M. Furzeland, and P.A. Zegeling, *A Moving Grid Method for One-Dimensional PDEs Based on the Method of Lines*, in *Adaptive Methods for Partial Differential Equations*, J.E. Flaherty, P.J. Paslow, M.S. Shephard, and J.D. Vasilakis, Editors. 1989, SIAM: Philadelphia. p. 160-175.

33. Kelling, R., J. Bickel, U. Nieken, and P.A. Zegeling, *An adaptive moving grid method for solving convection dominated transport equations in chemical engineering.* Computers & Chemical Engineering, 2014. **71**: p. 467-477.
34. Perini, F., E. Galligani, and R.D. Reitz, *An Analytical Jacobian Approach to Sparse Reaction Kinetics for Computationally Efficient Combustion Modeling with Large Reaction Mechanisms.* Energy & Fuels, 2012. **26**(8): p. 4804-4822.
35. Froment, G.F., *Kinetic modeling of acid-catalyzed oil refining processes.* Catalysis Today, 1999. **52**(2-3): p. 153-163.
36. Martinis, J.M. and G.F. Froment, *Alkylation on solid acids. Part 2. Single-event kinetic modeling.* Industrial & Engineering Chemistry Research, 2006. **45**(3): p. 954-967.
37. Lozano-Blanco, G., J.W. Thybaut, K. Surla, P. Galtier, and G.B. Marin, *Single-event microkinetic model for Fischer-Tropsch synthesis on iron-based catalysts.* Industrial & Engineering Chemistry Research, 2008. **47**(16): p. 5879-5891.
38. Bera, T., J.W. Thybaut, and G.B. Marin, *Single-Event MicroKinetics of Aromatics Hydrogenation on Pt/H-ZSM22.* Industrial & Engineering Chemistry Research, 2011. **50**(23): p. 12933-12945.
39. Toch, K., J.W. Thybaut, B.D. Vandegehuchte, C.S.L. Narasimhan, L. Domokos, and G.B. Marin, *A Single-Event Micro Kinetic model for "ethylbenzene dealkylation/xylene isomerization" on Pt/H-ZSM-5 zeolite catalyst.* Applied Catalysis a-General, 2012. **425**: p. 130-144.
40. Thybaut, J.W. and G.B. Marin, *Single-Event MicroKinetics: Catalyst design for complex reaction networks.* Journal of Catalysis, 2013. **308**: p. 352-362.
41. Schiesser, W.E., *The numerical method of lines : integration of partial differential equations*. 1991: Academic Press. 326.
42. Sweby, P.K., *High-resolution schemes using flux limiters for hyperbolic conservation-laws.* Siam Journal on Numerical Analysis, 1984. **21**(5): p. 995-1011.
43. Fromm, J.E., *A method for reducing dispersion in convective difference schemes.* Journal of Computational Physics, 1968. **3**(2): p. 176-189.
44. Roe, P.L., *Characteristic-based schemes for the euler equations.* Annual Review of Fluid Mechanics, 1986. **18**: p. 337-365.
45. Roe, P.L., *Some contributions to the modeling of discontinuous flow.* Lectures in Applied Mathematics, 1985. **22**: p. 163-192.
46. Koren, B., *A robust upwind discretization method for advection, diffusion and source terms*, in *Numerical methods for advection-diffusion problems*, C.B. Vreugdenhil and B. Koren, Editors. 1993, Vieweg: Braunschweig. p. 117 - 138.
47. Van Leer, B., *Towards the ultimate conservative difference scheme. IV. A new approach to numerical convection.* Journal of Computational Physics, 1977. **23**(3): p. 276-299.
48. van Leer, B., *Towards the ultimate conservative difference scheme. II. Monotonicity and conservation combined in a second-order scheme.* Journal of Computational Physics, 1974. **14**(4): p. 361-370.
49. Gaskell, P.H. and A.K.C. Lau, *Curvature-compensated convective-transport - SMART, a new boundedness-preserving transport algorithm.* International Journal for Numerical Methods in Fluids, 1988. **8**(6): p. 617-641.
50. van Albada, G.D.v.L., B.; Roberts, W. W., Jr., *A comparative study of computational methods in cosmic gas dynamics.* Astronomy and Astrophysics, 1982. **88**: p. 76-84.

51. Choi, S.K., H. Yun Nam, and M. Cho, *A comparison of higher-order bounded convection schemes.* Computer Methods in Applied Mechanics and Engineering, 1995. **121**(1–4): p. 281-301.
52. Blom, J.G. and P.A. Zegeling, *Algorithm 731 - a Moving-Grid Interface for Systems of One-Dimensional Time-Dependent Partial-Differential Equations.* Acm Transactions on Mathematical Software, 1994. **20**(2): p. 194-214.
53. Brown, P.N., G.D. Byrne, and A.C. Hindmarsh, *VODE - A variable-coefficient ODE solver.* Siam Journal on Scientific and Statistical Computing, 1989. **10**(5): p. 1038-1051.
54. Brown, P.N., A.C. Hindmarsh, and L.R. Petzold, *Using krylov methods in the solution of large-scale differential-algebraic systems.* Siam Journal on Scientific Computing, 1994. **15**(6): p. 1467-1488.
55. Hindmarsh, A.C., *ODEPACK, A Systematized Collection of ODE Solvers.* IMACS Transactions on Scientific Computation, 1983. **1**: p. 55-64.
56. Lozano-Blanco, G., J.W. Thybaut, K. Surla, P. Galtier, and G.B. Marin, *Fischer-Tropsch synthesis: Development of a microkinetic model for metal catalysis.* Oil & Gas Science and Technology-Revue D Ifp Energies Nouvelles, 2006. **61**(4): p. 489-496.
57. Brady, R.C. and R. Pettit, *On the Mechanism of the Fischer-Tropsch Reaction - the Chain Propagation Step.* Journal of the American Chemical Society, 1981. **103**(5): p. 1287-1289.
58. Gao, J., X.H. Mo, and J.G. Goodwin, *Relationships between oxygenate and hydrocarbon formation during CO hydrogenation on* Rh/SiO_2*: Use of multiproduct SSITKA.* Journal of Catalysis, 2010. **275**(2): p. 211-217.
59. van Dijk, H.A.J., J.H.B.J. Hoebink, and J.C. Schouten, *A mechanistic study of the Fischer-Tropsch synthesis using transient isotopic tracing. Part-1: Model identification and discrimination.* Topics in Catalysis, 2003. **26**(1-4): p. 111-119.
60. Markvoort, A.J., R.A. van Santen, P.A.J. Hilbers, and E.J.M. Hensen, *Kinetics of the Fischer-Tropsch Reaction.* Angewandte Chemie-International Edition, 2012. **51**(36): p. 9015-9019.
61. van Dijk, H.A.J., J.H.B.J. Hoebink, and J.C. Schouten, *A mechanistic study of the Fischer-Tropsch synthesis using transient isotopic tracing. Part 2: Model quantification.* Topics in Catalysis, 2003. **26**(1-4): p. 163-171.

Chapter 5 Microkinetic Model Validation Based on Steady State Isotopic Transient Kinetic Analysis

The Single-Event MicroKinetic (SEMK) model of Chapter 3 has been extended for the simulation of Steady State Isotopic Transient Kinetic Analysis (SSITKA) data for Co catalyzed Fischer-Tropsch Synthesis (FTS). The extended SEMK model considers two Co site types and both direct and H-assisted CO dissociation. The steps involved in the chain growth are the same as for the SEMK model of Chapter 3. In total 17 steady state experiments were used in the model regression together with 11 SSITKA experiments. The experimental data were acquired in a plug flow reactor with a H_2/CO molar inlet ratio of 5 and 10, a temperature between 483 and 503 K, a total pressure of 185 kPa, a CO inlet partial pressure of 5.5 kPa and space times, i.e., $W/F_{CO,0}$, varying between 7 and 29 $(kg_{cat}\ s)mol_{CO}^{-1}$. The regression resulted in physicochemically meaningful estimates for the activation energies and atomic chemisorption enthalpies. The application of the phenomenological UBI-QEP method allows to physically interpret the nature of the two site types considered in the SEMK model, i.e., terrace sites and step sites. The most abundant surface species are CO, H, metal alkyl species, HCO and water precursors. A reaction path analysis shows that more than 80 percent of the CO reacts on the step sites. Furthermore, chain growth exclusively occurs on these sites. The terrace sites are less reactive for CO dissociation. The CO which is converted on these sites ends up solely in methane. A fraction of the alkenes, produced on the step sites, are hydrogenated to alkanes on the terrace sites.

5.1 Introduction

In Chapter 3 a Single-Event MicroKinetic (SEMK) model that accurately describes the CO conversion and selectivities to alkanes and alkenes has been constructed. The experimental data that was used for the regression of this SEMK model was obtained via steady-state kinetic measurements and sample the experimental space by varying experimental settings such as temperature, pressure, … In this chapter, the SEMK model of Chapter 3 is tested for the simulation of Steady State Isotopic Transient Kinetic Analysis (SSITKA) experiments. In such an experiment, more information during the steady state operation of the catalyst is obtained by abruptly changing one of the reactants by one of its isotopologues. As explained in Chapter 1, by analyzing the transient responses, observed production rates can be decoupled in rate coefficients and surface concentrations [1].

As the transient responses acquired in a SSITKA experiment intrinsically contain information on the surface coverages of some of the kinetically relevant surface species, this type of data may impose additional constraints that need to be considered in the model construction. By testing the performance of an existing microkinetic model for the simulation of additional experimental data or experimental data of a different nature, the microkinetic model can be gradually extended. In this way, microkinetic models are constructed according to the data-driven refinement methodology as explained in Chapter 1.

For SSITKA data obtained for the Fischer-Tropsch Synthesis (FTS) reaction, microkinetic modeling studies have pointed out that CO dissociates to two types of carbonaceous species which both participate in the methane formation [2-6]. The microkinetic models considered in these modeling studies are based on irreversible elementary reaction steps. Hydrogen coverage is typically not explicitly accounted for causing the estimated rate coefficients to be dependent on the applied H_2/CO molar inlet ratio. Furthermore, these estimated rate coefficients are typically obtained without estimating the pre-exponential factor and activation energies separately. The goal of the work presented in this chapter is to test and potentially extend the SEMK model developed in Chapter 3 for the simulation of SSITKA data. The final model explicitly accounts for the hydrogen coverage and incorporates adsorption and activation energies. As such the model can describe more than one experiment with a single set of kinetic parameters.

5.2 Procedures

5.2.1 Experimental data

The experimental data have been acquired in the SSITKA set-up discussed in section 2.1.1 on the Co/CNT catalyst described in Section 2.1.3. In total 17 experiments were measured at a CO inlet partial pressure of 5.5 kPa, varying H_2/CO molar ratios between 5 and 10, temperatures between 483 K to 503 K and a total pressure of 1.85 kPa.

5.2.2 Modeling procedures

5.2.2.1 Reactor model

As explained in Section 2.2.4, the reactor can be modeled by a set of partial differential equations (PDEs), eqs. [2–30] and [2–31], complemented with the boundary conditions of eqs. [2–32] and [2–33] and a set of ordinary differential equations (ODEs) to model the steady state, eq. [2–35]. The concentrations of the gas phase components as a function of space and time are obtained by solving the set of PDEs by means of the method of lines, see Section 4.2.1. For the discretization of the spatial derivative, the second order central differencing scheme was used as the switch time constant amounts to 0.9 s, see Table 2–1 and Chapter 4. The resulting set of ODEs is solved by means of the DASPK solver [7], see Chapter 4. The numerical integration of the set of ODEs, eq. [2–35], is performed as explained in section 3.2.2.1.

5.2.2.2 Regression analysis

The steady state outlet concentration of C_1 to C_6 *n*-alkanes and C_2 to C_5 1-alkenes together with the transient responses of ^{12}CO and $^{12}CH_4$ were used as experimental responses in the objective function of eq. [2–45]. Hence, in total 13 responses were used in the objective function. This objective function is minimized by means of the two step minimization procedure as explained in section 2.2.6. The weights, w_i, used in the objective function, eq. [2–45], are determined by means of eq. [2–46].

It is noted that SSITKA data can also be used to obtain surface coverages of relevant intermediates. These are derived from the surface residence time and the exit molar flow rate [8]. The transient responses and the outlet concentrations of the gas phase components were used in the model regression. If these two quantities are accurately reproduced by the model, the surface coverages of the relevant intermediates determined from the experimental data can reasonably be expected to also be reproduced by the model. Furthermore, the shape of the transient response can also contain relevant information with respect to the reaction mechanism [3, 4].

The steady state concentration of the alkanes and alkenes of the 17 experiments were used in the model regression. The number of transient experiments was limited to 11 of these 17 experiments in order to limit the number of CPUs required for the model regression. The transient responses of the other 6 experiments were used for model validation purposes.

The Message Passing Interface (MPI) software library [9] has been used to distribute the simulation of the experiments to different CPUs. This is illustrated in Figure 5-1. The regression program runs on all $m + 1$ CPUs separately, i.e., the regression is performed on each CPU. The CPUs only communicate for the simulation of the experiments. The CPU which carries ‘0’ as identifier distributes the first m experiments of the n experiments to the other CPUs, i.e., the CPUs which carry ‘1’, 2’, … and ‘m’ as identifier. The simulation results of experiment i are sent back from CPU i to CPU 0. Subsequently, CPU 0 sends another experiment to CPU i which starts simulating this experiment. This is done until CPU 0 has received the simulation results of all the n experiments. Once the simulation results of all n experiments are available on CPU 0, the simulation results are sent to all other m CPUs and the calculation of the objective function, see eq. [2–45], is performed on all m CPUs separately which is subsequently used in order to continue the regression.

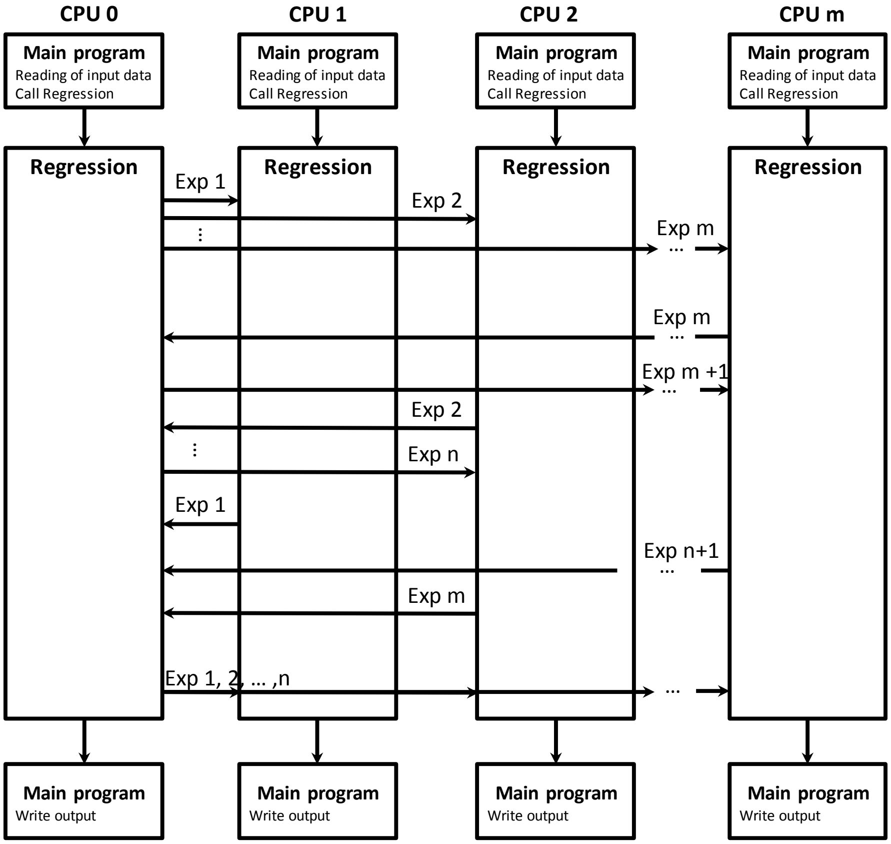

Figure 5-1: Schematic representation of the application of the Message Passing Interface (MPI) to the regression software.

5.3 The Single-Event MicroKinetic model

A SEMK model has been developed for the description of the CO conversion and alkanes and alkenes selectivity on a Co catalyst, see Chapter 3. This model was employed for the simulation of the experimentally measured transient responses. The results of this simulation are presented in Figure 5-2. The model, which was found to accurately predict the CO conversion and alkanes and alkenes selectivity, predicts satisfactorily the initial part of the $^{12}CH_4$ transient. This indicates that the elementary reactions included in the SEMK model allow to reproduce the initial part of the $^{12}CH_4$ transient. Once the $^{12}CH_4$ transient has dropped to 80% of its initial value, the model predictions and experimental measurements deviate significantly from each other. The model simulates a rapidly dropping $^{12}CH_4$ transient, i.e., the simulated $^{12}CH_4$ transient is significantly different from zero for 5 s after the switch while the experimentally measured $^{12}CH_4$ transient reaches zero after a time period of 50 s after the switch. This discrepancy indicates that additional reaction steps are required for the modeling of the transient behavior of methane.

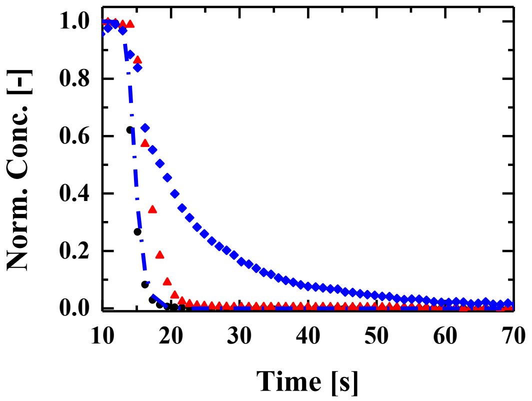

Figure 5-2: Transient responses of Ar (●), ^{12}CO (▲) and $^{12}CH_4$ (◆, — •) after a switch from Ar/$^{12}CO/H_2$ to Kr/$^{13}CO/H_2$ at a H_2/CO molar inlet ratio of 5, a CO inlet partial pressure of 5.5 kPa, a total pressure of 185 kPa, a temperature of 493 K and a space time, $W/F_{CO,0}$, of 23 (kg_{cat} s) mol_{CO}^{-1}. The symbols correspond to the experimental observations, the line to the model simulations obtained by integrating eqs. [2–30] – [2–35] in which the net formation rates are calculated as explained by eq [2–15] and using the reaction mechanism and set of parameters of the originally developed Single-Event MicroKinetic model, see Table 3–1 and Table 3–4. The simulated responses of Ar and ^{12}CO are not shown as these responses visually coincide with the response of $^{12}CH_4$.

In previous modeling studies of SSITKA data [2-6], two different carbon species have been identified to contribute to the transient response of $^{12}CH_4$ and were denoted as C_α and C_β. Based on these findings, two different types of metallic Co atoms have been considered to be simultaneously present on the Co surface, i.e., “*” sites and “#” sites. Figure 5-3 illustrates the considered reaction mechanism. On the “*” sites, CO is considered to chemisorb molecularly on the surface. In two consecutive hydrogenation steps, the chemisorbed CO^{**} is converted to $HCOH^{**}$ which is subsequently dissociated to OH^{*} and CH^{***}. The CH^{***} species are further hydrogenated to CH_2^{**} and CH_3^{*} which can combine into a $C_2H_5^{*}$ species in a methylene insertion step. A metal alkyl species, $C_nH_{2n+1}^{*}$, is susceptible to chain growth to $C_{n+1}H_{2n+3}^{*}$, hydrogenation to the corresponding alkane C_nH_{2n+2} or beta hydride elimination to the corresponding metal alkene species, $C_nnH_{2n}^{*}$, which can desorb as an alkene, C_nH_{2n}. The OH^{*} species are hydrogenated to H_2O. On the other type of metallic Co sites, the “#” sites, CO is also considered to chemisorb molecularly on the surface, however its adsorption is assumed to be followed by its dissociation into $C^{\#\#\#}$ and $O^{\#\#}$ rather than first being hydrogenated. The $C^{\#\#\#}$ species are subsequently hydrogenated to $CH_2^{\#\#}$ and $CH_3^{\#}$ which are further subject to the same reactions as considered for the “*” sites. Compared to the SEMK model of Chapter 3, The SEMK model developed in this chapter explicitly accounts for the presence of different site types on the Co catalyst surface. On both site types, i.e., the “*” and “#” sites, the same reaction network as the one considered for the SEMK model of Chapter 3 has been applied except for the steps involved in the CO dissociation on the “*” sites. On the latter sites, CO dissociation is considered to be H assisted. Diffusion of surface species from ‘*’ sites to ‘#’ sites or vice versa is not considered in the model. In case surface diffusion would be fast, the feature of two sites contributing independently to the transient response of $^{12}CH_4$ would potentially disappear. Furthermore, accounting for surface diffusion opens up additional reaction paths further complicating the model regression. The reaction network corresponding with the reaction mechanism of Figure 5-3 is generated using RenGep [10] with the extension for the inclusion of ^{12}C atoms as outlined in Chapter 4. The size of the longest hydrocarbon chains considered amounts to 7.

Although not explicitly illustrated in Figure 5-3, in many of the elementary steps, surface H is involved. Surface H was considered to occur on both site types. While ab initio calculations have shown that the hydrogen chemisorption enthalpy is not very sensitive to the type of site on which H is chemisorbed [11], it is significantly influenced by the local CO surface concentration [12]. Next to this, considering the narrow confidence interval on the Q_H, see Table 3–4, and the impact of Q_H on the X_{CO} and S_{C5+}, see Figure 3–9, two separate values are considered for Q_H, one for each site type.

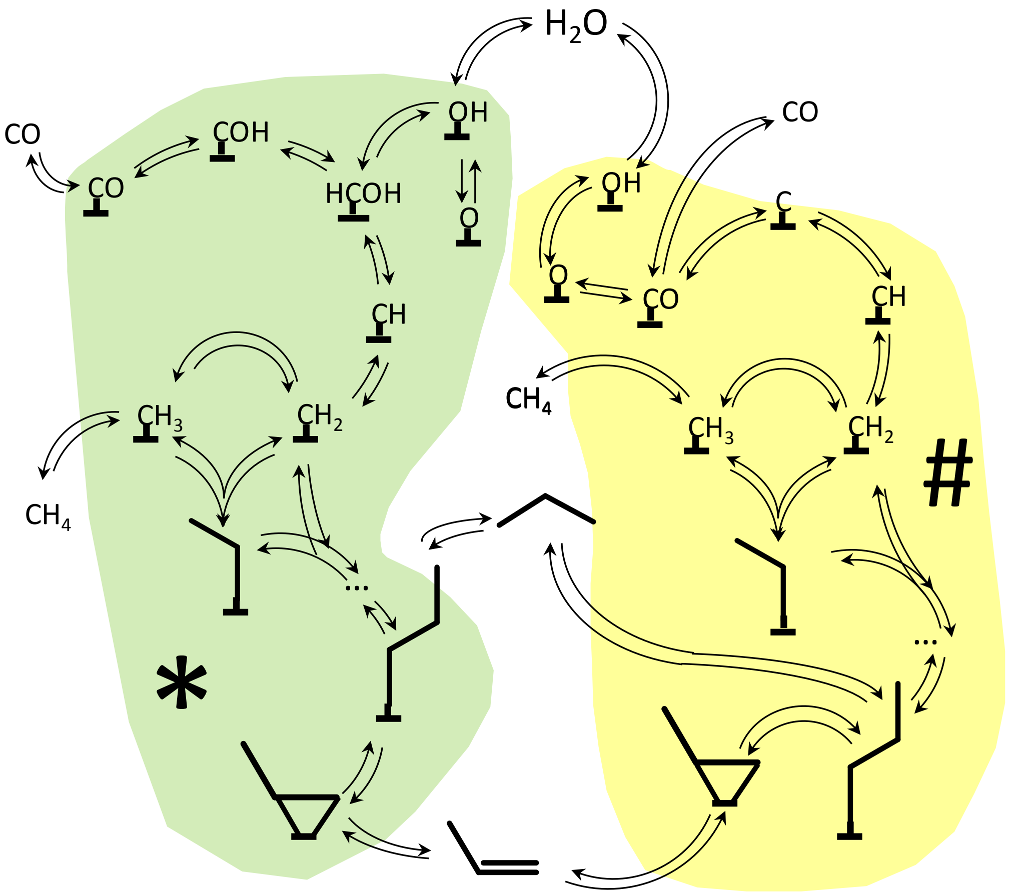

Figure 5-3: The considered Fischer-Tropsch Synthesis reaction mechanism.

5.3.1 Rate coefficients and reaction rate expressions

To the forward rate coefficients of a reaction family, the SEMK methodology is applied, see section 2.2.1.1. The reverse rate coefficients are obtained by applying the principle of microscopic reversibility at the elementary step level, see Section 2.2.1.3 and Section 2.2.1.4. The surface species chemisorption enthalpies are calculated by means of the UBI-QEP method [13, 14], see section 2.2.1.4. This introduces the atomic chemisorption enthalpies of H, C and O on two different site types into the SEMK model as adjustable model parameters.

The rate expressions for all the elementary reactions on the two different site types are provided in Table 3–2 except for the two hydrogen addition steps to CO and the subsequent dissociation of $HCOH^{**}$. The rate expression for the latter three elementary reactions are:

$$r_{CO\ re,oa,*} = \frac{z}{2}\frac{\sigma_r}{\sigma_\ddagger}\tilde{k}_{CO\ re}L_{CO^{**}}\frac{L_{H^*}}{L_{tot}} - \left(\frac{z}{2}\right)^2\frac{\sigma_r}{\sigma_\ddagger}\tilde{k}_{CO\ oa}L_{COH^*}\left(\frac{L_*}{L_{tot}}\right)^2 \qquad [5\text{-}1]$$

$$r_{COH\ re,oa,*} = \frac{z}{2}\frac{\sigma_r}{\sigma_\ddagger}\tilde{k}_{COHre}L_{COH^*}\frac{L_{H*}}{L_{tot}} - \frac{\sigma_r}{\sigma_\ddagger}\tilde{k}_{HCOHoa}L_{HCOH} \qquad [5\text{-}2]$$

$$r_{HCOH\ diss,ass,*} = \left(\frac{z}{2}\right)^2\frac{\sigma_r}{\sigma_\ddagger}\tilde{k}_{HCOH\ diss}L_{HCOH}\left(\frac{L_*}{L_{tot}}\right)^2 - \frac{z}{2}\frac{\sigma_r}{\sigma_\ddagger}\tilde{k}_{HCOH\ ass}L_{CH^{***}}\frac{L_{OH^*}}{L_{tot}} \qquad [5\text{-}3]$$

The number of nearest neighbors, z, in all the rate expressions was set equal to 6 for both the ‘*’ and ‘#’ sites.

By summation of all the rates of the elementary reactions in which a specific gas phase component or surface species is involved, the net formation rate of this gas phase component or surface species is obtained. Table 5-1 lists the net formation rates of all the gas phase components and surface species.

The balances for the total ‘*’ and ‘#’ site concentration are:

$$\begin{aligned} L_{tot,*} = {} & L_{H^*} + +2L_{CO^{**}} + L_{HCO^*} + 2L_{HCOH^{**}} + 3L_{CH^{***}} + 2L_{CH_2^{**}} \\ & + \sum_{i=1}^{CN_{max}} L_{C_iH_{2i+1}^*} + \sum_{i=2}^{CN_{max}} L_{C_iH_{2i}^*} + 2L_{O^{**}} + L_{OH^*} \end{aligned} \qquad [5\text{-}4]$$

$$\begin{aligned} L_{tot,\#} = {} & L_{H^\#} + 2L_{CO^{\#\#}} + 3L_{C^{\#\#\#}} + 3L_{CH^{\#\#\#}} + 2L_{CH_2^{\#\#}} + \sum_{i=1}^{CN_{max}} L_{C_iH_{2i+1}^\#} \\ & + \sum_{i=2}^{CN_{max}} L_{C_iH_{2i}^\#} + 2L_{O^{\#\#}} + L_{OH^\#} \end{aligned} \qquad [5\text{-}5]$$

The ratio, Γ, of the total '*' site concentration to the total site concentration, L_{tot}, is an adjustable model parameter. The abundance of the '#' sites is related to the total '*' site concentration and the total site concentration via the following site balance:

$$L_{tot} = L_{tot,*} + L_{tot,\#} \qquad [5\text{-}6]$$

The total site concentration, L_{tot}, is 0.179 mol $\text{kg}_{\text{cat}}^{-1}$, see also Section 2.1.3.

Table 5-1: The net formation rate of the various gas phase components and surface species.

Species	**Net rate of formation [mol (kg$_{cat}$ s)$^{-1}$]**
Gas phase components	
H_2	$R_{H_2} = -r_{H_2\ chem,des,*} - r_{H_2\ chem,des,\#}$
CO	$R_{CO} = -r_{CO\ chem,des,*} - r_{CO\ chem,des,\#}$
C_nH_{2n+2}	$R_{C_nH_{2n+2}} = r_{C_nH_{2n+1}\ hyd,dehyd,*} + r_{C_nH_{2n+1}\ hyd,dehyd,\#}$
C_nH_{2n}	$R_{C_nH_{2n}} = r_{C_nH_n des,chem,*} + r_{C_nH_n des,chem,\#}$
H_2O	$R_{H_2O} = r_{OH\ hyd,dehyd,*} + r_{OH\ hyd,dehyd,\#}$
“*” sites	
H^*	$R_{H^*} = 2r_{H_2\ chem,des,*} - r_{CO\ hyd,dehyd,*} - r_{HCO\ hyd,dehyd,*} - r_{CH\ hyd,dehyd,*} - r_{CH_2\ hyd,dehyd,*} - \sum_{i=1}^{CN} r_{C_iH_{2i+1}\ hyd,dehyd,*} + \sum_{i=2}^{CN} r_{C_iH_{2i+1}\ be,ba,*} - r_{O\ hyd,dehyd,*} - r_{OH\ hyd,dehyd,*}$
CO^{**}	$R_{CO^{**}} = r_{CO\ chem,des,*} - r_{CO\ hyd,dehyd,*}$
HCO^*	$R_{HCO^*} = r_{CO\ hyd,dehyd,*} - r_{HCO\ hyd,dehyd,*}$
$HCOH^{**}$	$R_{HCOH^*} = r_{HCO\ hyd,dehyd,*} - r_{HCOH\ diss,ass,*}$
CH^{***}	$R_{CH^{***}} = r_{HCOH\ diss,ass,*} - r_{CH\ hyd,dehyd,*}$
CH_2^{**}	$R_{CH_2^{**}} = r_{CH\ hyd,dehyd,*} - r_{CH_2^{**}\ hyd,dehyd,*}$
CH_3^*	$R_{CH_3^*} = r_{CH_2^{**}\ hyd,dehyd,*} - r_{CH_3^*\ hyd,dehyd,*} - r_{CH_3 mi,md,*}$
$C_nH_{2n+1}^*$	$R_{C_nH_{2n+1}^*} = r_{C_{n-1}H_{2n-1}^*\ mi,md,*} - r_{C_nH_{2n+1}^*\ mi,md,*} - r_{C_nH_{2n+1}^*\ hyd,dehyd,*} - r_{C_nH_{2n+1}^*\ be,ba,*} \quad (n > 1)$

Table 5–1: Continued

Species	**Net rate of formation [mol (kg$_{cat}$ s)$^{-1}$]**
	“*” sites
$C_nH_{2n}^*$	$R_{C_nH_{2n}^*} = r_{C_nH_{2n+1}^*\ be,ba,*} - r_{C_nH_{2n}^*\ des,chem,*} \quad (n > 1)$
O^{**}	$R_{O^{**}} = -r_{O\ hyd,dehyd,*}$
OH^*	$R_{OH^*} = r_{HCOH\ diss,ass,*} + r_{O\ hyd,dehyd,*} - r_{OH\ hyd,dehyd,*}$
	“#” sites
$H^\#$	$R_{H^\#} = 2r_{H_2\ chem,des,\#} - r_{C\ hyd,dehyd,\#} - r_{CH_2\ hyd,dehyd,\#} - \sum_{i=1}^{CN} r_{C_iH_{2i+1}\ hyd,dehyd,\#} + \sum_{i=2}^{CN} r_{C_iH_{2i+1}\ be,ba,\#} - r_{O\ hyd,dehyd,\#} - r_{OH\ hyd,dehyd,\#}$
$CO^{\#\#}$	$R_{CO^{\#\#}} = r_{CO\ chem,des,\#} - r_{CO\ diss,ass,\#}$
$C^{\#\#\#}$	$R_{C^{\#\#\#}} = r_{CO\ diss,ass,\#} - r_{C\ hyd,dehyd,\#}$
$CH^{\#\#\#}$	$R_{CH^{\#\#\#}} = r_{C\ hyd,dehyd,\#} - r_{CH\ hyd,dehyd,\#}$
$CH_2^{\#\#}$	$R_{CH_2^{\#\#}} = r_{CH\ hyd,dehyd,\#} - r_{CH_2\ hyd,dehyd,\#}$
$CH_3^\#$	$R_{CH_3^\#} = r_{CH_2\ hyd,dehyd,\#} - r_{CH_3\ hyd,dehyd,\#} - r_{CH_3 mi,md,\#}$
$C_nH_{2n+1}^\#$	$R_{C_nH_{2n+1}^\#} = r_{C_{n-1}H_{2n-1}\ mi,md,\#} - r_{C_nH_{2n+1}\ mi,md,\#} - r_{C_nH_{2n+1}\ hyd,dehyd,\#} - r_{C_nH_{2n+1}\ be,ba,\#} \quad (n > 1)$
$C_nH_{2n}^\#$	$R_{C_nH_{2n}^\#} = r_{C_nH_{2n+1}\ be,ba,\#} - r_{C_nH_{2n}\ des,chem,\#} \quad (n > 1)$
$O^{\#\#}$	$R_{O^{\#\#}} = r_{CO\ diss,ass,\#} - r_{O\ hyd,dehyd,\#}$
$OH^\#$	$R_{OH^\#} = r_{O\ hyd,dehyd,\#} - r_{OH\ hyd,dehyd,\#}$

5.4 Results

5.4.1 Experimental Results

Figure 5-4 shows the effect of temperature and H_2/CO molar inlet ratio on the CO conversion as a function of space time. The effects of increasing the temperature or the space time, Figure 5-4-a, were as expected, i.e., both result in a higher CO conversion. In the range of 5 to 10 mol mol^{-1}, a positive effect of the H_2/CO molar inlet ratio on the CO conversion is also observed.

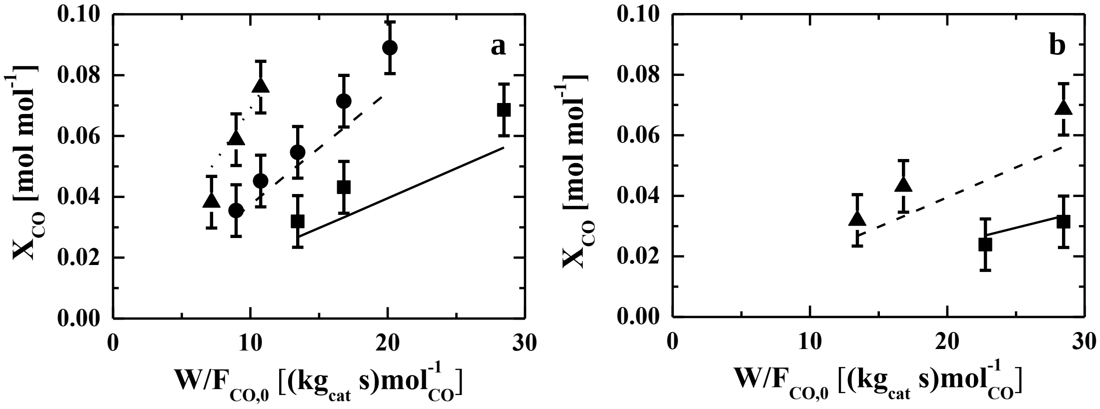

Figure 5-4: CO conversion, X_{CO}, as function of space time, W/$F_{CO,0}$. a: H_2/CO molar inlet ratio of 10, a CO inlet partial pressure of 5.5 kPa, a total pressure of 185 kPa and different temperature: ■, full line: 483 K; ●, dashed line: 493 K; ▲, dotted line: 503 K. b: temperature of 483 K, a CO inlet partial pressure of 5.5 kPa, a total pressure of 185 kPa and different H_2/CO molar inlet ratios: ■, full line: 5; ●, ▲, dashed line: 10. The symbols correspond to the experimental observations, the lines are obtained by integrating eq. [2–35] in which the net formation rates are calculated as explained by eq. [2–15] and using the set of parameters of Table 5-3.

The dependence of the product distribution on the temperature at CO isoconversion is represented in Figure 5-5 as an Anderson-Schulz-Flory (ASF) distribution plot, i.e., the outlet concentration of the alkanes and alkenes are plotted on a logarithmic scale as a function of the carbon number. The typical deviations from ASF behavior, i.e., a higher than expected methane concentration and lower than expected total C_2 concentration, are also observed for the Co/CNT catalyst at these operating conditions. Increasing the temperature increases the amount of methane that was produced, see inset of Figure 5-5–b, at the expense of higher alkanes. Figure 5-5–b also clearly shows a decreasing trend in the chain growth probability. Applying eq. [1–7] from n = 3 onwards results in α values of 0.17, 0.14 and 0.11 at respectively 483 K, 493 K and 503 K. The same effect is observed for the alkene concentration. Determining the chain growth probability for the alkenes from n = 3 onwards results in 0.13, 0.11 and 0.07 at respectively 483 K, 493 K and 503 K. No clear effect on the product distribution was observed when changing the H_2/CO molar inlet ratio at CO isoconversion.

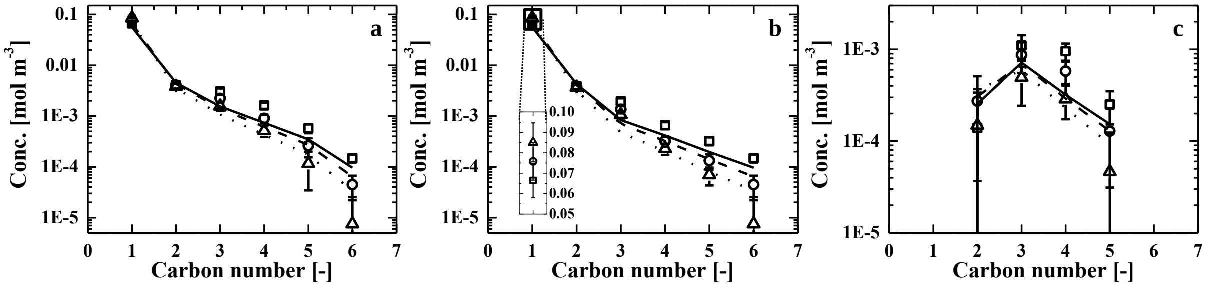

Figure 5-5: Anderson-Schulz-Flory distribution of total concentration of alkanes and alkenes (a), alkanes (b) and alkenes (c) at a H_2/CO molar inlet ratio of 10, a CO inlet partial pressure of 5.5 kPa, a total pressure of 185 kPa, CO conversion of 7% and different temperature: □, full line: 483 K; ○, dashed line: 493 K; △, dotted line: 503 K. The symbols correspond to the experimental observations, the lines are obtained by integrating eq. [2–35] in which the net formation rates are calculated as explained by eq. [2–15] and using the set of parameters of Table 5-3.

Figure 5-2 illustrates the typical transient responses of Ar, ^{12}CO and $^{12}CH_4$ following an isotopic switch from Ar/^{12}CO/H_2 to Kr/^{13}CO/H_2. The ^{12}CO transient has the same shape of the Ar transient but is delayed in time. This is related to the fast and reversible adsorption of CO on the Co surface also known as the chromatographic effect [1]. The $^{12}CH_4$ transient starts to deviate from the steady state almost at the same time of Ar. This indicates that $^{12}CH_4$ is not readsorbed on the Co surface. Compared to the ^{12}CO transient, the $^{12}CH_4$ transient is clearly affected by the surface reactions.

The effect of operating conditions, i.e., temperature and H_2/CO molar inlet ratio, on the CO and CH_4 surface residence time, eq. [2–7], as a function of space time is illustrated in Figure 5-6. The CO surface residence time, Figure 5-6–a and c, is essentially a function of space time. Both temperature and H_2/CO molar inlet ratio affect the CO surface residence time only to a minor extent. The linear dependence of the CO surface residence time on the space time clearly illustrates the chromatographic effect [1], i.e., if more sites are available for the same amount of

CO, the ^{12}CO transient will be more delayed. The CH_4 surface residence time, Figure 5-6–b and d, is independent of the space time. Increasing temperatures or H_2/CO molar inlet ratios clearly decrease the CH_4 surface residence time. As the final step in the CH_4 formation is the hydrogenation of a metal methyl surface species, the CH_4 surface residence time can be related to the reciprocal of an apparent rate constant with which the surface intermediate leading to methane is released from the surface [1], see also Section 1.4.2. This allows to explain both the effect of temperature and H_2/CO molar inlet ratio. An increasing temperature will increase this apparent reaction rate coefficient and as a consequence decrease the CH_4 surface residence time. Increasing the H_2/CO molar inlet ratio will increase the H surface coverage and, as the final step in the methane formation is a hydrogenation step, also increase this apparent rate coefficient and decrease the surface residence time.

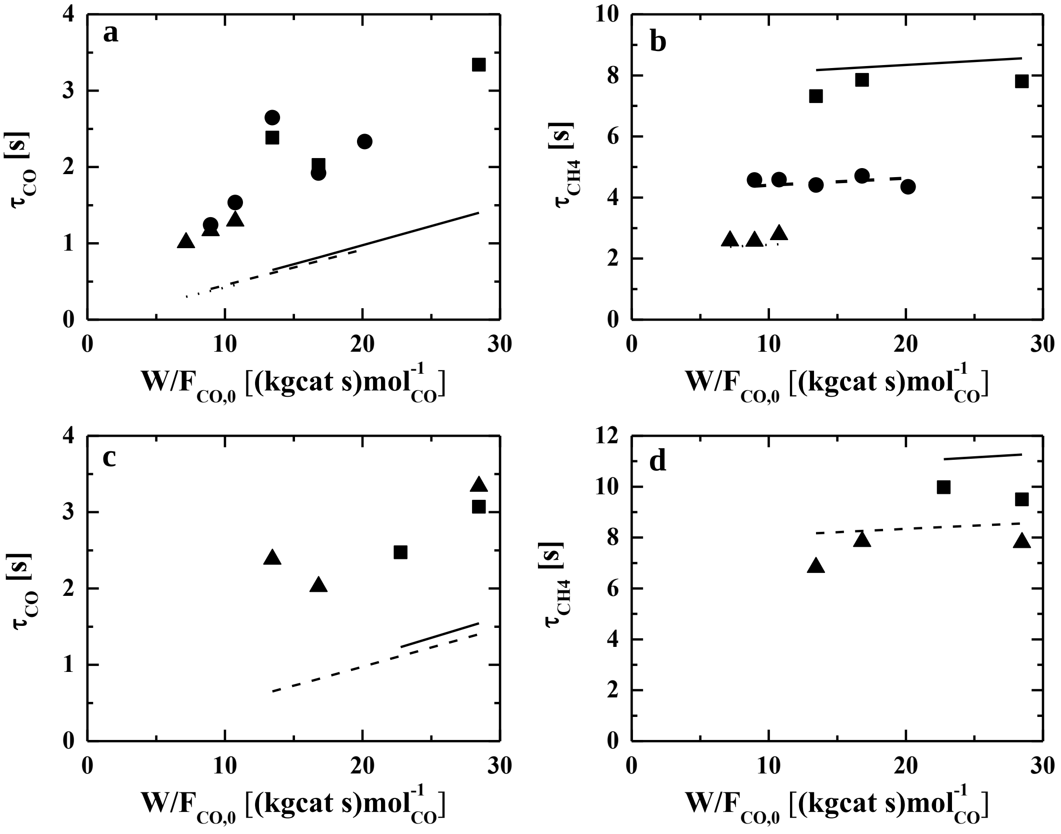

Figure 5-6: CO surface residence time, τ_{CO}, (a and c) and CH_4 surface residence time, τ_{CH4}, (b and d), see eq. [2–7], as function of space time, $W/F_{CO,0}$. a and b: H_2/CO molar inlet ratio of 10, a CO inlet partial pressure of 5.5 kPa, a total pressure of 185 kPa and different temperature: ■, full line: 483 K; ●, dashed line: 493 K; ▲, dotted line: 503 K. c and d: temperature of 493 K, a CO inlet partial pressure of 5.5 kPa, a total pressure of 185 kPa and different H_2/CO molar inlet ratios: ■, full line: 5; ▲, dashed line: 10. The symbols correspond to the experimental observations, the lines are obtained by integrating eqs. [2–30] – [2–35] in which the net formation rates are calculated as explained by eq. [2-15] and using the set of parameters of Table 5-3.

5.4.2 Chemisorption energies

The regression of the SEMK model as discussed in Chapter 3 pointed out that metal methyl species bind more strongly to the Co metal surface compared to metal alkyl species with more than one carbon atom, see section 3.3.3.1. Initial regression results indicated that the two site types present in the SEMK model developed in this chapter may represent terrace and step sites 5.4.4.1.

The Vienna Ab Initio Simulation Package (VASP) has been used to calculate chemisorption energies of alkyl species with 1 to 3 carbon atoms at 0 K. The terrace sites are modeled by means of a Co(0001) surface. The unit cell for this Co(0001) surface is 3×3 Co atoms large and 4 layers of Co atoms thick. The step sites are modeled by means of removing three rows of Co atoms from a Co(0001) surface to create a step of one Co atom high. A unit cell of 6×3 Co atoms large and 4 layers of Co atoms thick was considered for these calculations. The applied convergence settings for the calculations are discussed in section 2.2.2. The results of the ab initio calculations are reported in Table 5-2 as chemisorption energies.

Table 5-2: Ab initio determined chemisorption energies (kJ mol^{-1}) of metal alkyl species with 1 to 3 carbon atoms on a terrace site and a step site.

Alkyl species	Terrace site	Step site
CH_3	188.2	210.2
C_2H_5	144.0	183.4
C_3H_7	148.8	187.2

On the terrace sites a difference in chemisorption energy around 40 kJ mol^{-1} between metal methyl species and metal alkyl species with more than one carbon atom is obtained based on the ab initio calculations. On the step sites, this difference is reduced to 25 kJ mol^{-1}. These values have been used to obtain initial estimates for the superposition factor α of eq. [2–24] for the description of the chemisorption enthalpy of the metal methyl species compared to a fixed value of 0.5 for the metal alkyl species with more than one carbon atom. These initial estimates have been obtained by calculating the chemisorption enthalpies of metal ethyl and metal propyl with eq. [2–24] as a function of the carbon chemisorption enthalpy varying from 610 kJ mol^{-1} to 670 kJ mol^{-1} for the terrace sites and from 670 kJ mol^{-1} to 740 kJ mol^{-1} for step sites and minimizing the difference between the C_1 chemisorption enthalpy and C_2 and C_3 chemisorption enthalpy obtained from eq. [2–24] and the value obtained from the ab initio calculations. This led to 0.92 and 0.73 for α of eq. [2–24] for the terrace sites and step sites respectively.

5.4.3 Regression results

In total, 28 model parameters had to be estimated by regression to experimental data. The model parameter values are presented in Table 5-3. The values indicated in plain font have been determined a priori as explained in section 2.2.1.3. The values in bold font are estimates determined by regression. The values in italic font are derived from the parameter estimates.

The regression was found to be globally significant as the corresponding F value, eq. [2–47], amounts to 4.85 10^5 compared to the tabulated value of 2.79. Furthermore, all the parameter estimates are statistically significantly different from zero as the lowest calculated t value, eq. [2-48], amounts to 1.25 10^5 compared to the tabulated t value of 1.96. The t values for all the individual parameter estimates are indicated in parenthesis next to the parameter estimates. No correlation is found between the statistically significant parameters as all the binary correlation coefficients, eq. [2–49], vary between -0.73 to 0.64.

It is noted that the high values obtained for F and t values can probably be attributed to the fact that data points belonging to a time series are correlated. Accounting for this correlation reduces these values [15]. Furthermore, these high t values result in small confidence intervals. This is the reason why the confidence intervals have not been indicated in Table 5-3. Despite the high t values, the relative ordering between the t values will be preserved if the correlation between data points of a time series is accounted for [15]. Hence, it is anticipated that E_a for CH_2^{**} insertion and $OH^{\#}$ hydrogenation will have the widest confidence intervals. Based on the reaction path analysis presented in Section 5.4.6, these parameters correspond with reaction steps which practically do not take place or reaction steps which are at quasi-equilibrium.

Table 5-3: Forward single-event pre-exponential factors, $\tilde{A}^f$, activation energies, E_a^f, atomic chemisorption enthalpies of hydrogen, Q_H, carbon, Q_C, and oxygen, Q_O, on both type of surface sites, surface reaction enthalpies, ΔH_r^0, and single-event surface reaction entropies, $\Delta\tilde{S}_r^0$ at 493 K. The values in plain font are determined a priori from open source data banks and statistical thermodynamics calculations, see section 2.2.1.3. The values indicated in bold font are determined by non-linear regression of the model to the experimental data in which the model responses are obtained by integrating eqs. [2–30] to [2-35] in which the net production rates are calculated as explained by eq [2-15]. The values in italic font are derived values from the values obtained from the non-linear regression. The values in parenthesis next to the values in bold font are the t values, eq. [2–48], multiplied with 10^{-5}.

Reaction	$\tilde{A}^f$ **[s^{-1} or (Mpa s)$^{-1}$]**	E_a^f **[kJ mol^{-1}]**	ΔH_r^0 **[kJ mol^{-1}]**	$\Delta\tilde{S}_r^0$ **[J (K mol)$^{-1}$]**
Elementary reaction				
Reactant adsorption				
$H_{2,(g)} + 2\,* \rightleftarrows 2H^{*}$	$3.6\ 10^{9}$	0.0	*-52.9*	-60.0
$CO + 2\,* \rightleftarrows CO^{**}$	$2.6\ 10^{8}$	0.0	*-116.3*	-160.9
$H_{2,(g)} + 2\# \rightleftarrows 2H^{\#}$	$3.6\ 10^{9}$	0.0	*-58.1*	-60.0
$CO + 2\# \rightleftarrows CO^{\#\#}$	$2.6\ 10^{8}$	0.0	*-141.1*	-160.9
Initiation reactions				
$CO^{**} + H^{*} \rightleftarrows COH^{*} + 2\,*$	$9.7\ 10^{14}$	**76.7** (6.9)	*66.1*	37.8
$COH^{*} + H^{*} \rightleftarrows HCOH^{**}$	$5.9\ 10^{10}$	**86.8** (3.1)	*45.4*	-42.7
$HCOH^{**} + 2\,* \rightleftarrows CH^{***} + OH^{*}$	$1.2\ 10^{18}$	**60.9** (1.7)	*47.0*	54.9
$CH^{***} + H^{*} \rightleftarrows CH_2^{**} + 2\,*$	$4.4\ 10^{11}$	**37.7** (3.0)	*-29.2*	-26.2
$CH_2^{**} + H^{*} \rightleftarrows CH_3^{*} + 2\,*$	$1.7\ 10^{11}$	**63.6** (4.0)	*-113.2*	-33.9
$CO^{\#\#} + \#\#\# \rightleftarrows C^{\#\#\#} + O^{\#\#}$	$1.0\ 10^{13}$	**18.7** (1.7)	*-64.4*	-15.3
$C^{\#\#\#} + H^{\#} \rightleftarrows CH^{\#\#\#} + *$	$5.5\ 10^{14}$	**75.4** (2.6)	*74.5*	33.0
$CH^{\#\#\#} + H^{\#} \rightleftarrows CH_2^{\#\#} + 2\#$	$4.4\ 10^{11}$	**23.0** (4.6)	*-10.5*	-26.16
$CH_2^{\#\#} + H^{\#} \rightleftarrows CH_3^{\#} + 2\#$	$1.7\ 10^{11}$	**37.5** (1.6)	*-61.7*	33.9

Table 5–3: continued

Reaction	$\widetilde{A}^{f}$ [s^{-1} or (Mpa s)$^{-1}$]	E_a^f [kJ mol^{-1}]	ΔH_r^0 [kJ mol^{-1}]	$\Delta \tilde{S}_r^0$ [J (K mol)$^{-1}$]
Elementary reaction				
Water formation				
$O^{**} + H^{*} \rightleftarrows OH^{*} + 2\,*$	9.8 10^{11}	**96.2** (3.3)	*50.0*	32.0
$OH^{*} + H^{*} \rightleftarrows H_2O_{(g)}$	2.0 10^{11}	**81.7** (3.9)	*29.5*	70.7
$O^{\#\#} + H^{\#} \rightleftarrows OH^{\#} + 2\#$	9.8 10^{11}	**80.5** (1.3)	*62.7*	32.0
$OH^{\#} + H^{\#} \rightleftarrows H_2O_{(g)}$	2.0 10^{11}	**96.4** (1.6)	*74.6*	70.7
Reaction family				
Chain growth				
$C_nH_{2n+1}^{*} + CH_2^{**}$ $\rightleftarrows C_{n+1}H_{2n+3}^{*} + 2\,*$	4.5 10^{9}	**63.0** (1.2)	*-57.7 (n=1)* *-94.2 (n=2)* *-93.3 (n>2)*	-63.3
$C_nH_{2n+1}^{\#} + CH_2^{\#\#}$ $\rightleftarrows C_{n+1}H_{2n+3}^{\#} + 2\#$	4.5 10^{9}	**40.5** (4.0)	*-25.5 (n=1)* *-37.7 (n=2)* *-36.8 (n>2)*	-63.3
Alkanes formation				
$C_nH_{2n+1}^{*} + H^{*}$ $\rightleftarrows C_nH_{2n+2,(g)} + 2\,*$	2.9 10^{10}(n=1) 1.6 10^{10}(n>1)	**88.1** (2.8)	*15.7 (n=1)* *-9.0 (n=2)* *-8.2 (n>2)*	58.9
$C_nH_{2n+1}^{\#} + H^{\#}$ $\rightleftarrows C_nH_{2n+2,(g)} + 2\#$	2.9 10^{10}(n=1) 1.6 10^{10}(n>1)	**95.1** (1.9)	*26.1 (n=1)* *25.8 (n=2)* *26.7(n>2)*	58.9
Metal alkenes formation				
$C_nH_{2n+1}^{*} + * \rightleftarrows C_nH_{2n}^{*} + H^{*}$	1.1 10^{10}	**66.0** (3.0)	*15.3 (n=2)* *7.3 (n=3)* *7.9 (n>3)*	13.0
$C_nH_{2n+1}^{\#} + * \rightleftarrows C_nH_{2n}^{\#} + H^{*}$	1.1 10^{13}	**79.3** (2.2)	*31.2 (n=2)* *16.6 (n=3)* *17.4 (n>3)*	13.0

Table 5–3: continued.

Reaction	$\widetilde{\mathbf{A}}^{\mathbf{f}}$ [s^{-1} or (Mpa s)$^{-1}$]	$\mathbf{E_a^f}$ [kJ mol^{-1}]	$\mathbf{\Delta H_r^0}$ [kJ mol^{-1}]	$\mathbf{\Delta \tilde{S}_r^0}$ [J (K mol)$^{-1}$]
Reaction family				
Metal alkenes desorption				
$C_nH_{2n}^{*} \rightleftarrows C_nH_{2n,(g)} + *$	1.0 10^{13}	*62.2* (n=2) *59.3* (n=3)	*62.2* (n=2) *59.3* (n=3)	113.3
$C_nH_{2n}^{\#} \rightleftarrows C_nH_{2n,(g)} + \#$	1.0 10^{13}	*75.9 (n=2)* *79.7 (n=3)*	*75.9 (n=2)* *79.7 (n=3)*	113.3
Atomic chemisorption enthalpies [kJ mol^{-1}]				
Q_{H*}		**245.7** (4.4)		
Q_{C*}		**640.3** (6.5)		
Q_{O*}		**520.8** (4.2)		
$Q_{H\#}$		**248.2** (1.7)		
$Q_{C\#}$		**710.9** (2.0)		
$Q_{O\#}$		**573.4** (2.0)		
Superposition parameter in eq. [2–24]				
α_{*}		**0.94** (3.0)		
$\alpha_{\#}$		**0.69** (3.9)		
Total "*" site concentration to the total site concentration				
Γ		**0.72** (3.3)		

Figure 5-7 shows parity diagrams for the steady state outlet concentration of alkanes and alkenes. The performance of the model with respect to the description of the transient responses of ^{12}CO and $^{12}CH_4$ is presented in Figure 5-8 and Figure 5-9. In Figure 5-8 three of the eleven transient experiments which were considered in the regression are shown. Figure 5-9 shows the performance of the model with respect to three of the six experiments which were not part of the experimental data used for the regression.

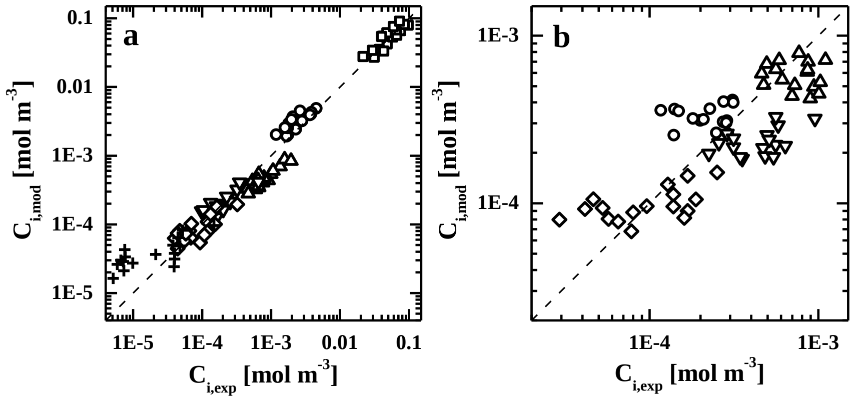

Figure 5-7: Experimental and model calculated outlet concentrations, C_i, at 5 – 10 H_2/CO molar inlet ratio, 483 K – 503 K, a CO inlet partial pressure of 5.5 kPa, a total pressure of 185 kPa and space time, $W/F_{CO,0}$, varying between 7 and 29 $(kg_{cat}\ s)mol^{-1}$. The calculated outlet concentrations are obtained by integrating eq. [2-30] to [2–35] in which the net production rates are calculated as explained by eq. [2–15] and using the set of parameters given in Table 5-3. (a): methane (□), ethane (○), propane (△), *n*-butane (▽), *n*-pentane (◇) and *n*-hexane (✚). (b): ethene (○), propene (△), 1-butene (▽) and 1-pentene (◇).

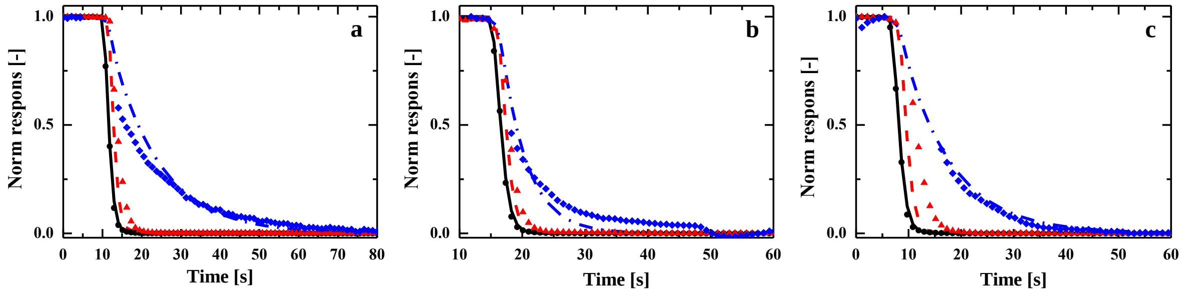

Figure 5-8: Experimental (symbols) and model calculated (lines) normalized outlet concentrations of Ar (●,—), CO(▲, – –) and CH_4 (◆, – •), at a CO inlet partial pressure of 5.5 kPa, total pressure of 185 kPa, a H_2/CO molar inlet ratio of 5 (a and b) or 10 (c), a temperature of 483 K (a and c) or 503 K (b) and a space time, $W/_{FCO,0}$, of 23 (a), 20 (b) and 29 (c) $(kg_{cat}s)mol_{CO}^{-1}$ The calculated normalized outlet concentrations are obtained by integrating eq. [2–30] to [2–35] in which the net production rates are calculated as explained by eq. [2–15] and using the set of parameters given in Table 5-3. These responses were part of the experimental data used in the regression.

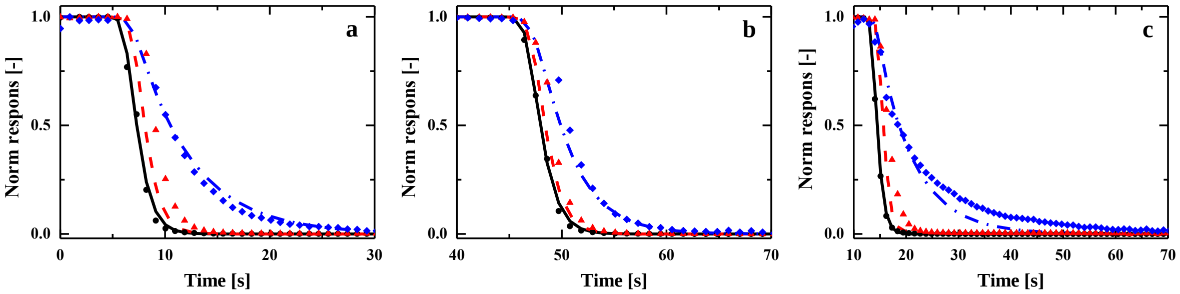

Figure 5-9: Experimental (symbols) and model calculated (lines) normalized outlet concentrations of Ar (●,—), CO(▲, – –) and CH_4 (◆, – •), at a CO inlet partial pressure of 5.5 kPa, total pressure of 185 kPa, a H_2/CO molar inlet ratio of 5 (b) or 10 (a and c), a temperature of 493 K (a and c) or 503 K (b) and a space time, $W/F_{CO,0}$, of 17 (a), 11 (b) and 23 (c) $(kg_{cat}s)mol_{CO}^{-1}$ The calculated normalized outlet concentrations are obtained by integrating eq. [2–30] to [2–35] in which the net production rates are calculated as explained by eq. [2–15] and using the set of parameters given in Table 5-3. These responses were not part of the experimental data used in the regression and, hence, are used for model validation purposes.

5.4.4 Assessment of the model parameters

5.4.4.1 Chemisorption enthalpies

The Q_H has been determined experimentally to amount to 251 kJ mol^{-1} approximately [16]. The Q_H on the “*” and“#” types corresponds well with this value, see Table 5-3. This value has also been determined via solid state ab initio calculations. On a flat hcp [12, 17, 18] or fcc [19] free Co surface this value is calculated to be in the range of 261 kJ mol^{-1} to 282 kJ mol^{-1}. On corrugated surfaces [18] and steps [17], a decrease in Q_H is typically reported but within 5 kJ mol^{-1} to 12 kJ mol^{-1} [18]. The local CO surface coverage has the most significant impact on Q_H, i.e., this value changes with 57 kJ mol^{-1} from a free Co(0001) to a precovered Co(0001) surface with a 0.5 CO surface coverage [12]. An experimental value for Q_C, based on the formation enthalpy of the bulk structure, is reported as 678 kJ mol^{-1} [16] which is in the center of the values for Q_C obtained in this chapter by regression, see Table 5-3. Solid state ab initio calculations have pointed out that this value is very sensitive to the site type [11, 17, 18, 20, 21] and the CO surface coverage [12]. Changes in surface structure or increasing the CO coverage from 0 to 0.5 can, in both cases, change the adsorption energy with almost 100 kJ mol^{-1}. An estimate for Q_O based on the formation enthalpy of the bulk structure is reported, i.e., 485.6 kJ mol^{-1} [16]. The values obtained from the regression, i.e., 520.8 kJ mol^{-1} and 573.4 kJ mol^{-1}, are significantly higher than this estimate. Q_O has also been reported for various Co surfaces based on solid state ab initio calculations. On Co(0001) [11, 12, 17, 18] and Co(111) [19] surfaces, Q_O has been reported to be situated within a range from within 513 kJ mol^{-1} to 586 kJ mol^{-1}. A CO precoverage can reduce this value by 100 kJ mol^{-1} [12]. On corrugated Co surfaces, the adsorption strength typically increases but the effect is less pronounced compared to the dependence of the C adsorption energies [11]. The maximum reported change is 38 kJ mol^{-1} [11]. The values obtained in this chapter for the atomic chemisorption enthalpies are, hence, in the range of ab initio calculated values. Furthermore, the higher Q_C and Q_O on the "#" sites are indicative that these sites correspond with step sites and the "*" sites correspond with terrace sites.

H_2 and CO chemisorption enthalpies obtained by regression of microkinetic models to experimental data are reported in literature. For H_2, chemisorption enthalpies have been reported in a range between 2 kJ mol^{-1} to 70 kJ mol^{-1} [22-26]. The CO chemisorption enthalpy is reported to vary between 37.3 kJ mol^{-1} to 111.6 kJ mol^{-1} [22-26]. A CO chemisorption energy of 160 kJ mol^{-1} is obtained on a Co(0001) surface by means of solid state ab initio calculations [17, 18, 21]. On a more corrugated surface or a step site, the absolute value of the CO adsorption energy typically increases [17, 18, 21] and this with about 20 kJ mol^{-1} maximally. Changing the CO surface coverage from an empty surface to a surface with a CO precoverage of 0.5 decreases the CO chemisorption energy with 100 kJ mol^{-1} [12]. The chemisorption enthalpies, see Table 5-3, obtained in this chapter are, hence, acceptable.

The chemisorption enthalpy for the methyl radical on the "*" sites amounts to 214 kJ mol^{-1} and to 222 kJ mol^{-1} on the "#" sites. For the heavier alkyl radicals, a value of 169 kJ mol^{-1} on the "*" and 202 kJ mol^{-1} on the "#" sites is obtained. These values are somewhat higher compared to the ab initio calculated values, see Table 5-2, but are considered reasonable. It is, furthermore, noted that the initially estimated differences in chemisorption enthalpies based on the ab initio calculations, see section 5.4.2, between methyl radicals and the heavier radicals are maintained, i.e., a difference of 40 kJ mol^{-1} on the "*" sites and 20 kJ mol^{-1} on the "#" sites.

The chemisorption enthalpy of alkenes on the "*" sites is equal to 59.3 kJ mol^{-1} and on the "#" sites to 79.7 kJ mol^{-1}. Both these values are close to an ab initio reported value of 75 kJ mol^{-1} [27]

and are in the range of reported values for alkenes chemisorption obtained by Azadi et al [24] after regression to experimental data.

5.4.4.2 Activation energies

The direct CO dissociation route on Co catalysts has been applied in microkinetic modeling studies [23, 28-30] but only one study reports on the corresponding activation energy which amounts to 72 kJ mol^{-1} [23]. In other microkinetic modeling studies this reaction step has been assumed a priori to be quasi-equilibrated [26, 29]. Ab initio calculations have pointed out the necessity of sites with a low coordination to facilitate the direct CO dissociation. Sites with an activation energy of 68 kJ mol^{-1} for direct CO dissociation have been reported. The value obtained in this chapter by regression, i.e., 18.7 kJ mol^{-1}, is lower than the reported values but is still considered to be reasonable.

The H assisted CO dissociation has also been applied in microkinetic modeling studies [22, 24-26, 31-33]. Typically the first hydrogen addition is considered to be irreversible and rate determining [25, 26, 31-33] and the reported corresponding range of activation energies varies from 87 kJ mol^{-1} to 100 kJ mol^{-1}[25, 26, 31-33]. Azadi et al. [24] considers the same reaction steps in CO dissociation and found 128 kJ mol^{-1}, 84 kJ mol^{-1} and 44 kJ mol^{-1} for the first hydrogenation, second hydrogenation and HCOH dissociation step respectively. Ab initio studies for the first hydrogenation step on a Co(0001) or a Co(111) surface report activation energies varying between 113 kJ mol^{-1} and 146 kJ mol^{-1} [12, 18, 19, 34]. The second hydrogenation step requires 90 kJ mol^{-1} on Co(0001) [12] or 104 kJ mol^{-1} on Co(111) [19] surfaces. The final HCOH dissociation activation barrier amounts to 106 kJ mol^{-1} on Co(0001) [12] or 71 kJ mol^{-1} on Co(111) [19] surfaces. The activation energy obtained in this chapter for the first hydrogenation, i.e., 76.7 kJ mol^{-1}, second hydrogenation, i.e., 86.8 kJ mol^{-1} and the final HCOH dissociation step, i.e., 60.9 kJ mol^{-1}, are within the ranges of reported activation energies.

The activation energies for hydrogenation of $C^{\#\#\#}$ and the hydrogenation of CH_2^{**} and $CH_2^{\#\#}$ types correspond well with the range of activation energies reported by ab initio studies [18, 20], i.e., $E_{a,Cre}$ ranges between 61 kJ mol^{-1} and 82 kJ mol^{-1} and E_{a,CH_2re} between 30 kJ mol^{-1} and 62 kJ mol^{-1}. The activation energy for CH^{***} or $CH^{\#\#\#}$ hydrogenation obtained in this chapter is lower than the activation energies reported by ab initio studies [18, 20]. This can be attributed to the chemisorption enthalpy obtained via the UBI-QEP method. As also explained in Chapter 3, the UBI-QEP method underpredicts the chemisorption enthalpy of CH^{***} or $CH^{\#\#\#}$ compared to the values obtained by ab initio calculations. This in turn decreases the activation energy of the CH^{***} or $CH^{\#\#\#}$ hydrogenation step. It is noted that, on the other hand, the activation energy of the CH^{***} hydrogenation corresponds well with the activation energy obtained at Co surfaces with co-adsorbed CO [35]. Although the structure sensitivity of the CH_x hydrogenation reaction is less pronounced compared to that of CO dissociation, it is noted that the trend in the CH_2 hydrogenation activation energies, i.e., a decrease on corrugated surfaces, is also supported by ab initio calculations [18, 20]. Activation energies for these reactions are rarely reported by microkinetic modeling. Azadi et al. [24] reports an activation energy for CH hydrogenation of 35 kJ mol^{-1} and 70 kJ mol^{-1} for CH_2 hydrogenation. The values obtained in this chapter correspond well with the values reported by this author.

A wide range of methylene insertion energies has been reported by microkinetic modeling studies. The value obtained for the methylene insertion for the “#” sites corresponds well with the value reported by Azadi et al. [24] for methylene insertion in $C_2H_5^{\#}$, i.e., 40.5 kJ mol^{-1} obtained in this chapter vs. 39.5 kJ mol^{-1} reported in literature. The activation energy on the “*” sites are at the higher range of values reported in literature. Furthermore, it is noted that Ab initio studies on CH_2 insertion in CH_2 or CH_3 indicate that these reactions have a lower activation barrier on step sites compared to flat sites [36].

Microkinetic modeling studies which report on activation energies for metal alkyl hydrogenation typically report values in the range of 80 kJ mol^{-1} [25, 26, 29, 31, 32], but values as high as 141 kJ mol^{-1}[24] have also been obtained by regression to experimental data. Ab initio calculations result in activation energies for alkyl hydrogenation between 64 kJ mol^{-1} to 105 kJ mol^{-1} [18, 20, 27, 37]. The values obtained here, i.e., 88.1 kJ mol^{-1} on the “*” sites and 95.1 kJ mol^{-1} on the “#” sites, are, hence, centrally situated in the range of reported values for metal alkyl hydrogenations.

The beta hydride elimination activation energies are lower than the activation energies obtained for metal alkyl hydrogenation. This is also found by ab initio calculations [27] and one other microkinetic modeling work [24]. Alternative microkinetic modeling studies [25, 29, 31, 32] report a reverse order for these activation energies, which is explained by the considered reaction mechanism, i.e., the formation of alkenes occurs in a direct step from the metal alkyl species. In such a single step scenario, a higher yield of alkenes compared to alkanes is avoided by a higher activation energy for the formation of alkenes compared to the activation energy for the formation of alkanes.

It is noted that the order of activation energies for methylene insertion, alkyl hydrogenation and beta hydride elimination is reflected in the product distribution. An increase in temperature increases the selectivity to methane and decreases the chain growth probability in the higher alkanes and alkenes. An increasing temperature increases the hydrogenation rate more than that of methylene insertion due to the higher activation energy of the former compared to the latter reaction step.

The steps involved in the water formation are typically considered as quasi-equilibrated steps in the microkinetic modeling studies reported in literature. Only Azadi et al. [24] reported an E_a for O hydrogenation step amounting to 86 kJ mol^{-1} and the activation energy for the hydroxyl hydrogenation by another hydroxyl species, i.e., OH+OH, to be 135 kJ mol^{-1}. An ab initio study on the oxygen removal resulted in high values for hydrogenation steps on Co(0001), i.e., 165 kJ mol^{-1} and 136 kJ mol^{-1} respectively. The values for a stepped surface change to 70 kJ mol^{-1} and 155 kJ mol^{-1}. The activation energies for the oxygen removal are, hence, considered to be reasonable.

Next to physically meaningful values for the activation energies, also reasonable values for the pre-exponential factors are derived and are within the range of values reported in literature [24, 38].

5.4.4.3 Abundance of the different sites

The total concentration of “*” sites relative to the total site concentration is estimated at a value of 0.72. Due to the total site balance, eq. [5-6], the relative abundance of the “#” sites amounts to 0.28. van Helden et al. [39] studied the presence of different site types on Co metal particles with sizes between 1 and 8 nm. The fraction of terrace sites according to these authors amounts to 0.82 for the largest metal particles studied, i.e., 8 nm. The fraction of step sites was equal to 0.18 for the 8 nm Co metal particles. The value obtained in this chapter for the fraction of “*” sites which correspond, based on the Q_C, to terrace sites is, hence, reasonable for Co metal particles with an average diameter of 11 nm, see Section 2.1.3.

5.4.5 Surface coverages

The surface coverage of the various surface species as a function of the space time, $W/F_{CO,0}$, at a CO inlet partial pressure of 5.5 kPa, a H_2/CO molar inlet ratio of 10, a total pressure of 1.85 kPa and 483 K is presented in Figure 5-10. Figure 5-10–a–c represents the surfaces coverages on both site types scaled with their relative abundance, i.e., 0.72 for the “*” sites and 0.28 for the “#” sites. This will be indicated by a “×”. The coverage on both site types are included in Figure 5-10 to make a direct comparison with surface coverages reported on by other microkinetic modeling studies of Co catalyzed FTS considering only one site type more straightforwardly. The surface coverages on the “*” sites are depicted in Figure 5-10–d–f. The surface coverages on the “#” sites are presented in Figure 5-10–g–i.

The most abundant surface species on the Co catalyst surface, see Figure 5-10–a, are $CO^{\times\times}$, $H^{\times}$ and $C_nH_{2n+1}^{\times}$. The oxygen containing species, i.e., $O^{\times\times}$, $OH^{\times}$ and $CHO^{\times}$ occupy 15% of the surface. The other species, i.e., $C_nH_{2n}^{\times}$, $C^{\times\times\times}$, $CH_2^{\times\times}$, $HCOH^{\times\times}$ and $CH^{\times\times\times}$are only present in minor amounts.

The reactants surface coverages, i.e., $CO^{\times\times}$ and $H^{\times}$, occupy 52 % and 22% of the Co surface respectively. van Dijk et al [4] obtained a CO surface coverage of 65% by mircokinetic modeling of SSITKA data. Other microkinetic modeling studies [24, 25, 33] report CO surface coverages between 10% and 65%. The H surface coverage reported by these microkinetic modeling studies is between 1% and 4%. The $C_nH_{2n+1}^{\times}$ surface coverage amounts to 10% which corresponds with the values obtained by Todic et al [25], i.e., 17%, and Visconti et al [33], i.e., 10 %. A surface coverage of methane precursors amounting to 10% has been determined by den Breejen et al [8] by analyzing SSITKA data. This corresponds well with the value for $CH_3^{\times}$ obtained in this chapter, i.e., 6.5%. Azadi et al. [24] reports an OH surface coverage of around 10 % based on a microkinetic modeling study. den Breejen et al. [8] estimated the water precursors to occupy 7.5% of the surface by analysis of SSITKA data. A combined value for $O^{\times\times}$ and $OH^{\times}$ of 12% found in this chapter corresponds well with these literature reported values. A low value for the sum of $C^{\times\times\times}$, $CH^{\times\times\times}$ and $CH_2^{\times\times}$ and for the $C_nH_{2n}^{\times}$ corresponds with the findings of Azadi et al

[24]. The surface coverages simulated with the SEMK model developed in this chapter, hence, correspond with results obtained by other microkinetic modeling studies and experimental studies.

The most abundant surface species on the “*” sites, see Figure 5-10-d, are also CO^{**}, H^{*} and HCO^{*}. These species cover the “*” sites for 99%. On the “#” sites, the most abundant surface species are $C_nH_{2n+1}^{\#}$, $CO^{\#\#}$ and the oxygen containing species $OH^{\#}$ and $O^{\#\#}$, see Figure 5-10-g. The free surface site coverage on the “*” sites is higher than the free surface site coverage on the “#”. This can be attributed to the higher atomic chemisorption enthalpies for the “#” sites.

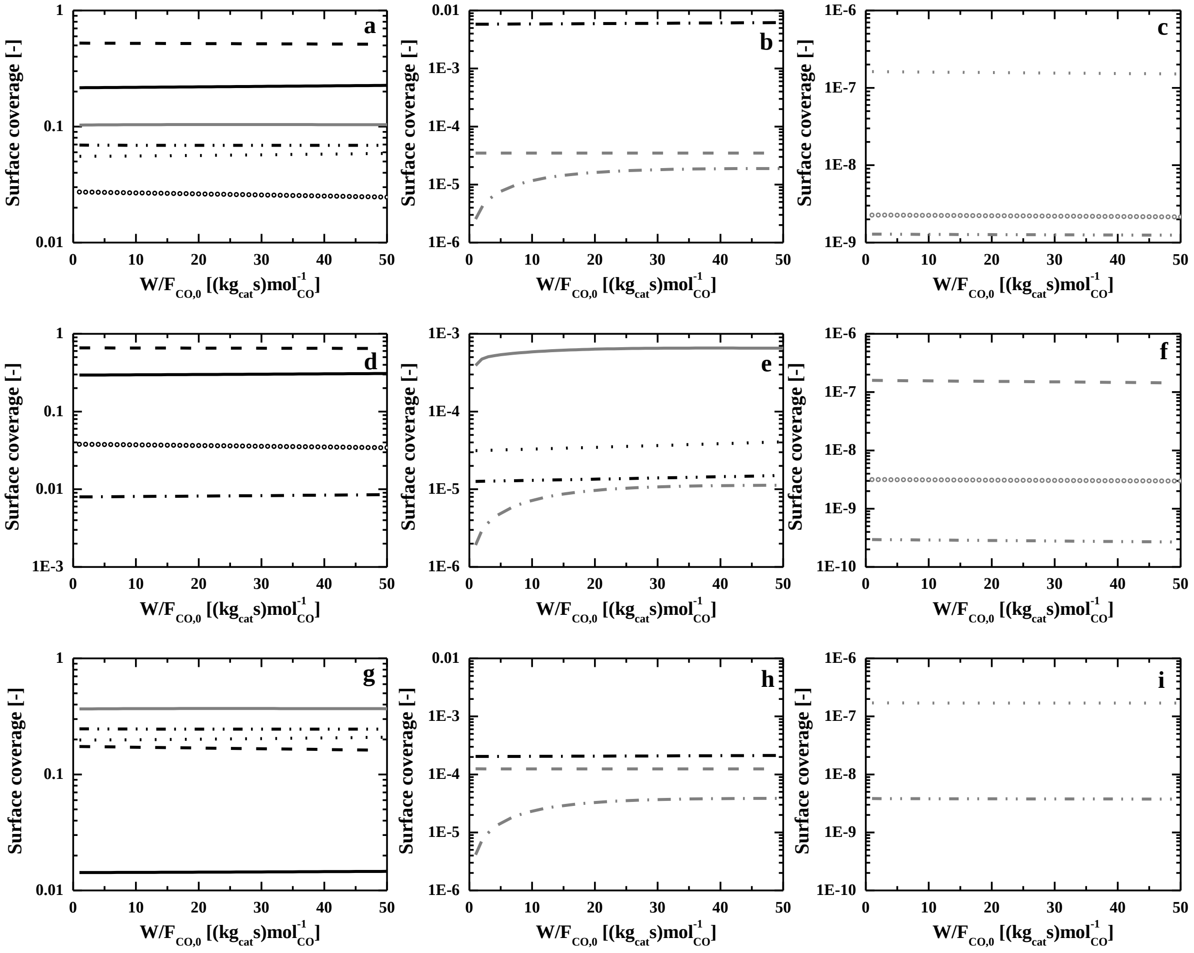

Figure 5-10: The surface coverage as a function of space time, W/F$_{CO,0}$. a-c: the surface coverage on both site types scaled with their relative abundance, indicated by "×". d-f: The surface coverage on the "*" sites. g-h: The surface coverage on the "#" sites. The simulation results are obtained by integrating eq. [2–35] in which the net formation rates are calculated as explained by eq. [2–15] and using the set of parameters of Table 5-3. The inlet conditions for the simulation are a CO inlet partial pressure of 5.5 kPa, a H$_2$/CO molar inlet ratio of 10, a temperature of 483 K and a total pressure of 185kPa. Full line – black:H$^{\$}$; dashed line – black: CO$^{\$\$}$; dotted line – black: O$^{\$\$}$; dash dotted line – black: \$; dash dot dotted line – black: OH$^{\$}$; open dotted line-black: HCO$^{\$}$; full line – grey: C$_nH_{2n+1}$$^{\$}$; dashed line-grey: C$^{\$\$\$}$; dotted line – grey: CH$_2$$^{\$\$}$; dash dotted line-grey: C$_n$H$_{2n}$$^{\$}$; dash dot dotted line – grey: CH$^{\$\$\$}$; open dotted line – grey: HCOH$^{\$\$}$. (\$ = ×, * or #).

5.4.6 Reaction path analysis

A reaction path analysis has been performed at a H$_2$/CO molar inlet ratio of 10, a CO inlet partial pressure of 5.5 kPa, a total pressure of 1.85 kPa, a temperature of 483 K and a space time of 23

$(kg_{cat}s)mol_{CO}^{-1}$. The results are presented in Figure 5-11. Black indicates the elementary reactions which are at quasi-equilibrium as determined from the corresponding affinity, see eq. [2–52]. The elementary reactions which are not at quasi-equilibrium are indicated by colored arrows. The color of the arrow of an elementary step is a measure for the reaction rate of that elementary step, i.e., blue is used for a slow reaction rate while red is indicative for a fast reaction. The triangles indicate the direction of the net rate of an elementary reaction and the value in the triangle is the net rate of the elementary reaction relative to the net CO consumption rate. If this ratio becomes smaller than 1%, the triangle has been discarded. The differential formation factor, eq. [2–51], is indicated at the top of an arrow of an elementary step. At the tail of the arrow, the differential disappearance factor, eq. [2–50] is reported.

The chemisorption of reactants and alkenes is quasi-equilibrated on both site types. The reactions involved in the CO dissociation at both site types are also at quasi-equilibrium. The reaction steps with the highest rates which are not at quasi-equilibrium are found for CH^{***} and $CH^{\#\#\#}$ hydrogenation, OH^{*} and $OH^{\#}$ hydrogenation, CH_2^{**} and $CH_2^{\#\#}$ hydrogenation, CH_3^{*} and $CH_3^{\#}$ hydrogenation and the first $CH_2^{\#\#}$ insertion step on the "#" sites. More than 80 % of the CO is converted on the "#" sites. Hence, the most significant contribution to the methane production comes from these sites. Furthermore, chain growth by $CH_2^{\#\#}$ insertion only takes place at the "#" sites. The contribution to the methane production from the "*" sites is significantly lower than the contribution from the "#" sites. Furthermore, CO^{**} exclusively ends up in CH_4. Next to this, the alkenes from the "#" sites are readsorbed on the "*" sites and, by beta hydride addition and hydrogenation of the resulting $C_nH_{2n+1}^{*}$, hydrogenated to the corresponding alkanes.

The reversibility of the first $CH_2^{\#\#}$ insertion on the "#" sites is much more pronounced compared to the other $CH_2^{\#\#}$ insertion steps on the "#" sites which is due to a higher chemisorption enthalpy of $CH_3^{\#}$ compared to $C_nH_{2n+1}^{\#}$. As explained in Section 3.4, this contributes to the typically experimentally observed deviations from ASF distribution, i.e., a higher than expected methane yield and lower than expected ethene yield. Furthermore, the higher selectivity to methane is in the SEMK model of this chapter also contributable to the fact that the "*" sites contribute exclusively to the methane production due to the absence of a significant chain growth on these sites.

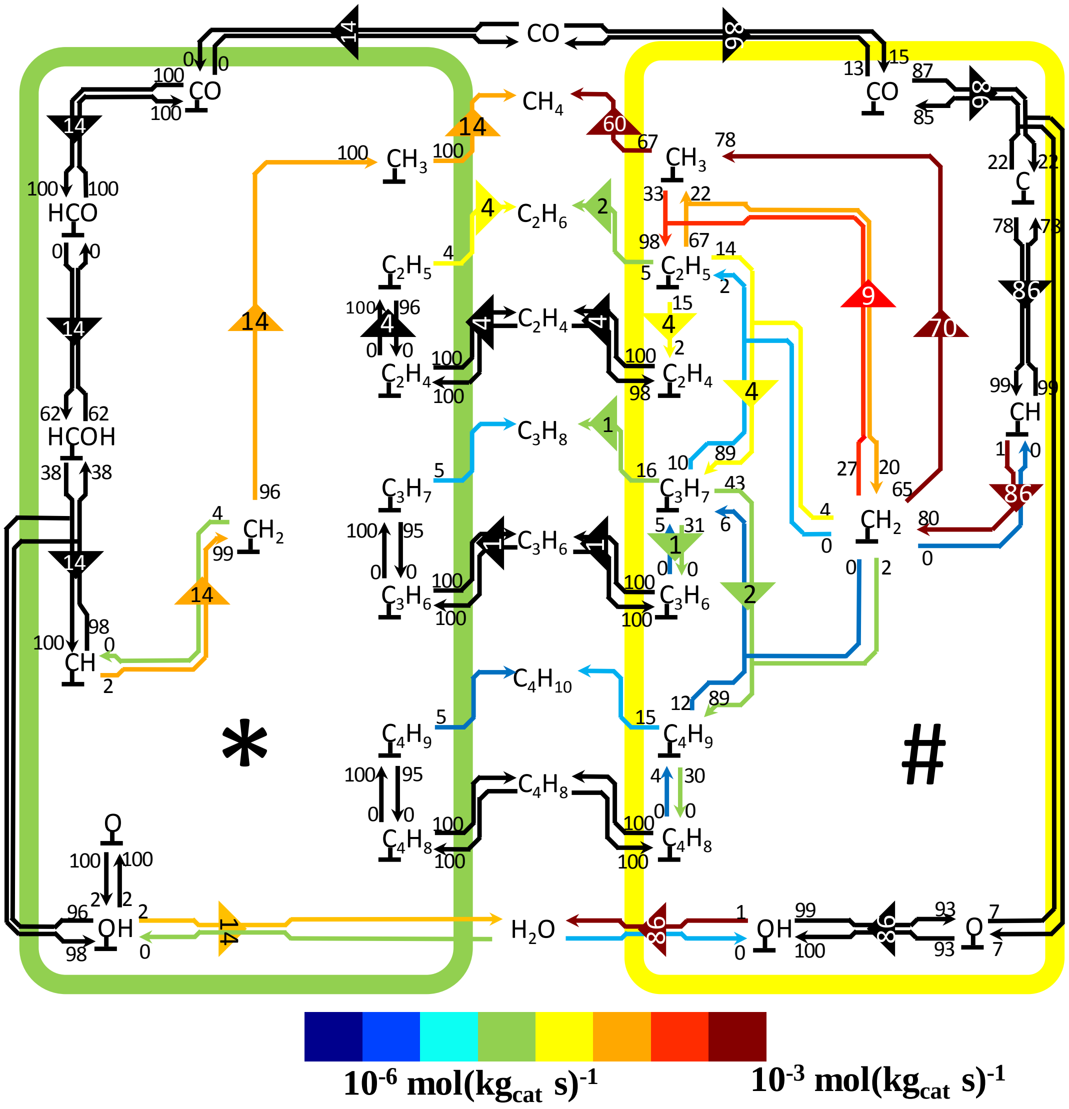
CO
14
98
CO
CO
CH4
60
14
CH3
CH3
C2H6
C2H5
C2H5
C2H4
C2H4
C2H4
C3H8
C3H7
C3H7
C3H6
C3H6
C3H6
C4H10
C4H9
C4H9
C4H8
C4H8
C4H8
H2O
HCO
HCOH
CH
CH
CH2
CH2
C
O
O
OH
OH
9
70
86
*
#
10-6 mol(kgcat s)-1
10-3 mol(kgcat s)-1

Figure 5-11: Reaction path analysis at a H_2/CO molar inlet ratio of 10, a temperature of 483 K, a CO inlet partial pressure of 5.5 kPa and space time, $W/F_{CO,0}$, of 23 $(kg_{cat}s)mol_{CO}^{-1}$. The simulation is performed by integrating eq. [2–35] in which the net formation rates are calculated as explained by eq. [2–15] and using the set of parameters of Table 5-3. The elementary reaction indicated by black arrows are at quasi-equilibrium as confirmed by affinity calculations, see eq. [2–52]. The reactions which are not at quasi-equilibrium are indicated by the colored arrows. The color of the arrow is related to the reaction rate of the elementary step as indicated. The numbers at the tail of an arrow are the differential disappearance factor, eq. [2–50]. The numbers at the tip are the differential formation factor, eq. [2–51]. The triangles indicate the direction of the net elementary reaction rate and the value in the triangle is the rate of the elementary reaction divided by the net CO consumption rate.

It is noted that in the SEMK model of this chapter the typically observed deviations from ASF distribution, i.e., a high methane yield and low ethene yield, are reproduced by carbon number independent activation energies. These deviations from the ASF distribution are described by the model by explicitly accounting for the symmetry numbers, introducing a higher chemisorption enthalpy of the metal methyl species compared to the heavier metal alkyl species and the fact that a number of sites, i.e., the “*” sites, only contribute to the methane production. Accounting for the symmetry numbers was also found to be important for Fe catalyzed FTS for the description of the deviations from ASF distribution [38].

The Turnover Frequency (TOF) of the FTS reaction on Co catalysts is found to increase with increasing metal particle size up to 6-8 nm after which the TOF is constant as a function of the metal particle size, see Section 1.3.4 [8]. Next to this, also the selectivity is affected by the metal particle size, i.e., small metal particles exhibit a higher methane selectivity compared to larger ones [8]. Increasing the fraction of terrace sites in the model decreases the CO conversion and increases the methane selectivity. Hence, according to the model, the experimentally observed changes in conversion and selectivity are explained by the fact that on smaller metal particles, a relatively higher number of terrace sites contribute to the reaction compared to step sites. A possible explanation for a relatively larger contribution of the terrace sites compared to step sites is that the smaller metal particles will irreversibly adsorb CO on (part of) the step sites [8]. Another study indicates that the fraction of step sites increases with the metal particles size and that small metal particles mainly consist of terrace sites [39] which indicates that a classical view of an increasing fraction of terrace sites compared to step sites with an increasing size of the metal particle is not necessarily valid. It is furthermore noted the results from the reaction path analysis indicating that step sites contribute to chain growth and have a higher CO dissociation rate corresponds with findings of Filot et al. [40]. These authors related the conversion and selectivity dependency to the stability of step-edge sites where the latter sites are not stable on small metal particles [40].

5.5 Conclusions

The Single-Event MicroKinetic (SEMK) model as discussed and applied in chapter 3 has been extended to simulate the transient responses measured in Steady State Isotopic Transient Kinetic Analysis (SSITKA) experiments next to the steady state CO conversion and product yields. The model takes into account two site types and H assisted CO dissociation and direct CO dissociation. The reaction steps considered in the alkanes and alkenes formation are the same reaction steps employed in the SEMK model of chapter 3. By regression to experimental data, physicochemically meaningful values for the adjustable model parameters are obtained. Furthermore, the regression resulted in acceptable parity diagrams for the steady state product yields and the transient responses for ^{12}CO and $^{12}CH_4$ are described reasonable by the model. It is noted that the model is capable of simulating experiments measured at varying reaction condition with a single set of parameters.

The Co catalyst can be thought of to exist of terrace and step sites. The terrace sites comprise 70% of the exposed sites of the Co metal particle. The terrace sites are primarily covered with CO, H and HCO. CO dissociation on these sites takes place through H-assisted reaction steps and ends up exclusively in CH_4. The step sites have a high coverage of metal alkyl species. CO on these sites dissociates into C and O. This C contributes most significantly to the methane production. Furthermore, chain growth exclusively takes place at the step sites. A fraction of the alkenes, produced on the step sites, are readsorbed on the terrace sites and are hydrogenated to the corresponding alkanes.

5.6 References

1. Shannon, S.L. and J.G. Goodwin, *Characterization of Catalytic Surfaces by Isotopic-Transient Kinetics during Steady-State Reaction.* Chemical Reviews, 1995. **95**(3): p. 677-695.
2. van Dijk, H.A.J., J.H.B. Hoebink, and J.C. Schouten, *Steady-state isotopic transient kinetic analysis of the Fischer-Tropsch synthesis reaction over cobalt-based catalysts.* Chemical Engineering Science, 2001. **56**(4): p. 1211-1219.
3. van Dijk, H.A.J., J.H.B.J. Hoebink, and J.C. Schouten, *A mechanistic study of the Fischer-Tropsch synthesis using transient isotopic tracing. Part-1: Model identification and discrimination.* Topics in Catalysis, 2003. **26**(1-4): p. 111-119.
4. van Dijk, H.A.J., J.H.B.J. Hoebink, and J.C. Schouten, *A mechanistic study of the Fischer-Tropsch synthesis using transient isotopic tracing. Part 2: Model quantification.* Topics in Catalysis, 2003. **26**(1-4): p. 163-171.
5. Yang, J., Y. Qi, J. Zhu, Y.A. Zhu, D. Chen, and A. Holmen, *Reaction mechanism of CO activation and methane formation on Co Fischer-Tropsch catalyst: A combined DFT, transient, and steady-state kinetic modeling.* Journal of Catalysis, 2013. **308**: p. 37-49.
6. Rebmann, E., P. Fongarland, V. Lecocq, F. Diehl, and Y. Schuurman, *Kinetic modeling of transient Fischer–Tropsch experiments over Co/Al2O3 catalysts with different microstructures.* Catalysis Today, 2016. **275**: p. 20-26.
7. Brown, P.N., A.C. Hindmarsh, and L.R. Petzold, *Using krylov methods in the solution of large-scale differential-algebraic systems.* Siam Journal on Scientific Computing, 1994. **15**(6): p. 1467-1488.
8. den Breejen, J.P., P.B. Radstake, G.L. Bezemer, J.H. Bitter, V. Froseth, A. Holmen, and K.P. de Jong, *On the Origin of the Cobalt Particle Size Effects in Fischer-Tropsch Catalysis.* Journal of the American Chemical Society, 2009. **131**(20): p. 7197-7203.
9. Snir, M., S. Otto, S. Huss-Lederman, D. Walker, and J. Dongarra, *MPI: The Complete Reference*. 1996, Cambridge: The MIT Press. 350.
10. Lozano-Blanco, G., J.W. Thybaut, K. Surla, P. Galtier, and G.B. Marin, *Fischer-Tropsch synthesis: Development of a microkinetic model for metal catalysis.* Oil & Gas Science and Technology-Revue D Ifp Energies Nouvelles, 2006. **61**(4): p. 489-496.
11. Liu, J.-X., H.-Y. Su, D.-P. Sun, B.-Y. Zhang, and W.-X. Li, *Crystallographic Dependence of CO Activation on Cobalt Catalysts: HCP versus FCC.* Journal of the American Chemical Society, 2013. **135**(44): p. 16284-16287.
12. Ojeda, M., R. Nabar, A.U. Nilekar, A. Ishikawa, M. Mavrikakis, and E. Iglesia, *CO activation pathways and the mechanism of Fischer-Tropsch synthesis.* Journal of Catalysis, 2010. **272**(2): p. 287-297.
13. Shustorovich, E. and H. Sellers, *The UBI-QEP method: a practical theoretical approach to understanding chemistry on transition metal surfaces.* Surface Science Reports, 1998. **31**(1-3): p. 5-119.
14. Shustorovich, E. and A.V. Zeigarnik, *The UBI-QEP method: Basic formalism and applications to chemisorption phenomena on transition metal surfaces.* Russian Journal of Physical Chemistry, 2006. **80**(4): p. 665-666.
15. Roelant, R., D. Constales, R. Van Keer, and G.B. Marin, *Second-order statistical regression and conditioning of replicate transient kinetic data.* Chemical Engineering Science, 2008. **63**(7): p. 1850-1865.

16. Benziger, J.B., *Thermochemical methods for reaction energetics on metal surfaces.* ChemInform, 1992. **23**(41).
17. Gong, X.-Q., R. Raval, and P. Hu, *CO dissociation and O removal on Co(0001): a density functional theory study.* Surface Science, 2004. **562**(1–3): p. 247-256.
18. Liu, J.-X., H.-Y. Su, and W.-X. Li, *Structure sensitivity of CO methanation on Co (0 0 0 1), and surfaces: Density functional theory calculations.* Catalysis Today, 2013. **215**: p. 36-42.
19. Chen, C., Q. Wang, G. Wang, B. Hou, L. Jia, and D. Li, *Mechanistic Insight into the C2 Hydrocarbons Formation from Syngas on fcc-Co(111) Surface: A DFT Study.* Journal of Physical Chemistry C, 2016. **120**(17): p. 9132-9147.
20. Gong, X.Q., R. Raval, and P. Hu, *CHx hydrogenation on Co(0001): A density functional theory study.* Journal of Chemical Physics, 2005. **122**(2).
21. Zhao, Y.H., J.X. Liu, H.Y. Su, K.J. Sun, and W.X. Li, *A First-Principles Study of Carbon-Oxygen Bond Scission in Multiatomic Molecules on Flat and Stepped Metal Surfaces.* Chemcatchem, 2014. **6**(6): p. 1755-1762.
22. Storsaeter, S., D. Chen, and A. Holmen, *Microkinetic modelling of the formation of C-1 and C-2 products in the Fischer-Tropsch synthesis over cobalt catalysts.* Surface Science, 2006. **600**(10): p. 2051-2063.
23. Klinke, D.J. and L.J. Broadbelt, *Construction of a mechanistic model of Fischer-Tropsch synthesis on Ni(111) and Co(0001) surfaces.* Chemical Engineering Science, 1999. **54**(15-16): p. 3379-3389.
24. Azadi, P., G. Brownbridge, I. Kemp, S. Mosbach, J.S. Dennis, and M. Kraft, *Microkinetic Modeling of the Fischer-Tropsch Synthesis over Cobalt Catalysts.* Chemcatchem, 2015. **7**(1): p. 137-143.
25. Todic, B., W.P. Ma, G. Jacobs, B.H. Davis, and D.B. Bukur, *CO-insertion mechanism based kinetic model of the Fischer-Tropsch synthesis reaction over Re-promoted Co catalyst.* Catalysis Today, 2014. **228**: p. 32-39.
26. Bhatelia, T., C.E. Li, Y. Sun, P. Hazewinkel, N. Burke, and V. Sage, *Chain length dependent olefin re-adsorption model for Fischer-Tropsch synthesis over Co-Al2O3 catalyst.* Fuel Processing Technology, 2014. **125**: p. 277-289.
27. Cheng, J., T. Song, P. Hu, C.M. Lok, P. Ellis, and S. French, *A density functional theory study of the a-olefin selectivity in Fischer-Tropsch synthesis.* Journal of Catalysis, 2008. **255**(1): p. 20-28.
28. Visconti, C.G., E. Tronconi, L. Lietti, R. Zennaro, and P. Forzatti, *Development of a complete kinetic model for the Fischer-Tropsch synthesis over Co/Al2O3 catalysts.* Chemical Engineering Science, 2007. **62**(18-20): p. 5338-5343.
29. Mosayebi, A. and A. Haghtalab, *The comprehensive kinetic modeling of the Fischer-Tropsch synthesis over Co@Ru/gamma-Al2O3 core-shell structure catalyst.* Chemical Engineering Journal, 2015. **259**: p. 191-204.
30. Kwack, S.H., M.J. Park, J.W. Bae, S.J. Park, K.S. Ha, and K.W. Jun, *Modeling a slurry CSTR with Co/P-Al2O3 catalyst for Fischer-Tropsch synthesis.* Fuel Processing Technology, 2011. **92**(12): p. 2264-2271.
31. Qian, W.X., H.T. Zhang, W.Y. Ying, and D.Y. Fang, *The comprehensive kinetics of Fischer-Tropsch synthesis over a Co/AC catalyst on the basis of CO insertion mechanism.* Chemical Engineering Journal, 2013. **228**: p. 526-534.

32. Todic, B., T. Bhatelia, G.F. Froment, W.P. Ma, G. Jacobs, B.H. Davis, and D.B. Bukur, *Kinetic Model of Fischer-Tropsch Synthesis in a Slurry Reactor on Co-Re/Al2O3 Catalyst.* Industrial & Engineering Chemistry Research, 2013. **52**(2): p. 669-679.
33. Visconti, C.G., E. Tronconi, L. Lietti, P. Forzatti, S. Rossini, and R. Zennaro, *Detailed Kinetics of the Fischer-Tropsch Synthesis on Cobalt Catalysts Based on H-Assisted CO Activation.* Topics in Catalysis, 2011. **54**(13-15): p. 786-800.
34. Zhuo, M.K., K.F. Tan, A. Borgna, and M. Saeys, *Density Functional Theory Study of the CO Insertion Mechanism for Fischer-Tropsch Synthesis over Co Catalysts.* Journal of Physical Chemistry C, 2009. **113**(19): p. 8357-8365.
35. Zhuo, M.K., A. Borgna, and M. Saeys, *Effect of the CO coverage on the Fischer-Tropsch synthesis mechanism on cobalt catalysts.* Journal of Catalysis, 2013. **297**: p. 217-226.
36. Cheng, J., X.-Q. Gong, P. Hu, C.M. Lok, P. Ellis, and S. French, *A quantitative determination of reaction mechanisms from density functional theory calculations: Fischer–Tropsch synthesis on flat and stepped cobalt surfaces.* Journal of Catalysis, 2008. **254**(2): p. 285-295.
37. Cheng, J., P. Hu, P. Ellis, S. French, G. Kelly, and C.M. Lok, *A DFT study of the chain growth probability in Fischer-Tropsch synthesis.* Journal of Catalysis, 2008. **257**(1): p. 221-228.
38. Lozano-Blanco, G., J.W. Thybaut, K. Surla, P. Galtier, and G.B. Marin, *Single-event microkinetic model for Fischer-Tropsch synthesis on iron-based catalysts.* Industrial & Engineering Chemistry Research, 2008. **47**(16): p. 5879-5891.
39. van Helden, P., I.M. Ciobîcă, and R.L.J. Coetzer, *The size-dependent site composition of FCC cobalt nanocrystals.* Catalysis Today, 2016. **261**: p. 48-59.
40. Filot, I.A.W., R.A. van Santen, and E.J.M. Hensen, *The Optimally Performing Fischer-Tropsch Catalyst.* Angewandte Chemie-International Edition, 2014. **53**(47): p. 12746-12750.

Chapter 6 Simulation of an Industrial Trickle Bed Reactor

The detailed Single-Event MicroKinetic (SEMK) model has been implemented in reactor models of varying levels of complexity. In a first step, a reaction-diffusion model is constructed to model the behavior at the catalyst pellet scale. The performance of this model is elaborately discussed as a function of the operating conditions. The effect of temperature, bulk syngas ratio, pressure and pellet diameter on the net CO consumption rate, C_{5+} selectivity and C_{5+} productivity are reported on to enhance the insight in the interplay of reaction and diffusion on the one hand and, on the other hand, to identify a possible combination of reaction conditions resulting in an optimization of these three performance indicators. The catalyst pellet is subsequently considered within a gas phase reactor model. The effect of reaction conditions on reactant conversion and product selectivity is also extensively investigated for this configuration. The impact of a liquid phase recycle on the reactor performance is evaluated in a next step. Next to this, two dimensional reactor models have been developed to assess the extent to which radial temperature gradients develop in a reactor. The above constitutes, a versatile modeling package which can be used to: (1) increase the insights in the complex interplay of reaction and transfer phenomena on the different scales, (2) optimization of a reactor by performing simulations for a large variation in operating conditions or design parameters with the one dimensional models or (3) detailed reactor simulations which yield information on the radial temperature profiles which can be used for operational or safety considerations.

6.1 Introduction

The Fischer-Tropsch Synthesis (FTS) reactor in a gas-to-liquids (GtL), biomass-to-liquids (BtL) or coal-to-liquids (CtL) conversion plant should convert the syngas as efficiently as possible to ensure the economic viability of the synthetic fuel production [1, 2]. At the industrial scale, the conversion and selectivities are typically no longer determined by reaction kinetics alone, but are also affected by mass and heat transfer phenomena occurring on different length and time scales. A more reliable scale-up and optimization of the FTS reactor can be obtained by the development of a multi-scale model. As such, insights in the complex interplay of kinetics and transport phenomena can be obtained in a fundamental manner. Next to this, the impact on the industrial scale of improvements in catalyst performance can be more straightforwardly assessed. Furthermore, by performing simulation studies at a large range of operating conditions, a more optimal operating point can potentially be found.

As already indicated in Chapter 1, the multi-scale model constructed as part of the present chapter is developed for a Multi-Tubular Trickle Bed Reactor (MTTBR) configuration. In order to model the yields of the individual components, a detailed kinetic model is required. The catalyst pellets loaded in the tubes of the MTTBR typically have diameters of a few millimeters [3-10] in order to avoid high pressure drops. This will cause the development of intrapellet pore diffusion limitations [11]. This necessitates the use of a model describing the simultaneous effect of reaction and diffusion in the catalyst pellets. Furthermore, possible mass transfer phenomena from the bulk to the catalyst pellet surface also require consideration and have to be accounted for. Hence, the successful construction of a multi-scale model for a FTS Trickle Bed Reactor (TBR) depends critically on an adequate quantitative description of the interaction of complex chemical kinetics on the one hand and transport phenomena and reactor hydrodynamics on the other hand.

A three-dimensional Computational Fluid Dynamics (CFD) model for a TBR coupled with a detailed microkinetic model requires a tremendous effort during the model construction stage as well as for the execution of the simulations. Existing simulation packages, such as catalyticFOAM [12], can be of aid in the model construction. These packages typically combine a set of libraries from which a suitable CFD framework can be constructed, e.g., the Euler-Euler approach combined with a turbulence model in the case of a TBR [13]. Once a specific CFD framework is constructed, other libraries have to be used in order to appropriately describe the closure terms for, e.g., the gas-liquid interactions or the turbulence [13]. Executing the simulations is time-consuming and requires significant computational resources, i.e. number of CPUs, memory and data storage. Furthermore, the CFD models which attain a high level of predictability, e.g., CFD models based on the discrete particle approach (Euler-Lagrange) in case of a TBR, can typically only be used to simulate small segments of a reactor [14] for reasons of computational cost. In contrast to this, process optimization requires to perform simulations at a wide range of operating conditions within a reasonable amount of time. For this purpose, a reactor model based on mass and enthalpy balances and description of heat and mass transfer by means of appropriate correlations, as developed in this chapter, is more suited. Furthermore, such reactor models are more easily extended to assess the impact of, e.g., the formation of a liquid phase inside the reactor, while in the case of CFD models, a new CFD model would have to be developed. Hence, both type of models, i.e., CFD models and reactor models as developed in this chapter, are valuable and indispensable tools for scale-up. Reactor models including all the relevant phenomena can be used for process optimization and a swift evaluation of changes in catalyst performance on the final reactant conversion and product selectivity. CFD models provide more insight into the complex flow pattern of multi-phase reactors and can be used to validate reactor models as developed in this chapter.

Modeling studies on FTS TBRs are widely described in literature [4-10, 15-24]. Only very few of these combine a detailed kinetic model with a reactor model accounting for transport phenomena occurring on both the pellet and reactor scale [5, 10]. The aim of the work presented in this chapter is to combine a detailed Single-Event Microkinetic (SEMK) model with reactor models with different levels of complexity in order to describe reactant conversion and product selectivities at varying operating conditions. The combination of a detailed SEMK model with reactor models which include different levels of detail, e.g., single-phase flow compared to two-phase flow, impact of radial temperature gradients on conversion and selectivity, … is described for the first time. The first part of the chapter is focused on enhancing insight in the interplay of reaction and transfer phenomena and identifying possible reaction conditions optimizing conversion and selectivity at the catalyst pellet scale and for a single-phase gas reactor. Next to this, the impact of a liquid recycle is assessed. Finally, the focus is shifted to the impact of the produced reaction heat of the highly exothermic FTS reaction. For this, the possible origination of radial temperature gradients are specifically taken into account.

6.2 Multi-scale reactor model

A schematic representation of the multi-scale reactor model constructed in this chapter is illustrated in Figure 6-1. Three scales are explicitly accounted for. The smallest scale comprises the reactions which take place on the Co metal particles. These phenomena occur at the nanometer scale. The second scale simulates the catalyst pellets and focuses on the interplay between simultaneously occurring diffusion and reaction. These considerations are made on the millimeter scale. The third and largest scale is that of the reactor itself. On this scale, the most important phenomena to account for are hydrodynamic phenomena.

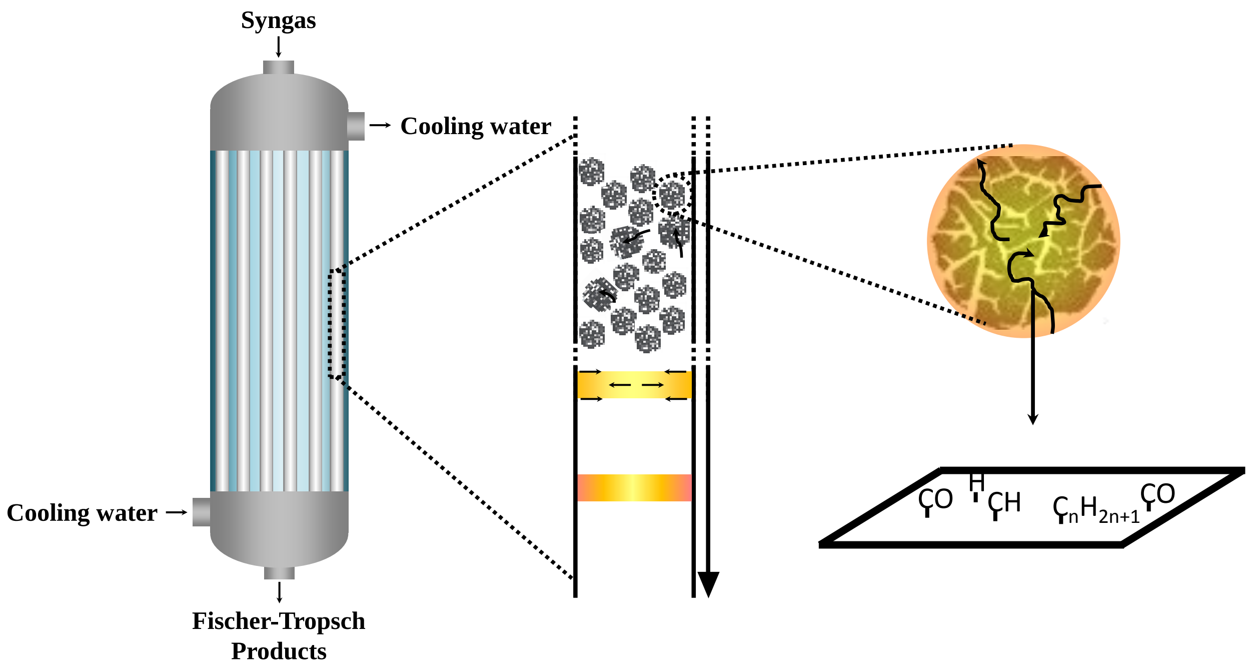

Figure 6-1: The Multi-Tubular Trickle Bed Reactor and the three scales which are accounted for by the multi-scale model.

6.2.1 Models for the different scales

Kinetic model

The Single-Event MicroKinetic (SEMK) model as developed in Chapter 3 for Co catalyzed Fischer-Tropsch Synthesis (FTS) is used to simulate the reactions on the Co metal particles. This SEMK model was chosen rather than the SEMK model of Chapter 5. Both SEMK models result in similar extrapolation capabilities at higher operating pressures. It is, hence, expected that simulation results presented in this chapter would not be altered significantly by changing the employed SEMK model. Furthermore, the SEMK model of Chapter 3 results in lower CPU times as the number of species considered in the reaction network is considerably lower.

A detailed description of the reaction mechanism provides a wealth of information which cannot be retrieved via simulations performed with a kinetic model limited to describing the CO conversion. As such, a detailed kinetic model allows to simulate the yield of each component individually. Additionally, the reaction heat, for example, can be estimated more accurately with such a detailed model and, hence, the produced heat can be evaluated more precisely.

Pellet scale model

The catalyst metal particles are deposited on a porous pellet. The reactants enter the pellets and are transported through the channels of the catalyst pellet to the Co metal particles where they react to products which have to be transported through the same channels to the outer surface of the catalyst pellet. Inside these catalyst pellets, significant concentration gradients may develop depending on the time scale of the aforementioned transport phenomena compared to that of the chemical reactions. It may significantly impact on both the selectivity and the reactant net consumption rate.

For an exothermic reaction occurring at gas-liquid conditions, the following phenomena need to be considered at the pellet scale [25, 26], i.e., transport through the catalyst pellet pores, external transport resistance, development of temperature gradients, wetting of the catalyst pellet, capillary effects and vapor-liquid equilibrium. As highlighted in Section 6.1, the aim of this chapter is to construct a model which can be used to describe the reactant conversion and product selectivity profiles in a TBR. Under steady state conditions, the catalyst pellet pores can be considered to be completely filled with a FTS wax phase [10, 27, 28]. The transport through this wax phase is primarily determined by diffusion. At the catalyst pellet surface, the gas phase reactants have to be dissolved in the wax phase. Furthermore, the catalyst pellets were assumed to be spherically symmetrical. The corresponding mass balance for a component i in the wax phase inside the catalyst pellet pores can be written as:

$$\varepsilon_p \frac{\partial C_{i,p}}{\partial t} = \frac{1}{r^2}\frac{\partial}{\partial r}\left(r^2 D_{e,i}\frac{\partial C_{i,p}}{\partial r}\right) + \rho_p R_{W,i} \qquad [6\text{-}1]$$

Where ε_p is the pellet porosity $[m_f^3\ m_p^{-3}]$, $C_{i,p}$ the concentration of component *i* in the wax phase inside the catalyst pellet pores $[mol\ m_f^{-3}]$, t the time $[s]$, r the radial position $[m_p]$, $D_{e,i}$ the effective diffusion coefficient of component i $[m_f^3 (m_p\ s)^{-1}]$, ρ_p the catalyst pellet density $[kg_{cat}\ m_p^{-3}]$, $R_{W,i}$ the net formation rate of component *i* $[mol\ (kg_{cat}\ s)^{-1}]$.

For the surface species *j* the following mass balance is considered:

$$\frac{\partial L_j}{\partial t} = R_{W,j} \qquad [6\text{-}2]$$

Where L_j represents the concentration of surface species *j* $[mol\ kg_{cat}^{-1}]$.

The temperature has a significant effect on the FTS activity and selectivity. Therefore, an enthalpy balance for the catalyst pellets is considered as well:

$$\left(\varepsilon_p \rho_L c_{p,L} + \rho_p c_{p,p}\right)\frac{\partial T}{\partial t} = \frac{1}{r^2}\frac{\partial}{\partial r}\left(\frac{\lambda_p}{r^2}\frac{\partial T}{\partial r}\right) + \sum_{i=1}^{n_{prod}} \rho_p R_{W,i}\,(-\Delta H_{r,i}) \qquad [6\text{-}3]$$

Where ρ_L is the mass density of the wax phase inside the catalyst pellet pores $[kg\ m_f^{-3}]$, $c_{p,L}$ the specific heat capacity of the wax phase inside the catalyst pellet pores $[J\ (kg\ K)^{-1}]$, T the temperature $[K]$, λ_p the effective conductivity of the catalyst pellet $[W(m_p^2\ K)^{-1}]$, $\Delta H_{r,i}$ the enthalpy change corresponding to the production of one mole *i* starting from CO and H_2 $[J\ mol^{-1}]$ and n_{prod} refers to all the alkanes and alkenes considered in the reaction network.

The mass and energy balances are complemented with a set of initial, eq. [6-4], and boundary conditions, eqs. [6-5]:

$$\begin{aligned} C_{i,p}(r,0) &= 0.0 \\ L_j(r,0) &= 0.0 \\ T(r,0) &= T_f \end{aligned} \qquad [6\text{-}4]$$

Where T_f is the temperature of the fluid surrounding the catalyst pellet $[K]$.

$$\begin{gathered}\frac{\partial C_{i,p}(0,t)}{\partial r} = 0\\ \frac{\partial T(0,t)}{\partial r} = 0\\ T\left(r_p, t\right) = T_f\end{gathered} \qquad [6\text{-}5]$$

Where r_p is the catalyst pellet radius $[m_p]$.

The boundary condition at the catalyst pellet surface depends on the type of simulation that is performed. When only pellet simulations are performed, the catalyst pellet surface concentration is assumed to be at equilibrium with the gas phase:

$$C_{i,p}\left(r_p, t\right) = \frac{p_i}{He_i} C_{tot,L} \qquad [6\text{-}6]$$

Where p_i represents the partial pressure of component i in the gas phase $[Pa]$, He_i the Henry coefficient $[Pa]$, $C_{tot,L}$ the total liquid concentration $[mol\ m_f^{-3}]$.

Reactor model

For a gas phase component i, the most important variations are induced typically by the convective transport along the axial direction of the reactor. Axial dispersion effects are not taken into account [4-8, 10, 20-22]. Furthermore, the mass transfer from the bulk gas phase to the catalyst pellet surface also needs to be taken into account. The resistances to mass transfer considered in this chapter for a single, gas phase reactor model are illustrated in Figure 6-2–a.

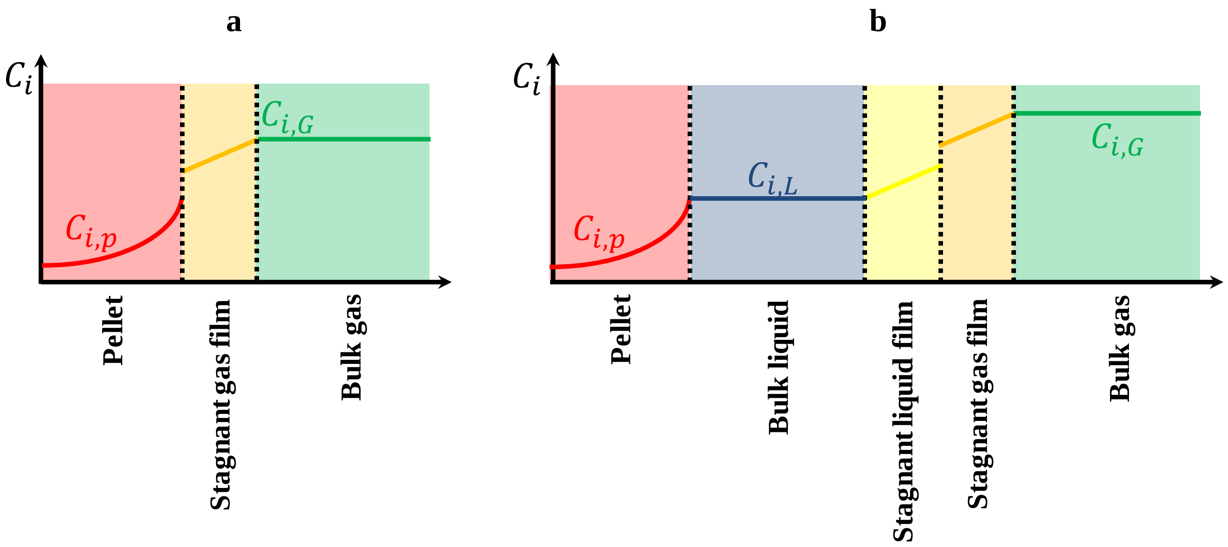

Figure 6-2: The different resistances to mass transfer considered in the single gas phase reactor (a) and the gas liquid reactor (b).

The continuity equations in case only a gas phase is considered, becomes:

$$\varepsilon_G \frac{\partial C_{i,G}}{\partial t} + u_{s,G} \frac{\partial C_{i,G}}{\partial z} = -k_{i,GS} a_{GS,v} \left(C_{i,G} - \frac{He_i C_{i,p}(r_p)}{C_{tot,L} RT} \right) \qquad [6\text{-}7]$$

Where ε_G is the fraction of the reactor volume occupied by the gas phase $[m_f^3\ m_r^{-3}]$, $C_{i,G}$ the concentration of component i in the gas phase $[mol\ m_f^{-3}]$, t time $[s]$, $u_{s,G}$ the superficial velocity $[m_f^3\ (s\ m_r^2)^{-1}]$, z the axial coordinate of the reactor $[m_r]$, $a_{GS,v}$ the external catalyst surface area per reactor volume $[m_p^2\ m_r^{-3}]$.

It is noted that in eq. [6-7] it has been assumed that the derivative of the superficial velocity, $u_{s,G}$,with respect to the axial reactor coordinate can be neglected compared to the derivative of the gas phase concentration of component i. In FTS reactors, a contraction of the gas phase takes place. Hence, the axial dependence of the superficial velocity itself has been taken into account through a total mole balance [29]:

$$\frac{du_{s,G} C_{tot,G}}{dz} = -\sum_{i=1}^{n_{comp}} k_{i,GS} a_{GS,v} \left(C_{i,G} - \frac{He_i C_{i,p}(r_p)}{C_{tot,L} RT} \right) \qquad [6\text{-}8]$$

Where $C_{tot,G}$ is the total gas phase concentration $[mol\ m_f^{-3}]$ and n_{comp} accounts for CO, H_2, all alkanes and alkenes and H_2O.

As the pellets are incorporated into a gas phase reactor model, the concentration at the catalyst pellet surface is determined by the mass transfer in the gas phase boundary around the catalyst pellet, see Figure 6-2–a:

$$D_{e,i}\left.\frac{dC_{i,p}}{dr}\right|_{r=r_p} = k_{i,GS}\left(C_{i,G} - \frac{He_i C_{i,p}(r_p)}{C_{tot,L}RT}\right) \qquad [6\text{-}9]$$

Where $k_{i,GS}$ is the gas phase mass transfer coefficient $[m_f^3\ (m_p^2\ s)^{-1}]$. It is noted that eq. [6-9], hence, replaces the boundary condition of eq. [6-6] for the pellet scale model in case the gas phase reactor model is used.

In case both gas and liquid phase are considered in the reactor, the gas is assumed to exchange mass with the liquid phase only, see Figure 6-2–b. the following continuity equations are used for a gas phase component i:

$$\varepsilon_G\frac{\partial C_{i,G}}{\partial t} + u_{s,G}\frac{\partial C_{i,G}}{\partial z} = -k_{i,GL}a_{GL,v}\left(\frac{C_i RT}{He_i}C_{tot,L} - C_{i,L}\right) \qquad [6\text{-}10]$$

Where, $k_{i,GL}$ is the gas liquid mass transfer coefficient $[m_f^3\ (m_{GL}^2\ s)^{-1}]$, $a_{GL,v}$ the contact area of gas and liquid per reactor volume $[m_{GL}^2\ m_r^{-3}]$ and $C_{i,L}$ the concentration of component i in the liquid phase $[mol\ m_f^{-3}]$.

The liquid phase exchanges mass with the catalyst pellet and the gas phase, see Figure 6-2–b. With the catalyst pellet, no external liquid-solid mass transfer resistance is considered, i.e., the bulk liquid concentration is assumed to be equal to the concentration at the catalyst pellet surface. At the gas-liquid interface, a mass transfer resistance is considered. This reactor model considers the same transfer phenomena as considered in a trickle bed reactor model for FTS constructed by Kaskes et al. [4] and a trickle bed reactor model for hydrocracking developed by Martens et al. [30] and Narasimhan et al. [31].These considerations result in the following continuity equations for a component i in the bulk liquid phase:

$$\varepsilon_L \frac{\partial C_{i,L}}{\partial t} + u_{s,L} \frac{\partial C_{i,L}}{\partial z} = K_{i,GL} a_{GL,v} \left(\frac{C_i RT}{He_i} C_{tot,L} - C_{i,L} \right) + (1 - \varepsilon_B) \rho_p R_{W,i}^{ave} \qquad [6\text{-}11]$$

Where ε_L is the liquid holdup in the reactor $[m_L^3\ m_r^{-3}]$, $u_{s,L}$ the superficial velocity of the liquid phase $[m_L^3\ (m_r^2\ s)^{-1}]$, ε_B the bed porosity $[m_f^3\ m_r^{-3}]$, $R_{W,i}^{ave}$ is the average reaction rate over the catalyst pellet $[mol\ (s\ kg_{cat})^{-1}]$ and which is calculated as:

$$R_{W,i}^{ave} = \frac{\int_0^{R_p} 4\pi r^2 R_{W,i} \rho_p dr}{\frac{4}{3}\pi r_p^3}$$

The axial dependence of the gas and liquid phase superficial velocity are determined by considering similar total mole balances as done for the single-gas flow reactor, see eq. [6-8].

For simulations of a reactor in which both gas and liquid are flowing, the catalyst surface is assumed to be completely wetted. The catalyst surface concentration is assumed to be equal to the concentration in the bulk liquid phase. The boundary conditions of eq. [6-6] is, hence, replaced by:

$$C_{i,p}(r_p, t) = C_{i,L} \qquad [6\text{-}12]$$

The enthalpy balance in case only convection and a gas phase are considered becomes:

$$\begin{aligned} &\left(\varepsilon_G \rho_G c_{p,G} + (1 - \varepsilon_B) \rho_p c_{p,p}\right) \frac{\partial T}{\partial t} + u_{s,G} \rho_G c_{p,G} \frac{\partial T}{\partial z} \\ &\qquad = (1 - \varepsilon_B) \rho_p \sum_i^{n_{prod}} R_{W,i}^{ave} (-\Delta H_{r,i}) - \frac{4U}{d_r} (T - T_{cool}) \end{aligned} \qquad [6\text{-}13]$$

Where ρ_G is the gas mass density $[kg_{gas}\ m_f^{-3}]$, $c_{p,G}$ the gas heat capacity $[J\ \left(kg_{gas}\ K\right)^{-1}]$, U the overall heat transfer coefficient $[W\ (m_r^2\ K)^{-1}]$, d_r the reactor diameter $[m_r]$ and T_{cool} the cooling temperature $[K]$.

The enthalpy balance in case also a liquid phase is considered is:

$$\left(\varepsilon_G\rho_G c_{p,G} + \varepsilon_L\rho_L c_{p,L} + (1-\varepsilon_B)\rho_p c_{p,p}\right)\frac{\partial T}{\partial t} + \left(u_{s,G}\rho_G c_{p,G} + u_{s,L}\rho_L c_{p,L}\right)\frac{\partial T}{\partial z} = (1-\varepsilon_G)\rho_p\sum_i^{n_{prod}} R_{W,i}^{ave}(-\Delta H_{r,i}) - \frac{4U}{d_r}(T - T_{cool}) \qquad [6\text{-}14]$$

The high exothermicity of the FTS reaction can cause the development of radial temperature gradients. To assess this, radial dispersion effects were included in the temperature balance by including the following term in Eq. [6-13] or Eq. [6-14]:

$$\lambda_{er}\frac{1}{r}\frac{\partial}{\partial r}\left(r\frac{\partial T}{\partial r}\right) \qquad [6\text{-}15]$$

Where λ_{er} represents the effective radial conductivity $[W(m_r\,K)^{-1}]$ and r the radial reactor coordinate $[m_r]$.

Radial concentration gradients can also be considered for the gas phase components as a result of potential temperature gradients. The following term was added to the continuity equation for both the gas and liquid phase:

$$D_{er,i,X}\frac{1}{r}\frac{\partial}{\partial r}\left(r\frac{\partial C_{i,X}}{\partial r}\right) \qquad [6\text{-}16]$$

Where $D_{er,i,X}$ is the effective radial diffusion coefficient of component i $[m_f^{-3}\ (m_r\,s)^{-1}]$ and X the gas or liquid phase.

The pressure drop in the reactor in case only a gas phase is considered is calculated according to :

$$\frac{dp_{tot}}{dz} = -\frac{2f_G\rho_G u_{s,G}^2}{d_p} \qquad [6\text{-}17]$$

Where p_{tot} is the total pressure $[Pa]$, f_G the gas phase friction factor [-] and d_p the catalyst pellet diameter $[m_p]$.

The pressure drop in case both liquid and gas phase are considered is calculated according to Ellman et al [32] for the trickle flow regime:

$$\frac{dp_{tot}}{dz} = -\frac{2f_{LGG}\rho_G u_{s,G}^2}{d_h} \qquad [6\text{-}18]$$

Where f_{LGG} is the gas-liquid friction factor and d_h the hydraulic diameter.

This set of equations has to be complemented with the appropriate initial and boundary conditions. For a one dimensional reactor, these initial and boundary conditions are:

$$\begin{gathered} C_{i,X}(z,0) = 0 \\ T(z,0) = T_0 \\ C_{i,X}(0,t) = C_{i,X,0} \\ T(0,t) = T_0 \\ p_{tot}(0) = p_0 \end{gathered} \qquad [6\text{-}19]$$

Where T_0 is the temperature at the reactor inlet, $C_{i,X,0}$ the concentration of component i in phase X at the reactor inlet and p_0 the total pressure at the reactor inlet $[Pa]$.

If radial concentration and temperature profiles are considered, the boundary conditions of eq. [6-19] are complemented with:

$$\begin{gathered} \left.\frac{\partial C_{i,X}}{\partial r}\right|_{r=0} = \left.\frac{\partial C_{i,X}}{\partial r}\right|_{r=r_r} = \left.\frac{\partial T}{\partial r}\right|_{r=0} = 0 \\ \lambda_{er}\left.\frac{\partial T}{\partial r}\right|_{r=r_r} = h_w(T - T_{cool}) \end{gathered} \qquad [6\text{-}20]$$

Where h_w is the heat transfer coefficient at the wall $[W(m_r^2K)^{-1}]$ and r_r the reactor radius m_r.

6.2.2 Correlations and thermodynamic models

Pellet scale diffusion coefficients

The effective diffusion coefficient of a component i through the wax phase in the catalyst pellet pores, $D_{e,i}$ in eq. [6-1], is calculated based on correlations for the diffusion of gas phase components through a wax phase with an average carbon number of 28, D_i, [27], see Appendix A, corrected for the porosity, ε_p $[m_f^3\ m_p^{-3}]$, and tortuosity, τ_p $[m_f^2\ m_p^{-2}]$, of the catalyst pellet:

$$D_{e,i} = \varepsilon_p \frac{D_i}{\tau_p} \qquad \text{[6-21]}$$

Gas and liquid phase fugacities

At the surface of the catalyst pellet, the gas phase components are dissolved in a liquid wax phase. The vapor phase can be considered as an ideal gas [4, 33]. The fugacity of a gas phase component i, $f_{i,G}$, is, hence, equal to its partial pressure calculated based on the ideal gas law. The liquid phase fugacity, $f_{i,L}$, of H_2, CO, H_2O and alkanes and alkenes with maximally 3 carbon atoms is calculated as [34]:

$$f_{i,L} = He_i^{\infty} x_i exp\left(\frac{\bar{v}_i^{\infty}\left(p_{tot} - p_{sat,solv}\right)}{RT}\right) \qquad \text{[6-22]}$$

Where He_i^{∞} is the Henry coefficient at infinite dilution $[Pa]$, x_i is the liquid mole fraction of component i, $\bar{v}_i^{\infty}$ is the partial molar volume at infinite dilution $[m^3\ mol^{-1}]$, p_{tot} is the total pressure $[Pa]$, $p_{sat,solv}$ the vapor pressure of saturated pure solvent at the system temperature. For the calculation of He_i^{∞}, $\bar{v}_i^{\infty}$ and $p_{sat,solv}$ see Appendix A.

The liquid phase fugacity of hydrocarbons with more than 3 carbon atoms is calculated as [34]:

$$f_{i,L} = \gamma_i^{\infty} p_{sat,i} x_i exp\left(\frac{v_{i,L}\left(p_{tot} - p_{sat,solv}\right)}{RT}\right) \qquad \text{[6-23]}$$

Where $\gamma_i^{\infty}$is the activity coefficient at infinite dilution, $v_{i,L}$ molar volume of pure i $[m^3 mol^{-1}]$. For the calculation of $p_{sat,i}$ and $v_{i,L}$ see Appendix A.

γ_i^{∞}, is calculated based on the following relation [34]:

$$ln(\gamma_i^\infty) = ln(\gamma_r^\infty)\frac{n-i}{n-r} \qquad [6\text{-}24]$$

Where γ_r^∞ is the activity coefficient at infinite dilution of a reference solute in an alkanes solvent, i the carbon number of component i and n the carbon number of the alkane solvent. For the calculation of γ_r^∞, see Appendix A.

Octacosane was assumed to resemble the physical properties of the wax phase inside the catalyst pores. For the calculation of the total liquid concentration, an ABC correlation, as proposed by Marano et al [35, 36], was used. Other properties of the catalyst pellet, i.e., porosity, tortuosity, …, are reported in Table 6-1.

Table 6-1: Properties of the catalyst pellet.

Quantity	**value**
ε_p	$0.5\ [m_f^3\ m_p^{-3}]$
ρ_{cat}	$1500\ [kg_{cat}\ m_p^{-3}]$
λ_e [37]	$0.8652 + 0.00108(\mathrm{T} - 273.15)\ [W\ (m\ K)^{-1}]$
τ_p	1.5

Mass transfer coefficients

In case a single gas phase is considered in the reactor, a mass transfer coefficient from the bulk gas phase to the catalyst pellet surface, $k_{i,GS}$, is required together with the external surface area of the catalyst bed, $a_{GS,v}$, see equation [6-7]. For this gas-solid transfer parameter, the correlation of Yoshida et al [38] is used:

$$\begin{aligned} Sh_i &= 0.983Re^{0.59}{Sc_i}^{1/3} \quad Re > 190 \\ Sh_i &= 1.66Re^{0.49}{Sc_i}^{1/3} \quad Re < 190 \qquad [6\text{-}25] \\ Sh_i &= \frac{k_{i,GS}d_p}{D_{im}} \end{aligned}$$

$$Re = \frac{\rho_G u_G d_p}{\mu_G}$$

$$Sc_i = \frac{\mu_G}{\rho_G D_{mi}}$$

Where D_{im} represents the molecular diffusion coefficient of component i in the gas phase $[m^2\ s^{-1}]$, μ_G the gas phase viscosity $[Pa\ s]$ and d_p the pellet diameter $[m_p]$. D_{im} is calculated according to Fuller et al [39-41] and μ_G according to Chung et al [42], See Appendix A.

The external surface area of the packed bed is calculated as [43]:

$$a_{GS,v} = \frac{6(1-\varepsilon_b)}{d_p} \qquad [6\text{-}26]$$

The gas-liquid mass transfer coefficient, $k_{i,GL}$, is calculated based on the two film model [29]:

$$\frac{1}{k_{i,GL}} = \frac{1}{He_i k_{i,GI}} + \frac{1}{k_{i,LI}} \qquad [6\text{-}27]$$

Where $k_{i,GI}$ and $k_{i,LI}$ represent the mass transfer coefficients from the bulk phase gas or liquid phase to the GL interphase.

Typically the mass transfer resistance at the gas side is negligible compared to that at the liquid side, hence, the gas-liquid transfer coefficient is calculated as:

$$k_{i,GL} = k_{i,LI} \qquad [6\text{-}28]$$

The correlations for the mass transfer coefficient at the liquid side frequently correlate the product of the mass transfer coefficient at the liquid side with the gas-liquid exchange area [44]:

$$k_{i,LI}a_{GL,v} = 0.980 d_p^{-0.5} u_{L,s}^{0.8} u_{G,s}^{0.8} \tag{6-29}$$

Effective radial diffusion coefficients

The effective diffusion coefficients for the radial dispersion have been calculated with the correlations reported by Wen and Fan [45]. In case of pure gas phase:

$$Pe_{i,G} = \left(\frac{0.4}{\left(Re_G Sc_{i,G}\right)^{0.8}} + \frac{0.09}{1 + \frac{10}{Re_G Sc_{i,G}}} \right)^{-1} \tag{6-30}$$

And for a gas liquid reactor:

$$\begin{gathered} Pe_L = \frac{17.5}{{Re_L}^{0.75}} + 11.4 \\ Re_L = \frac{\rho_L u_{L,s} d_p}{\mu_L} \end{gathered} \tag{6-31}$$

With

$$Pe_X = \frac{u_{X,s} d_p}{D_{er,X}} \tag{6-32}$$

Bed porosity and liquid holdup

The fraction of the reactor volume occupied by the gas, ε_G, is, in the case of gas phase reactor, equal to the bed porosity. The latter is calculated as [43]:

$$\varepsilon_B = 0.38 + 0.073\left(1 + \frac{\left(\frac{d_r}{d_p}\right)^2 - 2}{\left(\frac{d_r}{d_p}\right)^2}\right) \qquad [6\text{-}33]$$

In case both liquid and gas are present in the reactor, the void spaces in the catalyst bed are filled with gas and liquid:

$$\varepsilon_B = \varepsilon_G + \varepsilon_L \qquad [6\text{-}34]$$

The liquid holdup has been calculated as [46]:

$$\begin{aligned} \varepsilon_L &= \varepsilon_B(1 - 10^{-\Gamma}) \\ \Gamma &= \frac{1.22We_L^{0.15}}{X_G^{0.15}Re_L^{0.2}} \\ We_L &= \frac{\rho_L u_{L,s}^2 d_p}{\sigma_L} \\ X_G &= \frac{u_{G,s}}{u_{L,s}}\left(\frac{\rho_G}{\rho_L}\right)^{0.5} \end{aligned} \qquad [6\text{-}35]$$

And with We_L the weber number and X_G the Lockhart-Martinelli parameter. The factor $(1 - 10^{-\Gamma})$ is also referred to as the liquid saturation, β_t.

Heat transfer coefficients

The overall heat transfer coefficients, U see eq. [6-13] and eq. [6-14], are composed of three contributions, i.e., the heat transfer at the reactor side, through the reactor tube and at the heat transfer medium side [47]:

$$\frac{1}{U} = \frac{1}{\alpha_r} + \frac{\delta}{\lambda_r}\frac{A_r}{A_m} + \frac{1}{\alpha_u}\frac{A_r}{A_u} \qquad [6\text{-}36]$$

With α_r the heat transfer coefficient at the bed side $[W\ (m^2\ K)^{-1}]$, δ the reactor tube thickness $[m]$, λ_r the thermal conductivity of the reactor tube material $[W(m\,K)^{-1}]$, A_r the heat exchanging surface area at the bed side $[m^2]$, A_u the heat exchanging surface area at the heat transfer medium side $[m^2]$, A_m the logarithmic average of A_r and A_u and α_u the heat transfer coefficient at the heat transfer medium side.

It has been assumed that the resistance to heat transfer through the reactor tube material and at the heat transfer medium is negligible compared to resistance to heat transfer at the bed side:

$$U = \alpha_r \tag{6-37}$$

The heat transfer coefficient at the bed side is calculated with the correlation of Leva et al. [47] for cooling for a gas phase reactor:

$$\alpha_r = \frac{\lambda_G}{d_r}\left[3.5(Re_G)^{0.7} exp\left(-\frac{4.6 d_p}{d_r}\right)\right] \tag{6-38}$$

With λ_G the thermal conductivity of the gas mixture. This thermal conductivity was calculated according to Chung et al [42], see Appendix A.

Due to the presence of a liquid phase, the heat transfer is expected to increase. Only a limited number of correlations have been reported in literature which correlate the heat transfer coefficient at the bed side to dimensionless numbers. The correlation of Mariani et al [48] was considered for the calculation of the heat transfer coefficient in case of a gas liquid flow through the reactor:

$$\begin{gathered}\alpha_r = \frac{\lambda_L}{d_P}\left[\left(3.87 - 3.77 exp\left(-\frac{1.37}{a}\right)\right) Re_L^{0.643} Pr_L^{1/3}\right] \\ Pr_L = \frac{c_{p,L}\mu_L}{\lambda_L}\end{gathered} \tag{6-39}$$

Where μ_L and λ_L are calculated based on the ABC correlation proposed by Marano et al [49], see Appendix A.

Effective radial thermal conductivity coefficients

The effective radial thermal conductivity coefficient, in case of single gas phase operation, is composed of three contributions [45], i.e., a contribution from the catalyst bed, from the fluid in rest and from the flowing fluid:

$$\frac{\lambda_{er}}{\lambda_f} = \frac{\lambda_{er}^{b}}{\lambda_f} + \frac{\lambda_{er}^{f0}}{\lambda_f} + \frac{\lambda_{er}^{ff}}{\lambda_f} \qquad [6\text{-}40]$$

Where $\lambda_{er}^{b}/\lambda_f$ represents the contribution from the catalyst bed, $\lambda_{er}^{f0}/\lambda_f$ the contribution of the stagnant fluid and $\lambda_{er}^{ff}/\lambda_f$ the contribution of the flowing fluid.

With $\lambda_{er}^{b}/\lambda_f$ calculated based on the work reported by Zehner et al [45]:

$$\begin{aligned}
\frac{\lambda_{er}^{b}}{\lambda_f} &= \frac{2\sqrt{1-\varepsilon_B}}{M}\,\Theta \\
M &= 1 + \left(\frac{\lambda_2}{\lambda_f} - B\right)\frac{\lambda_f}{\lambda_s} \\
\lambda_2 &= 0.227 \cdot 10^{-6} T^3 d_p \\
B &= 1.25\left(\frac{1-\varepsilon_B}{\varepsilon_B}\right)^{10/9} \\
\Theta &= B\,\frac{\left[1 + \left(\frac{\lambda_2}{\lambda_f} - 1\right)\frac{\lambda_f}{\lambda_s}\right]}{M^2}\, ln\left(\frac{1 + \frac{\lambda_2}{\lambda_s}}{B\,\frac{\lambda_f}{\lambda_s}}\right) - \frac{B-1}{M} + \frac{B+1}{2B}\left(\frac{\lambda_2}{\lambda_f} - B\right)
\end{aligned} \qquad [6\text{-}41]$$

The contribution of the stagnant fluid has also been correlated by Zehner et al [45]:

$$\frac{\lambda_{er}^{f0}}{\lambda_f} = \left(1 - \sqrt{1-\varepsilon_B}\right)\left(1 + \varepsilon\,\frac{\lambda_2}{\lambda_f}\right) \qquad [6\text{-}42]$$

The contribution of the flowing fluid is calculated after Specchia et al [50]:

$$\frac{\lambda_{er}^{ff}}{\lambda_f} = Re_G Pr_G\left[8.65\left(1 + 19.4\left(\frac{d_p}{d_r}\right)^2\right)\right]^{-1} \qquad [6\text{-}43]$$

The heat transfer at the wall, h_w, is calculated as proposed by Hennecke et al [51]:

$$
\begin{gathered}
h_w = \frac{\lambda_f}{d_p}\left(Nu_p + \frac{\pi}{2}\left(\frac{\Lambda_w}{\lambda_f} - 1\right)\left(1 - \frac{1}{Nu_p}\right)\right) + \frac{\lambda_2}{\lambda_f} \\
\frac{\Lambda_w}{\lambda_f} = 1 - \sqrt{1 - \varepsilon_W} + \sqrt{1 - \varepsilon_W}\,\frac{\Lambda_w^*}{\lambda_f} \\
\frac{\Lambda_w^*}{\lambda_f} = \frac{2}{1 - B\dfrac{\lambda_f}{\lambda_s}}\Theta' \\
\Theta' = B\frac{\left(1 - \dfrac{\lambda_f}{\lambda_s}\right) ln\left(\dfrac{\lambda_s}{B\lambda_f}\right)}{\left(1 - B\dfrac{\lambda_f}{\lambda_s}\right)^2} - \frac{B - 1}{1 - B\dfrac{\lambda_f}{\lambda_s}} - \frac{B + 1}{2B}\frac{\lambda_s}{\lambda_f}\left[1 - \left(1 - B\frac{\lambda_f}{\lambda_s}\right)^2\right] \\
B = 1.25\left(\frac{1 - \varepsilon_w}{\varepsilon_w}\right)^{0.75} \\
\varepsilon_W = \frac{1}{2} - \frac{1}{6\left(Nu_p - 1\right)} \\
Nu_p = 1.3Pr^{-1/6}\left[0.194Pe_w^2 + 0.34\cdot 10^{-4}Pe_w^3Pr^{-2/3}\right]^{1/4} \\
Pe_W = \left[(Re_W Pr)^2 + \frac{51750}{d_r/d_p}\right]^{1/2} \\
Re_W = \frac{\rho d_p u_{s,G}}{\mu\varepsilon}\frac{K + \dfrac{P + 2}{2}}{K + 1} \\
K = 1.5 + 0.0006\left(\frac{d_r}{d_p} - 2\right)^3 \\
P = 1.14\left(\frac{d_r}{d_p} - 2\right)^{1/3}
\end{gathered}
\qquad [6\text{-}44]
$$

In case of a gas and liquid flow through the reactor, the effective thermal conductivity coefficient is composed of three additive contributions [52]:

$$\lambda_{er} = \lambda_{e0} + \lambda_{eG} + \lambda_{eL} \qquad [6\text{-}45]$$

Where λ_{e0} is the bed contribution without fluid flow, λ_{eG} contribution from gas flow due to lateral mixing and λ_{eL} contribution from liquid flow due to lateral mixing.

The bed contribution is calculated as [52]:

$$\lambda_{e0} = \left(1 - \sqrt{1-\varepsilon_B}\right)\lambda_G + \sqrt{1-\varepsilon_B}\Theta\lambda_L$$
$$\Theta = \frac{2}{N}\left[\left(\frac{B(\kappa-1)}{N^2\kappa}\right) ln\left(\frac{\kappa}{B}\right) - \frac{B+1}{2} - \frac{B-1}{N}\right]$$
$$B = 1.25\left(\frac{1-\varepsilon_B}{\varepsilon_B}\right)^{10/9} \qquad [6\text{-}46]$$
$$N = 1 - \frac{B}{\kappa}$$
$$\kappa = \frac{\lambda_s}{\lambda_L}$$

The lateral mixing contribution of the gas phase is typically negligible [52], while this contribution from the liquid flow is calculated as [52]:

$$\lambda_{eL} = 0.093\left(\frac{Re_L Pr_L}{\beta_t}\right)\lambda_L \qquad [6\text{-}47]$$

The heat wall transfer coefficient is calculated as:

$$h_w = \frac{\lambda_L}{d_p}\left[Nu_{w0} + 0.471 Re_L^{0.65} Pr_L^{1/3}\right] \qquad [6\text{-}48]$$
$$Nu_{w0} = 1.8 - 81 d_p$$

The heat capacity of the gas phase components are taken from open data bases [53] or group contribution methods [54, 55]. The heat capacity of the liquid phase was calculated with an ABC correlation proposed by Marano et al. [49], see Appendix A.

Friction factors

The friction factors for the pressure drop equation in case of single gas flow, eq. [6-17], is [56]:

$$f_G = 6.8\frac{(1-\varepsilon_B)^{1.2}}{{\varepsilon_B}^3} Re^{-0.2} \qquad [6\text{-}49]$$

Where ε_B is calculated according to eq. [6-33] and amounts to 0.5 for the reactor dimensions specified in Table 6-2.

The friction factor for a gas liquid flow, eq. [6-18], is calculated as [32]:

$$f_{LGG} = \left(200(\chi_G \xi)^{-1.2} + 85(\chi_G \xi)^{-0.5}\right)$$
$$\xi = \frac{Re_L^2}{0.001 + Re_L^{1.5}} \qquad [6\text{-}50]$$

The hydraulic diameter in eq. [6-18] is calculated as:

$$d_h = d_p \left(\frac{16\varepsilon_B^3}{9\pi(1-\varepsilon_B)^2}\right)^{\frac{1}{3}} \qquad [6\text{-}51]$$

6.3 Numerical solution strategy

6.3.1 Pellet scale

The equations describing the pellet scale are solved by means of the method of lines [57]. Due to the spherical geometry of the catalyst pellet, the control volumes considered for the discretization change as a function of the radial position in the pellet, see Figure 6-3. This is explicitly taken into account for the discretization of the pellet scale equations. The convention with respect to numbering of the grid points considered in the catalyst pellet is also indicated in Figure 6-3.

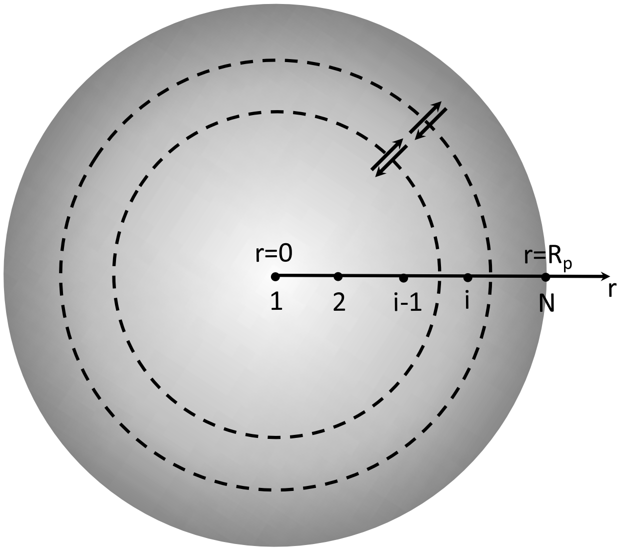

Figure 6-3: Discretization of the pellet. Dashed lines: spheres through which diffusive flux occurs. Area between the dashed lines: the spherical shell in which the reactions take place.

For the internal points, j=2,..N-1, the following equations are used:

$$\varepsilon_p \frac{\partial C_i}{\partial t} = \frac{3D_{e,i}\left(r^2_{j+\frac{1}{2}}\frac{C_i(r_{j+1},t)-C_i(r_j,t)}{r_{j+1}-r_j} - r^2_{j-\frac{1}{2}}\frac{C_i(r_j,t)-C_i(r_{j-1},t)}{r_j-r_{j-1}}\right)}{r^3_{j+\frac{1}{2}}-r^3_{j-\frac{1}{2}}} + \rho_{cat}R_{w,i} \qquad [6\text{-}52]$$

At the center, the second term between the brackets disappears. The expression at the catalyst pellet surface, i.e., point N, depends on the boundary condition, see eq. [6-6], eq. [6-9] and eq. [6-12].

The resulting set of time dependent ordinary differential equations (ODEs), eq. [6-52], is solved by means of the DASPK solver [58]. It is noted that the Jacobian matrix, see section 2.2.5, corresponding to the set of ODEs of eq [6-52] has a banded structure. This has been explicitly taken into account in the numerical procedures.

The number of discretization points considered in the radial direction was gradually increased until no significant differences were observed in the concentration profiles inside the catalyst pellet. From 70 discretization points onwards, convergence was obtained. In Section 6.4.1, it is illustrated that only in the outer shell of the catalyst pellet significant concentration gradients develop. Therefore, a non-equidistant discretization scheme with 24 discretization points was used in order to reduce the CPU time required for the simulations.

6.3.2 Reactor scale

The reactor equations, eqs. [6-7]-[6-18], are solved in an iterative manner. This is illustrated in Figure 6-4. In a first step, the reactant and product fluxes at the outer surface of the catalyst pellet at position k are used to calculate the gas or gas and liquid concentration at the next point in the reactor, i.e. $k+1$, by solving eqs. [6-7] and [6-13] in case of a gas phase reactor and eqs.[6-10], [6-11] and [6-14] in case both gas and liquid flow are considered. Subsequently, the pellet is recalculated at the average of the conditions at position k and position $k+1$ obtained in the previous step. The resulting fluxes are passed to the reactor equations, i.e., eqs. [6-7] and [6-13] or eqs.[6-10], [6-11] and [6-14], are solved with these new fluxes. This is continued until the relative change in gas or gas and liquid concentration of the reactants and products between two iterations is below a certain threshold. A correction to the superficial velocities, eq. [6-8], and pressure, eq. [6-17] or eq. [6-18], is performed after each iteration once the gas or gas and liquid concentration at point $k+1$ are known by calculating the right hand side of eq. [6-8] and eq. [6-18] at the average of the conditions at point k and $k+1$. This also explains why the equations for the gas or gas and liquid concentrations have been integrated as a function of time while the equations for the superficial velocities corrections or pressure drop have been considered to depend only on the axial reactor coordinate. Also the physical properties and transfer parameters are recalculated after each iteration. In the first step, the discretization of the first order spatial derivative of the reactor equations, eqs. [6-7]-[6-18], is done with the First Order Upwind discretization scheme. In the second step the implicit mid-point method is used. Once the iteration procedure to obtain the concentrations at point $k + 1$ is converged, the iteration procedure is repeated to obtain the concentration at the next discretization point in the reactor, i.e., $k + 2$.

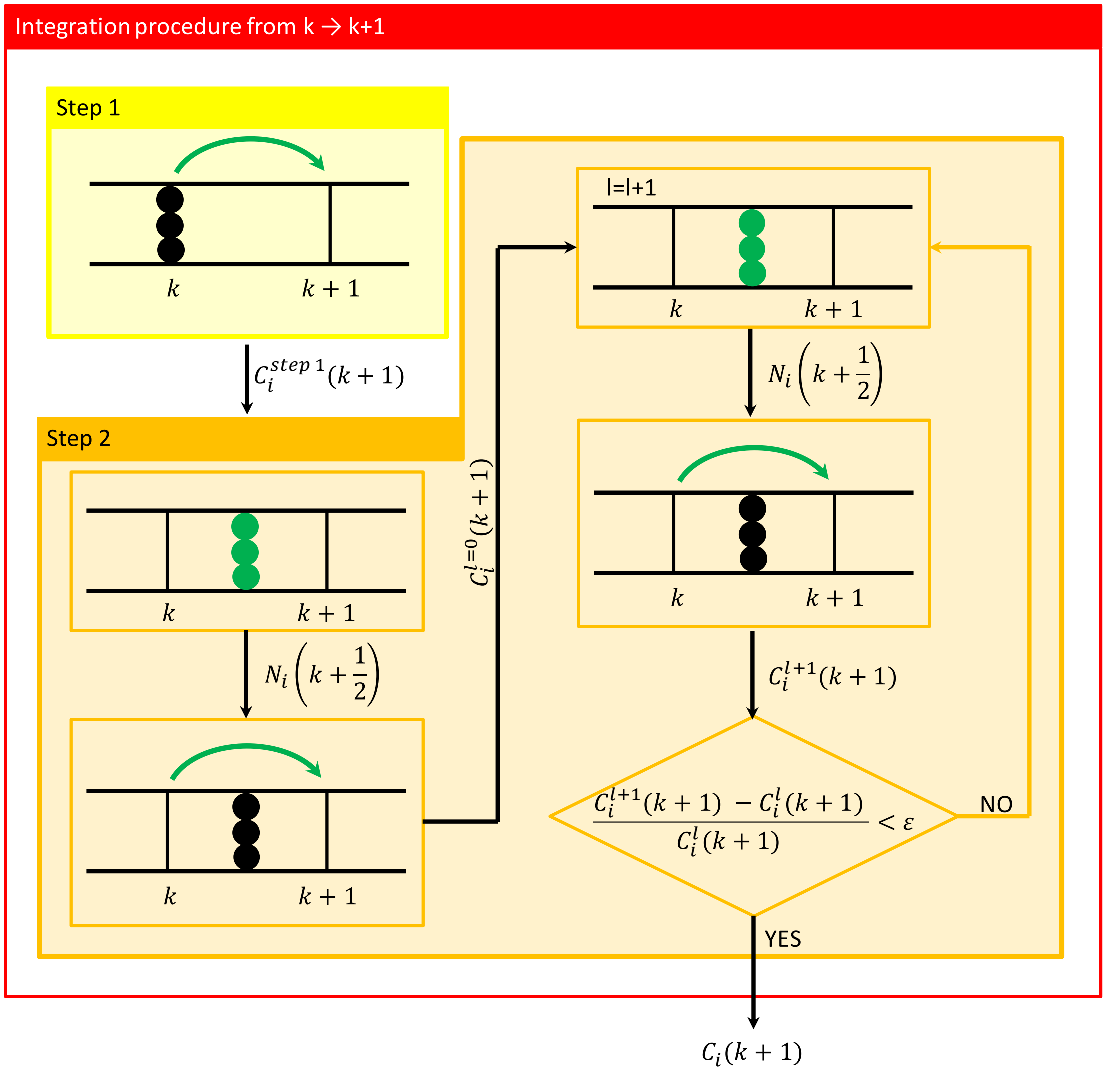
Integration procedure from k → k+1
Step 1
k
$k+1$
$C_i^{step\ 1}(k+1)$
Step 2
k
$k+1$
$N_i\left(k+\frac{1}{2}\right)$
k
$k+1$
$C_i^{l=0}(k+1)$
l=l+1
k
$k+1$
$N_i\left(k+\frac{1}{2}\right)$
k
$k+1$
$C_i^{l+1}(k+1)$
$\frac{C_i^{l+1}(k+1) - C_i^l(k+1)}{C_i^l(k+1)} < \varepsilon$
NO
YES
$C_i(k+1)$

Figure 6-4: Solution strategy for the reactor model equations. C_i^{step1} the concentration of species *i* after the first step of the integration procedure [mol m_f^{-3}], N_i the flux of species *i* at the catalyst pellet surface [mol $(m_p^2 s)^{-1}$] and C_i^l the concentration of species *i* at iteration l [mol m_f^{-3}] in the second step of the integration procedure.

The radial terms in the reactor equations, eq. [6-15], are discretized in a manner similar to the one applied to the pellet scale equations.

6.4 Simulation results

6.4.1 Pellet scale

The phenomena occurring in a single catalyst pellet will ultimately determine the performance of the FTS TBR. Therefore, simulations have been performed with the catalyst pellet separately to obtain a more profound insight in the interplay between reaction and diffusion at the catalyst pellet scale. Figure 6-5 depicts typical profiles in a catalyst pellet with a diameter of 4 mm at 495 K, a total pressure of 2.0 Mpa and H_2 to CO molar ratio of 2. It is noted that the results presented in Figure 6-5 are obtained by integrating only the mass balances, i.e., eqs [6-1] - [6-2]. The enthalpy balance, eq [6-3], is not solved simultaneously as the temperature was found to vary only within 1 K over the entire catalyst pellet. Hence, the catalyst pellet can be considered isothermal. This was also numerically verified in other studies by simultaneously solving the mass and enthalpy balance for a spherical catalyst pellet [5, 27, 59] and corresponds well with a small value for the Prater number for evaluating the presence of internal temperature gradients inside the catalyst pellet [59].

Figure 6-5-a clearly shows that the CO concentration rapidly decreases, i.e., CO is only present in significant amounts in the outer 10 % of the catalyst pellet. The other 90% of the catalyst pellet is not used for the FTS reaction at the aforementioned conditions. The H_2 concentration also decreases rapidly from the vapor liquid equilibrium concentration at the catalyst pellet surface to a steady value of 19 mol m $^{-3}$ in the outer 10 % of the catalyst pellet. It is remarkable that despite a bulk H_2 to CO molar ratio of 2, an accumulation of H_2 occurs in the catalyst pellet. This is caused by the higher diffusion coefficient of H_2 compared to CO in the wax phase which fills up the catalyst pellet pores, i.e., $D_{H_2}/D_{CO} = 2.7$. This in turn increases the H_2 to CO molar ratio in the catalyst pellet from 1.96 at the catalyst pellet surface to 288 at 10 % from the catalyst pellet surface.

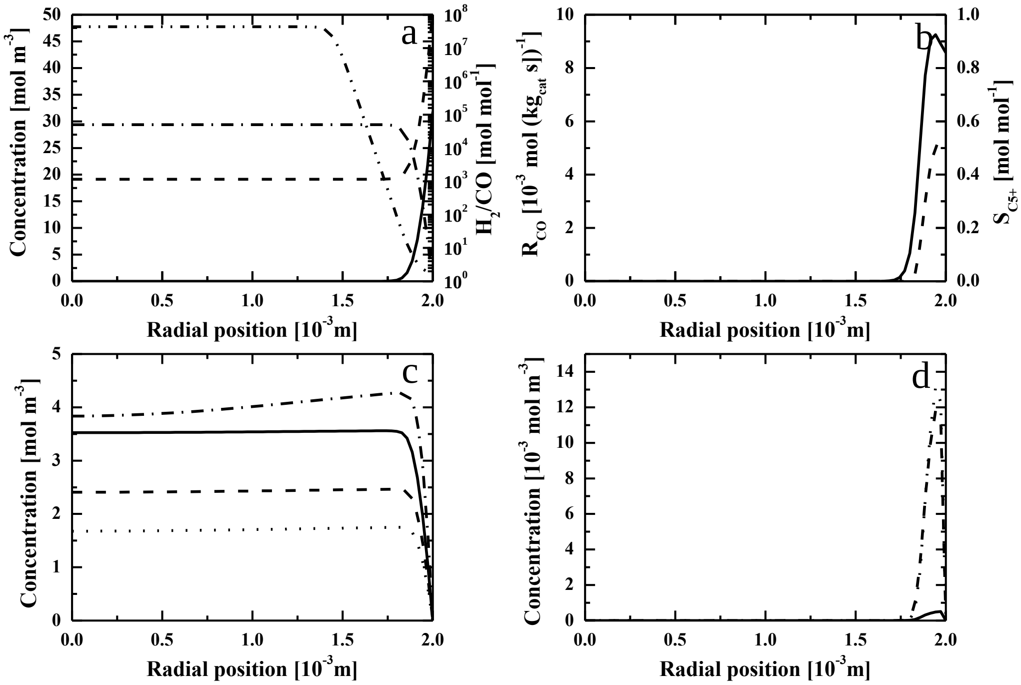

Figure 6-5: Typical profiles in a catalyst pellet with a 4 mm diameter at 495 K, a total pressure of 2.0 MPa and a bulk H_2 to CO molar ratio of 2. The simulation results are obtained by integrating eqs. [6-1] - [6-2] with eqs. [6-4] - [6-6] as boundary conditions. The integration is performed with the DASPK solver after applying the numerical methods outlined in section 6.3. Other specifications of the catalyst pellet are provided in Table 6-1. Diffusion coefficients, liquid properties, … are calculated as explained in section 6.2.2. a: concentration of CO (—), H_2 (– –), methane (–·) and the H_2/CO molar ratio (–··). b: R_{CO} (—) and S_{C5+} (– –). c: concentration of C_2H_6 (—), C_3H_8 (– –), $_n$-C_4H_{10} (···) and C_{5+} (–·). d: concentration of C_2H_4 (—), C_3H_6 (– –), 1-C_4H_8 (···).

The CO net consumption rate, R_{CO}, and the selectivity to C_{5+} components, S_{C5+}, in the catalyst pellet are illustrated in Figure 6-5-b. Both quantities are only different from zero in a small spherical shell. It is noted that near the catalyst pellet surface R_{CO} decreases less rapidly as compared to the CO concentration. This is due to the increasing H_2 to CO molar ratio in the catalyst pellet which enhances the reaction rate. The S_{C5+} is negatively impacted by the increasing H_2 to CO molar inlet ratio and strongly decreasing CO concentration. The S_{C5+} drops to zero before the R_{CO} reaches zero, hence, a part of the catalyst pellet in which reaction is still occurs does not contribute to the production of longer hydrocarbon chains.

The alkanes, see Figure 6-5-c, strongly increase from zero at the catalyst pellet surface to a constant level throughout the remaining part of the catalyst pellet. The alkenes are only different from zero in the outer 10% of the catalyst pellet, see Figure 6-5-d. This is explained by the strongly increasing H_2 to CO molar ratio in the catalyst pellet, resulting in hydrogenation of the alkenes.

As Figure 6-5 clearly illustrates, only the outer 10% of the catalyst pellet is employed at typical FTS conditions. Furthermore, the higher H_2 diffusion coefficient compared to that for CO, impacts negatively the selectivity to higher hydrocarbons. The impact of diffusion on the catalyst pellet performance can be reduced by reducing the catalyst pellet size but this can only be done in TBRs to a limited extend in order to avoid a significant pressure drop. The performance of a slurry bubble column reactor will be less affected by internal diffusion limitations as the catalyst pellets suspended in the slurry have a much smaller size. By performing simulations with the catalyst pellet model at varying operating conditions, a potentially more optimal operating point can be found, probably at a lower H_2/CO molar ratio in the bulk gas phase.

The impact of the bulk syngas ratio and temperature on the CO consumption rate, R_{CO}, selectivity to C_{5+}, S_{C5+}, and the catalyst productivity of C_{5+} components, STY_{C5+}, is illustrated in Figure 6-6 at a total pressure of 2 MPa and a catalyst pellet diameter of 4 mm. The R_{CO}, Figure 6-6-a, increases with increasing temperature for practically all bulk syngas ratios. At temperatures below 480 K, the R_{CO} increases with increasing bulk syngas ratio. At temperatures exceeding 490 K, the R_{CO} clearly goes through a maximum as function of the bulk syngas ratio. It is noted that this maximum in the R_{CO} shifts to lower bulk syngas ratios with increasing temperature. The S_{C5+}, Figure 6-6-b, at low bulk syngas ratios, i.e., < 1.5 mol mol^{-1}, does not show a strong variation with the temperature. At higher bulk syngas ratios, a much stronger detrimental impact of an increasing temperature on the S_{C5+} is observed. The impact of bulk syngas ratio and temperature on STY_{C5+}, which is the combination of R_{CO} and S_{C5+}, is illustrated in Figure 6-6-c. This clearly shows that the productivity of the catalyst can be increased by working at lower than stoichiometric bulk syngas ratios and higher temperatures.

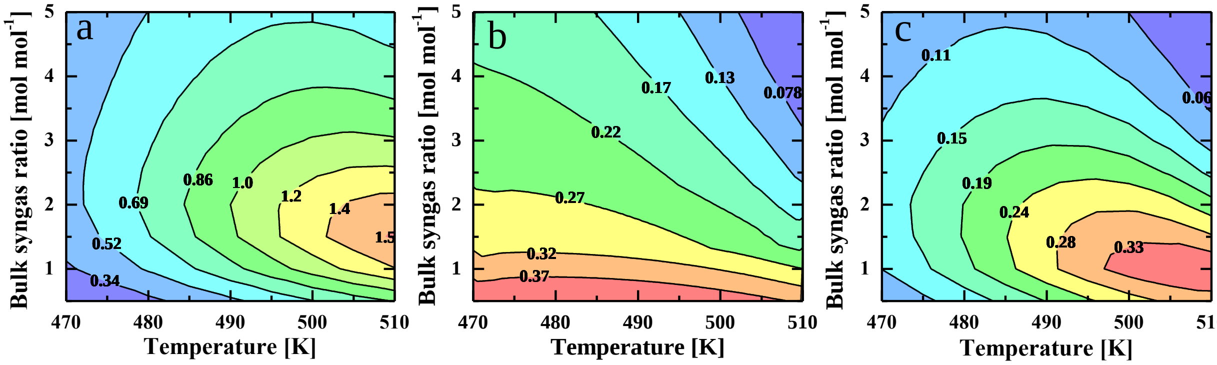

Figure 6-6: Contour plot of (a): CO consumption rate [10^{-3}mol$_{CO}$ (kg$_{cat}$ s)$^{-1}$], (b): selectivity to C_{5+} [mol mol^{-1}] and (c): C_{5+} productivity [10^{-3} mol (kg$_{cat}$s)$^{-1}$]. The total pressure was set at 2 MPa and the catalyst pellet diameter at 4 mm. The simulation results are obtained by integrating eqs. [6-1] and [6-2] with eqs. [6-4] and [6-6] as boundary conditions by applying the numerical methods outlined in section 6.3. Other specification of the catalyst pellet are provided in Table 6-1. Diffusion coefficients, liquid properties, … are calculated as explained in section 6.2.2.

Figure 6-7 illustrates the effect of pressure and temperature on R_{CO} (a), S_{C5+} (b) and STY_{C5+} (c). Increasing both operating conditions is beneficial for the R_{CO}. The highest S_{C5+} are obtained for pressures between 2 and 3 MPa and temperature up to 490 K. Increasing the temperature beyond 490 K decreases the S_{C5+} selectivity for practically all pressures, although the detrimental impact of temperature on the S_{C5+} is less pronounced at higher pressures. It is interesting to note that increasing the pressure beyond 4 MPa would tend to decrease the S_{C5+}. The catalyst productivity, STY_{C5+}, profits from both an increase in temperature as in pressure.

The variation in R_{CO}, S_{C5+} and STY_{C5+} with changes in bulk syngas ratio and pressure are illustrated in Figure 6-8 at a temperature of 495 K and a catalyst pellet with a diameter of 4 mm. The R_{CO}, Figure 6-8-a, increases with increasing pressure at all bulk syngas ratios. As a function of bulk syngas ratio, the R_{CO} goes through a maximum which lies close to the stoichiometric bulk syngas ratio. The S_{C5+}, Figure 6-8-b, benefits from working at bulk syngas ratios below the stoichiometric bulk syngas ratio of 2. At these substoichiometric bulk syngas ratios, the S_{C5+} is not significantly impacted by the total pressure. The STY_{C5+}, Figure 6-8-c, shows a comparable behavior to the R_{CO}.

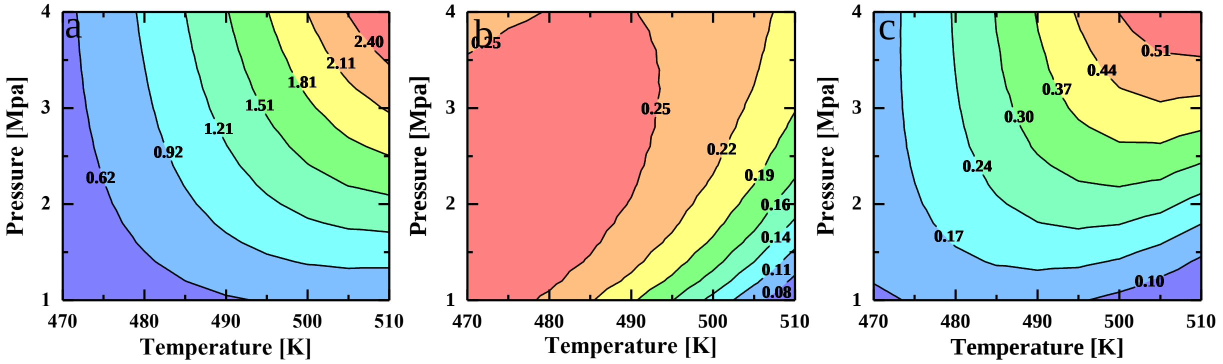

Figure 6-7: Contour plot of (a): CO consumption rate [10^{-3}mol$_{CO}$ (kg$_{cat}$ s)$^{-1}$], (b): selectivity to C5+ [mol mol^{-1}] and (c): C$_{5+}$ productivity [10^{-3} mol (kg$_{cat}$s)$^{-1}$]. The bulk syngas ratio was set at 2 and the catalyst pellet diameter at 4 mm. The simulation results are obtained by integrating eqs. [6-1] and [6-2] with eqs. [6-4] and [6-6] as boundary conditions by applying the numerical methods outlined in section 6.3. Other specification of the catalyst pellet are provided in Table 6-1. Diffusion coefficients, liquid properties, … are calculated as explained in section 6.2.2.

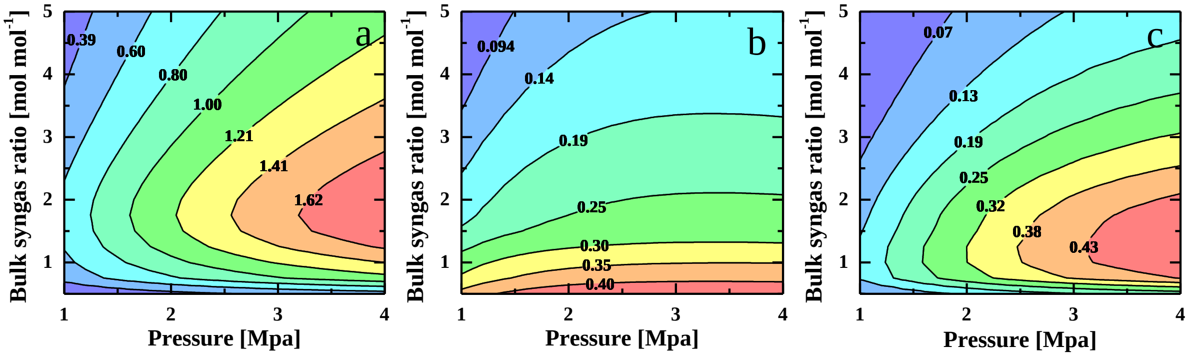

Figure 6-8: Contour plot of (a): CO consumption rate [10^{-3}mol$_{CO}$ (kg$_{cat}$ s)$^{-1}$], (b): selectivity to C$_{5+}$ [mol mol^{-1}] and (c): C$_{5+}$ productivity [10^{-3} mol (kg$_{cat}$s)$^{-1}$]. The temperature was set at 495 K and the catalyst pellet diameter at 4 mm. The simulation results are obtained by integrating eqs. [6-1] and [6-2] with eqs. [6-4] and [6-6] as boundary conditions by applying the numerical methods outlined in section 6.3. Other specification of the catalyst pellet are provided in Table 6-1. Diffusion coefficients, liquid properties, … are calculated as explained in section 6.2.2.

The effect of the catalyst pellet diameter at varying reaction conditions on R_{CO}, S_{C5+} and STY_{C5+} is represented in Figure 6-9. Reducing the catalyst pellet diameter is beneficial for both R_{CO} (Figure 6-9 I-III –a) and S_{C5+} (Figure 6-9 I-III-b). The R_{CO} as a function of the bulk syngas ratio exhibits a maximum, while the S_{C5+} selectivity decreases as a function of this operating condition. As a function of pressure, both the activity and selectivity will increase. The temperature increases R_{CO}, but impacts the S_{C5+} negatively.

The simulations performed with the pellet scale model, Figure 6-6 to Figure 6-9, can be used for various purposes. On the one hand, the simulations can be used to acquire a more fundamental insight in the interplay between reaction and diffusion and to better understand specific aspects of a full multi-scale model. For example, the simulations presented here show that R_{CO} does not increase monotonically as a function of the bulk syngas ratio. This in contrast to the effect of the H_2/CO molar inlet ratio on the R_{CO} in the absence of internal and external concentration gradients, see Section 3.3.1. The conversion in a diffusion controlled FTS TBR will rather experience a maximum as a function of the bulk syngas ratio. On the other hand, the simulations can be used to optimize a FTS TBR. For example, Figure 6-8 illustrates that if a FTS TBR is operated at 2 MPa and a syngas bulk ratio of 2, the S_{C5+} can be increased by decreasing the syngas bulk ratio to 1. The loss in activity can be compensated by a pressure increase.

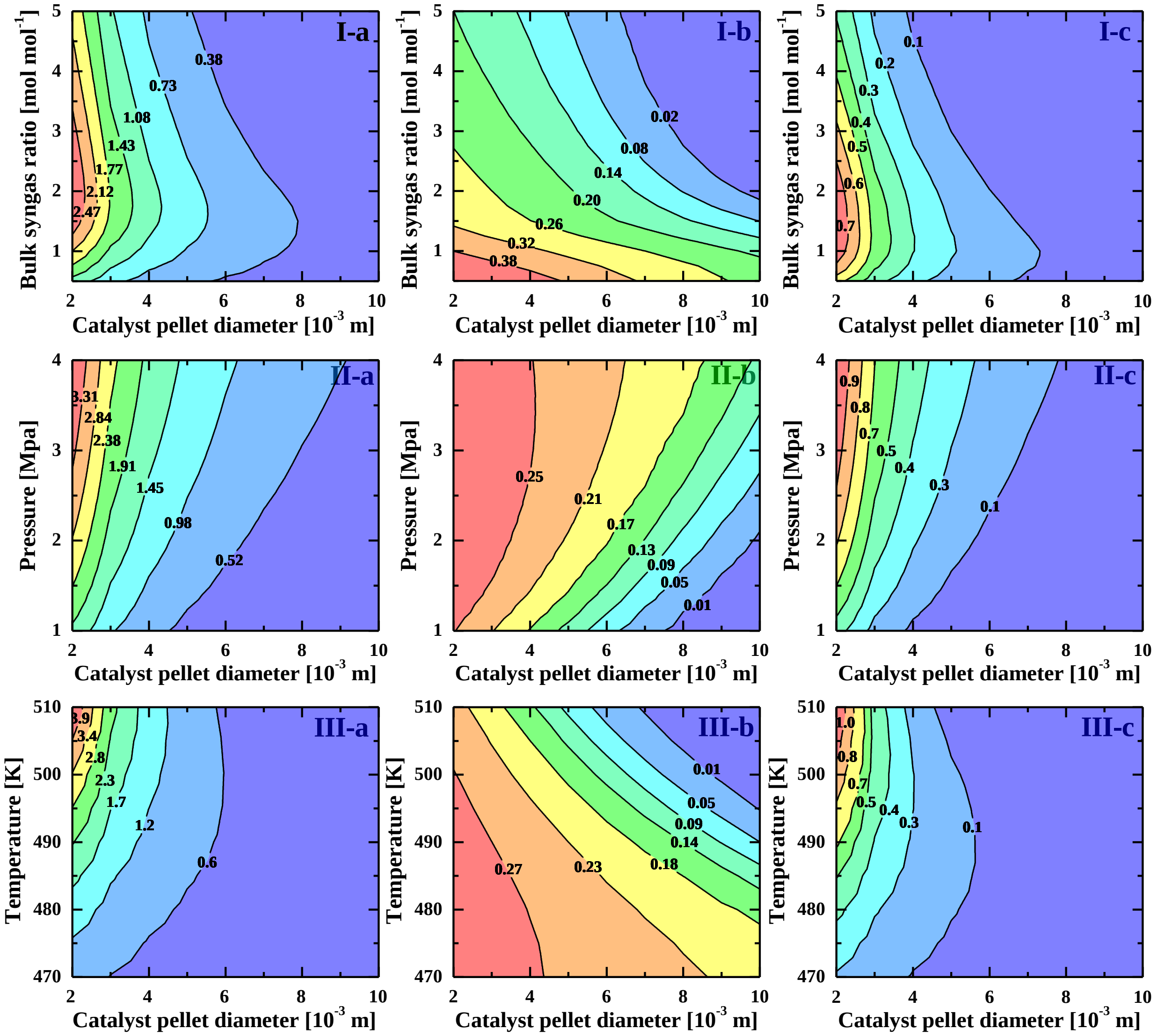

Figure 6-9: Contour plot of (a): CO consumption rate [10^{-3}mol$_{CO}$ (kg$_{cat}$ s)$^{-1}$], (b): selectivity to C$_{5+}$ [mol mol^{-1}] and (c): C$_{5+}$ productivity [10^{-3} mol (kg$_{cat}$s)$^{-1}$] at (I): 2 Mpa and 495 K, (II): syngas bulk ratio of 2 and 495 K and (III): 2 Mpa and syngas bulk ratio of 2. The simulation results are obtained by integrating eqs. [6-1] and [6-2] with eqs. [6-4] and [6-6] as boundary conditions by applying the numerical methods outlined in section 6.3. Other specification of the catalyst pellet are provided in Table 6-1. Diffusion coefficients, liquid properties, … are calculated as explained in section 6.2.2.

6.4.2 Reactor scale

The gas phase reactor model, eqs. [6-7], [6-8], [6-13] and [6-19], is used to simulate a base case for the industrial TBR for the FTS. The reactor dimensions and operating conditions at the reactor inlet are provided in Table 6-2 and taken from Kaskes et al. [4].

Table 6-2: Reactor and catalyst pellet dimensions, operating conditions and inlet stream specifications.

Reactor dimensions	
Length, L_r $[m_r]$	10.0
Diameter d_r $[m_r]$	0.025
Catalyst pellet dimension	
Diameter d_p $[m_p]$	0.004
Reactor operating conditions	
Inlet pressure p_0 $[MPa]$	3.0
Inlet temperature T_0 $[K]$	495.0
Cooling temperature T_{cool} $[K]$	495.0
Inlet stream specifications	
Inlet CO flow rate $F_{CO,0}$ $[mol\ s^{-1}]$	$1.79 \cdot 10^{-2}$
Inlet syngas ratio $F_{H_2,0}/F_{CO}$ $[mol\ mol^{-1}]$	2.0

Typical profiles of the reactant concentration and product selectivity, temperature and CO conversion are provided in Figure 6-10. The H_2 concentration decreases more rapidly than that of CO resulting in a decreasing bulk syngas ratio (Figure 6-10-a). This can be attributed to the stoichiometry of the FTS reaction. The inclusion of a detailed kinetic model allows to simulate the selectivity of all the individual components. This is illustrated in Figure 6-10-a for the alkanes and in Figure 6-10-b for the alkenes. The alkanes are produced in decreasing amounts with the carbon number, corresponding with the typical Anderson-Schulz-Flory (ASF) distributions observed in FTS. The alkenes are produced to a much lesser extent than the alkanes which can be related to the strong diffusion limitations on the pellet scale, see Figure 6-5. It is noted that ethene is produced in lower amounts than propene, which is consistent with typical product distributions obtained for alkenes in FTS. Furthermore, a maximum is observed in the alkenes concentration as a function of the axial coordinate (not shown in Figure 6-10) which is caused by secondary reactions of the alkenes in the considered reaction network, i.e., hydrogenation and incorporation in the chain growth process. This underlines the importance of combining a detailed kinetic model with a reactor model.

The temperature initially increases, see Figure 6-10-b. In the beginning of the reactor the highest reaction rate is observed. The produced reaction heat can only partly be removed by the cooling medium in the shell of the MTTBR. The increased temperature causes the reaction rate to increase which, in turn, increases the produced reaction heat. Due to the temperature increase, the heat removal by the cooling medium increases as the temperature difference between the cooling medium and catalyst bed has increased. From a reactor length of 2.5 m onwards, the produced reaction heat becomes lower than the heat removed by the cooling medium resulting in an overall temperature decrease of the catalyst bed. The pressure drop over the catalyst bed amounts to 3435 Pa.

The simulations with the pellet scale model clearly demonstrated that diffusion limitations have a significant impact on the CO consumption rate and C_{5+} selectivity. At the operating conditions used, external mass transfer limitations can practically be ignored. This corresponds well with an evaluation of the Mears criterion for external mass and heat transfer [20, 21, 59]. The reactor behavior can, hence, be understood based on the contour plots of Figure 6-6 and Figure 6-7.

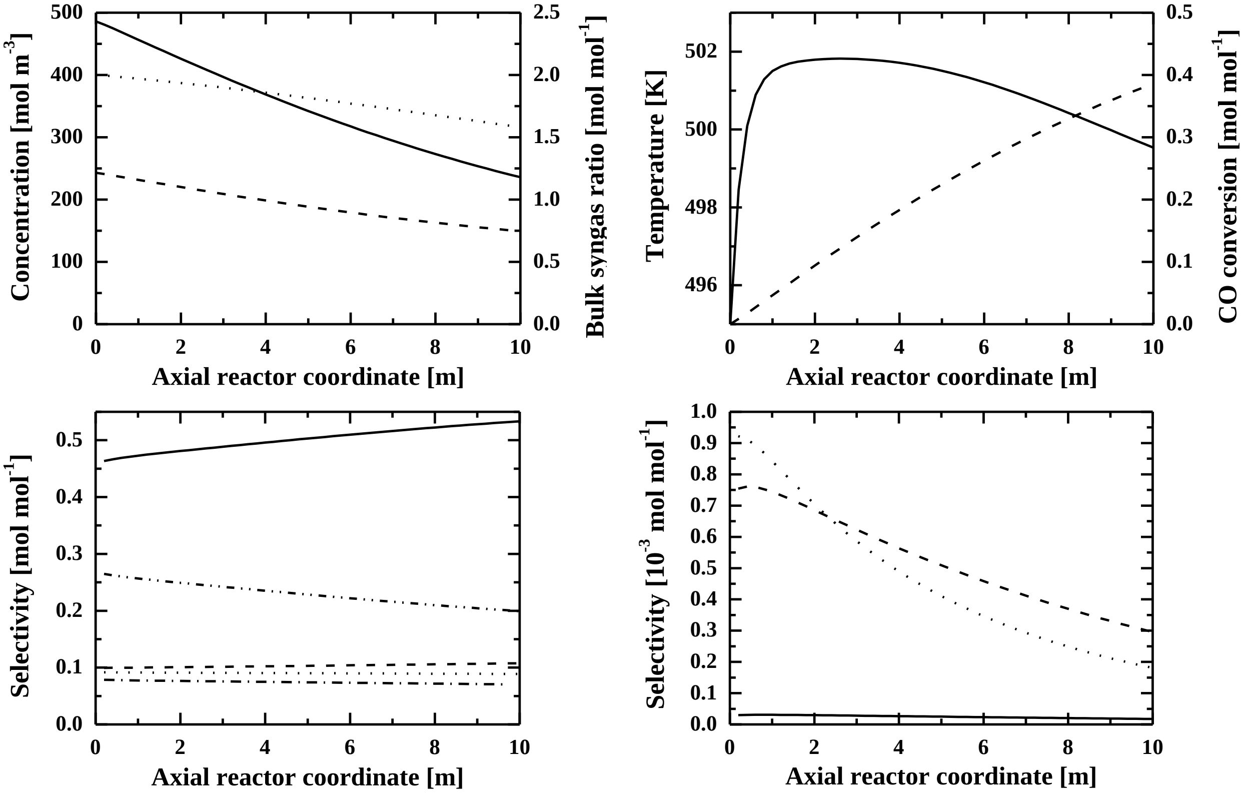

Figure 6-10: Typical profiles in a FTS reactor with reactor dimensions, operating conditions and inlet compositions as in Table 6-2. The simulation results are obtained by integrating eqs. [6-1], [6-2], [6-7], [6-8], [6-13] and [6-17] with eqs. [6-4], [6-5], [6-9] and [6-19] as boundary conditions. The integration is performed with the DASPK solver after applying the numerical methods outlined in section 6.3. Diffusion coefficients, liquid properties, … are calculated as explained in section 6.2.2 . a: concentration of H_2 (—), CO (– –), and the H_2/CO molar ratio (···). b: CO conversion (– –) and temperature (—). c: concentration of CH_4 (—), C_2H_6 (– –), C_3H_8 (···), *n*-C_4H_{10} (–·) and C_{5+} (–··). d: concentration of C_2H_4 (—), C_3H_6 (– –), 1-C_4H_8 (···).

Effect of operating conditions

The reactor performance in terms of CO conversion, X_{CO}, C_{5+} selectivity, S_{C5+} and C_{5+} yield has also been studied as a function of the operating conditions, i.e., the inlet pressure, inlet bulk syngas ratio and inlet temperature. The impact of inlet bulk syngas ratio and temperature on X_{CO}, S_{C5+} and C_{5+} yield is illustrated in Figure 6-11. As already indicated, the diffusion limitations within the catalyst pellet control the X_{CO} and S_{C5+} that can be obtained to a major extent. As a consequence, similar trends can be found for the X_{CO} and S_{C5+} as a function of inlet bulk syngas ratio or inlet temperature as was found for the R_{CO} and S_{C5+} for the pellet scale simulations, see

Figure 6-6. Figure 6-11 also illustrates that a higher yield to C_{5+} products would be obtained if the reactor would be operated at an inlet temperature of 500 K and a substoichiometric inlet bulk syngas ratio, i.e., 1.5 compared to 2.0. It is noted that this increase in C_{5+} yield is primarily due to an increase in S_{C5+}, i.e., 0.2 compared to 0.23, as the X_{CO} is similar for both operating points, i.e., close 0.35.

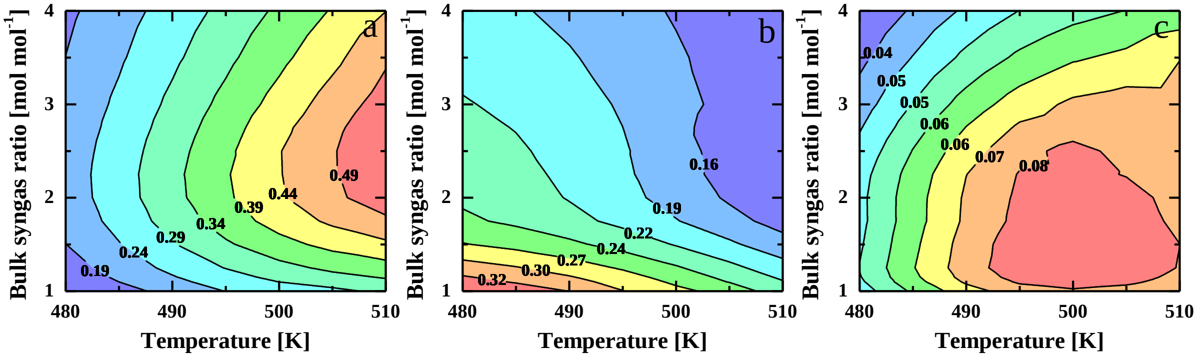

Figure 6-11: Contour plot of (a): CO conversion [mol mol^{-1}], (b): C_{5+} selectivity [mol mol^{-1}] and (c): C_{5+} molar yield [mol mol^{-1}] as function of inlet bulk syngas ratio [mol mol^{-1}] and inlet temperature [K]. Other inlet conditions, reactor dimension, … are taken from Table 6-2. The simulation results are obtained by integrating eqs. [6-1], [6-2], [6-7], [6-8], [6-13] and [6-17] with eqs. [6-4], [6-5], [6-9] and [6-19] as boundary conditions. The integration is performed with the DASPK solver after applying the numerical methods outlined in section 6.3. The transfer parameters and gas and liquid properties are calculated as explained in section 6.2.2.

Figure 6-12 illustrates the effect of changing the inlet pressure or inlet temperature on X_{CO}, S_{C5+} and C_{5+} yield. Also here similar trends are found for the X_{CO} and S_{C5+} as were found for the R_{CO} and S_{C5+} as function of the same operating conditions, see Figure 6-7. Only a small increase in inlet pressure would cause the X_{CO} and S_{C5+} to increase simultaneously. Increasing the temperature, increases the X_{CO} at each inlet pressure but impacts the S_{C5+} negatively.

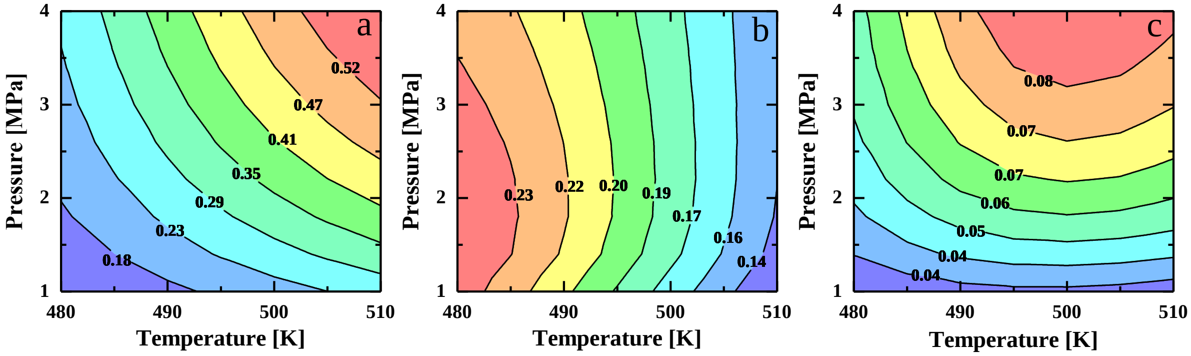

Figure 6-12: Contour plot of (a): CO conversion [mol mol^{-1}], (b): C_{5+} selectivity [mol mol^{-1}] and (c): C_{5+} molar yield [mol mol^{-1}] as function of inlet pressure [MPa] and inlet temperature [K]. Other inlet conditions, reactor dimension, … are taken from Table 6-2. The simulation results are obtained by integrating eqs. [6-1], [6-2], [6-7], [6-8], [6-13] and [6-17] with eqs. [6-4], [6-5], [6-9] and [6-19] as boundary conditions. The integration is performed with the DASPK solver after applying the numerical methods outlined in section 6.3. The transfer parameters and gas and liquid properties are calculated as explained in section 6.2.2.

The changes in X_{CO}, S_{C5+} and C_{5+} yield as function of the variation in inlet bulk syngas ratio and inlet pressure are illustrated in Figure 6-13. Again similar trends are found for X_{CO} and S_{C5+} as were found for R_{CO} and S_{C5+} for the pellet scale, see Figure 6-8. Only a different trend is observed for the S_{C5+} at higher bulk syngas ratios as a function of the pressure. This can be related to the decreasing S_{C5+} selectivity with increasing conversion. The simulations represented in Figure 6-13 also illustrate that a higher C_{5+} yield could be obtained at a higher inlet pressure and a substoichiometric bulk syngas ratio. The increase in C_{5+} yield is then primarily attributable to the beneficial effect of the pressure on the obtained X_{CO} as the S_{C5+} is more or less constant.

Figure 6-14 illustrates the effect of the catalyst pellet diameter at varying operating conditions on the X_{CO}, S_{C5+} and C_{5+} yield. The simulation results obtained for the X_{CO} can be understood based on the simulation results obtained for the pellet scale simulations, see Figure 6-9-a. A smaller catalyst pellet diameter increases the R_{CO} on the pellet scale and as a consequence the CO conversion will increase. The S_{C5+} shows a different behavior compared to the simulations performed with the pellet scale, see Figure 6-9-b, i.e., the S_{C5+} increases as a function of the catalyst pellet diameter. This is related to the higher X_{CO} obtained with smaller catalyst pellets as at a higher X_{CO} a lower S_{C5+} is obtained. Next to this, the higher R_{CO} will cause a much stronger temperature increase as function of the axial reactor coordinate, see Figure 6-15-a, which will impact the S_{C5+} negatively. A smaller catalyst pellet, hence, yields effectively a higher S_{C5+}, see Figure 6-9-b, but this effect is counteracted. Smaller catalyst pellets could be used to increase the S_{C5+} but a proper selection of inlet temperature and cooling medium temperature will be important. Furthermore, it is noted that the optimization should not only be performed with considerations with respect to CO conversion and S_{C5+} selectivity but also with respect to the maximum allowable temperature. The maximum temperature in the axial temperature profile for small catalyst pellets and inlet temperature above 495 K are clearly to be avoided both with respect to catalyst lifetime and possible reactor runaway. Figure 6-15-b shows the pressure drop as a function of the inlet temperature and catalyst pellet diameter. Changes in the inlet temperature have a negligible effect on the pressure drop. On the other hand, the pressure drop almost doubles when the catalyst pellet diameter is halved.

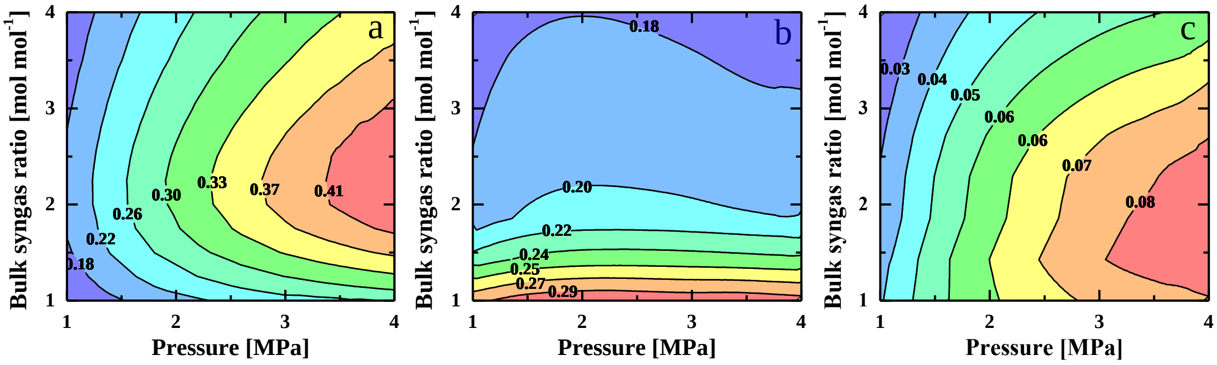

Figure 6-13: Contour plot of (a): CO conversion [mol mol^{-1}], (b): C_{5+} selectivity [mol mol^{-1}] and (c): C_{5+} molar yield [mol mol^{-1}] as function of the inlet bulk syngas ratio [mol mol^{-1}] and inlet pressure [MPa]. Other inlet conditions, reactor dimension, … are taken from Table 6-2. The simulation results are obtained by integrating eqs. [6-1], [6-2], [6-7], [6-8], [6-13] and [6-17] with eqs. [6-4], [6-5], [6-9] and [6-19] as boundary conditions. The integration is performed with the DASPK solver after applying the numerical methods outlined in section 6.3. The transfer parameters and gas and liquid properties are calculated as explained in section 6.2.2.

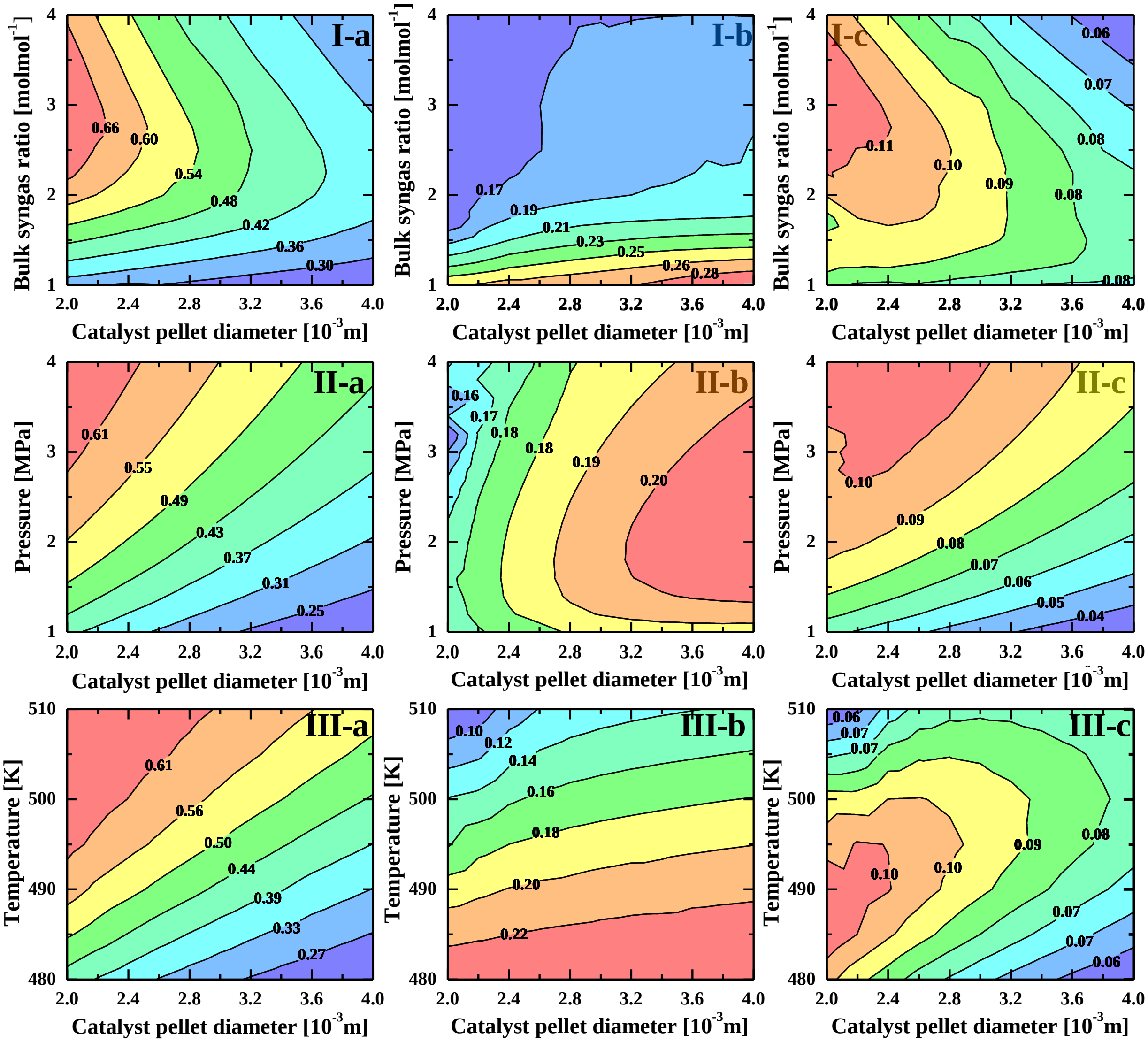

Figure 6-14: Contour plot of (a): CO conversion [mol mol^{-1}], (b): C_{5+} selectivity [mol mol^{-1}] and (c): C_{5+} molar yield [mol mol^{-1}] at (I): 3MPa and inlet temperature of 495 K, (II): inlet bulk syngas ratio of 2 and 495K and (III): 3MPa and bulk syngas ratio of 2. Other inlet conditions, reactor dimension, … are taken from Table 6-2. The simulation results are obtained by integrating eqs. [6-1], [6-2], [6-7], [6-8], [6-13] and [6-19] with eqs. [6-4], [6-5], [6-9] and [6-19] as boundary conditions. The integration is performed with the DASPK solver after applying the numerical methods outlined in section 6.3. The transfer parameters and gas and liquid properties are calculated as explained in section 6.2.2.

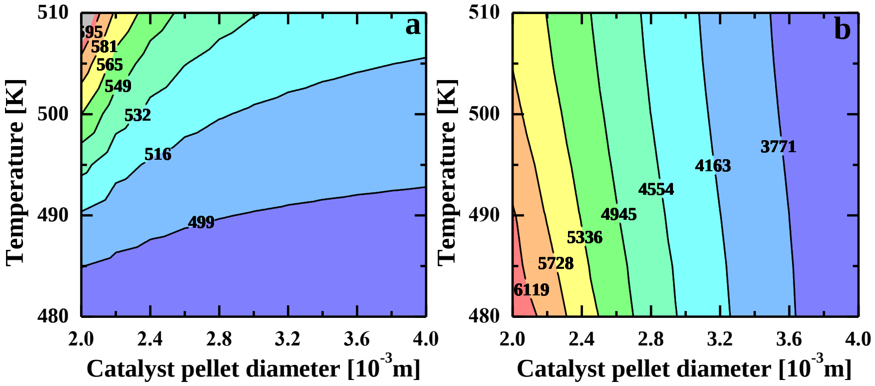

Figure 6-15: Contour plot of the (a) maximum temperature [K] in the reactor and pressure drop [Pa] (b) as function of the inlet temperature and catalyst pellet diameter. Other inlet conditions, reactor dimension, … are taken from Table 6-2. The simulation results are obtained by integrating eqs. [6-1], [6-2], [6-7], [6-8], [6-13] and [6-17] with eqs. [6-4], [6-5], [6-9] and [6-19] as boundary conditions. The integration is performed with the DASPK solver after applying the numerical methods outlined in section 6.3. The transfer parameters and gas and liquid properties are calculated as explained in section 6.2.2.

Effect of liquid recycle

A liquid recycle can be used to increase the heat transfer and, hence, mitigate the maximum temperature along the axial direction of the catalyst bed. The effect of a liquid recycle is assessed by solving eqs. [6-10], [6-11], [6-14] and [6-18] simultaneously with eqs. [6-1] and [6-2]. The reactor dimensions, inlet conditions, … are taken from Table 6-2. In addition, an inlet superficial velocity of 0.01 m s^{-1} of a liquid phase is considered. The recycled liquid stream is assumed to be free of H_2, CO, … and the properties of the liquid stream are approximated by those of octacosane. The differences between results obtained with the single, gas phase reactor model, see Figure 6-10, and the model considering both the gas and liquid flow is mainly situated in the maximum temperature obtained as a function of the axial reactor coordinate. The maximum temperature for the reactor with a liquid recycle is limited to 496 K compared to the maximum temperature of 502, see Figure 6-16. This is due to the higher heat transfer coefficient obtained in a gas liquid reactor, i.e., the heat transfer coefficient is 427 $W(m^2K)^{-1}$ higher, and a higher contribution of the liquid flow to the convective term in the enthalpy balance, eq. [6-16]. The latter is mainly related to the difference in density between a liquid and a gas, i.e., ρ_G=15 $kg\ m^{-1}$ compared to ρ_L= 676 $kg\ m^{-1}$.

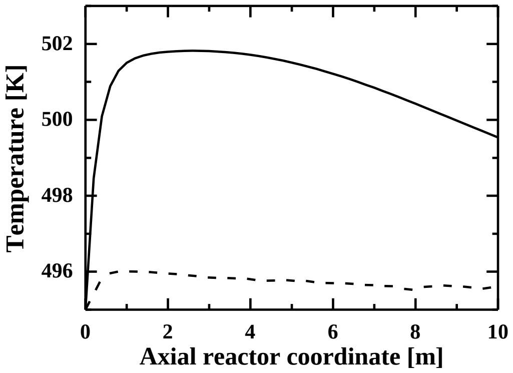

Figure 6-16: Temperature profile in the reactor in a gas (—) or a gas-liquid reactor (– –). Inlet conditions, reactor dimension, … are taken from Table 6-2. The simulation results are obtained by integrating eqs. [6-1], [6-2], [6-10], [6-11], [6-14] and [6-18] with eqs. [6-4], [6-5], [6-9] and [6-19] as boundary conditions. The integration is performed with the DASPK solver after applying the numerical methods outlined in section 6.3. The transfer parameters and gas and liquid properties are calculated as explained in section 6.2.2.

Radial temperature profiles

Temperature control in the catalyst bed is one of the major concerns in a MTTBR for FTS, see also Chapter 1. Apart from gradients in the axial direction, the highly exothermic FTS reaction can lead to temperature gradients in the radial direction of the catalyst bed. An evaluation of the Mears criterion for the existence of radial temperature gradients in the catalyst bed shows that these can effectively develop [20]. The existence of radial temperature gradients in the catalyst bed has also been numerically verified [22].

Assessing the origination of radial temperature gradients in the catalyst bed is important both from an operational and safety point of view. One dimensional reactor models can only be used to calculate the average temperature in the radial direction. Dimensioning the reactor based on such one dimensional models can result in reactor diameters which in reality suffer from a significant temperature gradient between the reactor wall and the center of the catalyst bed. For example, Rafiq et al. [22] estimated the radial temperature profiles in the catalyst bed and found that the maximum temperature difference between the reactor wall and center varies from 3K for a reactor tube diameter of 0.017 m to a temperature difference of 15K for a reactor tube diameter of 0.047 m. As such, the Co catalyst present in the part of the catalyst bed, which is at a higher temperature, will be susceptible to a faster deactivation. Furthermore, the center of the catalyst bed could be at the onset of reactor runaway. To avoid such situations, an estimate of the radial temperature profile is required. This can be obtained by incorporating the necessary expressions for radial heat, eq. [6-15], and mass, eq. [6-16], transfer to the one dimensional reactor equations, eqs. [6-7]-[6-14]. The temperature field in the catalyst bed in case a gas-solid reactor is considered, is presented in Figure 6-17 for the reactor dimensions, inlet conditions, … as in Table 6-2.

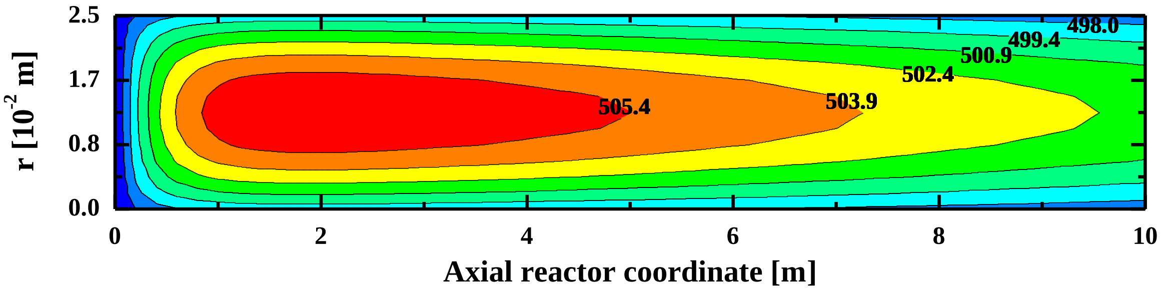

Figure 6-17: Temperature field in the catalyst bed of a gas-solid reactor. Inlet conditions, reactor dimension, … are taken from Table 6-2. The simulation results are obtained by integrating eqs. [6-1], [6-2], [6-7],[6-8],[6-13], [6-15], [6-16] and [6-17] with eqs. [6-4], [6-5], [6-9], [6-19] and [6-20] as boundary conditions. The integration is performed with the DASPK solver after applying the numerical methods outlined in section 6.3. The transfer parameters and gas and liquid properties are calculated as explained in section 6.2.2

The simulation results clearly indicate that a radial temperature profile is simulated to develop for the employed reactor configuration and operating conditions, i.e., at an axial distance of 2m the temperature difference between the temperature at the wall and the temperature in the center of the catalyst bed is 10K. The maximum temperature in the reactor amounts to 507 K compared to 502 K in case only the one dimensional reactor equations are used, see Figure 6-10. A liquid recycle reduces the maximum temperature. The maximum temperature in case a liquid recycle is considered is limited to 498K which is two degrees more compared to the simulation results with the one dimensional model, see Figure 6-16.

6.5 Conclusions

The Single-Event MicroKinetic (SEMK) model has been incorporated in a multi-scale model for a Trickle Bed Reactor (TBR). Three scales have been explicitly accounted for, i.e., the scale of the active site by means of the SEMK model, the interaction of reaction and diffusion at the catalyst pellet scale and the hydrodynamic and radial transport transport phenomena on the reactor scale. The combination of a microkinetic model with a reactor model allows to simulate the concentration profiles of all the individual components.

The combination of reaction and diffusion in the catalyst pellet results in strong concentration gradients. Furthermore, due to a difference in diffusion coefficients of CO and H_2, the H_2/CO molar ratio increases significantly. Moreover, only the outer shell of the catalyst pellet contributes to the CO conversion. These results clearly point out the importance of incorporating a reaction-diffusion model into an industrial reactor model. Studying the performance of the catalyst pellet at varying reaction conditions indicates that a substoichiometric H_2/CO molar ratio of 2 is beneficial for the S_{C5+} selectivity. Furthermore, the net CO consumption rate exhibits a maximum as a function of the H_2/CO molar ratio. It is interesting to note that at these lower H_2/CO molar ratios, an increasing temperature does not have a significant impact on the S_{C5+} selectivity.

In a TBR, the observed conversions and selectivities are primarily determined by the phenomena occurring on the catalyst pellet scale. As a consequence, including a liquid flow in the model does not significantly impact the simulation results. The most prominent result of a liquid flow is related to a higher heat transfer coefficient which in turn decreases the maximum temperature. The simulation results with the two dimensional models show that in FTS TBRs radial temperature profiles can develop.

6.6 References

1. Dry, M.E., *Practical and theoretical aspects of the catalytic Fischer-Tropsch process.* Applied Catalysis a-General, 1996. **138**(2): p. 319-344.
2. Dry, M.E., *Fischer-Tropsch reactions and the environment.* Applied Catalysis a-General, 1999. **189**(2): p. 185-190.
3. Pohlmann, F. and A. Jess, *Interplay of reaction and pore diffusion during cobalt-catalyzed Fischer-Tropsch synthesis with CO2-rich syngas.* Catalysis Today, 2016. **275**: p. 172-182.
4. Kaskes, B., D. Vervloet, F. Kapteijn, and J.R. van Ommen, *Numerical optimization of a structured tubular reactor for Fischer-Tropsch synthesis.* Chemical Engineering Journal, 2016. **283**: p. 1465-1483.
5. Ghouri, M.M., S. Afzal, R. Hussain, J. Blank, D.B. Bukur, and N.O. Elbashir, *Multi-scale modeling of fixed-bed Fischer Tropsch reactor.* Computers & Chemical Engineering, 2016. **91**: p. 38-48.
6. Brunner, K.M., H.D. Perez, R.P.S. Peguin, J.C. Duncan, L.D. Harrison, C.H. Bartholomew, and W.C. Hecker, *Effects of Particle Size and Shape on the Performance of a Trickle Fixed-Bed Recycle Reactor for Fischer-Tropsch Synthesis.* Industrial & Engineering Chemistry Research, 2015. **54**(11): p. 2902-2909.
7. Wu, J.M., H.T. Zhang, W.Y. Ying, and D.Y. Fang, *Simulation and Analysis of a Tubular Fixed-Bed Fischer-Tropsch Synthesis Reactor with Co-Based Catalyst.* Chemical Engineering & Technology, 2010. **33**(7): p. 1083-1092.
8. Jess, A. and C. Kern, *Modeling of Multi-Tubular Reactors for Fischer-Tropsch Synthesis.* Chemical Engineering & Technology, 2009. **32**(8): p. 1164-1175.
9. Guettel, R. and T. Turek, *Comparison of different reactor types for low temperature Fischer-Tropsch synthesis: A simulation study.* Chemical Engineering Science, 2009. **64**(5): p. 955-964.
10. Wang, Y.N., Y.Y. Xu, Y.W. Li, Y.L. Zhao, and B.J. Zhang, *Heterogeneous modeling for fixed-bed Fischer-Tropsch synthesis: Reactor model and its applications.* Chemical Engineering Science, 2003. **58**(3-6): p. 867-875.
11. Iglesia, E., S.C. Reyes, R.J. Madon, and S.L. Soled, *Selectivity control and catalyst design in the Fischer-Tropsch Synthesis - Sites, pellets and reactors.* Advances in Catalysis, 1993. **39**: p. 221-302.
12. Maestri, M. and A. Cuoci, *Coupling CFD with detailed microkinetic modeling in heterogeneous catalysis.* Chemical Engineering Science, 2013. **96**: p. 106-117.
13. Andersson, B., R. Andersson, L. Håkansson, M. Mortensen, R. Sudiyo, and B. van Wachem, *Computational Fluid Dynamics for Engineers*. 2011, Cambridge: Cambridge University Press.
14. Wang, Y., J. Chen, and F. Larachi, *Modelling and simulation of trickle-bed reactors using computational fluid dynamics: A state-of-the-art review.* The Canadian Journal of Chemical Engineering, 2013. **91**(1): p. 136-180.
15. Atwood, H.E. and C.O. Bennett, *Kinetics of Fischer-Tropsch Reaction over Iron.* Industrial & Engineering Chemistry Process Design and Development, 1979. **18**(1): p. 163-170.

16. Bub, G., M. Baerns, B. Bussemeier, and C. Frohning, *Prediction of the Performance of Catalytic Fixed-Bed Reactors for Fischer-Tropsch Synthesis.* Chemical Engineering Science, 1980. **35**(1-2): p. 348-355.
17. Jess, A., R. Popp, and K. Hedden, *Fischer-Tropsch-synthesis with nitrogen-rich syngas - Fundamentals and reactor design aspects.* Applied Catalysis a-General, 1999. **186**(1-2): p. 321-342.
18. Everson, R.C., H. Mulder, and M.J. Keyser, *The Fischer-Tropsch reaction with supported ruthenium catalysts: Modelling and evaluation of the reaction rate equation for a fixed bed reactor.* Applied Catalysis a-General, 1996. **142**(2): p. 223-241.
19. Blanks, R.F., *Fischer-Tropsch Synthesis Gas Conversion Reactor.* Chemical Engineering Science, 1992. **47**(5): p. 959-966.
20. Philippe, R., M. Lacroix, L. Dreibine, C. Pham-Huu, D. Edouard, S. Savin, F. Luck, and D. Schweich, *Effect of structure and thermal properties of a Fischer-Tropsch catalyst in a fixed bed.* Catalysis Today, 2009. **147**: p. S305-S312.
21. Sharma, A., R. Philippe, F. Luck, and D. Schweich, *A simple and realistic fixed bed model for investigating Fischer-Tropsch catalyst activity at lab-scale and extrapolating to industrial conditions.* Chemical Engineering Science, 2011. **66**(24): p. 6358-6366.
22. Rafiq, M.H., H.A. Jakobsen, R. Schmid, and J.E. Hustad, *Experimental studies and modeling of a fixed bed reactor for Fischer-Tropsch synthesis using biosyngas.* Fuel Processing Technology, 2011. **92**(5): p. 893-907.
23. Ermolaev, V.S., K.O. Gryaznov, E.B. Mitberg, V.Z. Mordkovich, and V.F. Tretyakov, *Laboratory and pilot plant fixed-bed reactors for Fischer-Tropsch synthesis: Mathematical modeling and experimental investigation.* Chemical Engineering Science, 2015. **138**: p. 1-8.
24. Haarlemmer, G. and T. Bensabath, *Comprehensive Fischer-Tropsch reactor model with non-ideal plug flow and detailed reaction kinetics.* Computers & Chemical Engineering, 2016. **84**: p. 281-289.
25. Kirillov, V.A., L.A. Mikhailova, S.I. Fadeyev, and V.K. Korolev, *Critical phenomena of an exothermic reaction proceeding on a partially wetted porous catalyst grain.* Combustion Explosion and Shock Waves, 2002. **38**(5): p. 508-517.
26. Mikhailova, I.A., V.A. Kirillov, S.I. Fadeev, and M.G. Slin'ko, *Mathematical modelling of exothermic catalytic reaction in a single partially-wetted porous catalyst particle.* Chemical Engineering Journal, 2003. **91**(2-3): p. 181-189.
27. Wang, Y.N., Y.Y. Xu, H.W. Xiang, Y.W. Li, and B.J. Zhang, *Modeling of catalyst pellets for Fischer-Tropsch synthesis.* Industrial & Engineering Chemistry Research, 2001. **40**(20): p. 4324-4335.
28. Madon, R.J. and E. Iglesia, *Hydrogen and Co Intrapellet Diffusion Effects in Ruthenium-Catalyzed Hydrocarbon Synthesis.* Journal of Catalysis, 1994. **149**(2): p. 428-437.
29. Welty, J.R., C.E. Wicks, R.E. Wilson, and G.L. Rorrer, *Fundamentals of Momentum, Heat, and Mass Transfer*. Fifth Edition ed. 2007, Oregon: John Wiley & Sons. 711.
30. Martens, G.G. and G.B. Marin, *Kinetics for hydrocracking based on structural classes: Model development and application.* Aiche Journal, 2001. **47**(7): p. 1607-1622.
31. Narasimhan, C.S.L., *Single-Event Microkinetic Modeling of Shape-Selective Hydroconversion*, Ghent University, Department: Chemical Engineering and Technical Chemistry, *PhD*, p. 352

32. Ellman, M.J., N. Midoux, A. Laurent, and J.C. Charpentier, *A New, Improved Pressure-Drop Correlation for Trickle-Bed Reactors.* Chemical Engineering Science, 1988. **43**(8): p. 2201-2206.
33. Lozano-Blanco, G., J.W. Thybaut, K. Surla, P. Galtier, and G.B. Marin, *Simulation of a Slurry-Bubble Column Reactor for Fischer-Tropsch Synthesis Using Single-Event Microkinetics.* AIChE Journal, 2009. **55**(8): p. 2159-2170.
34. Marano, J.J. and G.D. Holder, *Characterization of Fischer-Tropsch liquids for vapor-liquid equilibria calculations.* Fluid Phase Equilibria, 1997. **138**(1-2): p. 1-21.
35. Marano, J.J. and G.D. Holder, *General equation for correlating the thermophysical properties of n-paraffins, n-olefins, and other homologous series .2. Asymptotic behavior correlations for PVT properties.* Industrial & Engineering Chemistry Research, 1997. **36**(5): p. 1895-1907.
36. Marano, J.J. and G.D. Holder, *General equation for correlating the thermophysical properties of n-paraffins, n-olefins, and other homologous series .1. Formalism for developing asymptotic behavior correlations.* Industrial & Engineering Chemistry Research, 1997. **36**(5): p. 1887-1894.
37. Wu, J.M., H.T. Zhang, W.Y. Ying, and D.Y. Fang, *Thermal Conductivity of Cobalt-Based Catalyst for Fischer-Tropsch Synthesis.* International Journal of Thermophysics, 2010. **31**(3): p. 556-571.
38. Yoshida, F. and T. Koyanagi, *Mass Transfer and Effective Interfacial Areas in Packed Columns.* AIChE Journal, 1962. **8**(3): p. 309-316.
39. Fuller, E.N. and J.C. Giddings, *A Comparison of Methods for Predicting Gaseous Diffusion Coefficients.* Journal of Gas Chromatography, 1965. **3**(7): p. 222-&.
40. Fuller, E.N., Schettle.Pd, and J.C. Giddings, *A New Method for Prediction of Binary Gas-Phase Diffusion Coeffecients.* Industrial and Engineering Chemistry, 1966. **58**(5): p. 19-&.
41. Fuller, E.N., K. Ensley, and J.C. Giddings, *Diffusion of Halogenated Hydrocarbons in Helium . Effect of Structure on Collision Cross Sections.* Journal of Physical Chemistry, 1969. **73**(11): p. 3679-&.
42. Reid, R.C., J.M. Prausnitz, and B.E. Poling, *The Properties of Gases and Liquids*. Fourth Edition ed. Chemical Engineering Series. 1988: McGraw-Hill Internation Editions. 741.
43. Mederos, F.S., I. Elizalde, and J. Ancheyta, *Steady-State and Dynamic Reactor Models for Hydrotreatment of Oil Fractions: A Review.* Catalysis Reviews-Science and Engineering, 2009. **51**(4): p. 485-607.
44. Sato, Y., H. Hirose, F. Takahashi, and M. Toda. *Performance of fixed-bed catalytic reactor with co-current gas-liquid flow*. in *1st Pacific Chemical Engineering Congress*. 1974.
45. Schweich, D., *Génie de la réaction chimique*. 2001. 626.
46. Larachi, F., A. Laurent, N. Midoux, and G. Wild, *Experimental-Study of a Trickle-Bed Reactor Operating at High-Pressure: Two-Phase Pressure-Drop and Liquid Saturation.* Chemical Engineering Science, 1991. **46**(5-6): p. 1233-1246.
47. Froment, G.F. and K.B. Bischoff, *Chemical Reactor Analysis and Design*. 1979: John Wiley & Sons. 801.
48. Mariani, N.J., O.M. Martinez, and G.F. Barreto, *Evaluation of heat transfer parameters in packed beds with cocurrent downflow of liquid and gas.* Chemical Engineering Science, 2001. **56**(21-22): p. 5995-6001.

49. Marano, J.J. and G.D. Holder, *A general equation for correlating the thermophysical properties of n-paraffins, n-olefins, and other homologous series .3. Asymptotic behavior correlations for thermal and transport properties.* Industrial & Engineering Chemistry Research, 1997. **36**(6): p. 2399-2408.
50. Specchia, V., G. Baldi, and S. Sicardi, *Heat-Transfer in Packed-Bed Reactors with One Phase Flow.* Chemical Engineering Communications, 1980. **4**(2-3): p. 361-380.
51. Hennecke, F.W. and Schlunde.Eu, *Heat transfer in heated or cooled tubes with packings of spheres, cylinders and raschig rings.* Chemie Ingenieur Technik, 1973. **45**(5): p. 277-284.
52. Taulamet, M.J., N.J. Mariani, G.F. Barreto, and O.M. Martinez, *A critical review on heat transfer in trickle bed reactors.* Reviews in Chemical Engineering, 2015. **31**(2): p. 97-118.
53. *NIST Chemistry WebBook - NIST Standard Reference Database Number 69*. Available from: http://webbook.nist.gov/chemistry.
54. Cohen, N., *Thermochemistry of alkyl free-radicals.* Journal of Physical Chemistry, 1992. **96**(22): p. 9052-9058.
55. Cohen, N., *Revised group additivity values for enthalpies of formation (at 298 K) of carbon-hydrogen and carbon-hydrogen-oxygen compounds.* Journal of Physical and Chemical Reference Data, 1996. **25**(6): p. 1411-1481.
56. Hicks, R.E., *Pressure Drop in Packed Beds of Spheres.* Industrial & Engineering Chemistry Fundamentals, 1970. **9**(3): p. 500-&.
57. Schiesser, W.E., *The numerical method of lines : integration of partial differential equations*. 1991: Academic Press. 326.
58. Brown, P.N., A.C. Hindmarsh, and L.R. Petzold, *Using krylov methods in the solution of large-scale differential-algebraic systems.* Siam Journal on Scientific Computing, 1994. **15**(6): p. 1467-1488.
59. Vervloet, D., F. Kapteijn, J. Nijenhuis, and J.R. van Ommen, *Fischer-Tropsch reaction-diffusion in a cobalt catalyst particle: aspects of activity and selectivity for a variable chain growth probability.* Catalysis Science & Technology, 2012. **2**(6): p. 1221-1233.

Chapter 7 Conclusions and Future Work

Fischer-Tropsch Synthesis (FTS) has been recognized by both the scientific and industrial community as a key step in alternative production routes for base chemicals, liquid transportation fuels and high quality lubricants. A significant increase in the annual number of research publications on the topic and the installation of large-scale production facilities based on this reaction both illustrate a strongly increasing interest in this technology. Optimization of such large-scale production facilities is facilitated by the detailed fundamental understanding that can be obtained from multi-scale modeling. A crucial element of such a multi-scale model is the microkinetic model which simulates the phenomena occurring on the smallest scale, i.e., the transformation of reactants into products on the metal catalyst surface.

The Single-Event MicroKinetic (SEMK) methodology has been successfully extended from Fe catalyzed to Co catalyzed FTS. This SEMK model includes activation energies, i.e., kinetic descriptors, as well as atomic chemisorption enthalpies, i.e., catalyst descriptors. These atomic chemisorption enthalpies are used in the UBI-QEP method which is used to calculate the chemisorption thermodynamics starting from these atomic chemisorption enthalpies and adequate considerations about bonds that break and form. The rate of every elementary step is explicitly accounted for. Activation energies were considered to be carbon number independent. The reversibility of the first methylene insertion step is kinetically relevant due to the higher chemisorption enthalpy of metal methyl surface species compared to the heavier metal alkyl surface species. This in contrast to the SEMK for Fe catalyzed FTS in which the chemisorption enthalpies of the metal alkyl species was independent of the carbon number. The other methylene insertion steps can be considered irreversible. The reversibility of the first methylene insertion step is essential to simulate the experimentally observed deviations from Anderson-Schulz-Flory distribution, i.e., a high methane and low ethene selectivity. Also the symmetry numbers of reactants and transitions states, as required according to the SEMK methodology, contribute to the reproduction of these deviations. In the SEMK model for Fe catalyzed FTS, accounting for symmetry numbers was sufficient to describe the typical deviations from ASF distribution. The hydrogenation of OH^* and CH_2^{**} are the kinetically most significant steps in the reaction mechanism and explains the increase in CO conversion with increasing H_2/CO molar ratio. The activity difference as a function of space time between Fe and Co catalysts was mainly attributed to the oxygen atomic chemisorption enthalpy, being higher on Fe than on Co catalysts. This causes the elementary steps involved in the water formation to become quasi-equilibrated. As a consequence, the O^{**} and OH^* surface coverages increase with increasing H_2O vapor pressure decreasing the free site coverage which is essential for CO dissociation.

The validated SEMK model has been extended for modeling experimental data acquired in more complex set-ups than steady-state operated ones, e.g., in which isotopic transient kinetic analyses can be performed. In this thesis, the developed SEMK model has been validated against such Steady State Isotopic Transient Kinetic Analysis (SSITKA) data. One of the major advantages of the inclusion of SSITKA data into the regression of a microkinetic model is that the microkinetic model is forced to more realistic values for the surface coverages as this is intrinsically present in the SSITKA data. The modeling of such data first required to devise a dedicated simulation methodology. A careful selection of the numerical methods for the integration of the Partial Differential Equations (PDEs) had to be performed. For the discretization of the spatial derivative, flux limiters are required in case the switch time constant of the SSITKA set-up is lower than 0.1s. Of the 14 flux limiter functions considered, the van Albada and van Leer flux limiters result in the lowest CPU time. For switch time constants equal to or higher than 1s, second order upwinding or second order central differencing can be applied. Next to this, a network generation methodology which accounts for the isotopic labeling of the carbon atoms had to be developed. This reaction network methodology is conceived in such a way that the number of species and elementary reactions considered in the network are sufficient for the simulation of the gathered experimental data without losing required information for an adequate simulation of the considered reaction network. This methodology significantly reduces the required CPU time of a simulation, i.e., a reduction in CPU time up to a factor 5 – 10 was obtained without losing critical information on the labeling of the carbon atoms.

An extended version of the SEMK model could be efficiently used for simulation purposes with the devised methodology. This SEMK model was successfully regressed to experimental data consisting of the steady-state data outlet concentration of C_1-C_6 alkanes and C_2-C_5 alkenes and the CO and methane transient response. The salient feature of the extended SEMK model is the inclusion of two site types on the Co catalyst surface, i.e., terrace sites mainly covered with CO, H and HCO and step sites with high metal alkyl surface coverages. The ratio of terrace sites to the total site concentration amounts to 0.72 which is a reasonable value for Co metal particles of 11 nm. The step sites contribute most significantly to the CO dissociation and chain growth takes place exclusively on these sites. The terrace sites dissociate CO to a lesser extent and the converted CO on these sites ends up solely in methane. Alkenes, produced on the step sites, are hydrogenated on the terrace site to the corresponding alkanes.

A multi-scale model for a Multi-Tubular Trickle Bed Reactor (MTTBR) has been constructed. The diffusion of reactants and products through a wax phase inside the catalyst pellet pores significantly reduces the net CO consumption rate and selectivity to long chain hydrocarbons. The simulations demonstrate the strategic advantage not to say the necessity of a multi-scale reactor model for the combined optimization of a catalyst and the corresponding industrial reactor in which the catalyst is employed. Furthermore, the simulations with a multi-scale model can be used to identify the optimal operating conditions to which a catalyst should be exposed. Validation of the microkinetic model at these operating conditions can increase the accuracy of the multi-scale model. Next to this, including the formation of branched hydrocarbons and internal alkenes in the SEMK model would be highly beneficial for process simulations.

In summary, in this thesis, the tools required for microkinetic and multi-scale modeling of complex metal catalyzed reactions such as FTS have been developed and applied. Microkinetic models based on kinetic and catalyst descriptors offer the advantage that experimentally observed trends can be related to intrinsic differences of the catalyst material. By a combination of affinity calculations, differential formation and disappearance factors and a degree of rate control analysis, the underlying chemistry and the effect of parameter values on the observed conversion and selectivities could be quantified. The modeling of SSITKA data requires a specific combination of numerical methods and high performance computing. The combination of microkinetic modeling and SSITKA data further increases the physical significance of the model. The extrapolation of intrinsic kinetic measurements to industrial scale is significantly aided by the use of multi-scale models.

A validation of the SEMK model used in the trickle bed reactor model to experimental data acquired over a broad range of operating pressures would be beneficial. As such, insights can be obtained with respect to the surface coverage dependence of the adsorption of some key surface species. These insights can, subsequently, be helpful in extrapolating data measured at low pressures to higher, c.q., more relevant pressures. Moreover, data acquired at higher pressures will contain more information with respect to the longer chain hydrocarbons. This information can be used to further mechanistically interpret the typically experimentally observed deviations from the ASF distribution at these higher carbon numbers. Furthermore, the accuracy of the trickle bed reactor model would benefit from a microkinetic model validated at operating conditions more close to the industrially relevant conditions. Nevertheless, it is noted that interesting results were already obtained with the current trickle bed reactor model.

A further fine-tuning of the model could be pursued with respect to the number of sites to which some of the surface species bind to by, e.g., modeling adsorption experiments.

Furthermore, the UBI-QEP method could be replaced by other methods which relate the chemisorption enthalpies of surface species to atomic chemisorption enthalpies of H, C and O such as scaling laws.

Other mechanistic proposals for the Fischer-Tropsch Synthesis, e.g., chain growth by CH insertion or CO insertion, could be implemented according to the methodology employed in this thesis to validate them. Based on an assessment of the resulting microkinetic models by meticulously evaluating the atomic chemisorption enthalpies and activation energies and comparing the trends simulated by the different microkinetic models a more likely reaction mechanism could be retained. Next to this, once the different microkinetic models are constructed, a sequential experimental design could be used to discriminate between the different microkinetic models. A more comprehensive approach could be applied as well in which the different possible CO dissociation and chain growth steps are considered at once. Regression of such a microkinetic model to experimental data could be linked to reaction path analysis in order to automatically retain the most important reaction pathways. The development of such a regression methodology belongs to ongoing research currently performed at the Laboratory for Chemical Technology.

Appendix A: Gas and liquid properties

A.1 Gas phase properties

Gas phase molecular diffusion coefficients

The molecular diffusion coefficient of a gas phase component i, $D_{i,m}$ $[m^2 s^{-1}]$, through a gas mixture is calculated as [1]:

$$D_{im} = \left(\sum_{\substack{j=1 \\ j \neq i}}^{n} \frac{x_j}{D_{ij}} \right)^{-1} \qquad \text{[A-1]}$$

Where D_{ij} is the binary diffusion coefficient $[m^2 s^{-1}]$ and x_j the mole fraction of component j in the mixture.

The binary diffusion coefficient D_{ij} is calculated with the method of Fuller et al. [2-4] :

$$D_{ij} = \frac{0.0143 T^{1.75}}{p M_{ij}^{1/2} \left[(\Sigma_v)_i^{1/3} + (\Sigma_v)_j^{1/3} \right]^2} \qquad \text{[A-2]}$$

Where D_{ij} is the binary diffusion coefficient $[cm^2 s^{-1}]$, T the temperature $[K]$, p pressure $[bar]$.

M_{ij} is calculated as:

$$M_{ij} = \frac{2}{\frac{1}{M_i} + \frac{1}{M_j}} \qquad \text{[A-3]}$$

Where M_i is the molecular mass [$gmol^{-1}$].

$(\Sigma_v)_i$ is calculated by summing atomic diffusion volumes, see Table A-1 [1].

Table A-1: Atomic diffusion volumes [1].

Diffusion volumes of small molecules		Atomic diffusion volume increments	
CO	18.0	C	15.9
H_2	6.12	H	2.31

Gas Phase mixture viscosity

The method of Chung et al [1] is used to calculate the gas phase mixture viscosity, η_m [μP]:

$$\eta_m = \eta^* \frac{36.344(M_m T_{cm})^{1/2}}{V_{cm}^{2/3}} \qquad \text{[A-4]}$$

M_m the mixture molecular mass [$g\ mol^{-1}$], T_{cm} the mixture critical temperature [K] and V_{cm} the critical molar volume [$cm^3 mol$]. These mixture properties are calculated according to the binary mixing rules of Chung et al. [1].

η^* is calculated as:

$$\eta^* = \frac{(T_m^*)^{1/2}}{\Omega_v}\left[F_{cm}\left(\frac{1}{G_2} + E_6 y\right)\right] + \eta^{**} \qquad \text{[A-5]}$$

y is calculated as:

$$y = \frac{\rho_m V_{cm}}{6} \tag{A-6}$$

ρ_m mixture density [$mol\ cm^{-3}$]

G_2 is calculated as:

$$G_2 = \frac{E_1 \left[\frac{\left(1 - \exp(E_4 y)\right)}{y} \right] + E_2 G_1 \exp(E_5 y) + E_3 G_1}{E_1 E_4 + E_2 + E_3} \tag{A-7}$$

G_1 is calculated as:

$$G_1 = \frac{1 - 0.5y}{(1 - y)^3} \tag{A-8}$$

E_i with $i = 1, \dots, 10$ is calculated as:

$$E_i = a_i + b_i \omega_m + c_i \mu_{rm}^4 + d_i \kappa_m \tag{A-9}$$

With a_i, b_i, c_i and d_i provided in

Table A-2 and ω_m the mixture acentric factor, μ_{rm} the mixture reduced dipole moment and κ_m a correction factor for highly polar substances.

η^{**} is calculated as:

$$\eta^{**} = E_7 y^2 G_2 \exp\left(E_8 + \frac{E_9}{T_m^*} + \frac{E_{10}}{{T_m^*}^2} \right) \tag{A-10}$$

With T_m^* calculated as:

$$T_m^* = \frac{T}{\left(\frac{\epsilon}{k}\right)_m} \quad [A\text{-}11]$$

With T temperature $[K]$.

Ω_v calculated as:

$$\Omega_v = \frac{A}{(T_m^*)^B} + C\exp(-DT_m^*) + E\exp(-FT_m^*) \quad [A\text{-}12]$$

With A=1.16145, B=0.14874, C=0.52487, D=0.77320, E=2.1617 and F=2.43787

F_{cm} is calculated as:

$$F_{cm} = 1 - 0.2756\omega_m 0.059035\mu_{rm}^4 + \kappa_m \quad [A\text{-}13]$$

T_{cm} is calculated as:

$$T_{cm} = 1.2593\left(\frac{\epsilon}{k}\right)_m \quad [A\text{-}14]$$

V_{cm} is calculated as:

$$V_{cm} = \left(\frac{\sigma_m}{0.809}\right)^3 \quad [A\text{-}15]$$

M_m is calculated as:

$$M_m = \frac{\sum_i \sum_j y_i y_j \left(\frac{\epsilon_{ij}}{k}\right)\sigma_{ij}^2 M_{ij}^{1/2}}{\left(\frac{\epsilon}{k}\right)_m \sigma_m^2} \quad [A\text{-}16]$$

σ_m^3 is calculated as:

$$\sigma_m^3 = \sum_i \sum_j y_i y_j \sigma_{ij}^3 \quad \text{[A-17]}$$

σ_{ii} and σ_{ij} are calculated as:

$$\begin{gathered} \sigma_{ii} = 0.809 V_{ci}^{1/3} \\ \sigma_{ij} = \left(\sigma_i \sigma_j\right)^{1/2} \end{gathered} \quad \text{[A-18]}$$

With V_{ci} the critical molar volume of component i [$cm^3 mol^{-1}$]

$\left(\frac{\epsilon}{k}\right)_m$ is calculated as:

$$\left(\frac{\epsilon}{k}\right)_m = \frac{\sum_i \sum_j y_i y_j \left(\frac{\epsilon_{ij}}{k}\right) \sigma_{ij}^3}{\sigma_m^3} \quad \text{[A-19]}$$

With $\frac{\epsilon_{ii}}{k}$ and $\frac{\epsilon_{ij}}{k}$ calculated as:

$$\begin{gathered} \frac{\epsilon_{ii}}{k} = \frac{T_{ci}}{1.2593} \\ \frac{\epsilon_{ij}}{k} = \left(\frac{\epsilon_i}{k} \frac{\epsilon_j}{k}\right)^{1/2} \end{gathered} \quad \text{[A-20]}$$

T_{ci} the critical temperature of component i [K].

M_{ij} is calculated as:

$$M_{ij} = \frac{2 M_i M_j}{M_i + M_j} \quad \text{[A-21]}$$

With M_i the molecular mass of component i [$g\ mol^{-1}$].

ω_m is calculated as:

$$\omega_m = \frac{\sum_i \sum_j y_i y_j \omega_{ij} \sigma_{ij}^3}{\sigma_m^3} \qquad \text{[A-22]}$$

ω_{ij} is calculated as:

$$\omega_{ij} = \frac{\omega_i + \omega_j}{2} \qquad \text{[A-23]}$$

κ_m is calculated as:

$$\kappa_m = \sum_i \sum_j y_i y_j \kappa_{ij} \qquad \text{[A-24]}$$

κ_{ij} calculated as:

$$\kappa_{ij} = \left(\kappa_i \kappa_j\right)^{1/2} \qquad \text{[A-25]}$$

μ_m^4 is calculated as:

$$\mu_m^4 = \sigma_m^3 \sum_i \sum_j \left(\frac{y_i y_j \mu_i^2 \mu_j^2}{\sigma_{ij}^3}\right) \qquad \text{[A-26]}$$

μ_i the dipole moment of component i $[debyes]$

μ_{rm} is calculated as:

$$\mu_{rm} = 131.3 \frac{\mu_m}{(V_{cm} T_{cm})^{1/2}} \qquad \text{[A-27]}$$

Table A-2: Coefficients for estimating the gas mixture viscosity based on the method of Chung et al. [1].

i	a_i	b_i	c_i	d_i
1	6.324	50.412	-51.680	1189.0
2	$1.210\ 10^{-3}$	$-1.154\ 10^{-3}$	$-6.257\ 10^{-3}$	0.03728
3	5.283	254.209	-168.48	3898.0
4	6.623	38.096	-8.464	31.42
5	19.745	7.630	-14.354	31.53
6	-1.900	-12.537	4.985	-18.15
7	24.275	3.450	-11.291	69.35
8	0.7972	1.117	0.01235	-4.117
9	-0.2382	0.06770	-0.8163	4.025
10	0.06863	0.3479	0.5926	-0.727

Gas phase mixture thermal conductivity

The gas phase mixture thermal conductivity, λ_m $[W(m\,K)^{-1}]$, is calculated according to the method of Chung et al. [1]:

$$\lambda_m = \frac{31.2\eta_m^0\Psi}{M_m}\left(\frac{1}{G_2} + B_6 y\right) + qB_7 y^2 T_{rm}^{1/2} G_2 \qquad \text{[A-28]}$$

With M_m, G_2 and $y$calculated as explained in eq. [A-16], [A-7] and [A-6] respectively. For the correlation of eq. [A-28], the mixture molecular mass has units of $[kg\ mol^{-1}]$.

Ψ is calculated as:

$$\Psi = 1 + \alpha\frac{0.215 + 0.28288\alpha - 1.061\beta + 0.26665Z}{0.6366 + \beta Z + 1.061\alpha\beta} \qquad \text{[A-29]}$$

α is calculated as:

$$\alpha = \frac{c_{vm}}{R} - \frac{3}{2} \qquad \text{[A-30]}$$

With c_{vm} the heat capacity at constant volume [$J(molK)^{-1}$]

β is calculated as:

$$\beta = 0.7862 - 0.7109\omega_m + 1.3168\omega_m^2 \qquad \text{[A-31]}$$

Z is calculated as:

$$Z = 2.0 + 10.5T_{rm}^2 \qquad \text{[A-32]}$$

T_{rm} is calculated as:

$$T_{rm} = \frac{T}{T_{cm}} \qquad \text{[A-33]}$$

With T_{cm} calculated as in eq. [A-14].

η_m^0 is the gas phase mixture at low pressure, calculated as:

$$\eta_m^0 = \frac{26.69F_{cm}(M_mT)^{1/2}}{\sigma_m^2\Omega_v} \qquad \text{[A-34]}$$

With F_{cm}, M_m, σ_m and Ω_v calculated with eq. [A-13], [A-16], [A-17] and [A-12] respectively. The unit of η_m^0 to be used in the correlation of eq. [A-28] has to in [$Pa\ s$]. The correlation of eq. [A-34] provides η_m^0 in [μP]. The unit of M_m for eq. [A-35] is [$g\ mol^{-1}$]

q in eq. [A-28] is calculated as:

$$q = \frac{3.586 \cdot 10^{-3}\left(\frac{T_{cm}}{M_m}\right)^{1/2}}{V_{cm}^{2/3}} \qquad \text{[A-35]}$$

With T_{cm}, M_m and V_{cm} calculated according to eq. [A-14], [A-15] and [A-16] respectively. The units of M_m for the calculation of q is in $[kg\ mol^{-1}]$.

B_i with $i = 1, \ldots, 7$ in eq. [A-28] is calculated as E_i of eq. [A-9] but with the coefficients of Table A-3.

Table A-3: Coefficients for the calculation of B_i.

i	a_i	b_i	c_i	d_i
1	2.4166	7.4824 10^{-1}	-9.1858 10^{-1}	1.2172 10^{+2}
2	-5.0924 10^{-1}	-1.5094	-4.9991 10	6.9983 10
3	6.6107	5.6207	6.4760 10	2.7039 10
4	1.4543	-8.9139	-5.6379	7.4344 10
5	7.9274 10^{-1}	8.2019 10^{-1}	-6.9369 10^{-1}	6.3173
6	-5.8634	1.2801 10	9.5893	6.5529 10
7	9.1089 10	1.2811 10^{2}	-5.4217 10	5.2381 10^{2}

A.2 Liquid phase properties

Molecular diffusion coefficients in the liquid phase

The molecular diffusion coefficient of a component i in the liquid,$D_{i,L}$ $[m^2 s^{-1}]$, is calculated as [5]:

$$
\begin{aligned}
D_{H_2,L} &= 1.085 \cdot 10^{-6} exp\left(\frac{-1625.63}{T}\right) \\
D_{CO,L} &= 5.584 \cdot 10^{-7} exp\left(\frac{-1786.29}{T}\right) \\
D_{i,L} &= D_{CO,L}\left(\frac{V_{mol,CO,L}}{V_{mol,i,L}}\right)^{0.6}
\end{aligned}
$$

[A-36]

With $V_{mol,i,L}$ $[m^3 mol^{-1}]$ the molar volume of H_2O, alkanes and alkenes [5]:

$$V_{mol,CO,L} = 14.8 + 7.4$$

[A-37]

$$V_{mol,H_2O,L} = 2 \cdot 3.7 + 7.4$$

$$V_{mol,C_nH_{2n+2},L} = 14.8n + 3.7(2n + 2)$$

$$V_{mol,C_nH_{2n},L} = 14.8n + 7.4n$$

Partial molar volume at infinite dilution

The partial molar volumes at infinite dilution, $\bar{v}_i^{\infty}$ $[cm^3mol^{-1}]$, of H_2, CO CH_4, C_2H_6 and C_2H_4 are calculated as [6]:

$$\bar{v}_i^{\infty} = A_i + B_iT + n\Delta V_i \qquad \text{[A-38]}$$

Where A_i, B_i, ΔV_i are provided in Table A-4 and n is the carbon number of the alkanes solvent.

Table A-4: Coefficient to calculate the partial molar volume at infinite dilution [6].

	H_2	CO	CH_4	C_2H_6	C_2H_4
ΔV_i	0.704424	1.50538	2.47603	8.02413	5.08308
A	-64.9424	-183528	-7.41354	66.4657	93.6738
B	0.237301	0.160773	0.169051	0	0

Infinite henry coefficients

The Henry coefficients at infinite dilution, He_i^{∞} $[bar]$, is calculated according to Marano et al. [6]:

$$He_i^{\infty} = exp\left(A_i + \frac{B_i}{T} + C_i ln(T) + D_iT^2 + \frac{E_i}{T^2} - n\Delta H_i\right) \qquad \text{[A-39]}$$

Where A_i B_i C_i D_i E_i and ΔH_i are provided in Table A-5 and n is the carbon number of the alkanes solvent.

ABC correlations

The ABC correlations of Marano et al [7-9] are employed to calculated physical properties of the Fischer-Tropsch wax phase. A physical property, Y, is correlated with the general expression:

$$Y = Y_{\infty,0} + \Delta Y_{\infty}(n - n_0) - \Delta Y_0 \exp(-\beta(n \pm n_0)^{\gamma}) \quad \text{[A-40]}$$

With an expression for ΔY_{∞}, ΔY_0, the value of $Y_{\infty,0}$, n_0, β and γ and the $\pm$ depending on the physical property which has to be calculated, see Table A-6. n is the carbon number of the hydrocarbon chain for which the physical property has to be calculated.

The liquid molar volume, $V_{mol,L}$, has unit of $[cm^3 mol^{-1}]$, surface tension, σ_L, $[dyn\, cm^{-1}]$, liquid viscosity, η_L, $[cP]$, saturation pressure, P_{sat}, $[bar]$ and the thermal conductivity, λ_L, $[W(mK)^{-1}]$.

Table A-5: Coefficients to calculate the Henry coefficients at infinite dilution [6].

	H_2	CO	CH_4	C_2H_6	C_3H_8
ΔH_i	0.0200959	0.0173238	0.0190354	0.0226055	0.0214924
A	12.9353	5.79833	0.300209	6.66047	5.22622
B	22.9058	19.5937	-114.655	15.1525	7.43296
C	-0.974709	0.152199	1.02385	-0.0745718	0.0598087
D	$-1.20408 \cdot 10^{-6}$	$-1.89733 \cdot 10^{-6}$	$2.53913 \cdot 10^{-6}$	$-2.55981 \cdot 10^{-7}$	$6.02721 \cdot 10^{-7}$
E	2244.61	2031.63	-4257.18	-239557	-291596

	C_2H_4	C_3H_6	n-C_6H_{14}	H_2O
ΔH_i	0.0246608	0.0202632	0.0173970	0.0605329
A	6.61084	6.33671	5.03841	7.88232
B	15.2170	15.0950	102.049	14.4370
C	-0.0751183	-0.07432429	0.0782713	-0.0648305
D	$-2.56655 \cdot 10^{-7}$	$-2.54569 \cdot 10^{-7}$	$-2.31129 \cdot 10^{-7}$	0
E	-183928	-314944	-650347	-465952

Table A-6: The liquid physical properties [7-9].

Physical property	Correlation	Parameter values	
$V_{mol,L}$	$Y_{\infty,0} + \Delta Y_{\infty}(n - n_0) - \Delta Y_0 \exp(-\beta(n + n_0)^{\gamma})$ $\Delta Y_0 or \Delta Y_{\infty} = A + BT + CT^2 + DT^3$ $Y_{\infty,0} = 0, n_0 = -1.388524, \beta = 5.519846$ and $\gamma = 0.0570632$	$A_{\Delta Y_0} = 8592.30$ $B_{\Delta Y_0} = -85.7292$ $C_{\Delta Y_0} = 0.280284$ $D_{\Delta Y_0} = -4.48451 \cdot 10^{-4}$	$A_{\Delta Y_{\infty}} = 12.7924$ $B_{\Delta Y_{\infty}} = 0.0150627$ $C_{\Delta Y_{\infty}} = -1.30794 \cdot 10^{-5}$ $D_{\Delta Y_{\infty}} = 1.59611 \cdot 10^{-8}$
$\frac{c_{p,L}}{R}$	$Y_{\infty,0} + \Delta Y_{\infty}(n - n_0) - \Delta Y_0 \exp(-\beta(n + n_0)^{\gamma})$ $\Delta Y_0 or \Delta Y_{\infty} = A + BT + CT^2 + DT^3$ $Y_{\infty,0} = 0, n_0 = 1.153418, \beta = 0.183717$ and $\gamma = 0.753795$	$A_{\Delta Y_0} = -58.0001$ $B_{\Delta Y_0} = 0.3304530$ $C_{\Delta Y_0} = -5.86037 \cdot 10^{-4}$ $D_{\Delta Y_0} = 3.24382 \cdot 10^{-8}$	$A_{\Delta Y_{\infty}} = 0.0178118$ $B_{\Delta Y_{\infty}} = 0.0214194$ $C_{\Delta Y_{\infty}} = -3.44532 \cdot 10^{-5}$ $D_{\Delta Y_{\infty}} = 2.00373 \cdot 10^{-8}$
σ_L	$Y_{\infty,0} + \Delta Y_{\infty}(n - n_0) - \Delta Y_0 \exp(-\beta(n - n_0)^{\gamma})$ $\Delta Y_0 or Y_{\infty,0} = A + BT + CT^2$ $\Delta Y_{\infty} = 0, n_0 = 0.264870, \beta = 2.511846$ and $\gamma = 0.201325$	$A_{\Delta Y_0} = 627.213$ $B_{\Delta Y_0} = -0.882888$ $C_{\Delta Y_0} = 0.00268188$	$A_{Y_{\infty,0}} = 73.8715$ $B_{Y_{\infty,0}} = -0.177123$ $C_{Y_{\infty,0}} = 1.54517 \cdot 10^{-4}$
$\ln(\eta_L)$	$Y_{\infty,0} + \Delta Y_{\infty}(n - n_0) - \Delta Y_0 \exp(-\beta(n + n_0)^{\gamma})$ $\Delta Y_0 or \Delta Y_{\infty} = A + \frac{B}{T} + Cln(T) + DT^2 + \frac{E}{T^2}$ $Y_{\infty,0} = 57.8516, n_0 = -2.293981, \beta =$ 2.476409 and $\gamma = 0.0112117$	$A_{\Delta Y_0} = -602.866$ $B_{\Delta Y_0} = 77866.8$ $C_{\Delta Y_0} = 198.006$ $D_{\Delta Y_0} = -4.18077 \cdot 10^{-5}$ $E_{\Delta Y_0} = -2.49477 \cdot 10^{6}$	$A_{\Delta Y_{\infty}} = 0.0290196$ $B_{\Delta Y_{\infty}} = -241.023$ $C_{\Delta Y_{\infty}} = 0.0440959$ $D_{\Delta Y_{\infty}} = -1.84891 \cdot 10^{-7}$ $E_{\Delta Y_{\infty}} = 56561.7$

Table A–6: Continued

Physical property	Correlation	Parameter values	
$ln(P_{sat})$	$Y_{\infty,0}+\Delta Y_{\infty}(n-n_0)-\Delta Y_0\exp(-\beta(n-n_0)^{\gamma})$ $\Delta Y_0 or \Delta Y_{\infty}=A+\frac{B}{T}+Cln(T)+DT^2+\frac{E}{T^2}$ $Y_{\infty,0}=2.7271$, $n_0=1.126231$, $\beta=$ 0.619226 and $\gamma=0.416321$	$A_{\Delta Y_0}=-5.75509$ $B_{\Delta Y_0}=-7.56568$ $C_{\Delta Y_0}=0.0857734$ $D_{\Delta Y_0}=-1.41964\cdot 10^{-5}$ $E_{\Delta Y_0}=2.67209\cdot 10^{5}$	$A_{\Delta Y_{\infty}}=15.8059$ $B_{\Delta Y_{\infty}}=-1496.56$ $C_{\Delta Y_{\infty}}=-2.17342$ $D_{\Delta Y_{\infty}}=7.27763\cdot 10^{-7}$ $E_{\Delta Y_{\infty}}=37876.2$
$\frac{\Delta H_{vap}}{RT_0}$	$Y_{\infty,0}+\Delta Y_{\infty}(n-n_0)-\Delta Y_0\exp(-\beta(n-n_0)^{\gamma})$ $Y_{\infty,0}=812.14$, $\Delta Y_{\infty}=0$, $\Delta Y_0=3080.98$, $n_0=0.112756$, $\beta=1.293274$, $\gamma=$ 0.0156185 and $T_0=298.15$		
λ_L	$Y_{\infty,0}+\Delta Y_{\infty}(n-n_0)-\Delta Y_0\exp(-\beta(n-n_0)^{\gamma})$ $\Delta Y_0 or Y_{\infty,0}=A+BT+CT^2$ $\Delta Y_{\infty}=0$, $n_0=-1.201270$, $\beta=1.241494$ and $\gamma=0.235832$	$A_{\Delta Y_0}=0.0690955$ $B_{\Delta Y_0}=0.00173044$ $C_{\Delta Y_0}=0.0$	$A_{Y_{\infty,0}}=0.212451$ $B_{Y_{\infty,0}}=-04.10325\cdot 10^{-5}$ $C_{Y_{\infty,0}}=0$

A.3 References

1. Reid, R.C., J.M. Prausnitz, and B.E. Poling, *The Properties of Gases and Liquids*. Fourth Edition ed. Chemical Engineering Series. 1988: McGraw-Hill Internation Editions. 741.
2. Fuller, E.N. and J.C. Giddings, *A Comparison of Methods for Predicting Gaseous Diffusion Coefficients.* Journal of Gas Chromatography, 1965. **3**(7): p. 222-&.
3. Fuller, E.N., Schettle.Pd, and J.C. Giddings, *A New Method for Prediction of Binary Gas-Phase Diffusion Coeffecients.* Industrial and Engineering Chemistry, 1966. **58**(5): p. 19-&.
4. Fuller, E.N., K. Ensley, and J.C. Giddings, *Diffusion of Halogenated Hydrocarbons in Helium . Effect of Structure on Collision Cross Sections.* Journal of Physical Chemistry, 1969. **73**(11): p. 3679-&.
5. Wang, Y.N., et al., *Modeling of catalyst pellets for Fischer-Tropsch synthesis.* Industrial & Engineering Chemistry Research, 2001. **40**(20): p. 4324-4335.
6. Marano, J.J. and G.D. Holder, *Characterization of Fischer-Tropsch liquids for vapor-liquid equilibria calculations.* Fluid Phase Equilibria, 1997. **138**(1-2): p. 1-21.
7. Marano, J.J. and G.D. Holder, *A general equation for correlating the thermophysical properties of n-paraffins, n-olefins, and other homologous series .3. Asymptotic behavior correlations for thermal and transport properties.* Industrial & Engineering Chemistry Research, 1997. **36**(6): p. 2399-2408.
8. Marano, J.J. and G.D. Holder, *General equation for correlating the thermophysical properties of n-paraffins, n-olefins, and other homologous series .2. Asymptotic behavior correlations for PVT properties.* Industrial & Engineering Chemistry Research, 1997. **36**(5): p. 1895-1907.
9. Marano, J.J. and G.D. Holder, *General equation for correlating the thermophysical properties of n-paraffins, n-olefins, and other homologous series .1. Formalism for developing asymptotic behavior correlations.* Industrial & Engineering Chemistry Research, 1997. **36**(5): p. 1887-1894.